

# **Optimizing the design of the Final-Focus region for the International Linear Collider**

**Zur Erlangung des akademischen Grades einer  
DOKTORIN DER NATURWISSENSCHAFTEN (Dr. rer. nat.)**

von der KIT-Fakultät für Physik des  
Karlsruher Instituts für Technologie (KIT)  
angenommene und genehmigte

**DISSERTATION**  
von

**M. Sc. Anne Schütz**

Tag der mündlichen Prüfung: 25. Mai 2018

Erstgutachter: Prof. Dr. Günter Quast (KIT)  
Zweitgutachter: Prof. Dr. Eckhard Elsen (CERN)  
Betreuernder Mitarbeiter: Dr. Marcel Stanitzki (DESY)

Karlsruher Institut für Technologie (KIT)  
Fakultät für Physik  
Wolfgang-Gaede-Str. 1  
76128 Karlsruhe

Deutsches Elektronen-Synchrotron (DESY)  
Notkestr. 85  
22607 Hamburg

---

I declare that I have developed and written the enclosed thesis completely by myself, and have not used sources or means without declaration in the text.

Ich versichere wahrheitsgemäß, die vorliegende Doktorarbeit selbstständig angefertigt, alle benutzten Hilfsmittel vollständig und genau angegeben und alles kenntlich gemacht zu haben, was aus Arbeiten anderer unverändert oder mit Änderungen entnommen wurde.

**Hamburg, 04.05.2018**

.....  
(M. Sc. Anne Schütz)



# Zusammenfassung

Der “International Linear Collider” (ILC) ist ein geplanter Linearbeschleuniger für die Kollisionen von Elektronen und Positronen bei einer anfänglichen Schwerpunktsenergie von 250 GeV. Mit seinen Forschungszielen steht er in einem ergänzenden Zusammenhang mit dem “Large Hadron Collider” (LHC). Denn nach der Entdeckung des Higgs-Bosons am LHC in 2012 ist eines der Ziele des ILC, die Eigenschaften und Wechselwirkungen des Higgs-Bosons und des Top-Quarks mit nie dagewesener Präzision zu messen. Auch die Suche nach Teilchen aus Modellen jenseits des Standardmodells, welche ebenfalls auf dem Programm der verschiedenen ILC-Phasen steht, wird durch diese Präzision erleichtert.

Sowohl das Layout des Beschleunigers als auch das der Detektoren muss optimiert werden, um Untergrundraten unterhalb einer gewissen Grenze zu halten und damit die angestrebte Präzision zu erreichen. Hierzu wurden einige Studien durchgeführt, um verschiedene Untergrundquellen zu untersuchen und die Raten im SiD Detektor, einer der beiden für den ILC vorgeschlagenen Detektorexperimente, zu analysieren. Diese Studien basieren auf Monte Carlo Generatoren, welche Untergrundereignisse aus verschiedenen Quellen simulieren. Nach einer vollen Detektorsimulation wurden diese Ereignisse dann in Hinsicht auf die SiD Detektorokkupanz beurteilt. Liegt diese Okkupanz nahe oder sogar oberhalb der von der SiD-Gruppe festgelegten Akzeptanzgrenze, so wurden Vorschläge zur Beschleuniger- und Detektoroptimierung unterbreitet und getestet, mit denen die Okkupanz reduziert werden kann.

Zu den hier untersuchten Untergründen gehören sowohl der  $e^+e^-$ -Paaruntergrund, der durch die Wechselwirkung der elektromagnetischen Felder der kollidierenden Strahlbündel entsteht, als auch der Myonen-Maschinenuntergrund aus der Wechselwirkung des Strahls mit den Beschleunigerinstrumenten, sowie der Neutronenuntergrund, der von den Strahl-Dumps aus in Richtung der Detektoren gerichtet ist. Zusätzliche Simulationen umfassen die Untersuchung des Designs der Strahl-Dumps im Hinblick auf die Bestrahlungsdosis in der Dump-Halle. Die Abhängigkeit des  $e^+e^-$ -Paaruntergrundes von den ILC-Strahlparametern wurde für die in 2017 beantragte Änderung der Parameter für die erste ILC-Phase evaluiert. Die Ergebnisse der in der vorliegenden Arbeit präsentierten Studie haben dabei zur Entscheidungsfindung maßgeblich beigetragen. Neben den Simulationsstudien wurden auch Messungen in der japanischen Beschleunigeranlage “Accelerator Test Facility 2” durchgeführt, um die Maschinenuntergrundrate in Abhängigkeit von verschiedenen Beschleunigerzuständen zu messen. Das Ziel war hierbei die Funktionalität eines Strahlkollimators zu testen.

Bei allen präsentierten Studien werden Vorschläge zur Beschleuniger- und Detektoroptimierung genannt, um die Untergrundraten in SiD zu reduzieren und somit die geplanten Präzisionsmessungen ermöglichen.



# Abstract

The International Linear Collider (ILC) is a proposed linear electron positron collider with a center-of-mass energy of 250 GeV in its first stage. After the discovery of the Higgs boson at the Large Hadron Collider (LHC) at CERN in 2012, the physics goals of the ILC include the measurements of the Higgs boson properties and its interactions, but also measurements of the top quark and searches beyond the Standard Model are part of the ILC program in the different ILC stages. The ILC, however, is not in competition with the LHC, but is a complementary collider experiment, since it is aimed at unprecedented precisions rather than at high collision energies.

In order to achieve such precisions, both the accelerator design and the detector designs have to be optimized with respect to limiting the detector background below an acceptable limit. For the evaluation of various background sources, different Monte Carlo event generators have been used to generate background events that were then analyzed in a full detector simulation of the SiD detector. SiD is one of the proposed detector concepts for the ILC, for which a specific critical acceptance limit for background rates has been set. Throughout the chapters of this thesis, the acceptance limit has been used to assess the arising background occupancy in SiD. If the occupancy has been found to be close to or to exceed the limit, possibilities to reduce the background level have been tested and recommendations for design optimizations have been made.

The presented background simulation studies contain three major background sources: the  $e^+e^-$  pair background from beam-beam interactions, the machine background created by interactions of the beam with the accelerator components, and the neutron background produced in the ILC main beam dumps. In addition to the background study for the main beam dumps, the beam dump designs that are based on water dumps have also been analyzed with respect to the arising irradiation of the surroundings. The pair background was studied with respect to its dependency on different ILC running schemes, such as the proposed changes in the beam parameter sets for the ILC stage at 250 GeV. The results of these studies have been used in 2017 to inform the ILC design decision regarding these beam parameters. Besides the mentioned simulation studies, measurements of the machine background in dependency of certain accelerator conditions have been performed at the Accelerator Test Facility 2 at KEK in Japan. The goal of these measurements was to validate the functionality of a recently installed vertical beam halo collimator that is planned to be used at the ILC as well.

For all the presented topics, recommendations for accelerator and detector design optimizations are given, with which the background level in the SiD detector can be reduced in order to reach the aimed-for precision at the ILC.



# Contents

<b>Zusammenfassung</b>	i
<b>Abstract</b>	iii
<b>1. Introduction</b>	1
<b>2. Physics at lepton colliders</b>	3
2.1. The Standard Model . . . . .	4
2.2. Production modes at lepton colliders . . . . .	8
2.3. Background processes at lepton colliders . . . . .	9
2.3.1. High cross section background processes from beam-beam interactions . . . . .	10
2.3.1.1. Pair background . . . . .	10
2.3.1.2. Bhabha scattering and $\gamma\gamma \rightarrow$ hadrons . . . . .	11
2.3.2. Machine backgrounds . . . . .	12
<b>3. Accelerator physics of linear colliders</b>	15
3.1. Principles of particle acceleration . . . . .	15
3.2. Transverse beam dynamics . . . . .	17
3.3. Longitudinal beam dynamics . . . . .	21
3.4. Linear colliders in comparison to circular colliders . . . . .	23
<b>4. The International Linear Collider</b>	27
4.1. Physics motivation . . . . .	27
4.1.1. How to reach unprecedented precisions . . . . .	28
4.1.2. ILC as a Higgs factory . . . . .	29
4.1.2.1. The Higgs production modes at an $e^+e^-$ collider . . . . .	30
4.1.2.2. The Higgs measurements . . . . .	30
4.1.3. Physics at later ILC stages . . . . .	34
4.2. The ILC layout . . . . .	36
4.2.1. From beam generation to collision . . . . .	37
4.2.2. Staging . . . . .	44
4.3. Possible site . . . . .	46
4.4. The detector experiments . . . . .	46
4.4.1. The Silicon Detector . . . . .	47
4.4.1.1. SiD subdetectors . . . . .	48
4.4.1.2. SiD detector variants . . . . .	53
4.4.1.3. Detector readout architecture . . . . .	54
4.4.2. The International Large Detector . . . . .	55

<b>5. <math>e^+e^-</math> pair background</b>	<b>57</b>
5.1. The Monte Carlo event generator GuineaPig . . . . .	57
5.2. Characteristics of the fermion pair processes . . . . .	59
5.3. Pair background dependency on ILC beam parameters . . . . .	63
5.3.1. Pair background envelopes . . . . .	63
5.3.2. SiD vertex detector occupancy studies and buffer depth . . . . .	65
5.3.3. Pair background occupancy in further SiD subdetectors . . . . .	69
5.3.4. Impact of the pair background studies on ILC design choices . . . . .	69
5.4. Dependency of the pair background occupancy on detector design choices . . . . .	72
5.5. Hit maps of the SiD subdetectors . . . . .	73
5.6. Comparing the pair background occupancy of different ILC stages . . . . .	75
5.7. Conclusion . . . . .	77
<b>6. Muon background from the Beam Delivery System</b>	<b>81</b>
6.1. MUCARLO . . . . .	82
6.2. Effect of muons on the SiD performance . . . . .	85
6.2.1. Muon hit distribution . . . . .	85
6.2.2. SiD occupancy . . . . .	88
6.3. Conclusion . . . . .	90
<b>7. Beam halo collimators for machine background reduction</b>	<b>93</b>
7.1. The Accelerator Test Facility 2 . . . . .	93
7.2. Vertical beam halo collimator . . . . .	95
7.3. Background studies . . . . .	97
7.3.1. RHUL Cherenkov detector . . . . .	97
7.3.2. Collimator apertures scan at different intensities and vacuum pressures . . . . .	100
7.4. Simulation study of the vertical beam halo collimator . . . . .	101
7.4.1. BDSIM . . . . .	101
7.4.2. Modeling the vertical beam halo collimator . . . . .	101
7.4.3. Simulation results . . . . .	102
7.5. Conclusion . . . . .	106
<b>8. Background from the main beam dumps</b>	<b>109</b>
8.1. FLUKA and <i>flair</i> . . . . .	110
8.2. ILC main beam dump designs . . . . .	111
8.2.1. Design 1 . . . . .	111
8.2.2. Design 2 . . . . .	112
8.3. Simulation studies of the beam dump surrounding . . . . .	112
8.3.1. Energy deposition . . . . .	113
8.3.2. Irradiation dose . . . . .	114
8.3.3. Particle fluxes . . . . .	117
8.4. Simulation studies of the extraction line . . . . .	120
8.5. SiD occupancy study of the beam dump neutrons . . . . .	122
8.6. Alternative beam dump design . . . . .	126
8.6.1. Deposited energy and irradiation dose . . . . .	127
8.6.2. Neutron flux . . . . .	127

---

8.7. Conclusion and outlook . . . . .	127
<b>9. Results: prospects, requirements, and limits for the International Linear Collider</b>	<b>131</b>
9.1. Keeping the detector background below the critical acceptance limit . . . . .	131
9.2. Impact of the ILC running scheme on the background level . . . . .	132
9.3. Impact of the SiD design on the background level . . . . .	133
<b>10. Conclusion</b>	<b>135</b>
<b>A. Pair background</b>	<b>137</b>
A.1. GuineaPig event generation . . . . .	137
A.2. SiD occupancy for the ILC250 parameter sets . . . . .	138
A.2.1. Pair background occupancy in the SiD vertex detector . . . . .	138
A.2.2. Pair background occupancy in further SiD subdetectors . . . . .	142
<b>B. Muon background from the Beam Delivery System</b>	<b>143</b>
<b>C. Background from the main beam dumps</b>	<b>145</b>
<b>Bibliography</b>	<b>149</b>
<b>Acknowledgments</b>	<b>159</b>



# List of Figures

2.1. Table of the elementary particles of the Standard Model . . . . .	4
2.2. SM Feynman diagram of the EM interaction . . . . .	6
2.3. SM Feynman diagrams of the strong interactions . . . . .	7
2.4. SM Feynman diagram of the weak interactions . . . . .	7
2.5. Production cross sections for ILC and LHC . . . . .	9
2.6. Illustration of secondary $e^+e^-$ pair production from beamstrahlung photons . . . . .	10
2.7. Feynman diagrams of the production of the secondary $e^+e^-$ pairs from beamstrahlung. .	11
2.8. Feynman diagrams of Bhabha scattering and the $\gamma\gamma \rightarrow$ hadrons process. . . . .	12
3.1. Schematic layout of a Widerøe linac . . . . .	16
3.2. Picture and schematic of multi-cell RF cavities . . . . .	16
3.3. Schematic drawings of a quadrupole magnet with magnetic field lines . . . . .	19
3.4. Schematic of a FODO structure . . . . .	19
3.5. Schematic of a phase space ellipse . . . . .	20
3.6. Illustrations explaining “phase focusing” . . . . .	22
3.7. Illustration explaining “velocity bunching” . . . . .	22
3.8. Illustration explaining “magnetic compression” in a chicane . . . . .	23
3.9. Construction cost of linear and circular colliders . . . . .	26
4.1. Higgs event displays at LHC and ILC . . . . .	28
4.2. Cross sections for the Higgs production modes at ILC as a function of $\sqrt{s}$ . . . . .	31
4.3. Plot of the Higgs decay branching ratios as a function of the Higgs mass . . . . .	32
4.4. Higgs coupling precisions for various SM particles in model dependent and independent analyses . . . . .	33
4.5. Top quark pair production cross section . . . . .	34
4.6. Feynman diagrams of double Higgs production processes . . . . .	35
4.7. Double Higgs production cross sections . . . . .	35
4.8. Predicted MSSM deviations from SM Higgs couplings . . . . .	36
4.9. Feynman diagrams of radiative WIMP pair production . . . . .	36
4.10. Schematic layout of the ILC . . . . .	37
4.11. Schematic layout of an undulator . . . . .	38
4.12. ILC damping ring layout . . . . .	39
4.13. Histogram of the occurring XFEL cavity gradients . . . . .	40
4.14. Layout of the ILC Beam Delivery System . . . . .	41
4.15. Schematic of a beam crossing with crab cavities . . . . .	42
4.16. Illustration of the ILC interaction region hall . . . . .	43
4.17. Different accelerator layouts for the ILC250 stage . . . . .	44
4.18. ILC staging run plans . . . . .	45
4.19. Possible site for the ILC . . . . .	46

4.20. Visualization of the SiD detector . . . . .	47
4.21. Visualization of the SiD vertex detector . . . . .	49
4.22. Plot of reconstructed SiD vertex positions . . . . .	49
4.23. Flavor tagging purity vs. efficiency in SiD . . . . .	49
4.24. Material budget of the SiD vertex and tracker detector . . . . .	50
4.25. Material budget of the CMS pixel detector . . . . .	50
4.26. Drawing of the SiD tracking detector . . . . .	51
4.27. Visualization of the granular SiD calorimeters . . . . .	52
4.28. Drawing of the SiD forward detectors . . . . .	53
4.29. Design variants of the SiD BeamCal . . . . .	54
5.1. Pair background event displays . . . . .	58
5.2. Plots of pair background longitudinal and transverse momentum distributions . . . . .	59
5.3. Schematic projection of a helix track on the xy-plane . . . . .	60
5.4. Pair background density distribution for the ILC500 . . . . .	60
5.5. Pair background density distributions at different center-of-mass energies . . . . .	62
5.6. Pair background density for the proposed ILC250 beam parameter sets . . . . .	64
5.7. Pair background density projection for different ILC250 beam parameter sets . . . . .	65
5.8. Pair background occupancy in the SiD vertex detector for the ILC250 . . . . .	67
5.9. Pair background occupancy in the SiD vertex detector barrel layers for the ILC250 SetA . . . . .	68
5.10. Pair background occupancy in the SiD vertex detector layer 0 for the ILC250 . . . . .	70
5.11. Pair background occupancy in various inner SiD subdetectors for the ILC250 . . . . .	71
5.12. Pair background occupancy in the SiD vertex detector for the ILC250 set (A) for different SiD geometry variants . . . . .	72
5.13. Pair background vertex maps in the SiD detector . . . . .	74
5.14. Pair background hit time maps in the SiD vertex detector . . . . .	75
5.15. Pair background occupancy in the SiD vertex detector for the ILC500 and the ILC250 . . . . .	76
5.16. Pair background occupancy in the SiD vertex detector for the ILC500 and the ILC500 “Lumi Up” . . . . .	76
5.17. Pair background occupancy in the SiD vertex detector for the ILC250, ILC500 and the ILC500 “Lumi Up” with time gates . . . . .	78
6.1. Muon production processes . . . . .	82
6.2. BDS muon shielding options . . . . .	83
6.3. Muon tracks in the Beam Delivery Systems . . . . .	84
6.4. SiD Event displays of muon background from the ILC Beam Delivery System . . . . .	86
6.5. Muon energy . . . . .	87
6.6. Number of muon hits in the SiD subdetectors . . . . .	87
6.7. Muon hit time in the SiD subdetectors . . . . .	88
6.8. SiD HCAL barrel occupancy from BDS muons . . . . .	89
6.9. SiD tracker endcap occupancy from BDS muons . . . . .	89
6.10. BDS muons looping . . . . .	90
7.1. ATF accelerator . . . . .	94
7.2. ATF2 schematic . . . . .	95
7.3. Drawing of the beam halo collimator . . . . .	96

7.4. Picture of the installed beam halo collimator . . . . .	96
7.5. Schematic drawing of the RHUL Cherenkov detector setup . . . . .	97
7.6. Pictures of the RHUL Cherenkov detector . . . . .	98
7.7. RHUL Cherenkov detector calibrations . . . . .	99
7.8. RHUL Cherenkov detector signal vs. collimator aperture . . . . .	100
7.9. ATF2 lattice in BDSIM . . . . .	101
7.10. Model of the vertical beam halo collimator used in the BDSIM simulation . . . . .	102
7.11. Comparison of the ATF2 beam size development in BDSIM and MADX . . . . .	102
7.12. Number of secondary particles created in the ATF2 components . . . . .	103
7.13. Number of particles at the beam halo collimator . . . . .	104
7.14. Number of particles at the RHUL Cherenkov detector . . . . .	105
8.1. Schematic of the ILC interaction region with extraction line . . . . .	109
8.2. Preview of the geometry construction in <i>flair</i> . . . . .	110
8.3. Geometry visualization of the ILC main beam dump hall . . . . .	111
8.4. ILC main beam dump design 1 . . . . .	112
8.5. ILC main beam dump design 2 . . . . .	113
8.6. Energy deposition in the ILC main beam dump . . . . .	114
8.7. Dose equivalent in the ILC main beam dump . . . . .	115
8.8. Dose rate comparison of the ILC main beam dump designs . . . . .	116
8.9. Dose rate in the ILC main beam dump after one year . . . . .	116
8.10. Residual nuclei in the ILC main beam dump after one year . . . . .	117
8.11. Electron flux in the ILC main beam dump . . . . .	118
8.12. Neutron flux in the ILC main beam dump . . . . .	118
8.13. Neutron scoring plane in the main beam dump hall . . . . .	119
8.14. FLUKA model of the ILC extraction line . . . . .	120
8.15. Spatial distribution of the neutron density and the deposited energy in the ILC extraction line tunnel . . . . .	121
8.16. Beam dump neutron momenta in SiD . . . . .	122
8.17. Beam dump neutrons absorbed without leaving hit in SiD . . . . .	123
8.18. Event displays of the beam dump neutron hits in SiD . . . . .	124
8.19. Number of hits in the SiD subdetectors of the ILC main beam dump neutrons . . . . .	125
8.20. Neutron hit time in the SiD subdetectors . . . . .	125
8.21. Neutron occupancy in the SiD muon system and BeamCal . . . . .	126
8.22. Deposited energy and dose equivalent in a gaseous beam dump . . . . .	128
A.1. Pair background occupancy in all SiD vertex detector barrel layers for the ILC250 . . . . .	138
A.1. Pair background occupancy in all SiD vertex detector barrel layers for the ILC250 . . . . .	139
A.2. Pair background occupancy in all SiD vertex detector endcap layers for the ILC250 . . . . .	140
A.2. Pair background occupancy in all SiD vertex detector endcap layers for the ILC250 . . . . .	141
A.3. Pair background occupancy in the SiD calorimeter barrels for the ILC250 . . . . .	142
B.1. Occupancy from BDS muons of various SiD subdetectors . . . . .	143
B.1. Occupancy from BDS muons of various SiD subdetectors . . . . .	144
C.1. Dose rate in the ILC main beam dump Design 1 after cooling times . . . . .	145
C.1. Dose rate in the ILC main beam dump Design 1 after cooling times . . . . .	146

C.2. Dose rate in the ILC main beam dump Design 2 after cooling times . . . . .	147
C.2. Dose rate in the ILC main beam dump Design 2 after cooling times . . . . .	148

# 1

## Chapter 1.

# Introduction

Since the 1920's, accelerator physics research has been rapidly advancing, and with it, so is high-energy particle physics. Starting with the first accelerating structures, which could accelerate particles to no more than a few hundred keV, the reach to higher and higher center-of-mass energies requires new inventions in the field of particle accelerators. Along with this goes the development of particle detectors, which need to adapt to the increasingly demanding environments of particle collisions that are created by the high-performing colliders. Also other areas benefit from the fast pace in the research efforts and scientific breakthroughs, such as the development of sensor technologies for mobile phones, materials for the aerospace industry, or medical applications like cancer therapy. High-energy and accelerator physics are therefore pioneering in many different scopes.

In the field of particle physics, discoveries of new particles and measurements of their characteristics have given explanations and insights to some of the key questions about the composition of matter, the fundamental forces that describe all physical interactions, and about the beginning of the universe. The first experimental evidence of the Higgs boson in 2012 [1, 2] was the discovery of one of the missing pieces in the current understanding of the fundamental building blocks of the universe. This was accomplished at the Large Hadron Collider (LHC) at CERN [3]. With the LHC being the particle collider with the world's highest nominal collision energy of 14 TeV, the pursuit for the highest energies has reached its peak for the moment. This does however not mean that the end of this pursuit is near, future colliders at the energy frontier are proposed for the coming decades.

After a synopsis of the current knowledge of fundamental particle physics and accelerator physics in Chapters 2 and 3, it will be derived that colliders at the energy frontier need a complementary collaborator in order to provide a complete understanding of open issues of particle physics, such as the properties of the Higgs boson. The International Linear Collider (ILC) is such a collaborator. It is a proposed linear electron positron collider designed for high-energy physics experiments, not at the energy frontier but at the precision frontier. Its collision energy will hence be in the range of 250 GeV to 1 TeV, aiming to measure particle physics processes with an unprecedented precision that is orders of magnitude better than the LHC. Chapter 4 will give an overview of the ILC accelerator design and its detector experiments, and will motivate its physics goals. An important goal is the measurements of the Higgs boson couplings to elementary particles. Due to the high precision, the ILC will be able to measure these couplings to  $\sim 1\%$  accuracy, which is needed to distinguish different physics models. Herein lies the discovery potential of the ILC.

In order to achieve these goals, precision detector experiments are needed with high tracking resolutions and granular calorimeter designs. To this end, the detector requirements are strict, and

emphasize a low material budget for improving the tracking performance. The ILC aims for nanometer-sized beams to gain high luminosities and to allow the experiments' vertex detector to have a minimal radius. This leads to high vertex reconstruction efficiencies, but also to the fact that the detector environment has to rely on minimal background levels. If the occupancy in the innermost subdetectors is too high, the vertex detector performance declines and the ILC goal of unprecedented precision cannot be achieved.

A complete understanding of the detector background and its impact on the detector performance is therefore crucial, especially because of the ILC beam timing structure and the readout architecture of the detectors. Chapters 5 - 8 present detailed studies of various background sources, and show that the background can be constrained by optimizing the accelerator and the SiD detector layout. SiD is one of the two proposed detector experiments for the ILC, and the focus of the presented detector occupancy studies. The chapters are sorted by beam induced backgrounds, machine backgrounds, and backgrounds from the ILC main beam dumps. All of these backgrounds originate inside the detectors (in the case of the beam induced backgrounds), or in parts of the ILC accelerator close to the detectors. The results of the studies have been used to inform design decisions of the ILC accelerator on different topics.

First, the simulation studies concerning the substantial  $e^+e^-$  pair background arising from beam-beam interactions will be discussed in Chapter 5. Since this background is directly dependent on ILC running schemes, various studies of its dependencies have been conducted. A study of the timing of the background hits in the individual SiD subdetectors gave hints on how to reduce the background occupancy further.

Chapters 6 and 7 then investigate the backgrounds from the interaction of the beam with machine components, and the possibilities to reduce these backgrounds. Chapter 6 presents a simulation study of the muon background from the ILC Beam Delivery System, whereas for Chapter 7 both direct measurements and simulation studies of machine background levels at the Accelerator Test Facility 2 were done.

Finally, as discussed in Chapter 8, the ILC main beam dumps present another source of detector background, and have been studied in a detailed simulation. Due to their current design, several issues have to be addressed, not only because of the arising background but also because of the irradiation of the beam dump surroundings.

The results of all studies done for this thesis are then summarized in Chapter 9. It shows that analyzing the sources of background in detail provides crucial input for the optimization of the ILC accelerator itself. Recommendations are given for optimizing the accelerator with respect to the beam parameters and possible shielding options for the Final-Focus region, which contains the parts of the ILC close to the detectors. Afterwards, the detector collaborations have to consider the impact of the background in the design of the detector geometry and its readout architecture, and refine them accordingly. Also here, recommendations for the SiD detector have been made. This will bring the ILC closer to its goal of measurements at unprecedented precision.

# 2

## Chapter 2.

# Physics at lepton colliders

*The physics at particle colliders, where two particle beams are brought into collision, is the physics of atoms and quanta, of nuclei and partons, of particles that build up everything we know, but also of new particles, physics beyond our current knowledge. After a brief introduction of the Standard Model (a theory describing the elementary particles and the fundamental forces) in Section 2.1, the physics processes including their production modes (Section 2.2) and background processes (Section 2.3) at a lepton collider will be explained in more detail.*

Particle physics extends back to the ancient Greek times, when the idea was developed that matter is made of “indivisible” (átomos, Greek) parts. Atoms are, in fact, not indivisible at all. When the electron was experimentally discovered in 1897 by J.J. Thomson, it was proposed that these particles must be a component of every atom [4, p. 13ff]. This sparked the interest of many physicists in the early 20<sup>th</sup> century to perform experiments probing atoms. One of them was Ernest Rutherford, who fired alpha particles<sup>1</sup> through a thin gold foil, and thereby found that atoms are mostly empty with a positively charged nucleus that is only a fraction of the size of the atom itself [5]. This discovery was a crucial step towards the modern atomic model.

Closer to our current understanding of the atomic model is the Bohr model, developed by Niels Bohr in 1914 [4, p. 15]. It asserts that electrons orbit the positively charged nucleus on stable shells with distinct radii. The shells correspond to discrete energies, such that an electron switching from one shell to a shell with a larger or smaller radius would have to absorb energy, or emit energy respectively. This energy quantum is absorbed or emitted in the form of light, or more precisely, in the form of a photon. Nowadays, it is known that the electrons do not orbit the nucleus on discrete shells but rather in orbital zones, where the electron has a higher probability to be observed.

In order for an atom to have a neutral charge, the number of electrons in the atomic shells has to be balanced by an equal amount of positive charge in the nucleus. It was already proven by Rutherford that nuclei of different atoms are built from the hydrogen nucleus. He thereby discovered the proton, and explained that the positive charge of the nucleus is the summed up charges of the protons inside the nucleus. In 1932, it was found that atoms can not only consist of electrons and protons. [4, p. 15] The mass measurements of various isotopes showed that their masses differed by concrete amounts.

---

<sup>1</sup> Alpha particles are the nuclei of Helium atoms. Ernest Rutherford obtained them from decays of uranium and other radioactive elements.

The explanation was that the nucleus must consist of protons and particles with a similar mass but a neutral charge, the neutrons. Isotopes are therefore atoms of the same element with the same number of electrons and protons, but with a different amount of neutrons.

Over the years, the development of particle accelerators that can accelerate particles to higher and higher energies allowed to probe even the constituents of the atom. This showed that the end had not been reached yet, that protons and neutrons are not elementary but composite particles. Their partons, the quarks and gluons, are part of the current theory of all elementary particles and the fundamental forces they interact with, the Standard Model.

## 2.1. The Standard Model

The Standard Model (SM) was developed and formulated around the 1960s and 1970s, when the theories of the electromagnetic and the strong interaction, namely quantum electrodynamics (QED) [6, 7, 8] and quantum chromodynamics (QCD) [9, 10], were combined into one mathematical model that explains how the elementary particles interact with each other via the fundamental forces of the universe [4, p. 3]. Since then, high-energy particle physics experiments could verify the SM predictions so well, that it has proven itself to currently be the best theoretical model of all subatomic particles that we know of. The most recent measurements of the masses and other SM properties of the particles are summarized by the Particle Data Group (PDG) in the “Review of Particle Physics” in yearly editions [11].

The SM differentiates between two classes of fundamental particles: the particles that make up all matter are called *fermions*, whilst the force mediators, through which the fermions can interact, are called *gauge bosons*.

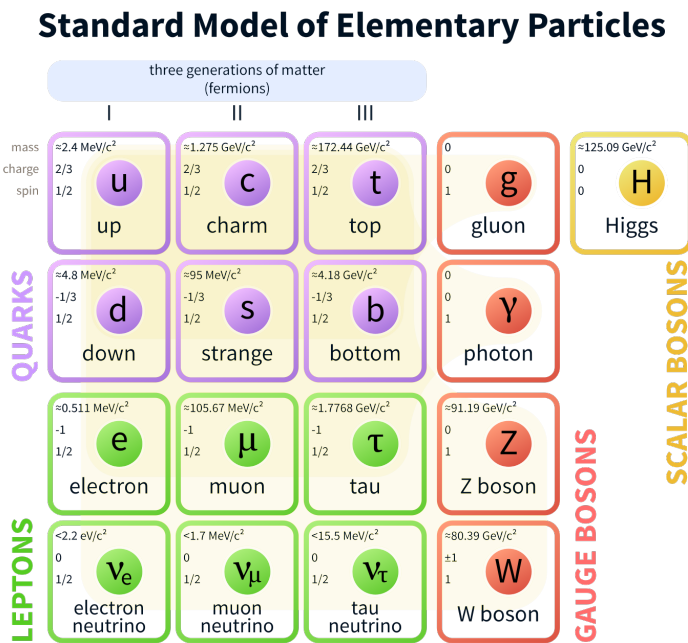


**Figure 2.1.:** The Standard Model describes all elementary particles, the twelve fermions in their three generations and the four gauge bosons, as well as the Higgs boson. The shadows indicate possible interactions between the fermions and gauge bosons [12].

**Table 2.1.:** *Quantum numbers of the Standard Model fermions.* The table lists the values for the electric charge  $q$ , and the spin  $s$  for all fermions, as well as the lepton number  $L$  of the leptons and the quark flavor of the quarks. Their respective antiparticles are highlighted by the shaded background [4, cf. p. 49].

	Leptons	$q$	$s$	$L_e$	$L_\mu$	$L_\tau$	Quarks	$q$	$s$	$U$	$D$	$C$	$S$	$T$	$B$
First generation	$e^-$	-1	1/2	+1	0	0	$u$	+2/3	1/2	+1	0	0	0	0	0
	$e^+$	+1	1/2	-1	0	0	$\bar{u}$	-2/3	1/2	-1	0	0	0	0	0
	$\nu_e$	0	1/2	+1	0	0	$d$	-1/3	1/2	0	-1	0	0	0	0
	$\bar{\nu}_e$	0	1/2	-1	0	0	$\bar{d}$	+1/3	1/2	0	+1	0	0	0	0
Second generation	$\mu^-$	-1	1/2	0	+1	0	$c$	+2/3	1/2	0	0	+1	0	0	0
	$\mu^+$	+1	1/2	0	-1	0	$\bar{c}$	-2/3	1/2	0	0	-1	0	0	0
	$\nu_\mu$	0	1/2	0	+1	0	$s$	-1/3	1/2	0	0	0	-1	0	0
	$\bar{\nu}_\mu$	0	1/2	0	-1	0	$\bar{s}$	+1/3	1/2	0	0	0	+1	0	0
Third generation	$\tau^-$	-1	1/2	0	0	+1	$t$	+2/3	1/2	0	0	0	0	+1	0
	$\tau^+$	+1	1/2	0	0	-1	$\bar{t}$	-2/3	1/2	0	0	0	0	-1	0
	$\nu_\tau$	0	1/2	0	0	+1	$b$	-1/3	1/2	0	0	0	0	0	-1
	$\bar{\nu}_\tau$	0	1/2	0	0	-1	$\bar{b}$	+1/3	1/2	0	0	0	0	0	+1

**Fermions** Fermions are particles with a half-integer spin  $s$  as one of their quantum numbers. The spin has a direction, and a specific amplitude, which can be calculated as  $\frac{h}{2\pi}\sqrt{s(s+1)}$ , with  $h$  being the Planck constant [4, p. 121]. All fermions have a specific set of quantum numbers, so that by giving the electric charge, the spin, and the flavor, all fermions can be identified precisely. Table 2.1 lists all Standard Model fermions with their quantum numbers.

Fermions are further categorized as *leptons* and *quarks*, as well as in three generations, which can be seen in Figure 2.1. Among the leptons are the electron and its heavier brothers, the muon and the tau. In their respective generation, each of them has a neutrino, respectively named the electron-neutrino, muon-neutrino, and tau-neutrino. They are electrically neutral particles.

Additionally, every particle has an antiparticle, so there are actually not only six leptons but twelve. The SM does in general not remark the antiparticles, because it assumes that the physics of particles and antiparticles is the same. The only difference between them is the sign of their internal quantum numbers: The electron's antiparticle is the positron, which has the same mass and spin as the electron, but has a positive electric charge of +1, and a negative lepton number  $L_e$  of -1. The antiparticles of the muon ( $\mu^-$ ) and the tau ( $\tau^-$ ) hence are  $\mu^+$  and  $\tau^+$ , respectively. As neutrinos on the other hand have no electric charge, they can only be distinguished from their respective antineutrino by their lepton number and their helicity. The helicity describes the state of the particle's spin direction in comparison to the particle's momentum. When the spin direction and the momentum are parallel, the particle is called right-handed. It is called left-handed, when they are antiparallel. In the SM, neutrinos are always left-handed, whilst antineutrinos are right-handed.

Every generation of quarks consists of one up- and one down-type quark, where the up-type quarks have an electric charge of 2/3, whilst down-type quarks have a charge of -1/3. However, they do not only carry the electric charge, but also the so-called color charge. The color charge is unrelated to the common meaning of color. The different quark colors are used as quantum numbers to differentiate between quarks. Every quark has one of three colors (red, green, and blue), every antiquark has one of three anti-colors (anti-red, anti-green, and anti-blue). Thus, there are overall 36 different quarks

and antiquarks. Due to the law of confinement, there can only be color-neutral particles. Quarks are therefore not free, but hadronize and form a bound state together with other quarks. These bound quark states, called hadrons, consist of several quarks. A particle with a quark of a specific color and an antiquark of the corresponding anti-color is called a meson. Together, the color and anti-color of the quarks make the meson color-neutral. A baryon, which is a particle with three quarks, can only be color-neutral when it carries three quarks with three different colors (or anti-colors), so red–green–blue or anti-red–anti-green–anti-blue, any other combination is not possible.

In everyday nature, the only observable hadrons are the protons and neutrons due to their constituents. They are baryons, hence are built from three quarks: protons contain two up-quarks and one down-quark, giving the proton its positive electric charge of +1. Neutrons on the other hand are formed by one up-quark and two down-quarks, resulting in an electrically neutral particle. As the up-quark is the lightest quark, it is stable and does not decay. All other quarks decay after certain lifetimes into another quark with smaller mass. That is the reason why all hadrons that are produced artificially in a high-energy particle collider are unstable. Since the down-quark is the second lightest quark, it can decay into the up-quark, giving reason to the spontaneous decay of free neutrons into protons when one of the down-quark decays. The proton is the lightest existing baryon, and can not decay further according to the Standard Model, since its quantum numbers have to be conserved. Together, the protons and neutrons construct the nuclei of every atom of every element.

**Table 2.2.:** *The fundamental forces and their mediators [4, cf. p. 59]. The strength of a force is dependent on various external factors, such as its source and its distance to the observer. Therefore, the listed values are a rough guideline of the orders of magnitude of difference between the effective strengths of the forces.*

Force	Strength	Mediators
Strong	10	Gluons
Electromagnetic	$10^{-2}$	Photons
Weak	$10^{-13}$	W, Z
Gravitational	$10^{-42}$	Gravitons

**Bosons** The *gauge bosons* described in the SM are the force mediators of the fundamental forces of nature: the electromagnetic, the weak, and the strong force. Gravity is the only fundamental force that is not represented by the SM. On the scale of ranges in particle physics, it is by far the weakest force, as can be seen from Table 2.2.

The fermions explained in the paragraph above are subject to these fundamental forces, and can interact with each other by exchanging the force mediators. The mediating particles are gauge bosons, which are particles with an integer spin.

The *photon* is a massless, electrically neutral particle mediating the electromagnetic (EM) force between electrically charged particles only. The photon couples therefore to all charged SM particles and their antiparticles, such that the electric charge is conserved in this interaction. The EM interaction, which is pictured in a Feynman diagram in Figure 2.2, does not change the flavor of the particle.

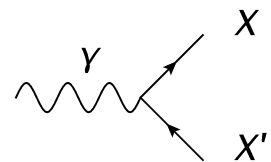


**Figure 2.2.:** *SM Feynman diagram of the EM interaction*

*Gluons* are massless particles as well. They carry the strong force, and like the quarks they are also color-charged, because of which they cannot occur in isolation. Due to their color-charge, gluons only couple to quarks (Figure 2.3 (a)) or to themselves (Figure 2.3 (b)). The latter is called gluon self-coupling.

The gluons mediating the strong force bind the quarks together in all hadrons. Since the proton is the only stable hadron, it is probed in high-energy particle physics experiments in order to investigate its constituents. This probing is called “deep inelastic scattering”, where an electron for instance is brought into collision with a proton. The electron penetrates the proton and scatters off one of the partons. By observing such processes, the distribution of the partons inside the proton can be determined, which is then summarized as a “parton distribution function” (PDF) [11, p. 134]. Free partons, such as the remaining constituents of the proton, hadronize due to the color confinement, and form clusters of hadrons. In the detector these clusters produce particle showers, which are called “jets”. A jet typically consists of about 65 % charged hadrons, 26 % photons and neutral pions, and 9 % neutral hadrons [13, p. 2].

$W^\pm$  and  $Z$  bosons on the other hand are massive particles, which are the mediators of the weak force. All fermions can interact via the weak force, including the neutrinos, which cannot interact via any other force. Weak interactions differentiate between particles of certain handedness, and can therefore only be undertaken by left-handed particles and right-handed antiparticles. Due to the electric charge of the  $W^\pm$  boson, its exchange involves a transfer of electric charge, and is therefore called “charged current”. The exchange of a neutral  $Z$  boson on the other hand is called “neutral current”.

Similar to the electromagnetic interaction via a photon, the electric charge has to be conserved in the neutral current interaction as well, which is shown in Figure 2.4 (a). Therefore, the flavor of the fermions involved in this first-order interaction does not change, since only particle-antiparticle pairs are taking part.

Interactions involving a  $W$  boson on the other hand can either happen between a lepton and a neutrino (Figure 2.4 (b)), or between an up- and a down-type quark (Figure 2.4 (c)). In both cases, the flavor of the particles can change, so that interactions between all generations are possible.

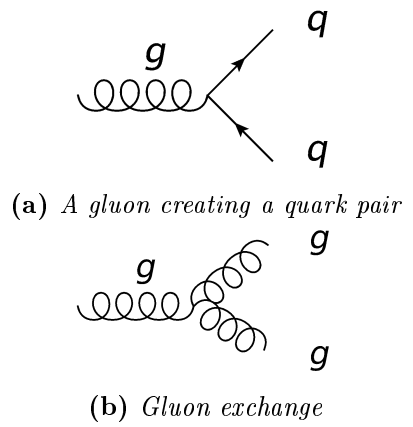


**Figure 2.3.:** SM Feynman diagrams of the strong interactions

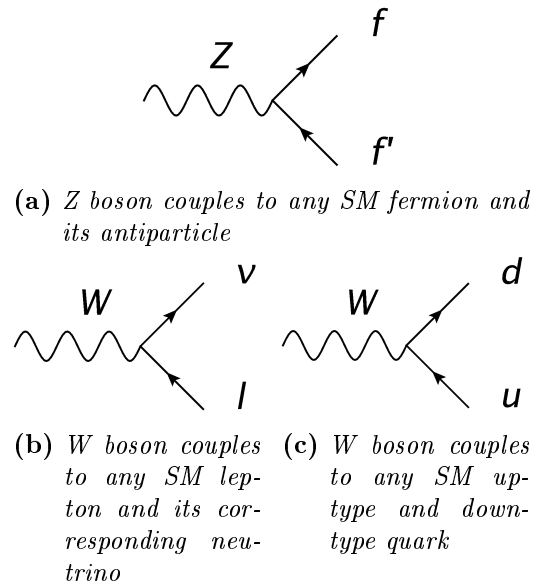


**Figure 2.4.:** SM Feynman diagram of the weak interactions

In contrast to the gauge bosons, the *Higgs boson* does not have a spin of +1, but a spin of 0. It is therefore a scalar boson. The Higgs  $h$  couples to all massive SM particles  $X$  with a certain coupling strength  $g_{hXX}$ . Since the coupling strength is proportional to the mass of the particle, it determines how heavy the elementary particles are. As the Higgs boson is a massive particle itself, it also couples to itself. The Higgs self-coupling, as well as all couplings to other SM particles are not well measured yet, since the Higgs discovery is the Standard Model's most recent addition [1, 2]. The precise measurements of all Higgs boson properties is an important physics goal of all current and future high-energy particle physics experiments, such as the International Linear Collider.

## 2.2. Production modes at lepton colliders

The production modes in high-energy lepton colliders are quite different from the production modes at hadron colliders, such as the Large Hadron Collider (LHC) for instance. Since at the LHC two proton beams are brought into collision, the dominant processes that occur are via the strong interaction. The QCD processes, such as the jet production processes, therefore have an event rate that is up to seven orders of magnitude higher than Higgs boson production processes, as shown in Figure 2.5 (b). As these QCD jet production processes are often not the main focus of physics analyses, they then count as physics background. With a background rate larger than the main focus process (the signal event) by several orders of magnitude, the signal-to-noise ratio can be very small, which makes the use of triggers necessary and the analysis of the collision data challenging.

The production modes at  $e^+e^-$  colliders on the other hand are all through weak and electromagnetic interactions, since leptons do not interact via the strong force. QCD jet production via gluon exchange therefore does not occur at a lepton collider. All production modes are through direct  $e^+e^-$  annihilation and  $e^+e^-$  scattering. Figure 2.5 (a) shows that the rates of possible production modes, such as the production of quark-antiquark pairs or of bosons, are all within a range of only four orders of magnitude for a collision energy of 250 GeV.

The collision energy  $\sqrt{s}$ , or often called center-of-mass energy  $E_{cm}$ , between two relativistic beams with four-vectors<sup>2</sup>  $p_1$  and  $p_2$  is calculated as follows:

$$\begin{aligned}s &= (p_1 + p_2)^2 \\ &= p_1^2 + 2p_1p_2 + p_2^2 \\ &= m_1^2 + 2(E_1E_2 - \vec{p}_1\vec{p}_2) + m_2^2\end{aligned}$$

by using  $E^2 - p^2c^2 = m^2c^4$ . In a particle collider, where the beam particles have the same mass  $m$  and beam energy  $E$ , but opposite momentum ( $\vec{p}_1 = -\vec{p}_2$ ), it follows:

$$\begin{aligned}&\approx 2m^2 + 2E^2 + 2|\vec{p}|^2 \\ &\approx 4E^2\end{aligned}$$

with  $E^2 \approx p^2 \gg m^2$ . The collision energy in a particle collider can therefore be approximated as  $\sqrt{s} = 2E$ .

Figure 2.5 does not only show the event rate on the right hand y-axis, but also the cross section on the left hand y-axis. The cross section  $\sigma$  for the occurring interaction can be thought of as an effective

---

<sup>2</sup>The four-vectors contain the particle's total energy and its momentum vector:  $p = (E, \vec{p})$

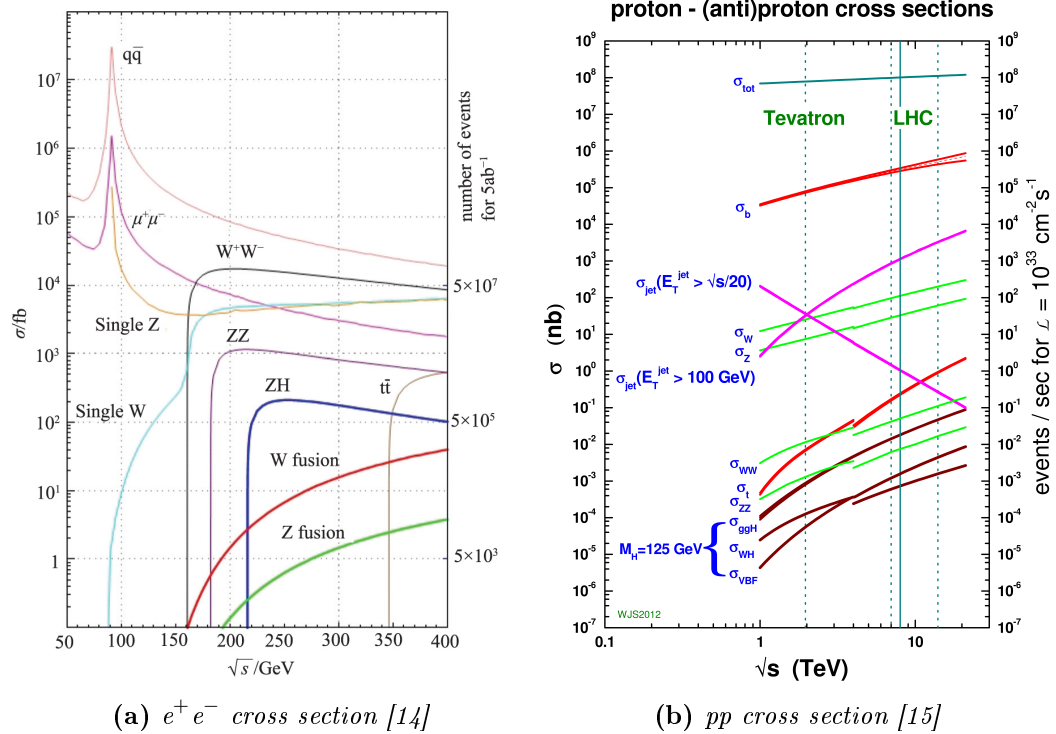


Figure 2.5.: Cross section at  $e^+e^-$  (a) and  $pp$  colliders (b) as a function of the collision energy.

cross-sectional area of the target particles. It is therefore the fraction of the number of interactions (per unit time) over the number of incident particles (per unit time per unit area). The unit of cross sections in particle physics is called “barn” (“b”), which is equivalent to  $10^{-28} \text{ m}^2$ .

## 2.3. Background processes at lepton colliders

As discussed in the section above, there are no QCD processes at lepton colliders. Instead, the beam particles are elementary and their energies are well defined, which has a big impact not only on the possible physics processes but also on the background sources for the particle detectors.

At hadron colliders, the backgrounds are dominated by the QCD background and by underlying events, since the actual collision happens between constituents of the two colliding hadrons. The remaining constituents, however, do not disappear but hadronize and leave their traces in the detector as well. Since this is not the case in lepton collisions, the events are in comparison very clean. Nonetheless, there are still different background sources, from beam-beam interactions and from interactions of the beam particles with the accelerator itself. The background processes will be explained in detail in the following.

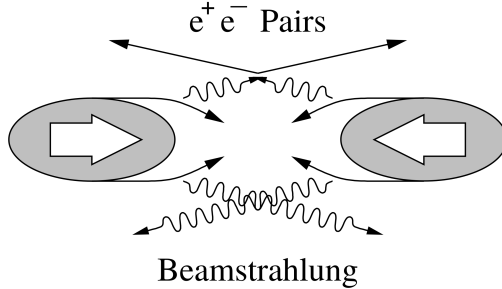


**Figure 2.6.:** Creation of a secondary  $e^+e^-$  pair through the collision of beamstrahlung photons arising from the electromagnetic field of the colliding beam bunches [19, p. 29].

### 2.3.1. High cross section background processes from beam-beam interactions

A significant background source for the particle detectors arises from the electromagnetic fields created by the highly focused beam bunches. Before the collision, the particle beams are focused down to a small beam size, which enhances the electromagnetic field around the bunches. This causes the beam particles to emit photons in the forward direction, the so-called beamstrahlung.

The beamstrahlung can be characterized through the beamstrahlung parameter  $\Upsilon$ , which is for Gaussian lepton beams with  $N$  beam particles per bunch and with the beam dimensions  $\sigma_{x,y,z}$  [16, 17]:

$$\Upsilon = \frac{5}{6} \frac{\gamma N r_e \lambda_e}{(\sigma_x + \sigma_y) \sigma_z} \quad (2.1)$$

with  $r_e$  being the classical electron radius ( $r_e = \frac{e^2}{4\pi\epsilon_0 m_e}$ ),  $m_e$  the electron mass, and  $\lambda_e = \frac{1}{m_e}$ . From that, one can calculate the average energy  $E_\gamma$  of the beamstrahlung photons [18, p. 77]:

$$E_\gamma \propto \frac{N}{(\sigma_x + \sigma_y) \sigma_z} \quad (2.2)$$

The average number  $n_\gamma$  of beamstrahlung photons that are emitted is proportional to:

$$n_\gamma \propto \frac{N}{(\sigma_x + \sigma_y)} \quad (2.3)$$

The number of photons is therefore dependent on the beam size and the number of particles per beam bunch. Beamstrahlung also causes the creation of other particle types that can be misinterpreted in the detectors as part of the signal events. The processes involving beamstrahlung interactions are discussed in the following.

#### 2.3.1.1. Pair background

Due to the high density of beamstrahlung photons at the collision point, particle interactions between photons from opposite beam bunches or between photons and the actual beam particles can occur, which is illustrated in Figure 2.6. Such interactions are then called beam-beam interactions, since they arise from interactions between the two colliding beams.

One possible outcome is the production of an electron-positron pair through three different physics

processes, which are depicted in Figure 2.7. In all three cases a “secondary”  $e^+e^-$  pair is produced, either through the interaction between a beamstrahlung photon and a virtual photon emitted by a primary beam particle (Bethe-Heitler process, Figure 2.7 (a)), or through the interaction of two beamstrahlung photons (Breit-Wheeler process, Figure 2.7 (b)), or lastly through the interaction of two virtual photons being emitted from particles of the two opposite beams (Landau-Lifschitz process, Figure 2.7 (c)).

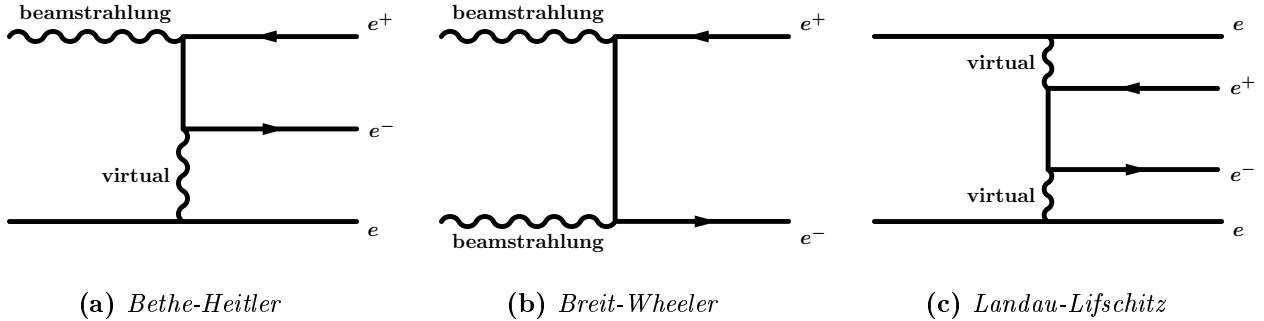


**Figure 2.7.:** The first-order Feynman diagrams of the production processes of background pairs at an  $e^+e^-$  collider: Bethe-Heitler, Breit-Wheeler, and Landau-Lifschitz.

For the three processes, the effective total cross section for a single final-state particle can be written as [16]:

$$\sigma_{BH} = 15.4 \frac{\alpha^2 r_e^2}{\gamma^2} K \left( \frac{\gamma m_e}{p^*} \right)^{5/3} (\tau_0^{1/3} - \tau_0^{-1/3}) \left[ \log \left( \frac{p^* \tau_0}{2\gamma m_e} \right) + 0.21 \right] \quad (2.4)$$

$$\sigma_{BW} = 4.9 \frac{\alpha^2 r_e^2}{\gamma^2} K^2 \left( \frac{\gamma m_e}{p^*} \right)^{4/3} \log(1/\tau_0) \quad (2.5)$$

$$\sigma_{LL} = 5.09 \frac{\alpha^2 r_e^2}{\gamma^2} \left( \frac{\gamma m_e}{p^*} \right)^2 \log(1/\tau_0) \left[ \log \left( \frac{p^* \tau_0}{2\gamma m_e} \right) \log \left( \frac{p^*}{2\gamma m_e \tau_0} \right) + 3 \log \left( \frac{p^*}{2\gamma m_e} \right) + 4.44 \right] \quad (2.6)$$

with the variables being: the Lorentz factor  $\gamma$ , the fine-structure constant  $\alpha$ , the minimal required transverse momentum  $p^*$ , and the tangent  $\tau_0 = \tan(\theta_0/2)$  with the (minimal) angle  $\theta_0$  to the z-axis of the produced particle. The  $K$  factor represents the dependence on the beam parameters and the beamstrahlung parameter  $\Upsilon$ :

$$K = \frac{\sigma_z}{\gamma \lambda_e} \Upsilon^{2/3} \quad (2.7)$$

The produced  $e^+e^-$  pairs are low  $p_T$  particles, which means that they have a small momentum in the transverse beam direction. The reason for that is the fact that the beamstrahlung photons are already boosted in the forward direction, i.e. in the beam direction. Further characterizations of this pair background can be found in Chapter 5.

### 2.3.1.2. Bhabha scattering and $\gamma\gamma \rightarrow$ hadrons

Further background particles are produced by processes with much smaller cross sections than for the pair background in the section above. At the International Linear Collider for example, about  $1-2 \times 10^5$

electrons and positrons from the pair background are expected per bunch collision, whilst only around one event per bunch collision is expected for the productions of hadrons from beamstrahlung photons, and even less than one for the Bhabha scattering [20].

Figure 2.8 shows the Feynman diagrams for Bhabha scattering and the  $\gamma\gamma \rightarrow$  hadrons process. Although both of these processes produce particles with low transverse momentum as well, the interaction products leave traces in the detectors, which overlay with signal physics events.

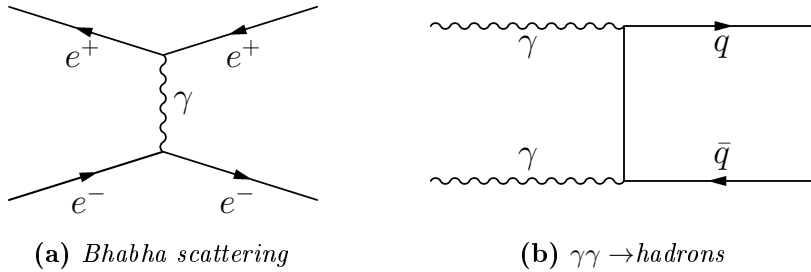


**Figure 2.8.:** The first order Feynman diagrams of the Bhabha scattering and the  $\gamma\gamma \rightarrow$  hadrons process.

### 2.3.2. Machine backgrounds

Apart from the backgrounds induced from beam-beam interactions, there are also secondary particles which are created from beam interactions with the accelerator components. Especially those created in the proximity to the collision region can reach the particle detectors and cause background levels that need to be investigated. Besides synchrotron radiation photons, which are emitted due to the deflection of charged particle beams in a magnetic field (see also Section 3.4), and the beamstrahlung mentioned above, the most prominent machine backgrounds are the following:

- Muons emitted from beam interactions with the accelerator machine components:  
Due to beam orbit disruptions, the beam halo particles of the beam bunches hit components of the accelerator, and interact with the material. This leads to the emission of secondary particles, such as muons, which are boosted in the beam direction. When these muons are created in the final accelerator sub-systems close to the collision region, the muons reach the particle detectors and penetrate them almost perfectly horizontally due to their momentum.  
This muon background was studied in a detailed Monte Carlo simulation presented in Chapter 6.
- Neutrons emitted from the main beam dumps:  
After the beam collision, the spent beams of linear colliders are passed to the beam dumps. By dumping the beam into the beam dumps, which often consist of water tanks, low momentum neutrons are produced which are also directed backwards towards the collision region. This causes a high-radiation environment in the beam dump hall, limiting the possible duration of stay for maintenance personnel. Additionally, those neutrons reaching the detectors, do not only leave tracks in the detector, but also cause radiation damage to the detector material.  
The simulation study of neutrons originating in water beam dumps is explained in Chapter 8.

All the mentioned background sources combined represent a significant background for particle detectors, and define their performance requirements. Detailed simulations of the sources and the effect of

the background particles on the detector performance is a crucial task for the research and development phase for detectors and machines, and are the focus of this thesis. Further details of the background creation and characterization are given in the respective chapters.



# 3

## Chapter 3.

# Accelerator physics of linear colliders

Since the invention of the first particle accelerators in the late 1920s, many different forms of accelerators were invented and developed over the years. Even though they may differ in shape and form, they all rely on the same principles. After a brief introduction of the principles of accelerator physics in Sections 3.1 - 3.3, there will be a description of the two classes of particle accelerators that are mainly used for high-energy physics nowadays: linear and circular accelerators. By looking at their advantages and disadvantages, the differences between them will be highlighted in Section 3.4.

After Ernest Rutherford had demonstrated the nuclear reactions of nitrogen with alpha particles from radioactive decays in 1919, he recognized the need for other more controlled sources of accelerated particles [21]. In the following years, physicists endeavored to develop necessary devices, and found that the key principle in particle acceleration lies in electrostatics [22, p. 3f].

### 3.1. Principles of particle acceleration

Charged particles are accelerated inside an electric field. In a time independent electric field  $\vec{E}$  with potential  $U$ , the particle with charge  $q$  experiences a change in its kinetic energy  $E$  by passing through this electric field:

$$\Delta E = q \int \vec{E} d\vec{r} = qU \quad (3.1)$$

The particle's charge, expressed in the elementary charge  $e$ , is simply multiplied by the electric potential difference in Volts in order to calculate the gain or loss of the particle's kinetic energy. Out of convenience, the unit for energy in particle physics is therefore "electronvolt" ("eV").

By this logic, a particle is accelerated to higher energies by applying higher and higher electrostatic fields. This was done in the beginning of particle accelerators by increasing the voltage applied to a capacitor and passing the charged particle through the field. Unfortunately, there are limits to the amount of voltage that can be applied before an electric breakdown. The solution seems simple: putting several capacitors in a row. But again, this can not be done with electrostatic capacitors since the field gradient between two different capacitors is directed in the opposite direction. A particle traveling from one capacitor to the next would then lose kinetic energy again in the gap between two capacitors. A solution was quickly found by using time dependent electric fields, which change their field orientation periodically.

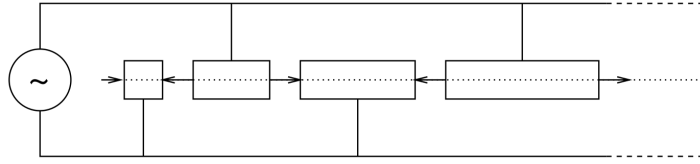
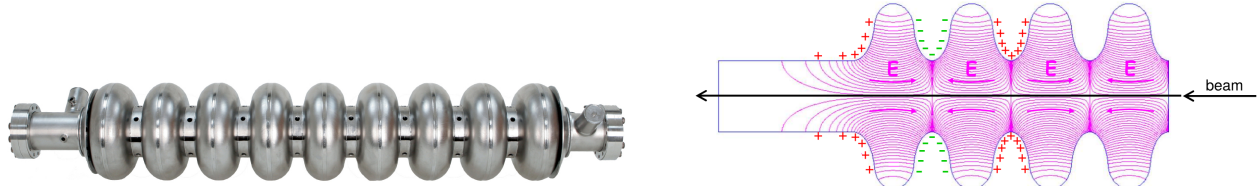


**Figure 3.1.:** Schematic layout of a linear accelerator with drift tubes of increasing lengths after the design by Rolf Widerøe [24, p. 40].



**(a)** Picture of a TESLA-style 9-cell niobium cavity [25, p. 15]. **(b)** Schematic drawing of the electric field lines inside a cell cavity [26, p. 47].

**Figure 3.2.:** The multi-cell RF cavities have a characteristic shape which is modeled in such a way that the electromagnetic (EM) RF field inside the cavities resonates. Figure (a) shows a 9-cell cavity with the “TESLA” shape. Figure (b) illustrates the field vectors of the EM field in the single cells of the cavity.

In simple terms, these are the key principles of linear particle accelerators. Better accelerating structures such as drift tubes and later on superconducting radio frequency (RF) cavities were developed over the years. The first linear accelerator using normal conducting drift tubes of increasing lengths was built and demonstrated by Rolf Widerøe in 1928 [23, p. 6]. A schematic drawing of such a structure is shown in Figure 3.1. RF fields are applied to the drift tubes such that the particles are accelerated when passing through the gaps in between the tubes. Due to the increase in the particles' energy, the tubes need to have increasing lengths in order to guarantee the particles being accelerated by the same phase of the RF field.

Nowadays, particle accelerators all over the world mainly use RF cavities instead of drift tubes. High-power RF cavities are made of superconducting material, since its electric resistance is minimal. Unlike before, the acceleration takes place inside the cavities, and all cavity cells are of the same length and shape. Their characteristic shape has the effect that the electromagnetic (EM) wave inside the cavity is resonant with a high quality factor. The quality factor  $Q$  describes how large the damping of the EM wave is, as it is the ratio of the stored energy over the dissipated energy [23, p. 148]. The larger the quality factor, the smaller the damping effect. Figure 3.2 (a) shows a 9-cell niobium cavity developed at Deutsches Elektronen-Synchrotron (DESY) in Hamburg. Its shape is called “TESLA-style”, its accelerating gradient exceeds  $35 \text{ MV m}^{-1}$ , and it can be tuned to an RF frequency of  $1.3 \text{ GHz}$  [25, p. 15f]. The RF field direction inside a cell is oscillating with the RF frequency, and neighboring cavity cells show opposite field directions (see Figure 3.2 (b)). The frequency is then tuned such that the beam always experiences an accelerating RF phase. In contrast to the drift tubes explained above, the matching of the particles to the wanted accelerating RF phase is therefore done by time dependent frequencies, whilst for the drift tube structures it is done purely by the change in the geometry of the tubes.

The development of the linear accelerating structures remains a significant factor for modern particle accelerators. Nevertheless, the advance in the research efforts for other accelerator designs has also an essential impact: The drift tube linac (short for linear accelerator) was not the only accelerator concept developed by Rolf Widerøe, he even more importantly invented the very first accelerating structures using magnetic fields. By using a magnetic field, the charged particles are deflected on a radial path, which therefore allows the accelerator to be much smaller than before [23, cf. p. 8]. This idea was needed in order to advance from purely linear to circular particle accelerators.

## 3.2. Transverse beam dynamics

Although completely new accelerator designs are now possible by using magnetic fields, circular acceleration of charged particles has certain challenges. From the equilibrium of the Lorentz and the centripetal force follows:

$$q(\vec{v} \times \vec{B}) = \frac{m\vec{v}^2}{\vec{r}} \quad (3.2)$$

$$\begin{aligned} qvB\vec{e}_r &= \frac{mv^2}{r}\vec{e}_r \\ r &= \frac{mv}{qB} \end{aligned} \quad (3.3)$$

$$= \frac{p}{qB} \quad (3.4)$$

Since the momentum  $p$  of the charged particle rises over time during the acceleration, the radius  $r$  of its circular path increases if the magnetic field  $B$  is constant. The accelerator hence has to be built accordingly, taking the increase in the radius into account, or needs to use magnets with variable field strengths. The latter is done in synchrotron machines, a type of circular accelerator combining the principles of all particle accelerators mentioned above: acceleration in RF cavities, variation of the RF frequency, and variable magnetic field strengths. In this way, the particles are traveling along a stationary orbit, passing through the same bending dipole magnets and cavities over and over again until the desired beam energy is reached.

To ensure the stability of the orbit, additional quadrupole magnets focus the beam horizontally and vertically onto the ideal particle orbit. However, as the focal length of these quadrupole magnets depends on the particle momentum, off-momentum particles due to the natural spread in the particle energy cause the quadrupoles to introduce chromatic aberrations. Therefore, sextupole and possibly octupole magnets are needed, which then correct orbital fluctuations. The need for higher order correction magnets can also be derived from the expansion of the magnetic field around the ideal path of the particle ( $x = 0$ ):

$$B_y(x) = B_{y0} + \frac{\partial B_y}{\partial x}x + \frac{1}{2!} \frac{\partial^2 B_y}{\partial x^2}x^2 + \frac{1}{3!} \frac{\partial^3 B_y}{\partial x^3}x^3 + \dots \quad (3.5)$$

When multiplying with  $\frac{q}{p}$ :

$$\frac{q}{p} B_y(x) = \frac{q}{p} B_{y0} + \frac{q}{p} \frac{\partial B_y}{\partial x} x + \frac{1}{2!} \frac{q}{p} \frac{\partial^2 B_y}{\partial x^2} x^2 + \frac{1}{3!} \frac{q}{p} \frac{\partial^3 B_y}{\partial x^3} x^3 + \dots \quad (3.6)$$

$$= \frac{1}{r} + kx + \frac{1}{2!} mx^2 + \frac{1}{3!} ox^3 + \dots \quad (3.7)$$

→ dipole + quadrupole + sextupole + octupole + ...

and equivalently for  $B_x(y)$ .

Equation 3.7 shows the connection between the radius and the magnetic field in the dipole component (using Equation 3.4). In the quadrupole, sextupole and octupole components, factors for the magnet strength are introduced. According to the Maxwell equation  $\vec{\nabla} \cdot \vec{B} = \frac{\partial B_y}{\partial x} - \frac{\partial B_x}{\partial y} = 0$ , the Lorentz force on a particle in a quadrupole magnet, has therefore to be written as [27, cf. p. 372]:

$$F_x = -qv \frac{\partial B_y}{\partial x} x \\ = -q\beta c \frac{\partial B_y}{\partial x} x \quad (3.8)$$

$$= -gx \quad (3.9)$$

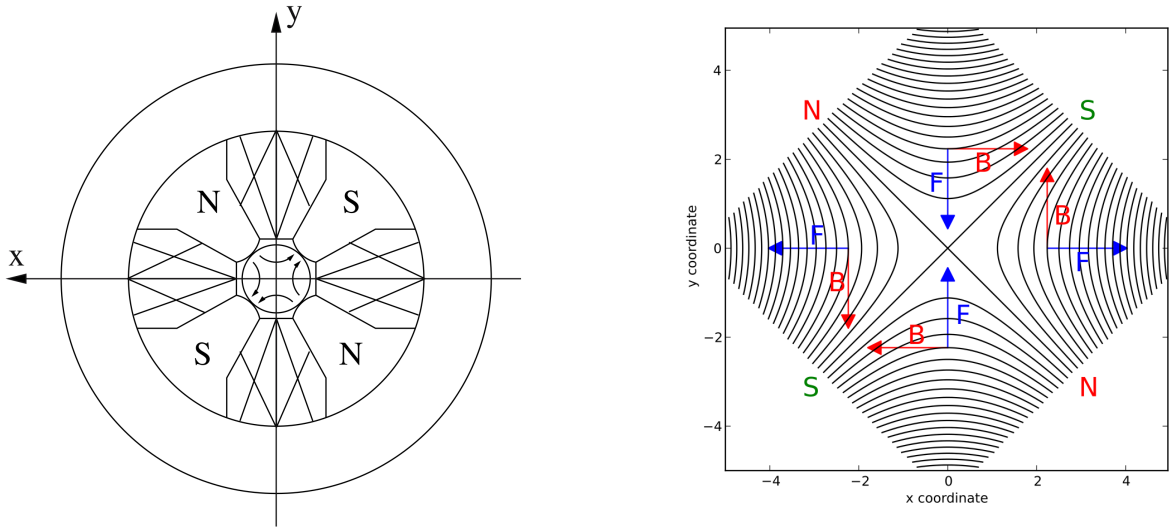
$$F_y = qv \frac{\partial B_x}{\partial y} y \\ = q\beta c \frac{\partial B_x}{\partial y} y \quad (3.10)$$

$$= gy \quad (3.11)$$

From the opposite signs in Equations 3.9 and 3.11, it becomes clear that quadrupoles can only focus in one direction, whilst they defocus in the other. A schematic cross section of a quadrupole magnet is shown in Figure 3.3, in which a positively charged particle beam would be focused in the y-direction and defocused in the x-direction. The magnetic field lines point from the magnetic north pole to the south pole, and get denser towards the edges of the beam pipe. The further a beam particle is away from the center, the stronger is the magnetic field it experiences, and the more it is deflected towards (or away from) the center, much like light in an optical lens.

Due to the fact that there are focusing and defocusing quadrupoles, so-called FODO structures are commonly used in particle accelerators. FODO is an alternating structure made out of focusing quadrupole magnets (“F”) and defocusing ones (“D”), with drift paths (“O”) in between (see Figure 3.4). The naming only refers to one of the planes (either horizontally or vertically), since a quadrupole focuses horizontally whilst it defocuses vertically or vice versa. Theoretically, a “FODO” cell in x is therefore a “DOFO” cell in y. Hence, several of these structures, which act like optical lenses, are needed to focus the particle beam in both directions, horizontally and vertically. Due to the restoring force, particles that were deflected by the focusing magnets start to perform betatron oscillations around the ideal particle trajectory. The amplitude of these oscillations is the beam envelope that covers the paths of all beam particles, i.e. the transverse beam dimension at a given location. It can be expressed by the two beam parameters  $\beta$  and  $\epsilon$  which will be explained in the following:

- The beta function  $\beta$  describes the spatial dependency of the amplitude and the wave length of the betatron oscillations. It is a periodic function, dependent on the focusing strengths and the location of the magnets along the beam path. At any given point along the path, the  $\beta$  value can be given in units of length. Of particular interest is its value at the interaction point (IP), the point of the beam collisions, where it is then called  $\beta^*$ . In order to minimize the beam size at the IP, the beta function is tailored such that it has a local minimum at this point.



(a) Schematic cross section of a quadrupole magnet with the four magnetic north and south poles. The beam pipe is centered in the middle between the pole shoes [24, p. 88].

(b) Magnetic field lines inside an ideal quadrupole magnet [28]. The field lines are directed from the north to the south poles, and become denser towards the edges. At any given point, the direction of the magnetic field ( $B$ ) and the resulting Lorentz force ( $F$ ) can be determined. A beam of positively charged particles going into the page would be focused in the  $y$ -direction and defocused in  $x$ .

**Figure 3.3.:** Schematic drawings of the cross section of an ideal quadrupole magnet (a), and of the magnetic field lines in the center of such a quadrupole magnet (b).

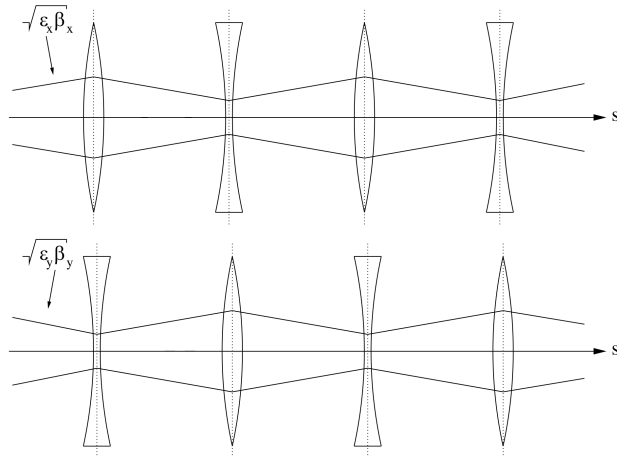


**Figure 3.4.:** Schematics of a FODO structure in the horizontal and vertical plane. The particles are focused and defocused by the quadrupoles that act as lenses [24, p. 65].

- Like the beta function, the transverse emittance  $\epsilon$  is defined in the horizontal and vertical plane. In simple terms,  $\epsilon$  is a direct measure of the convergence of the beam with respect to its spread in space and in transverse momentum. A small emittance therefore means that the beam particles are confined to a small space, with a narrow transverse momentum distribution. It also has the units of length, and is often given as the normalized emittance  $\epsilon^* = \epsilon\beta\gamma$ , with  $\beta = \frac{v}{c}$  and the relativistic Lorentz factor  $\gamma = \frac{1}{\sqrt{1-\beta^2}}$ .

Together, the spatial amplitude of the betatron oscillations can be written as  $\sqrt{\epsilon\beta}$ . Since the amplitude of these oscillations counts towards the size of the beam, its contribution to the beam size can then be written as  $\sigma_{\text{betatron}} = \sqrt{\epsilon\beta}$ . The amplitude is also shown as the maximum extent in  $x$  in the phase-space ellipse, shown in Figure 3.5. The phase-space is spanned by  $x$  and  $x'$ , where  $x$  can stand for the  $x$  and  $y$ -direction.  $x$  represents the position of the particle, and  $x'$  represents the change in position along the particle trajectory  $s$ , so that  $x' = \frac{dx}{ds}$ . The beam emittance  $\epsilon$  can be defined in terms of the phase-space ellipse more accurately than it was done above.  $\epsilon$  is hence defined as the area (divided by  $\pi$ ) of the phase-space ellipse.

The ellipse drawn in the phase-space illustrates the qualities of the particle beam. Since the particles' spread in position and momentum varies along the beam line, the shape of the ellipse changes constantly, but the area of the ellipse stays the same for energy-conserving systems. The normalized emittance  $\epsilon^*$ , which was explained above, is the quantity which is adiabatically invariant under energy change.

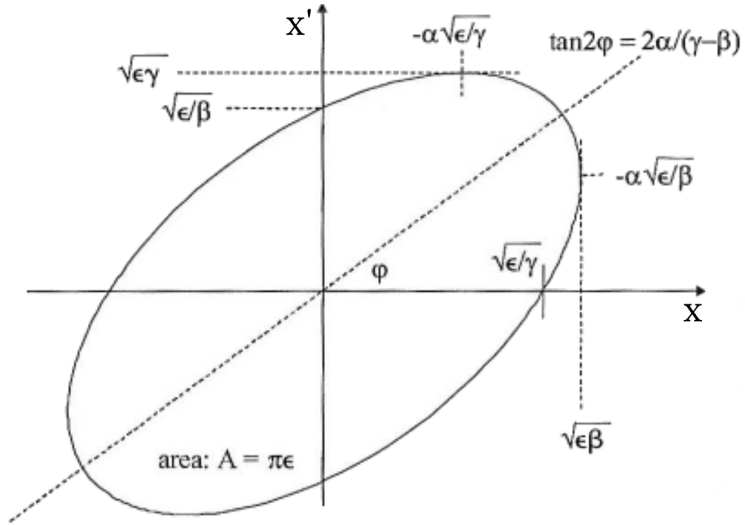


**Figure 3.5.:** Phase space ellipse [29, based on p. 158]

The variables  $\alpha$  and  $\gamma$  are defined here as:  $\alpha = -\frac{1}{2}\beta'$  and  $\gamma = \frac{1+\alpha^2}{\beta}$  [30, cf. p. 283ff].

The actual transverse size of the beam is not yet fully defined by the spatial amplitude of the betatron oscillations [31, cf. p. 108ff]. The deviation from the ideal particle trajectory due to the momentum spread has to be taken into account, which is defined by the dispersion function  $\eta$ . Like  $\epsilon$  and  $\beta$ , it is dependent on the position along the beam trajectory, and can be defined as  $\eta = \frac{dx}{d\delta}$ , with the fractional deviation from the ideal particle momentum  $p_0$ :  $\delta = \Delta p/p_0$ .

With this knowledge, the overall beam size can be calculated by using the betatron oscillation amplitude as well as the spread in the particle momentum distribution for all particles:

$$\sigma = \sqrt{\sigma_{\text{betatron}}^2 + \sigma_{\text{dispersion}}^2} \quad (3.12)$$

$$= \sqrt{\epsilon \cdot \beta + \left( \eta \frac{\Delta p}{p_0} \right)^2} \quad (3.13)$$

### 3.3. Longitudinal beam dynamics

Apart from the transverse beam dynamics, there are also effects in the longitudinal direction, concerning the movement of the particles along the beam trajectory. As mentioned above, both modern accelerator concepts, linear accelerators as well as synchrotrons, use RF cavities in order to accelerate the particles. Due to the nature of these accelerating structures, there is a certain phase of the RF frequency that can accelerate the particles in an optimal way. In order to provide this ideal acceleration to all beam particles, the beam has to be bunched.

In circular accelerators, this bunching happens naturally due to the choice of the RF frequency and the timing of the beam arriving at the accelerating cavities. The RF frequency is chosen such that the particles with the ideal momentum  $p_0$  arrive at the cavity at the synchronous phase  $\psi_s$ , which is off the crest of the RF wave. Depending on the system,  $\psi_s$  is then appointed to be either on the rising or the falling edge of the accelerating RF wave, or at the zero crossing. In a circular accelerator, such as a storage ring, the particles are to be constantly accelerated and longitudinally focused at the same time.  $\psi_s$  is therefore off-crest on the falling edge of the RF wave. For relativistic particles traveling close to the speed of light, their orbit along the storage ring depends on the difference of their momentum  $\Delta p$  to the ideal momentum  $p_0$ . Particles with a smaller momentum travel on an orbit that is smaller than the ideal orbit. This is due to the fact that the radius of the particle's path in a magnetic dipole field depends on the momentum of the particle, which is shown in Equation 3.4. These particles on a smaller orbit will arrive at the next accelerating cavity earlier than the ideal particles (which arrive at the synchronous phase  $\psi_s$ ), and will therefore experience a larger field which accelerates the particles to higher energies. Particles that have energies larger than the ideal particles are deflected onto a larger orbit and will therefore arrive late at the RF cavity, where they then gain less energy. Hence, particles are accelerated by different phases of the RF field, as can be seen in Figure 3.6. Particles arriving later will be accelerated less, particles arriving too early will be accelerated more. The particles oscillate about this ideal stable phase  $\psi_s$ , and are therefore focused longitudinally. This effect is called “phase focusing”.

However, in linear accelerators bunching is done differently and in several stages. The initial bunching is done directly after the particle source, which is the very first stage of acceleration. As the particles at this stage are still non-relativistic, one of the possible methods that can be used is “velocity bunching” [29, cf. p. 541ff]. For this, the continuous stream of particles is passed through a set of RF cavities, where the velocity spread induced by the RF frequency causes bunches to form. Particles arriving at the cavity at a phase with negative voltage will be decelerated, whilst particles arriving at a phase with positive voltage will be accelerated (see Figure 3.7). Over a set of several cavities, bunches are formed.

After the pre-acceleration, the now relativistic bunches can be further compressed to the desired bunch length by so-called bunch compressors, which use “magnetic compression”. There are several

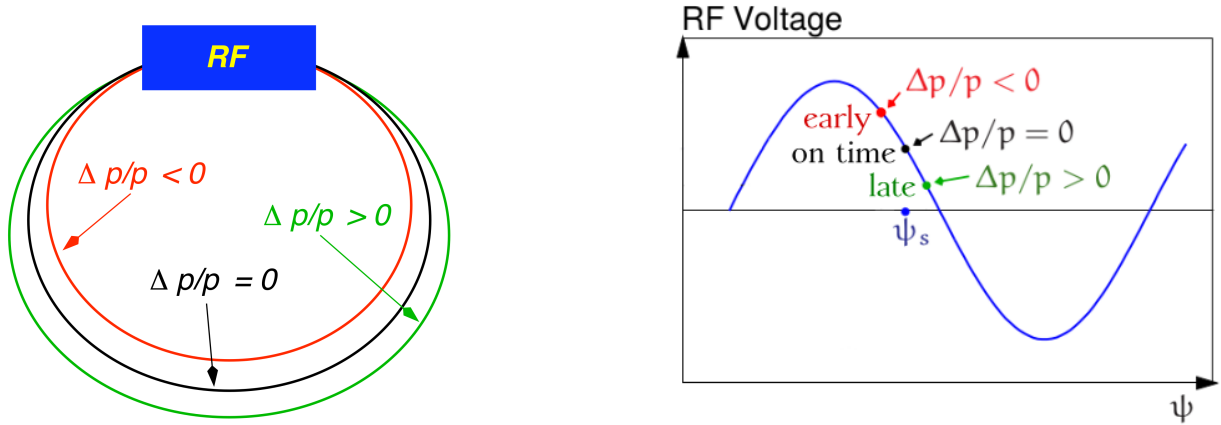


**Figure 3.6.:** Relativistic charged particles with the ideal momentum ( $\Delta p/p = 0$ ) travel on the ideal orbit of the accelerator, and arrive at the next accelerating RF structure at the RF phase  $\psi_s$ , the so-called “synchronous phase”. Particles with a smaller momentum ( $\Delta p/p < 0$ ) travel on a shorter orbit, and will arrive earlier than the ideal particles. These particles will therefore be accelerated more, whilst particles with a larger momentum will be accelerated less respectively. Illustrations based on [32].

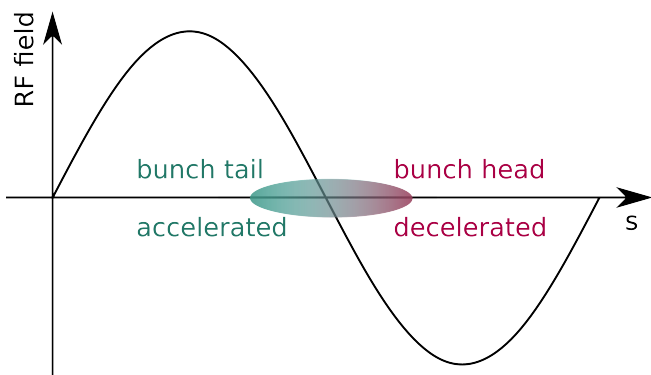


**Figure 3.7.:** Velocity bunching: The beam arrives at the RF cavity such that the bunch head experiences a decelerating RF phase, whilst the bunch tail experiences an accelerating force.

methods used, which all in principle are based on the idea of shortening the bunch by exploiting the momentum spread of the beam particles [29, cf. p. 378ff]. One of the methods uses the same idea as explained above for circular accelerators. It is illustrated in Figure 3.8. By sending the bunches through a chicane<sup>1</sup> with bending magnets, the particles' orbit though the chicane depends on their relativistic momentum. Before the chicane, the still elongated bunches are passed through an RF cavity such that the bunch heads experience a decelerating RF phase, whilst the tails experience an accelerating phase. The synchronous phase  $\psi_s$  is hence designed to be at the zero crossing of the RF wave. In the chicane, the high-momentum particles of the tail are deflected less, and will travel on a shorter orbit than the low-momentum particles. At the end of the chicane, the difference between the time of arrival of the head and the tail particles is smaller, the bunches have been compressed longitudinally. Another method of “magnetic compression” is explained in Section 4.2.1.

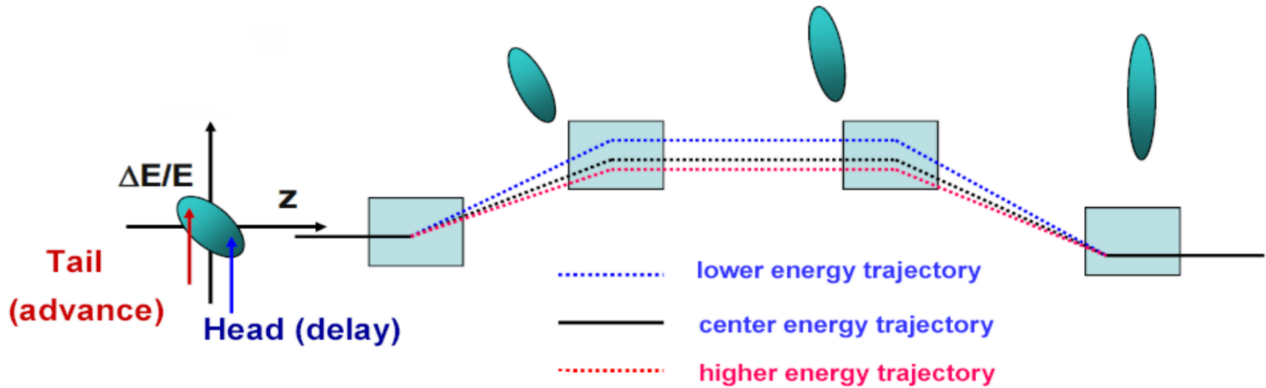


**Figure 3.8.:** Magnetic compression: After passing through an RF cavity, the particles in the bunch head have a lower momentum compared to the particles of the bunch tail. This causes the particles of the bunch to travel along different orbits in the chicane depending on their momentum. Since the tail particles have a higher momentum, they travel on a shorter orbit and will arrive at the end of the chicane at a similar time as the bunch head particles. Illustration based on [33, p. 75].

## 3.4. Linear colliders in comparison to circular colliders

These transverse and longitudinal beam dynamics described in the sections above are of course valid for circular as well as linear accelerators. In both machines, the acceleration with RF cavities, for instance, is accompanied by beam deflections and corrections with the help of magnets. Naturally, the beam line of a circular accelerator contains on average more bending magnets than a linear accelerator.

Currently, the world's largest circular particle collider is the Large Hadron Collider (LHC) at CERN, a synchrotron with a circumference of approximately 27 km. The design collision energy of the two colliding proton beams is 14 TeV, and its nominal peak luminosity  $\mathcal{L}$  is  $10^{34} \text{ cm}^{-2}\text{s}^{-1}$  [34, p. 3]. The collision energy  $\sqrt{s}$ , or often called center-of-mass energy  $E_{cm}$ , between two relativistic beams is calculated as shown in Section 2.2.

<sup>1</sup> A chicane is a deviation from the original direction of the beam line using bending magnets. Chicanes are used for certain processes, such as energy or particle filtering.

The luminosity of a particle collider is proportional to the rate of collisions that can occur, and it is defined as:

$$\mathcal{L} = \frac{N_1 N_2 \cdot n_b \cdot f_{rep}}{2\pi \cdot \sqrt{\sigma_{x,1}^2 + \sigma_{x,2}^2} \sqrt{\sigma_{y,1}^2 + \sigma_{y,2}^2}} \quad (3.14)$$

If the bunch sizes  $\sigma_x$  and  $\sigma_y$  of the opposite beams are equal:

$$= \frac{N_1 N_2 \cdot n_b \cdot f_{rep}}{4\pi \cdot \sigma_x \sigma_y} \quad (3.15)$$

$N_{1,2}$  is the number of particles per bunch, which is usually similar for both beams, so that  $N_1 \approx N_2$ .  $f_{rep}$  is the beam pulse repetition frequency. Together with  $n_b$ , the collision frequency is then  $n_b \cdot f_{rep}$ , i.e. the number of bunches  $n_b$  colliding per second.  $\sigma_{x,y}$  is the beam size in the horizontal and the vertical plane. Table 4.1 in Chapter 4 lists these parameters and their values for the LHC in comparison to the International Linear Collider (ILC). In order to translate the luminosity into an event rate  $\dot{N}$ , the luminosity value has to be multiplied by the cross section  $\sigma_{\text{process}}$  of the physics process that is of interest. Since the LHC detectors only measure events from inelastic scattering, the LHC event rate can be calculated by taking only the cross section for inelastic proton-proton scattering into account, which is measured to be approximately 78 mb [35].

$$\dot{N} = \mathcal{L} \cdot \sigma_{\text{inelastic}} \quad (3.16)$$

$$= 10^{34} \text{ cm}^{-2} \text{ s}^{-1} \cdot 78 \text{ mb} \quad (3.17)$$

$$= 7.8 \times 10^8 \text{ s}^{-1} \quad (3.18)$$

Every second about 780 million events are occurring at the LHC. With its high luminosity and high collision energy, the possible physics processes from the hadron collisions cover wide energy ranges, because of which it is a so-called “discovery machine”. New particles, often seen as resonance peaks in the measured mass spectra, can be discovered more easily than at accelerators with smaller collision energy due to the large phase-space. This was the case in 2012 for instance, when the LHC experiments found a peak at an invariant mass of about 126 GeV, shortly thereafter recognized as the very first measurement of a Higgs boson [1, 2].

Why these “discovery machines” are hadron and not lepton colliders, and why they are circular and not linear, is to be explained with the physical qualities of the colliding particles. Hadrons are by definition composite particles, the actual colliding particles in a collision are therefore their partons, the constituents of the hadrons. The energy that the single partons have follows a certain probability function, leading to the fact that the collision energy in hadron colliders can cover a large range. This so-called deep inelastic scattering is explained in more detail in Section 2.1.

In contrast to that, a collision of leptons as elementary particles is the interaction of exactly these leptons at exactly their given energy. This is one of the reasons why lepton colliders are called “precision machines”. Nevertheless, discoveries of new particles have also happened at lepton machines, such as the discovery of the charm quark in 1974 [36] and the tau lepton in 1975 [37] at the  $e^+ e^-$  collider SPEAR [38]. The decision whether to build a lepton or a hadron collider therefore depends mainly on the physics goal.

The next question to be answered is which design the collider should have, linear or circular. Again, both alternatives have advantages and disadvantages. One advantage of circular accelerators

was already mentioned, namely the possibility to go to high energies by letting the beams perform more revolutions and hence gain more and more energy from every turn. This is not possible in linear colliders, since the beams are not reused but dumped after every collision. The full collision energy has to be gained in a single go. The only way to increase the collision energy of a linear collider is to make the accelerating line longer, or to use accelerating structures with higher gradients. So, why do linear colliders exist at all?

The answer lies in the synchrotron radiation, radiation in the form of photons being emitted by deflected charged particles. Every deflection in a magnetic field yields an energy loss in the form of this synchrotron light, and the smaller the radius of the accelerator's bending magnets, the more energy loss the beam suffers from. The synchrotron radiation power is given as [39, p. 33]:

$$P_S = \frac{e^2 c}{6\pi\epsilon_0} \frac{1}{(m_0 c^2)^4} \frac{E^4}{R^2} \quad (3.19)$$

This directly leads to the energy loss per turn in a circular accelerator with a bending radius  $R$ .  $T$  is the time duration per turn, in which the particle beam is bend in the dipole magnets:

$$\Delta E = P_S \cdot T \quad (3.20)$$

$$= P_S \frac{2\pi R}{c} \quad (3.21)$$

$$= \frac{e^2}{3\epsilon_0 (m_0 c^2)^4} \frac{E^4}{R} \quad (3.22)$$

In order to counteract the loss, the beam has to be accelerated by at least  $\Delta E$  for every turn. Equation 3.22 also implies that a circular accelerator with high beam energies either has to have accelerating cavities with extremely high gradients and strong dipole magnets, or that its radius has to be so large that it can compensate for the factor  $E^4$ . Having a closer look at the equation, it now becomes clear why the LHC is a hadron collider: Due to the factor  $m_0^{-4}$ , the synchrotron radiation is much lower for particles with higher masses. When comparing two versions of the LHC: one version with 6.5 TeV beams of protons, and one version with electrons, then it can be calculated directly that an "Electron-LHC" would lose about  $1.14 \cdot 10^{13}$  times as much energy from synchrotron radiation as the existing LHC, simply because of the electron-proton mass ratio:

$$\begin{aligned} \frac{\Delta E_e}{\Delta E_p} &= \frac{m_p^4}{m_e^4} \\ &= \frac{7.75 \cdot 10^{11} \text{ MeV}^4}{6.82 \cdot 10^{-2} \text{ MeV}^4} \\ &= 1.14 \cdot 10^{13} \end{aligned}$$

Constant beam energy loss is not the only way in which synchrotron radiation affects the operation of the accelerator. The synchrotron radiation also causes damage to the particle detectors as well as to the diagnostic devices along the accelerator ring. The only way to prevent the sensitive devices from the radiation damage is to use shielding materials and to build up shielding walls where needed. Additionally, the constant (but fluctuating) beam energy loss increases the uncertainties on the physics measurements, as the measurements rely on a precise knowledge of the beam energy.

Overall, synchrotron radiation is a critical issue for circular accelerators, and is always aimed to be minimized by using beam particles with high masses and by building accelerator rings with large radii.

Concluding, a circular hadron collider lends itself to be a particle accelerator in the high-energy frontier, whereas a linear lepton collider is destined to be a collider in the precision frontier. Nevertheless, there have also been circular lepton colliders in the past, such as the Large Electron-Positron Collider (LEP) at CERN before the LHC was built into the same tunnel. LEP was in use from 1989 until 2000, and accelerated electrons and positrons to a center-of-mass energy of up to 209 GeV [40]. At such energies, the loss due to synchrotron radiation can be calculated as above, and is with 3.79 GeV per turn still tolerable. Although it was a circular collider, it was still possible to collide leptons at reasonably high energies and to do important precision measurements of the W and Z boson.

**A question of money** In the end, the deciding factor when considering the design for a future collider is not only the physics goal, but also the cost for the accelerator. For the overall expected cost, there is a rough rule of thumb formulated by Burton Richter in 1979 [41, p. 87ff]. Based on cost estimates of previous accelerators, the cost of circular accelerators tends to grow quadratically with the nominal center-of-mass energy, whilst it grows linearly with the energy for linear colliders.

Strictly speaking, the proportional cost growth for linear colliders is true considering only the accelerating structures, since the achievable energy is increasing linearly with the length of the accelerator. But there is more to a linear collider than just the accelerating structure: damping rings, focusing systems and beam dumps are only a few examples of what a linear collider layout contains as well. These elements, which add inevitable basic costs, are explained in more detail in Chapter 4.2. Apart from the basic costs, the increase in costs when reaching higher center-of-mass energies is therefore larger for circular than for linear colliders. This is true from about 200 GeV for circular machines with normal conducting accelerating structures, and about 350 GeV with superconducting accelerating structures, as illustrated in Figure 3.9.

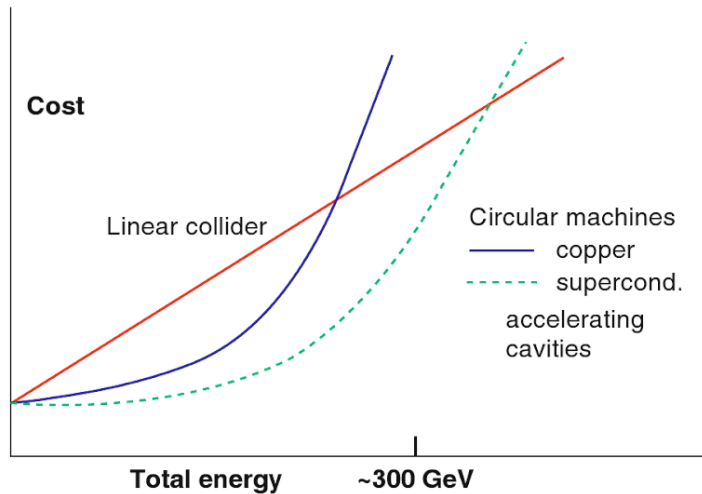


**Figure 3.9.:** Relations between the construction cost and the center-of-mass energy for linear and circular  $e^+e^-$  colliders [42, p. 13].

# 4

## Chapter 4.

# The International Linear Collider

*For answering the fundamental questions of mankind, it is necessary to understand the world in great detail. In order to confirm theories in particle physics, or to disprove them, it is often important to be able to measure the properties of particles or their interactions to high accuracy. For measurements in high-energy particle colliders, such precisions can only be reached in lepton colliders. This chapter will present a new design for a collider at the precision frontier: the International Linear Collider (ILC). The physics motivation (Section 4.1), the proposed layout (Section 4.2), the possible construction site (Section 4.3), and the detectors (Section 4.4) for such a capable accelerator will be explained.*

The world's currently largest particle collider for high-energy physics experiments is the Large Hadron Collider (LHC). It is a machine at the energy frontier, aimed at discovering new particles at high center-of-mass energies. As explained in Section 3.4, both hadron and lepton colliders have advantages and disadvantages. In the end, the decision on the collider layout depends on the physics goals of the future collider experiment.

The last lepton collider for high-energy physics experiments was the Large Electron-Positron Collider (LEP) with a center-of-mass energy of 209 GeV [40]. It was running from 1989 until 2000, as mentioned in Section 3.4. A new lepton collider at higher collision energies was therefore envisioned, that would be complementary to the LHC, aiming rather for much needed precision than for searching for new particles at high energies. The International Linear Collider (ILC) was hence proposed, which intends to find new particles and new physics in highest precision measurements at center-of-mass energies between 250 GeV and 1 TeV. In the following section, the ILC is motivated through its physics goals.

## 4.1. Physics motivation

The ILC is often called the future Higgs factory, which will measure the properties of the Higgs boson with much higher precision than has been done so far. The full ILC program includes also measuring the top quark properties, and Beyond Standard Model (BSM) searches. Since the first ILC stage will run at a center-of-mass energy of 250 GeV, this section will focus on the measurements of the Higgs boson. In Section 4.1.3, a brief overview of further physics goals is given.

### 4.1.1. How to reach unprecedented precisions

To reach the precision the ILC promises, it must achieve four different objectives, which are pointed out in its Technical Design Report<sup>1</sup> (TDR) [44, p. 2ff]. These objectives are all linked so that each one is dependent on the others. In the following paragraphs, these four objectives of the ILC are explained in comparison to the LHC.

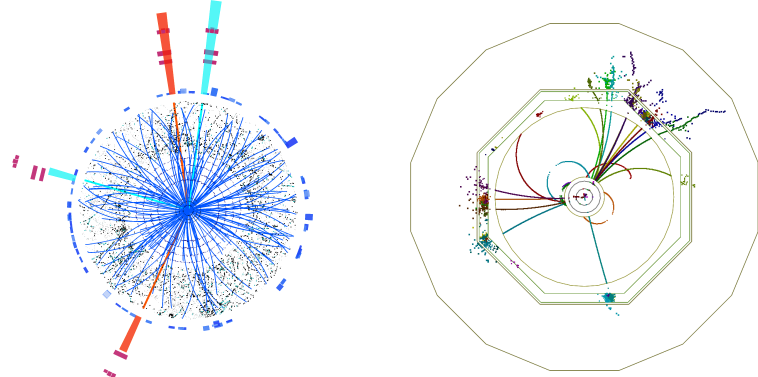


**Figure 4.1.:** Comparison of the event displays of a Higgs event at the LHC and at the ILC. The left figure shows an event of a Higgs boson decaying to two  $e^+e^-$  pairs at the LHC [47]. On the right, an event display of a  $Zh \rightarrow e^+e^- h$  event at the ILC is shown [48]. At the LHC, underlying events and pileup events populate the detector, whilst at the ILC the hits are mainly from the final state particles of the physics interaction of interest.

**Minimal background** Due to leptons in the initial state<sup>2</sup>, there will be one physics process per colliding lepton pair. Leptons are elementary and not composite particles like the proton, therefore there are no underlying events which arise from other partons of the composite particle. The energy range of the final state particles is restricted, since the initial energy of the colliding beams can be set precisely and only point-like particles collide. By adjusting the center-of-mass energy of the collision and running threshold scans at the mass of the particle of interest, the rate of the desired process can be increased. This is only possible at lepton colliders.

Additionally, the ILC shall have polarized beams. Beam polarization contributes to reducing the background level as well, since the polarization can be set in such a way that weak interactions are either enhanced or suppressed. As the weak interaction acts only on left-handed fermions, the polarization (or handedness) of the beam particles has an effect on the processes that can occur. This effect can be seen directly by looking at the two possible production modes at an  $e^+e^-$  collider (see also Chapter 2.2): direct  $e^+e^-$  annihilation, and  $e^+e^-$  scattering. In the SM annihilation process, the electron and positron have to be of opposite handedness due to the nature of weak interactions. The annihilation cross-section can therefore be enhanced by polarizing the beams to have opposite polarization. For the  $e^+e^-$  scattering process, the handedness of the final state particles is dependent on the handedness

<sup>1</sup>The four volumes of the ILC TDR were published in 2013, and contain apart from an executive summary [43] also all details about the physics goal [44], the layout [25, 45], and the detector experiments [46].

<sup>2</sup>The initial state of a process is the set of incoming particles that undergo an interaction. The final state particles are therefore the particles leaving the process.

of the incoming particles. By setting different polarization combinations, the properties of the final state particles, the interactions, and the couplings can be studied. Therefore, depending on the physics process of interest, the polarization can enhance the signal whilst suppressing the background. Figure 4.1 shows two event displays of a Higgs event at the LHC and the ILC in comparison. Due to the nature of composite particles, event displays at the LHC are dominated by underlying events and pileup events. At the ILC, the event displays are clean, and the tracks from the final state particles of the physics event can be distinguished easily.

**Democratic particle cross sections** Because the elementary coupling of Z bosons and photons is of the same order for all quarks and leptons, the  $e^+e^-$  annihilation produces pairs of all species at similar rates. In addition, the ILC will record all events without triggers. This means that no process will be rejected, and the complete readout of all events measured with the detectors will be stored for later analysis. This is only possible because the total number of detector hits from background events is small. Small background levels therefore imply small detector occupancies.

**Small uncertainties** The initial state of all events is precisely known, both in terms of the particles undergoing the interactions and in terms of the energies involved in the initial states. Additionally, there are only events with couplings to electroweak interactions, so that PDF uncertainties and systematic uncertainties due to QCD corrections are omitted.

The small uncertainties enhance theoretical and experimental precisions at  $e^+e^-$  colliders.

**Complete knowledge** Because of the small background and the possibility to record and store the complete detector readouts, processes can be reconstructed in completeness without theoretical assumptions. The quark and lepton momenta can therefore be determined by kinematic fits. Studies of the spin-dependence of the production and decay processes are also possible.

Due to the high energy resolution and the fact that the initial particle energies are precisely known, particles with small mass differences are distinguishable, i.e. peaks in mass spectra that are close together are more likely to be separable. That means that new particles might indeed be found at the ILC.

Additionally, c-tagging will be a possible tool for physics analyses, and will improve many physics studies at the ILC. The lifetime  $\tau$  of charm mesons before they decay is between  $\sim 0.4$  and  $1.1$  ps, which corresponds to a decay path  $c\tau$  of between  $\sim 120$  and  $330$   $\mu$ m [11, p. 1044ff]. The lifetime for bottom mesons in comparison is between  $\sim 0.5$  and  $1.6$  ps [11, p. 1137ff]. Since distinguishing the distance between the primary and the secondary vertex (where the meson decays) for bottom and charm mesons is only possible with a vertex detector with micrometer resolution, c-tagging is in general very difficult. However, it will be possible at the ILC, because the detector concepts foresee such a resolution, and because of the nanometer-sized ILC beams. The ILC will have a Final-Focus system as the final part of the accelerator, which focuses the beam bunches before the collision (see Section 4.2.1). The nanometer-sized beam allows the inner layer of the vertex detector barrel to be very close to the beam, and thereby improves the flavor tagging efficiency.

### 4.1.2. ILC as a Higgs factory

The first ILC stage will be a so-called Higgs factory, tuned to a center-of-mass energy of 250 GeV, where the cross section for Higgs production is at its maximum. As the ILC is planned to have a large luminosity and the capability for precision measurements, the individual Higgs boson qualities can be

measured to a percent accuracy in a completely model independent way. These Higgs boson properties include the Higgs mass, its couplings to Standard Model particles, as well as its total decay width. In contrast, for the LHC experiments, global fits to all Higgs signals together with theoretical assumptions of its decay width are the only way to gain the Higgs couplings.

After a brief overview of the Higgs production modes and the determination of the Higgs properties, it will be shown how the unprecedented precisions of the physics measurements are achievable at the ILC.

#### **4.1.2.1. The Higgs production modes at an $e^+e^-$ collider**

There are three main production modes for Higgs bosons at an  $e^+e^-$  collider, such as the ILC. As can be seen in Figure 4.2, the largest contribution to the overall production cross section is the Higgsstrahlung process, where a Higgs boson is produced in association with a Z boson ( $e^+e^- \rightarrow Zh$ ). In vector boson fusion (VBF) processes, like the WW fusion and the ZZ fusion, the fusion of two bosons produces a Higgs boson and a pair of leptons. For the WW fusion, an electron-neutrino and its antineutrino are produced ( $e^+e^- \rightarrow \nu\bar{\nu}h$ ), whilst for the ZZ fusion it is an electron and a positron ( $e^+e^- \rightarrow e^+e^-h$ ). The production cross sections for these processes as a function of the center-of-mass energy behave quite differently: The dominant process at energies between 200 and 450 GeV is the Higgsstrahlung process, replaced by the WW fusion process above 450 GeV. The ZZ fusion cross section contributes the least, with less than 10 fb. It is suppressed, since the couplings of the neutral current are smaller than the charged current couplings.

As the cross section of the Higgsstrahlung process peaks at 250 GeV, the first ILC stage will mainly use this production mode for the precision measurements of the Higgs boson qualities. At 250 GeV, the ILC will provide an even more precise measurement of the Higgsstrahlung cross section and hence of the branching ratios of the various decay modes of the Higgs boson than at a center-of-mass energy of 500 GeV [49, p. 14]. This is true despite the lower luminosity at 250 GeV, due to the larger cross section and the smaller background occupancy of the detectors (see Chapter 5.6).

#### **4.1.2.2. The Higgs measurements**

To know the Higgs couplings to Standard Model (SM) particles as precisely as possible is one of the most important goals for the ILC. Many theories about particles beyond the SM predict deviations from the SM couplings at the 1% level. Therefore, if these theories prove to be true, only with the highest precisions could a new particle be discovered, and a different model beyond the Standard Model be acknowledged.

As shown in the section above, the Higgsstrahlung production mode presents a prominent way to measure the Higgs boson properties. Due to the accurate knowledge of the initial state particles (the colliding electron and positron) and their energies, the unambiguous reconstruction of the Z boson recoiling against the Higgs boson makes the identification of the Higgs possible without the need to reconstruct its decay particles. This recoil method to identify the Higgs independently of its decay channels therefore allows a model independent way to determine the Higgs mass, its total decay width, the branching ratios, and the Higgs couplings. The high precision of the Higgs measurements will furthermore be a result of the high luminosity of the ILC and of the peak cross section of the Higgsstrahlung mode.

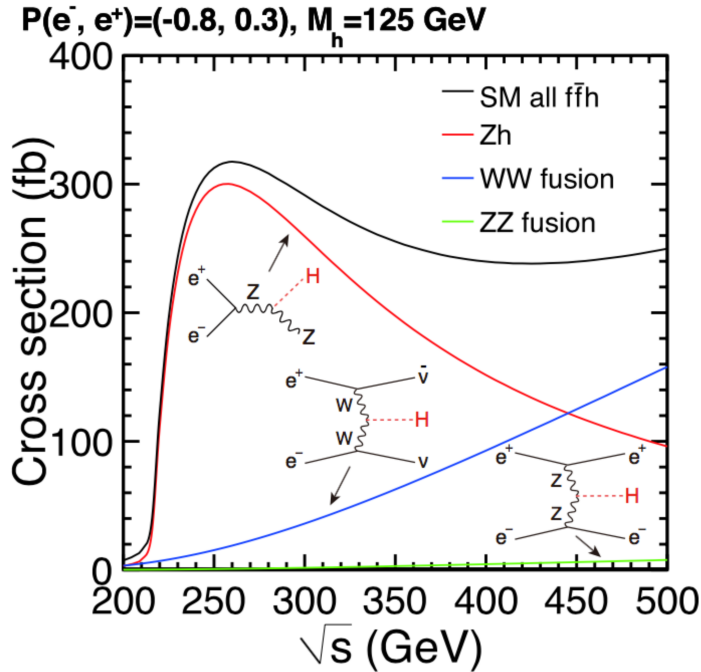


**Figure 4.2.:** Cross sections for the Higgs production modes at the ILC, with a beam polarization of 80 % for the electron and 30 % the positron beam [49, p. 13]. These are the design beam polarization values for the ILC beams (see Section 4.2.1). The three main processes are ZZ fusion, WW fusion, and Higgsstrahlung. The black line (“SM all  $f\bar{f}h$ ”) represents all Standard Model processes producing a fermion-antifermion pair and a Higgs boson.

**Higgs mass** To gain the recoil mass  $m_{recoil}$  of the Higgs boson, the difference in the four-momenta between the Z boson decay particles and the initial state particles has to be calculated [50, cf. p. 7]:

$$m_{recoil} = P_{ini} - (P_{f+} + P_{f-}) \quad (4.1)$$

$P_{ini}$  is the sum of the four-momenta of the initial state particles,  $P_{f+}$  and  $P_{f-}$  are the measured four-momenta of the fermionic decay products of the Z boson.

Higgsstrahlung events with the Z boson decaying into two leptons, especially muons, are the cleanest events, yielding the highest precisions of the Higgs measurements due to the high-resolution tracking detectors and the muon-veto system of the detector concepts. By counting such events, the full Higgsstrahlung cross section  $\sigma(e^+e^- \rightarrow Zh)$  can be determined to a 1 % precision [49, p. 12].

**Higgs decay width** The total decay width  $\Gamma_{h,tot}$  can be measured through [49, p. 14]:

$$\Gamma_{h,tot} = \frac{\Gamma(h \rightarrow XX)}{BR(h \rightarrow XX)} \quad (4.2)$$

where  $\Gamma(h \rightarrow XX)$  is the partial decay width, specific for the Higgs decay to any SM particle X.  $BR(h \rightarrow XX)$  is the corresponding branching ratio.

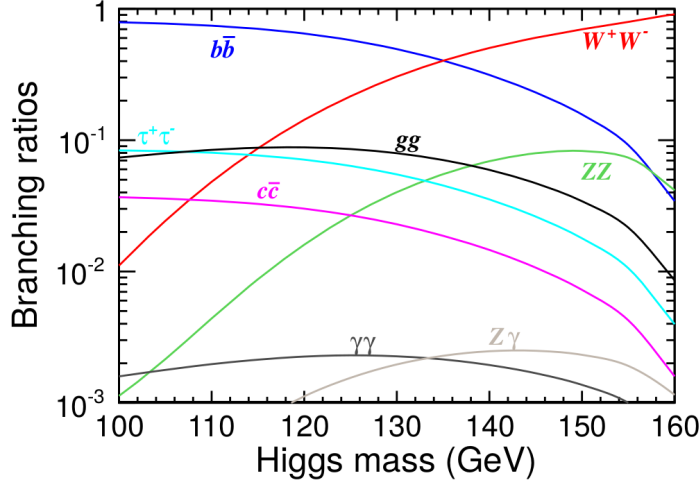


**Figure 4.3.:** Branching ratios of the Standard Model Higgs decay channels, as a function of the Higgs mass [44, p. 15].

The branching ratios are calculated by first measuring the rates of the occurring decay channels. A branching ratio of a certain decay channel is then determined by dividing the measured event rate by the production cross section  $\sigma$ , since event rates are given as  $\sigma \cdot BR$ . Due to the high precision measurement of the Higgsstrahlung cross section, as discussed in the paragraph above, the branching ratios can be calculated equally precisely. Figure 4.3 shows the branching ratios of the Higgs boson as a function of the Higgs mass.

The partial decay width of a given decay is measured as the resonance width in the mass spectrum of the decay particles. However, the decay width  $\Gamma(h \rightarrow ZZ^*)$  can be gained through the relation [49, p. 14]:

$$\Gamma(h \rightarrow ZZ^*) \propto g_{hZZ}^2 \propto \sigma(e^+e^- \rightarrow Zh) \quad (4.3)$$

with the Higgsstrahlung production cross section, and the Higgs coupling  $g_{hZZ}$  to the Z boson.

Finally, by combining the branching ratio with the partial decay width, the total Higgs width is determined in a model independent way without theoretical assumptions, since both the branching ratio and the partial width were measured independently of the Higgs decay channels.

**Higgs couplings** The coupling of the Higgs boson to any Standard Model particle X is given with the notation  $g_{hXX}$ , and expresses the strength of the interaction between the Higgs and particle X. This coupling constant is involved in both the Higgs production and its decay, and is hence a dependency of the production cross sections as well as of the decay branching ratios.

The dependence between the coupling constant and the cross section for the Higgsstrahlung, for instance, is given as [51, p. 4]:

$$\sigma(e^+e^- \rightarrow Zh) = F_1 \cdot g_{hZZ}^2 \quad (4.4)$$

where  $F_1$  is a parameter that can be calculated unambiguously from the Feynman diagram for this process.  $g_{hZZ}$  can therefore be determined with high precision, comparable to the precision of the Higgsstrahlung cross section determination itself.

All other couplings however are gained via the partial decay width  $\Gamma$ , which is calculated through the total Higgs width and the various branching ratios:

$$g_{hXX}^2 \propto \Gamma(h \rightarrow XX) = \Gamma_{h,tot} \cdot BR(h \rightarrow XX) \quad (4.5)$$

The precision on the couplings is directly dependent on how accurately the full process can be measured and recorded. As explained above, the reconstruction of complete events at the ILC with its low background occupancies enables a *model independent* determination of the Higgs boson qualities. The recoil method to gain the full Higgsstrahlung cross section allows the calculation of the Higgs branching ratios and the total decay width without theoretical assumptions.

In contrast to that, due to large background levels and therefore high detector occupancies in hadron colliders, specific processes are not easily distinguishable from background events. Additionally, the main Higgs production mode at hadron colliders is gluon-gluon fusion, which is open to processes beyond the Standard Model. These are the reasons why LHC experiments can not measure the full Higgs cross section without *model dependent* assumptions, which is the key to a model independent determination of the Higgs properties.

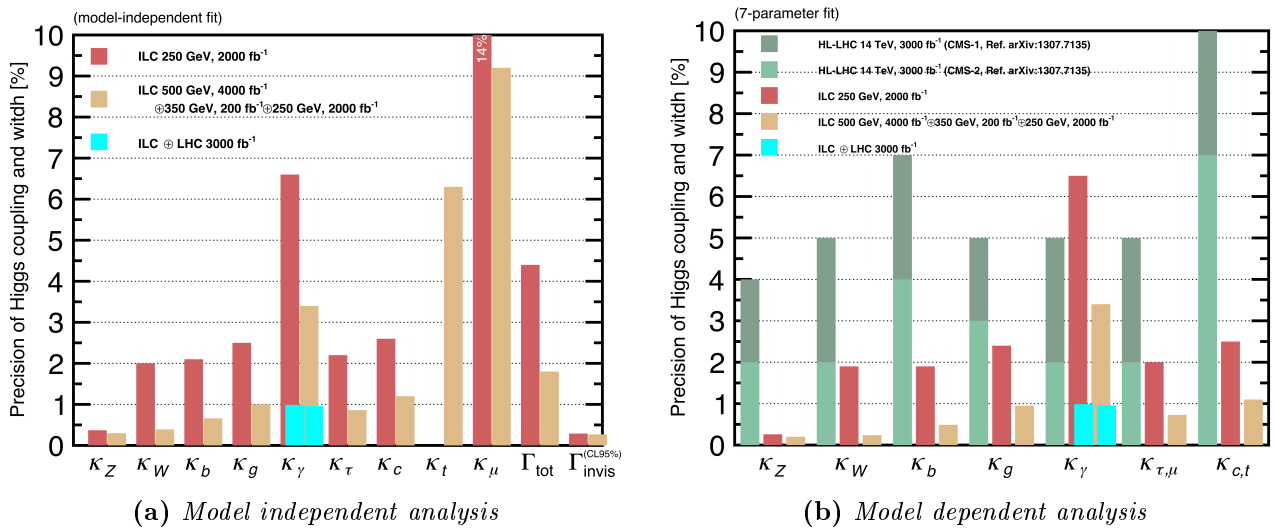


**Figure 4.4.:** Comparison of the precision reached at the ILC and at the High-Luminosity LHC (HL-LHC) for couplings  $g_{hXX}$  (here named as  $\kappa_X$ ) of the Higgs boson ( $h$ ) to SM particles ( $X$ ) [52].

Plot (a) shows the relative precisions for the Higgs couplings calculated from **model independent** fits to simulated data from the ILC with different center-of-mass energies. Plot (b) shows the Higgs coupling precisions calculated from **model dependent** fits to simulated data from the HL-LHC in comparison to simulated data from the ILC.

This leads to differences in the relative Higgs boson coupling precisions of a factor of up to 10 between High-Luminosity LHC (HL-LHC) and ILC results, as can be seen in Figure 4.4. The ILC stage at a center-of-mass energy of 250 GeV will deliver Higgs coupling precisions to a percent level. As discussed above, the coupling to the Z boson can be measured with such high accuracy that even in the initial ILC run a precision of about 0.75 % can be achieved [52, p. 6]. After an upgrade to a center-of-

mass energy of 500 GeV, the precisions for all couplings will improve by at least a factor of two. When comparing the coupling precisions achieved through model dependent fits of the High-Luminosity LHC (HL-LHC) to precisions achieved at the ILC (see Figure 4.4b), the differences between the two machines become clear. Nevertheless, a synergy of the data collected at both machines is beneficial for the Higgs coupling to photons for instance. The combined knowledge reduces the relative precision from a few percent to below 1% precision.

#### 4.1.3. Physics at later ILC stages

The ILC physics program has an excellent discovery potential for new physics. The first stage at 250 GeV has the capability to make prominent progress in the Higgs sector by measuring the Higgs branching ratios to the highest precisions, as shown in the Figure 4.4. The later stages will complete this picture: precision measurements of the top quark, further Higgs measurements, and BSM searches will be accessible at 350 GeV, 500 GeV, and possibly 1 TeV.

The ILC at a center-of-mass energy of 350 GeV will enable a threshold scan of  $t\bar{t}$  production in order to measure the top quark mass and its total decay width to unprecedented accuracy. This will be the first time that the top quark properties are measured at a  $e^+e^-$  collider. To this end, the top quark mass measurements are aimed at a precision of around 40 - 75 MeV, with a statistical precision of about 13 MeV [53, p. 24]. The most recent value for the total uncertainty from direct top quark measurements is 600 MeV, given in the Review of Particle Physics (2017) [54]. Figure 4.5 shows the cross section of the top quark pair production at the  $t\bar{t}$  threshold.

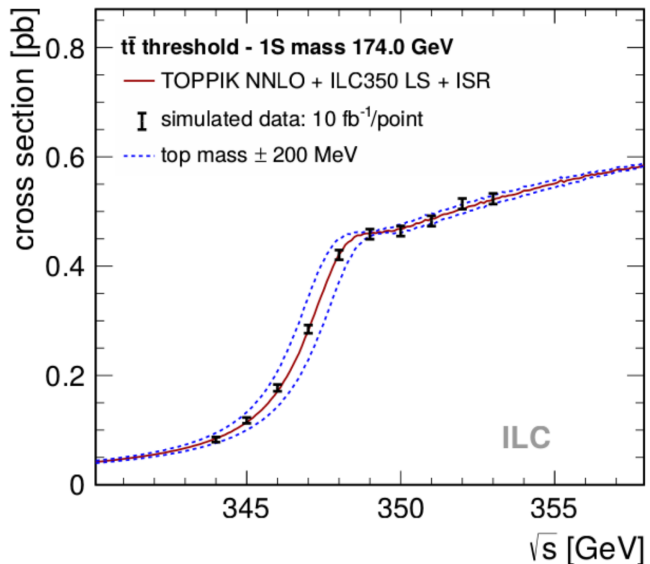


**Figure 4.5.:** Top quark pair production cross section at the ILC at a center-of-mass energy of 350 GeV after one year at the design luminosity [50, p. 15].

At a center-of-mass energy of 500 GeV, further improvements in the precision measurements of the Higgs boson properties can be achieved. As has been shown in Figure 4.4, the Higgs coupling precisions will be improved by a factor of two. The Higgs coupling to the top quark can be derived from precision cross section measurements of  $t\bar{t}h$  processes. Since the top quark is the heaviest known elementary particle, it is expected to have the strongest coupling in the Higgs sector. Therefore, its mass and its

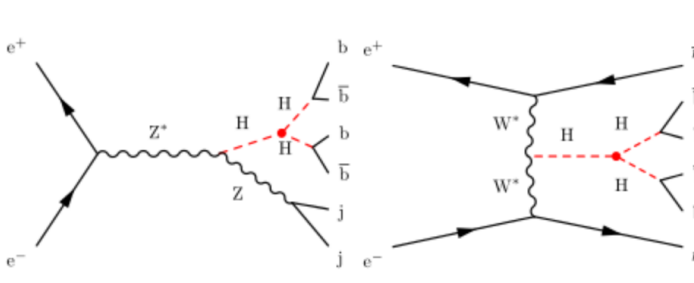


**Figure 4.6.:** Feynman diagrams of the Higgs self-coupling processes:  $e^+ + e^- \rightarrow Zhh$  and  $e^+ + e^- \rightarrow \nu\bar{\nu}hh$ , with the subsequent decay of the Higgs boson to bottom quarks [55].

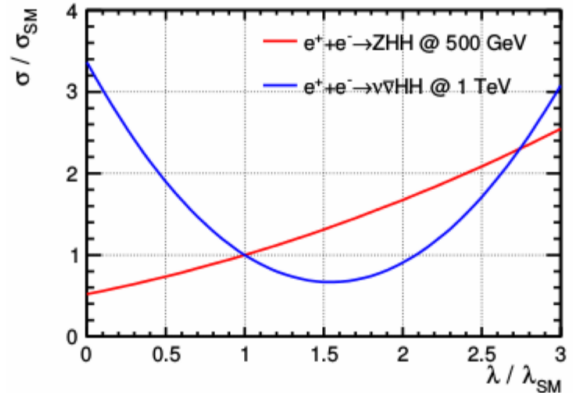


**Figure 4.7.:** Double Higgs production cross sections at the ILC normalized to the Standard Model cross section for different values of  $\lambda$  [53, p. 23].

coupling to the Higgs boson are important quantities in many particle physics theories, and will be measured in a model independent manner as described in the section above. The full ILC program will yield a precision of the Higgs coupling to the top quark of about 2% in model independent analyses [55]. Only with such precisions, can deviations from Standard Model predictions be discovered, which has implications for new physics beyond the Standard Model.

Additionally, measuring the Higgs self-coupling in double Higgs production processes is another goal of the ILC. In the processes  $e^+ + e^- \rightarrow Zhh$  and  $e^+ + e^- \rightarrow \nu\bar{\nu}hh$  (see Figure 4.6), the Higgs self-coupling can be measured to an accuracy of 16% at the ILC stages at 500 GeV and 1 TeV [55]. With these processes, the precision on the cross sections can indicate deviations from the Standard Model. For higher and lower values for  $\lambda$  (which is a coefficient in the Higgs potential [11, p. 174]) compared to its Standard Model prediction, deviations from the Standard Model cross section can be observed, as shown in Figure 4.7. For the case that  $\lambda = 2\lambda_{SM}$ , the cross section for  $e^+ + e^- \rightarrow Zhh$  at a center-of-mass energy of 500 GeV is increased by about 60%.

In all stages, the discovery potential in precision measurements is considerably improved. This includes searches for dark matter, supersymmetry (SUSY), and further beyond the Standard Model theories. Figure 4.8 shows the predicted MSSM<sup>3</sup> Higgs coupling deviations from Standard Model couplings. For the bottom quark and the tau, the deviation is about 3%. As shown in Figure 4.4 (b), the achievable HL-LHC coupling precision in these channels, however, ranges between 2% and 7%. The aimed-for ILC precisions of between 0.5% and 2% for the coupling to the bottom quark and the tau will allow to distinguish the MSSM model from the Standard Model.

Searches for dark matter in the form of WIMPs (weakly interacting massive particles) ( $\chi$ ) at a particle collider is challenging, since they are neutral and weakly interacting, and therefore do not leave signals in collider detector experiments. One of the ILC strategies is to observe the pair production

<sup>3</sup>The Minimal Supersymmetric Standard Model (MSSM) is a supersymmetry model that considers the minimum amount of particle states in addition to the Standard Model, in order to realize the SUSY phenomenology [56].

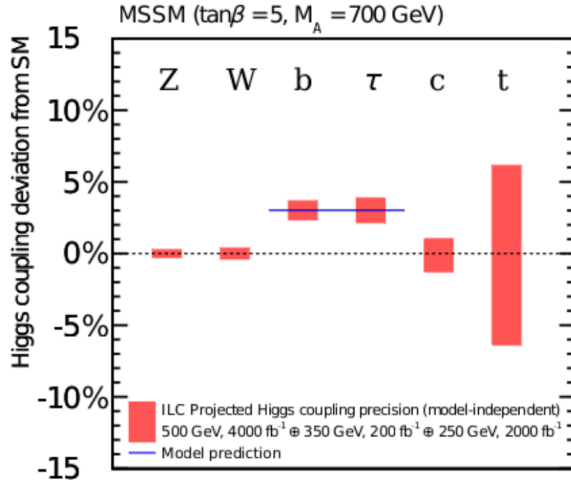


**Figure 4.8.:** Predicted MSSM deviations from Standard Model Higgs couplings [50, p. 12]. The error bars represent the uncertainties expected from model independent analyses of the given ILC data set.

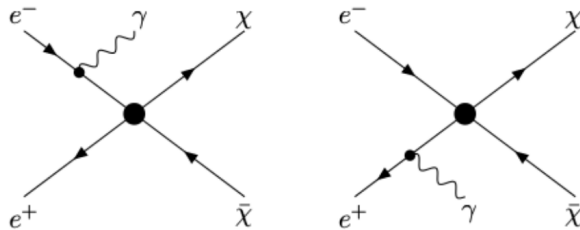


**Figure 4.9.:** Feynman diagrams of a WIMP pair production in a  $e^+e^-$  collider, with initial state radiation [57, p. 4].

of such invisible dark matter particles through the initial state radiation<sup>4</sup> in the form of a photon. Figure 4.9 shows two Feynman diagrams of such processes. As there is no QCD background and the QED background can be addressed by the beam polarization (see Section 4.1.1), the ILC experiments can detect particles with energies of about 1 GeV and below [50, p. 20]. Once such a WIMP candidate was found, its mass could be determined with an accuracy of approximately 1% [53, p. 27]. A complete overview of the physics motivation for the various ILC stages can be found in [49].

## 4.2. The ILC layout

After having defined the ILC goals, a layout for the accelerator was then formulated, which would be able to deliver its objectives. The ILC is envisioned as an  $e^+e^-$  collider with a high luminosity and state-of-the-art technologies for the detectors and the machine.

The following sections will explain the designs of the collider and the detector concepts, which are the result of over twenty years of research at over 300 science laboratories and universities all over the world [43]. The ILC project is therefore truly an international project.

<sup>4</sup>Initial state radiation is the radiative emission of a particle from the process's incoming particles

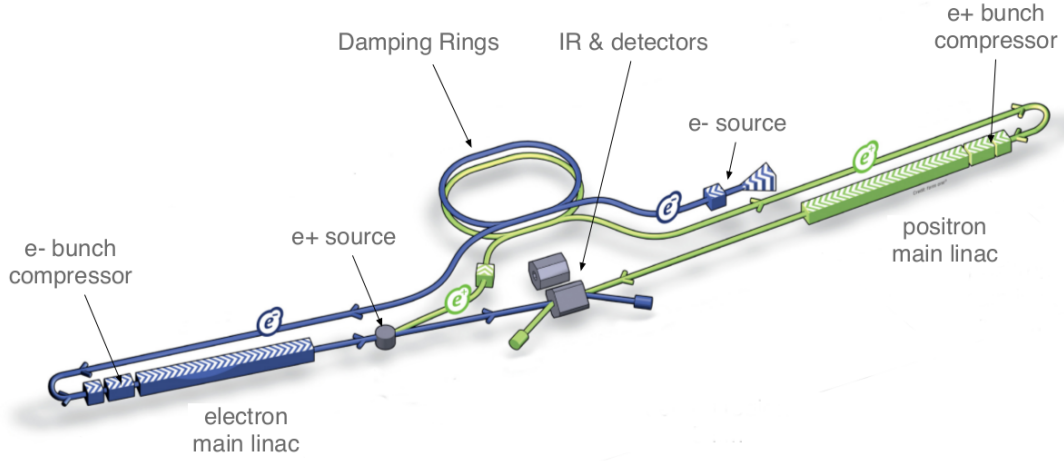


Figure 4.10.: Schematic layout of the ILC [43, based on p. 9]

Figure 4.10 shows the schematic layout of the ILC. By choosing it to be a linear collider, it is extendable in length allowing to upgrade the accelerator to higher center-of-mass energies. With an initial center-of-mass energy of 250 GeV for its first stage, the ILC is proposed to be upgraded to 350-500 GeV and possibly even 1 TeV.

The ILC was originally designed to collide electron and positron beams with a center-of-mass energy of 500 GeV in the first stage of operation. The layout of this 500 GeV machine is summarized in great detail in the Technical Design Report (TDR) [58]. Because of political developments and the request in 2017 to reduce the initial construction cost, the first stage collision energy was reduced to 250 GeV. As it is in the nature of linear accelerators that the beam energy is linearly proportional to the accelerator length, the basic layout of the ILC as stated in the TDR is still the same for the new so-called ILC250. However, the changes that were made to the layout are given in this section, together with an overview of the generation, preparation and collision of the particle beams in this linear collider concept.

#### 4.2.1. From beam generation to collision

**Beam sources** The electrons are produced by a GaAs photocathode in a DC electron gun [45, p. 13]. By shining a circularly polarized laser on the electron beam, a beam polarization  $P_e$  of at least 80 %<sup>5</sup> is achieved, i.e. more than 80 % of all electrons have the same handedness. In the following equation, a beam polarization of 80 % is shown [45, p. 81]:

$$P_e = \frac{N_L - N_R}{N_L + N_R} > 0.8 \quad (4.6)$$

where  $N_L$  is the number of left-handed electrons, and  $N_R$  is the number of right-handed electrons. The electrons from the electron source are captured and continue along the electron beam line. The beam lines contain several sub-systems that prepare the beams for the main acceleration and the final collision. One of the first sub-systems of the electron beam line is the initial bunching and pre-acceleration of

<sup>5</sup>This is a design choice of the ILC. For the positron beam an opposite polarization of 30 % is envisioned (see below).

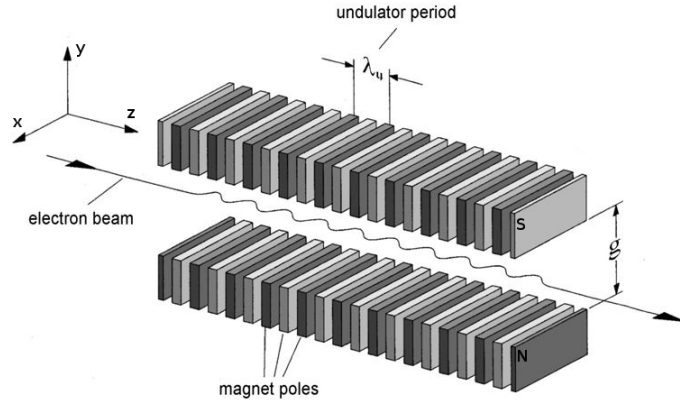


**Figure 4.11.:** Schematic of an electron beam traveling through an undulator with dipole magnets in alternating order [39, based on p. 41].

the beam with normal-conducting RF cavities. This is done using “velocity bunching”, as explained in Section 3.3. Being pre-accelerated to 76 MeV in this step, the now bunched electron beams are accelerated to 5 GeV by a superconducting booster linac [45, p. 81f].

The positron source consists of an undulator and a conversion target [45, p. 90f]. In an undulator, dipole magnets are placed in a line in such a way that their polarity alternates periodically (see Figure 4.11). For the creation of the positrons, the electron beam is used, which is guided through a 231 m long helical undulator after being accelerated to the final beam energy of 125 GeV. Using an undulator with a helical magnetic field causes the electrons to be deflected on a helical trajectory, and to emit synchrotron radiation photons that are circularly polarized<sup>6</sup>. The high-energy photons are then converted in the 7 mm thick titanium-alloy conversion target, where  $e^+e^-$  pairs are produced due to pair production. As the pair production from circularly polarized photons yields longitudinally polarized  $e^+e^-$  pairs [59], the beam of the captured positrons will have a polarization of at least 30 % [45, p. 14]. The whole process leads to an effective positron yield of 1.5 positrons per original beam electron passing through the undulator [60]. Due to the fact that the positrons were produced by using an already bunched electron beam, the positron beam is bunched as well.

**Damping rings** Since the electrons and positrons still have a large emittance from when they originated from their sources, their momentum and beam sizes have to be condensed. This is done in the damping rings, which have a circumference of 3.2 km [45, p. 14]. A layout of the ILC damping rings is shown in Figure 4.12. As discussed before, the beams will emit synchrotron radiation when they are deflected in a magnetic field. This is desired in the damping rings in order to “cool” the beams, i.e. to reduce their momenta due to the emission of photons. The emission of synchrotron radiation happens in the curved sections of the damping rings, but also in the straight sections by the use of wigglers. Wigglers are similar to undulators, but use fewer magnet pairs and higher magnetic fields. Charged particles are therefore deflected more in wigglers. Since the synchrotron radiation photons are emitted tangentially to the beam particle’s path, the particle’s momentum in the forward direction is reduced. By accelerating the beams in RF cavities in the straight sections, the beam momentum in the z-direction is increased. Overall, the momentum in the desired direction rises, whilst the momentum spread shrinks.

<sup>6</sup>For circularly polarized light, the field vector of its electromagnetic wave rotates around the direction of propagation.

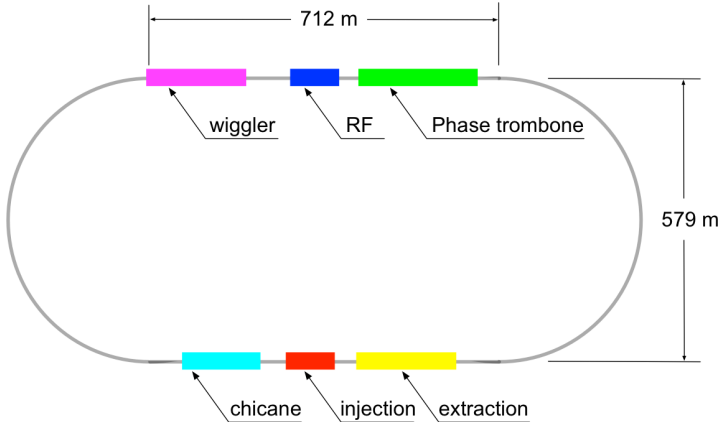


**Figure 4.12.:** Schematic layout of the ILC damping rings. Next to the injection and extraction system, there are wigglers and RF cavities for the emittance reduction, as well as a chicane for circumference adjustments, and a phase trombone for accommodating changes in the RF phase [45, p. 15].

This is, however, not the only effect of damping rings. As shown in Section 3.3, the orbit of charged particles in an external magnetic field depends on their momenta. In the bends, off-momentum particles travel on an orbit with a different radius than particles with the ideal momentum. Entering the straight sections from suboptimal orbits causes orbit distortions and aberrations in the straight sections, which again causes a rise in the beam emittance. To counteract this effect, a chicane (see Chapter 3.3) is needed for adjusting the circumference. An additional phase trombone system, which consists of sets of alternating quadrupoles, regulates the orbit aberrations due to changes in the RF phase. Because of the design choice of having a pulse repetition rate of 5 Hz, the beams are stored for 200 ms in the damping rings, performing about 18 000 turns. After this amount of turns, an equilibrium emittance is reached, and the high quality beam with small beam emittance is extracted and continues along the beam lines.

**Bunch compressors** After passing the damping rings, the electron and positron beams are compressed in bunch length by a two-stage compressor system, using “magnetic compression”. Here, the bunch length is reduced from several millimeters to 300  $\mu\text{m}$ . In both compressor systems, RF cavities are used together with wigglers, which compact the beam momentum by exploiting the momentum spread within the beam bunch. As discussed in Section 3.3, the RF frequency and the timing is chosen such that the bunch tail experiences an accelerating phase in the RF cavity, whilst the bunch head experiences a decelerating phase. The low-momentum particles of the bunch head will therefore be deflected more in the wiggler, whilst the high-momentum particles of the tail are deflected less. At the end of the compressor system, the particles of the bunch tail and head will have gotten closer, leading to a shortened beam bunch.

The usage of two separate systems relaxes the requirements a single system would need to fulfill, and allows more flexibility in the operation, e.g. to reduce the beam length below 300  $\mu\text{m}$  [45, p. 124]. In the process of the bunch compression, the beam bunches will be accelerated from 5 GeV to 15 GeV.

**Main linacs** Continuing along the beam line, the bunches are injected into the main linear accelerator structures (main linacs). The two main linacs are designed to accelerate the beams from 15 GeV to

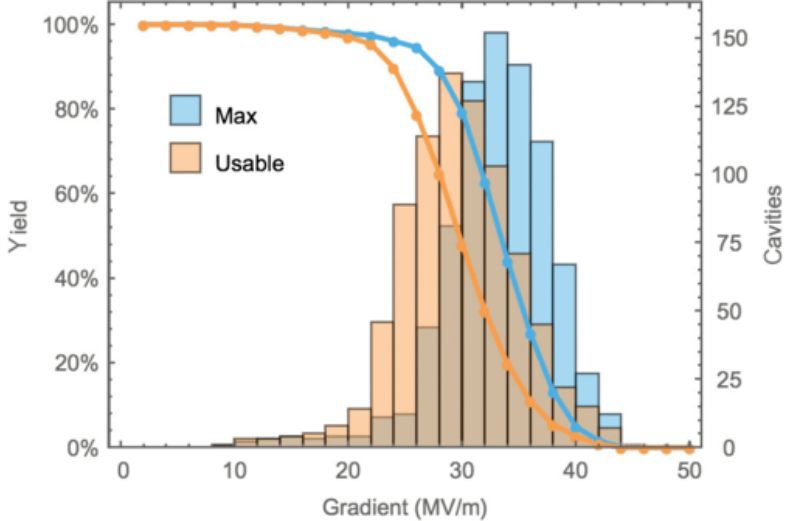


**Figure 4.13.:** Maximum and usable gradient distribution of the final European XFEL cavities. The number of cavities showing a certain gradient is displayed as the bar chart. The so-called usable gradient is the effective gradient a cavity reaches under strict requirements, such as achieving the operational specification for the quality factor. The yield, which is shown as the line graphs, is defined as the fraction of cavities which have a gradient higher than the specified value [61, p. 18].

the final beam energy of 125 GeV, leading to a center-of-mass energy of 250 GeV. They have a length of 5 km each, and use 1.3 GHz superconducting RF cavities with an average accelerating gradient of  $31.5 \text{ MV m}^{-1}$  [62]. A picture of one of these cavities is shown in Figure 3.2a. Since cavities of the same design are already in use for the European XFEL (X-Ray Free-Electron Laser) at Deutsches Elektronen-Synchrotron (DESY) in Hamburg, their high performance has already been demonstrated [63]. The gradient distribution of the cavities used at the European XFEL is shown in Figure 4.13. The average of the maximum gradient reachable per cavity module is about  $35 \text{ MV m}^{-1}$ , which is higher than the ILC requirements. This is especially remarkable, as the cavity specifications for the European XFEL are lower than for the ILC. Another key point is that the production of the cavities is an industrialized process. The high gradients are therefore not demonstrated in a laboratory environment only, but the gradients are also achieved in a more automated procedure.

**Beam Delivery System** The Beam Delivery System (BDS), which has an overall length of about 4.4 km, transports the bunches from the linacs to the interaction point (IP). In the BDS, the beams are focused to nanometer size by the Final-Focus (FF) system, which is a crucial part of the ILC program. Only with nanometer-sized bunches can the ILC reach luminosities comparable to or beyond the LHC, since the total production cross section for  $e^+e^-$  colliders is several orders of magnitude smaller than for proton-proton colliders, such as the LHC, at their respective collision energies (see Figure 2.5). To demonstrate the feasibility of nanometer-scale beams, a test facility was built that is a small scale prototype of the FF system for the ILC: the Accelerator Test Facility 2 (ATF2), which will be presented in more detail in Section 7.1.

The BDS system not only contains the FF system, but also various feedback diagnostics and beam-halo collimators for removing the halo of particles around the beam core in order to reduce the

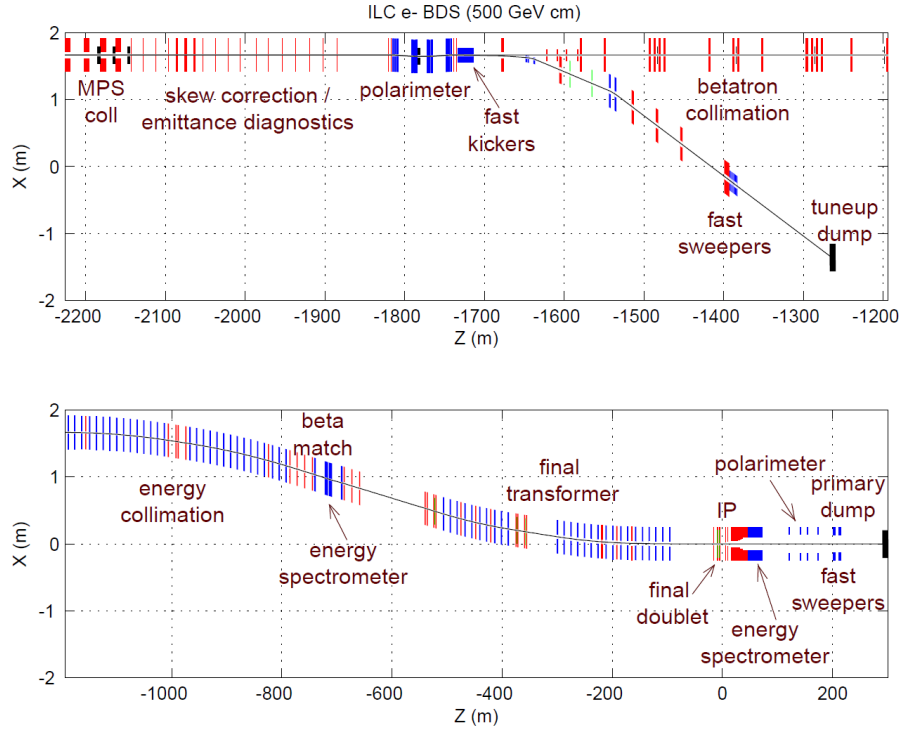


**Figure 4.14.:** Schematic layout of the Beam Delivery System (BDS) for the electron beam line. After the main linac, the BDS for the electron beam line reaches from about  $Z = -2.2$  km to the interaction point (IP) at  $Z = 0$ . The vertical colored lines along the beam line represent the magnets and other devices of the various sub-systems. Next to diagnostic devices, such as the polarimeter and the energy spectrometer, there are collimation systems to focus and to prepare the beam for the collision at the IP. The primary dump at  $Z = 300$  m is the electron beam dump [45, p. 135].

beam background at the IP. The sub-system layout for the sophisticated BDS is shown in Figure 4.14. Additionally, shielding systems are installed at various locations along the BDS line, again in order to keep the background level at the IP as low as possible. Chapter 6 will talk about muon shielding options that are considered for the ILC.

The background studies done for this thesis are focused on background sources close to the IP. All of these background particles originate therefore in the “Final-Focus region”, containing the BDS, the FF system, the IP, and the beam dumps (which will be explained below).

**Beam collision** After the Final-Focus system, the beams are then finally brought into collision with a crossing angle  $\theta_C$  of 14 mrad at the IP [43, p. 9-10]. With so-called crab cavities, the bunches are rotated horizontally so that effective head-on collisions are possible. This is illustrated in Figure 4.15. The crab cavities are also superconducting RF cavities, but designed for an RF frequency of 3.9 GHz and an accelerating gradient of  $5 \text{ MV m}^{-1}$  [45, p. 154]. The RF phase is modeled in such a way that only the head and the tail of the beam bunch experience acceleration, but in opposite directions.

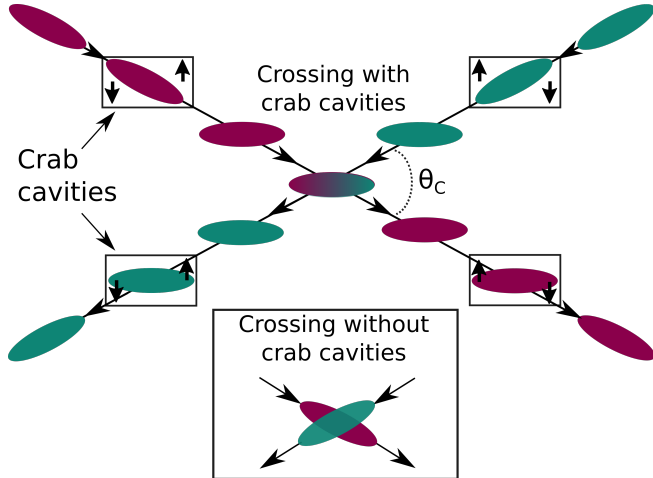


**Figure 4.15.:** Schematic of a beam crossing with crab cavities. In a crossing with crossing angle  $\theta_C$ , head-on collisions are only possible with crab cavities that rotate the beam in the horizontal plane.

The voltage  $V_{crab}$  needed to rotate a bunch with energy  $E_{bunch}$  can be calculated as follows [64]:

$$V_{crab} = \frac{cE_{bunch}\theta_C}{2\omega R} \quad (4.7)$$

$\theta_C$  is the crossing angle,  $\omega$  is the RF frequency of the crab cavity, and  $R$  is the ratio of the bunch displacement at the IP to its divergence, i.e. the ratio of the spatial shift at the IP to the increase in the beam size. With all other quantities fixed, only  $R$  can be increased in order to reduce the required voltage. Therefore, the crab cavities are positioned at locations where this ratio  $R$  between the spatial shift and the beam size increase is calculated to be large. For the ILC, it was calculated that the crab cavities should be located 13.4 m up- and downstream of the IP [45, p. 154].

**Beam parameters** Table 4.1 shows the beam parameters for the baseline design at 250 GeV center-of-mass energy, and for the energy and the luminosity upgrade stages. These beam parameters and the according machine parameters from [43, p. 11, 65] were used for the simulation studies of the  $e^+e^-$  pair background in Chapter 5.

For all ILC running scenarios, the beam sizes are several orders of magnitude smaller than for the LHC Run 2, which is the reason for the comparable luminosities as mentioned above. Despite the number of bunches per pulse and the bunch population being smaller, the LHC luminosity can be exceeded. It is striking that the beam sizes in the horizontal and vertical plane are symmetric for the LHC, whereas they are different for the ILC. This is a design choice, reducing the effect of beamstrahlung whilst enhancing the luminosity. As shown in Equation 2.3, the number of background particles from beamstrahlung is inversely proportional to the sum of the beam sizes ( $\sigma_x + \sigma_y$ ). At the same time, the luminosity is inversely proportional to the product of the beam sizes ( $\sigma_x \cdot \sigma_y$ ), as shown in Equation 3.15. By choosing the beam sizes to be  $\sigma_x \gg \sigma_y$ , the product is small leading to large luminosities, while the sum is large leading to a diminished background rate.

**Table 4.1.:** Baseline beam parameters for different phases in the ILC operation scenario (ILC250, ILC500, Luminosity Upgrade, TeV Upgrade) [43, p. 11, 65] in comparison to LHC Run 2 beam parameters [66, p. 3ff, 67].

		ILC250	ILC500	Lumi Up	TeV Up	LHC 25ns
$E_{CM}$	Center-of-mass energy (GeV)	250	500	500	1000	14 000
$n_b$	Number of bunches	1312	1312	2625	2450	2808
$f_{rep}$	Pulse repetition rate (Hz)	5	5	5	5	11 245
$\Delta t_b$	Bunch separation (ns)	554	554	366	366	25
$N$	Bunch population	$2.0 \cdot 10^{10}$	$2.0 \cdot 10^{10}$	$2.0 \cdot 10^{10}$	$1.74 \cdot 10^{10}$	$11.5 \cdot 10^{10}$
$q_b$	Bunch charge (nC)	3.2	3.2	3.2	2.7	18.4
$\sigma_x^*$	Horiz. beam size at IP (nm)	515.5	474	474	481	16 700
$\sigma_y^*$	Vert. beam size at IP (nm)	7.7	5.9	5.9	2.8	16 700
$\sigma_z$	Longit. beam size (mm)	0.3	0.3	0.3	0.25	0.755
$\mathcal{L}$	Luminosity ( $\text{cm}^{-2} \text{s}^{-1}$ )	$1.35 \cdot 10^{34}$	$1.8 \cdot 10^{34}$	$3.6 \cdot 10^{34}$	$3.6 \cdot 10^{34}$	$1.0 \cdot 10^{34}$

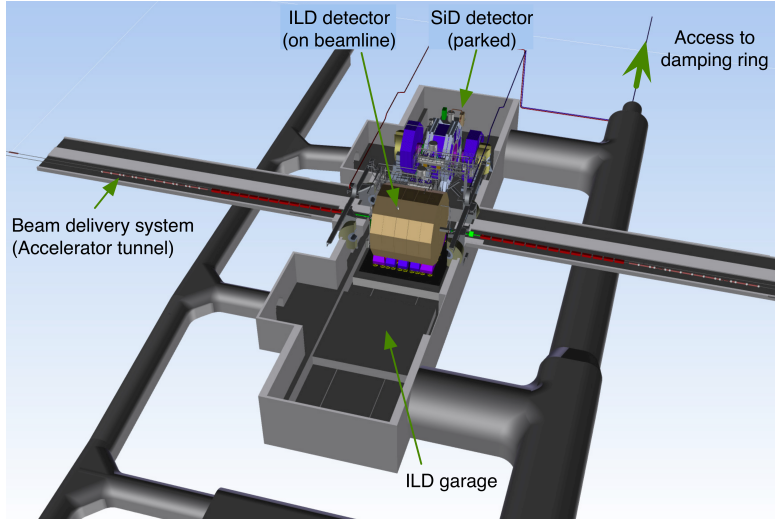


**Figure 4.16.:** Hall of the ILC interaction region with the two detectors in the “push-pull” system [43, p. 29].

**Interaction region and beam dumps** The interaction region (IR) houses the two detectors for the ILC: the Silicon Detector (SiD) and the International Large Detector (ILD), which are in a so-called “push-pull” system. The detectors are explained in more detail in Section 4.4. The layout of the IR hall and the two detectors is shown in Figure 4.16.

After the collision, the spent beams are guided through the extraction line towards the main beam dumps, where they are dumped. The current designs for the main beam dumps are based on a water tank, using high-pressure water with velocity flow systems. Since the water tanks are designed to be sufficient for all energy and luminosity stages, they are supposed to withhold a particle beam with a beam power of 17 MW for the 1 TeV operation [45, p. 18]. This leads to high irradiation of the beam

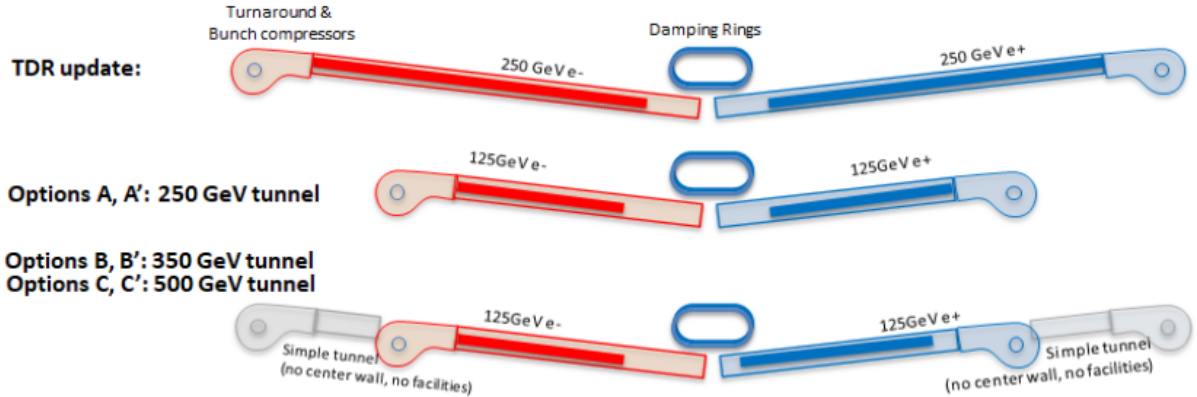


**Figure 4.17.:** Different layouts for the ILC250 stage. The original layout has foreseen a 31 km long tunnel fitting linacs for 250 GeV beam acceleration, which would lead to a center-of-mass energy of 500 GeV.

For the ILC250 stage, the linacs are reduced in length. The discussions about the layout involves also the length of the tunnel. Option B and C foresee longer tunnels that would facilitate a later energy upgrade to 350 or 500 GeV.

Options A', B', and C' correspond to options A, B, and C regarding the tunnel length, but they assume RF cavities with a gradient of  $35 \text{ MV m}^{-1}$  instead of  $31.5 \text{ MV m}^{-1}$  in order to reduce the number of cavities needed [69, p. 19].

dump surrounding and dangerous conditions for maintenance staff. In Chapter 8, which talks about the simulation of the main beam dumps done for this thesis, more details are given for the current beam dump designs.

## 4.2.2. Staging

As mentioned above, the panel of the International Committee for Future Accelerators (ICFA) officially decided in 2017 to reduce the center-of-mass energy of the first ILC stage to 250 GeV, in order to reduce the total costs of the ILC project. ICFA's official statement declares that the "[...] International Linear Collider (ILC) operating at 250 GeV center-of-mass energy will provide excellent science from precision studies of the Higgs boson. Therefore, ICFA considers the ILC a key science project complementary to the LHC and its upgrade. ICFA welcomes the efforts by the Linear Collider Collaboration on cost reductions for the ILC [...]" [68].

The total costs for realizing the ILC includes the manpower, the costs for the construction of the conventional facilities, such as the underground tunnels and the surface buildings, and the costs for the production and assembling of the accelerator and detector components. When breaking the total costs down into the subsystems, then the conventional facilities together with the production of the RF modules for the main linacs make up almost 75 % of the total costs [43, p. 20f]. These estimations are based on cost inquiries with several industrial companies, as well as on experiences gained at other accelerator projects, such as the European XFEL which uses the same design for the RF cavities as planned for the ILC.

Regarding the ILC layout, several options are under discussion which are shown in Figure 4.17. These options would yield a cost reduction of up to 34 % [70], resulting in about 66 % of the initial costs

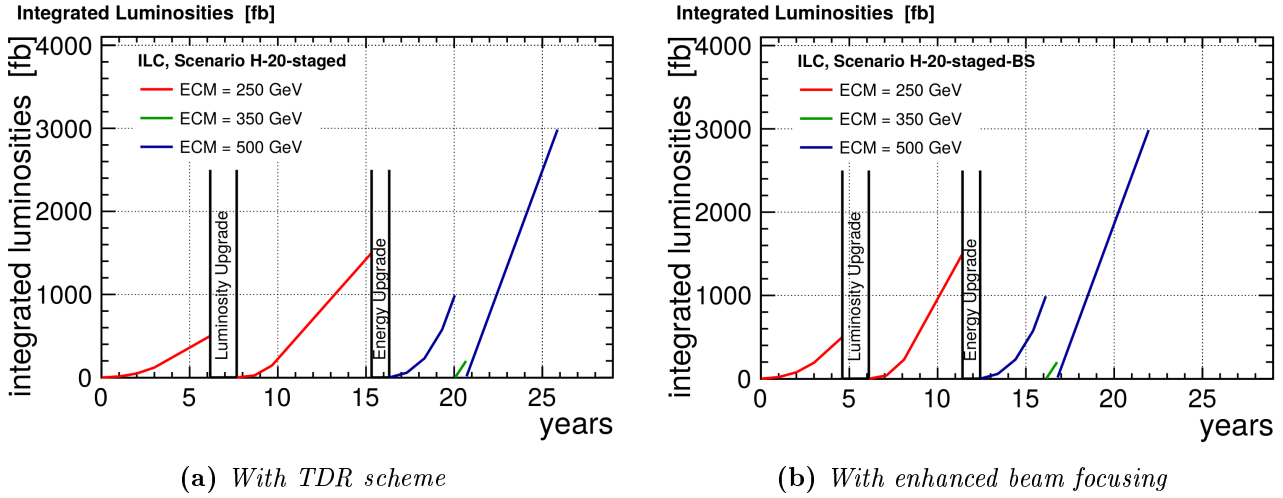


Figure 4.18.: Two possible run plans for the staged ILC [49, p. 8].

for the 500 GeV machine by reducing the length of the tunnel (options A, B, and C), or by additionally reducing the number of RF cavities (options A', B', and C').

In option A, the tunnel is shortened from 31 km for the original TDR design to 20.5 km, fitting merely the main linac modules for a center-of-mass energy of 250 GeV. Options B and C are already taking into account the possibility of upgrading the ILC to higher center-of-mass energies in later stages, so that the longer tunnels of 27 km and 33.5 km leave room for the upgrades to 350 GeV and 500 GeV respectively [69, p. 19].

In options A', B', and C', the RF cavities are planned to have on average a larger accelerating gradient of  $35 \text{ MV m}^{-1}$  (instead of  $31.5 \text{ MV m}^{-1}$  for the TDR cavities) so that a smaller number of cavities would still lead to the same beam energy as for options A, B, and C [69, p. 19]. Overall, option A' foresees the shortest possible tunnel for 250 GeV and the smallest number of cavities, and therefore results in the highest cost reduction.

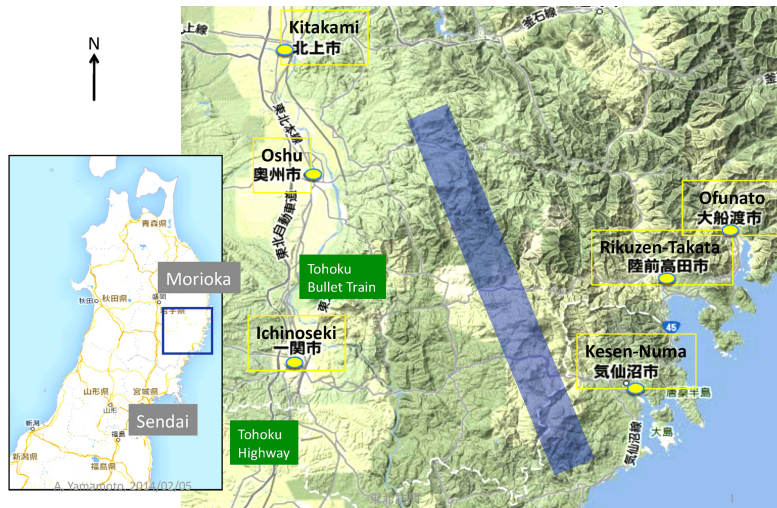
As explained before, the costs for the tunnel and the accelerating structures represent indeed the largest fraction of the total costs, and will be reduced by the staging options. However, the other parts of the accelerator and the surface buildings will not change with the staging scenarios but form basic costs because of which the maximum cost reduction cannot exceed 34 %. Therefore, it has to be considered whether the cost cutback of option A' outweighs all other options with a tunnel length suitable for an energy upgrade. An extended tunnel would give a positive sign to the ILC community that an energy upgrade is definitely foreseen for the future.

Figure 4.18 shows two possible running scenarios for the staged ILC. In both cases, the ILC will have energy and luminosity upgrades, so that it will reach the same integrated luminosity. Figure 4.18 (a) shows an expected operation time of 15 years for the ILC250 with a luminosity upgrade at the midway-point. As shown in Equation 3.15, the luminosity of a particle collider is directly proportional to the number of bunches colliding in every beam pulse. Hence, by increasing the number of bunches by a factor of two, the luminosity for the luminosity upgrade stage is doubled. After an energy upgrade by extending the main linacs, the operation at 500 GeV and a short run at 350 GeV for dedicated measurements of the top quark qualities would be possible. The overall operation time would stretch out to 26 years.

For the second scenario in Figure 4.18 (b), it was assumed that the beam parameters are changed in such a way that the beam is more strongly focused at the IP and therefore that the instantaneous luminosity is enhanced. This shortens the operation time of the ILC250 stage to 11 years, and the overall run time to 22 years, whilst still achieving the same integrated luminosity [49, p. 7].

### 4.3. Possible site

Out of originally more than ten potential ILC sites in Japan, the Kitakami mountains in the Tohoku Prefecture were chosen by a committee of scientists as the preferred site for the ILC [71]. This decision was made in August 2013 after a detailed study of all site specific factors, like the geological conditions, the infrastructure, and the impact on the environment and the economy. Measurements of the Kitakami mountains have shown that it consists mostly of granite rock with the best qualities for the ILC, with respect to vibration and rock stress. As can be seen in Figure 4.19, the closest city (with about 120 000 citizens) would be Ichinoseki. Morioka and Sendai are the biggest cities close to the candidate site, with Tokyo being about 430 km away. Although being in the north of Japan, the travel time from Tokyo is only about three hours by Shinkansen, Japan's high-speed bullet train, and the proximity to the coast line allows the transportation of construction, machine, and detector parts by ship. Additionally, there are local airports in both, Morioka and Sendai, presenting further options for traveling and the transportation of construction materials.



**Figure 4.19.:** The possible site for the ILC is the Kitakami mountains in the Tohoku prefecture [72]. The blue stripe indicates the proposed position for the original ILC TDR design with a length of 31 km.

### 4.4. The detector experiments

The accelerator layout explained in Section 4.2 can deliver the requirements for the ILC objectives, which were presented in Section 4.1. It was shown that the physics goals are based on precision measurements that heavily rely on an outstanding detector performance in order to achieve the promised goals. The performance requirements are accordingly strict, and the detectors are designed to fulfill

them for the full energy range of operation. Some of the requirements are: exceptional energy and spatial resolution, vertex recognition, and reliable flavor tagging. Additionally, the detector designs have to address the background arising from beam-beam interactions and the accelerator itself, which is explained in Section 2.3. Especially the forward detector systems have to be radiation hard to avoid radiation damage. All these requirements are fulfilled in the design of the two ILC experiments.

In order to preserve competitive spirit and the ability to cross-check results, the ILC has two detectors despite the fact that it is a linear and not a circular collider. The so-called “push-pull” system makes this possible by allowing the detectors to switch position after a certain amount of data-taking time. The whole detector together with the last quadrupole magnet (QD0) of the accelerator Final-Focus system will be pulled out of the beam line, and the other detector takes its place. The whole process is designed to take from several hours up to 1-2 days, but involves some challenges especially for the magnets, the cryogenics, and the detector and machine alignment [43, p. 28-29].

The two detectors, the Silicon Detector (SiD) and the International Large Detector (ILD), will be explained in detail in the following sections. The focus will lie on SiD, since all the background studies presented in this thesis were done in the context of the SiD detector.

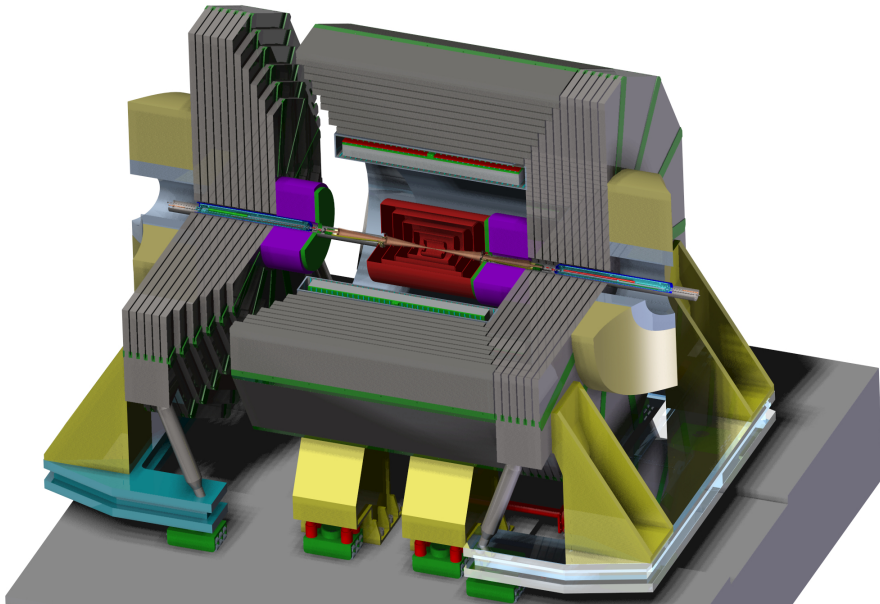


**Figure 4.20.:** The SiD detector consists of the vertex and tracking detectors (red), the electromagnetic calorimeter (ECAL) (green), the hadronic calorimeter (HCAL) (purple) and the muon system (gray). All subdetectors except the muon system are inside the solenoid magnet. Outside the muon endcaps is the detector specific background shielding, called “Pacman” with an inner (light gray) and an outer (beige) layer [73].

#### 4.4.1. The Silicon Detector

The SiD is designed to be a robust, compact multi-purpose detector. Its vertex and tracker system, as well as the electromagnetic calorimeter (ECAL) are purely based on silicon sensors. The silicon design, in comparison to other designs for the vertex and tracking detectors, is more robust regarding the beam background and timing [46, cf. p. 57ff].

Being designed to be compact, the measurements for the full detector are 14 m in height and 11 m in length. To compensate the small radius, the magnetic field of the superconducting solenoid magnet is 5 T, so that SiD is hermetic and contains the full particle showers. The detector is optimized for Particle Flow Algorithms (PFA), in order to improve on the jet energy reconstruction capability. PFA is a method that reconstructs each particle of the final state individually and uses the different subdetectors for specific purposes. Therefore, charged particles are reconstructed from tracks in the tracker device. The electromagnetic calorimeter (ECAL) is used for photons, and the electromagnetic (ECAL) and hadronic calorimeter (HCAL) together for other neutral particles [13].

Table 4.2 lists the key parameters and measurements of the SiD subdetector systems together with the technologies for the individual sub-systems. Additionally, Figure 4.20 shows a visualization of the SiD detector and its subdetectors, which will be explained in the following paragraphs. A more detailed description can be found in [46].

**Table 4.2.:** *Key parameters and technologies foreseen for the baseline SiD design. All dimensions are given in cm [73].*

*The column “Technology” states the detector readout technology and the material of the absorbing layer for the calorimeter systems, e.g. tungsten (W). For the solenoid magnet, superconducting coils are foreseen, creating a magnetic field of 5 T.*

SiD Barrel	Technology	Inner radius	Outer radius	z extent
Vertex detector	Silicon pixels	1.4	6.0	$\pm 6.3$
Tracker	Silicon strips	21.5	121.5	$\pm 150.3$
ECAL	Silicon pixels-W	126.5	140.3	$\pm 176.5$
HCAL	SiPM-steel	140.3	256.8	$\pm 295.0$
Solenoid	5 T SC	260.4	342.9	$\pm 295.0$
Muon System	Scintillator-steel	345.4	605.4	$\pm 416.0$
SiD Endcap	Technology	Inner z	Outer z	Outer radius
Vertex detector	Silicon pixels	7.3	83.4	7.1
Tracker	Silicon strips	77.0	164.3	125.5
ECAL	Silicon pixel-W	165.7	180.0	126.5
HCAL	SiPM-steel	180.5	300.0	140.3
Muon System	Scintillator-steel	300.0	560.0	605.4
LumiCal	Silicon-W	155.7	169.55	20.0
BeamCal	Semiconductor-W	326.5	344	14.0

#### 4.4.1.1. SiD subdetectors

SiD is a multi-purpose detector aimed for providing unprecedented precision measurements of physics events. In order to achieve the strict SiD requirements, the individual subdetectors have to be optimized with respect to their explicit tasks and specifications. The following paragraphs give an overview of all SiD subdetectors.

**Vertex detector** The vertex detector, shown in Figure 4.21, will be the innermost subdetector with the measurements of a soda can. With its five layers for the barrel and four layers for the endcaps, it will be able to do very precise measurements.

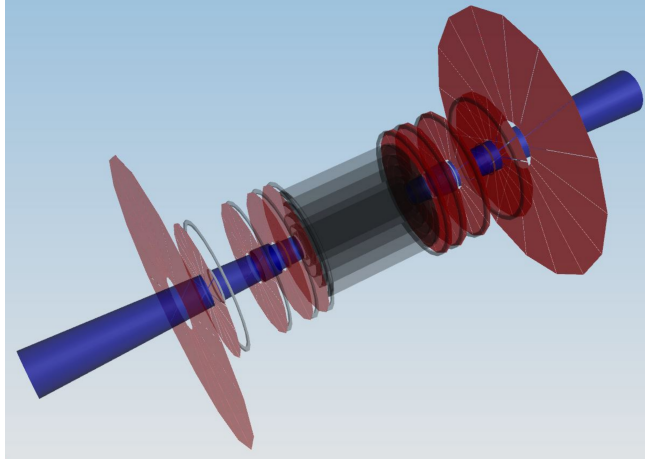


**Figure 4.21.:** Visualization of the SiD vertex detector [74].

The requirements for the vertex detector performance are very demanding: The spatial resolution with less than  $5\text{ }\mu\text{m}$  allows very precise tracking, whilst the impact parameter resolution is aimed for about  $3\text{ }\mu\text{m}$  for the verification of the primary vertex (see Figure 4.22), as well as of the secondary vertex of a bottom quark (b-tagging) and even of a charm quark (c-tagging). The radius of the innermost layer of the vertex detector barrel is only 14 mm, which contributes to the high impact parameter resolution. Figure 4.23 shows the flavor tagging efficiency and the corresponding purity in di-jet samples. Depending on the physics analysis, a working point can be chosen from the plot in order to find the correct balance between high statistics and low backgrounds. The expected flavor tagging efficiencies at the ILC are 96 % and 35 % for b-tagging and c-tagging respectively [44, p. 54].

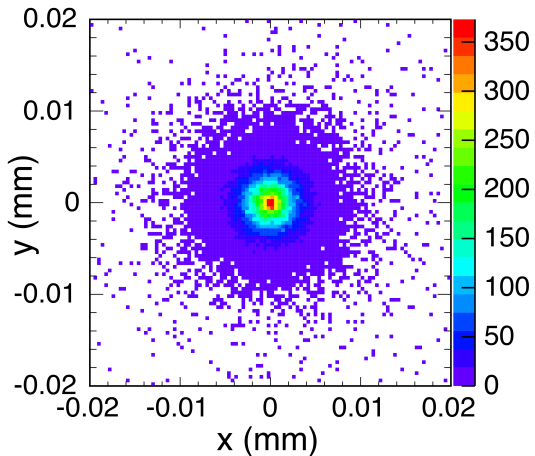


**Figure 4.22.:** Positions of reconstructed primary vertices in simulated processes of the  $Z$  boson decaying to light quarks [46, p. 148].

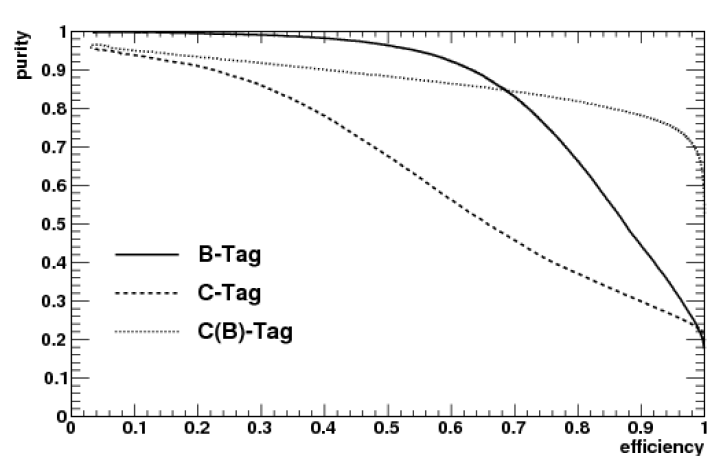


**Figure 4.23.:** Purity as a function of the flavor tagging efficiency in SiD for di-jet samples [75, p. 99]. The curves show the relation for b-tagging, c-tagging, and c-tagging with bottom quark background only.

Additionally, a very small material budget of about  $0.1\% X_0$  per layer is foreseen for the vertex detector in order to limit particle showers and multiple scattering in this subdetector [76, 77]. To achieve this minimal material budget, sensor technologies are considered that foresee the implementation of the sensor buffers on the chips directly to minimize the used material. For a comparison to the CMS pixel detector, Figure 4.25 shows the material budget of the original and the upgraded detector. The material budget is significantly reduced for the upgrade for  $\eta$  above one<sup>7</sup>. In the high- $\eta$  ranges, the material budget reaches  $0.7 X_0$ . The SiD vertex detector material budget, which is shown in Figure 4.24, reaches only  $0.04 X_0$  up to the very forward regions.

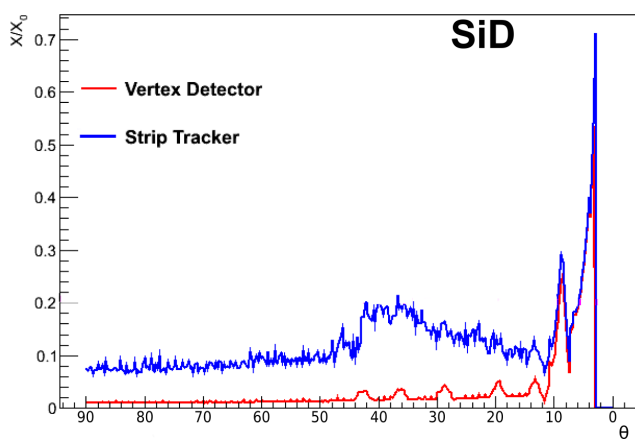


**Figure 4.24.:** Stacked plot of the material budget of the SiD vertex and tracker detector expressed in radiation lengths as a function of the angle to the beam axis [77, cf. p. 51].

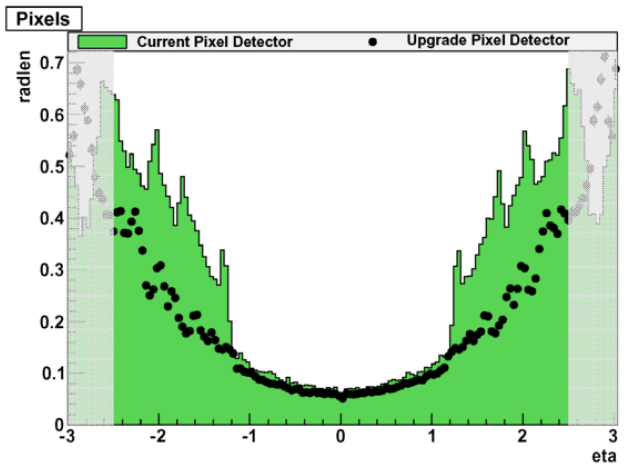


**Figure 4.25.:** Material budget of the original and the upgraded CMS pixel detector expressed in thickness normalized by the radiation length ( $x/X_0$ ), as a function of  $\eta$  [78].

The final decision on the SiD sensor technology and the required pixel sizes is not made yet, which allows the detector to have the most recent state-of-the-art technology. The currently foreseen technology candidates are various designs based on silicon diode pixels, such as Monolithic Active Pixels (MAPS), Chronopix, Vertically Integrated (“3D”) chips, as well as High Voltage CMOS sensors [46, p. 70 ff, 79, p. 319 ff].

The vertex detector is the focus of the  $e^+e^-$  pair background simulation study presented in Chapter 5. Since the actual readout technology is not yet decided, the simulation assumes the readout sensors to have silicon as their sensitive material, and a pixel size of  $20\mu\text{m} \times 20\mu\text{m}$ . It will be shown that the pair background populates the inner SiD subdetectors and causes high detector occupancies. As also explained in Section 4.4.1.3, this implies that the vertex detector sensors will either need to be cooled (increase in the material budget), or that the barrel radius needs to be increased (worse vertex resolution). In both cases, the vertex detector performance declines. Since the

<sup>7</sup> $\eta$  is the pseudorapidity, which is commonly used in LHC experiments to express the angle relative to the beam axis:  $\eta = -\ln[\tan(\theta/2)]$

ILC goal of achieving unprecedented precision relies on excellent vertex reconstruction efficiencies, the vertex detector design will have to be optimized according to the recommendations from simulation studies.

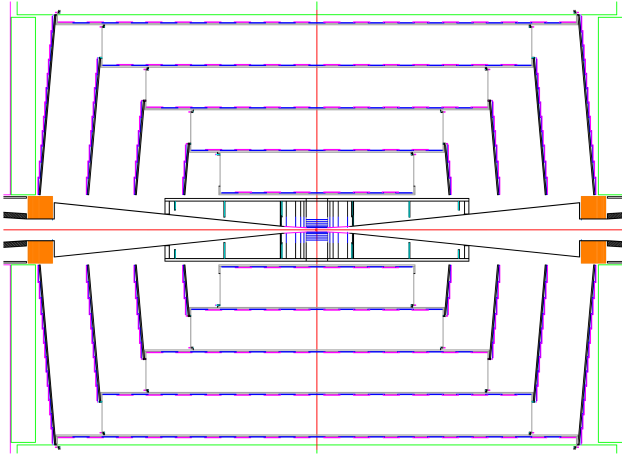


**Figure 4.26.:** The SiD tracking detector layout [74]. The drawing includes the vertex detector in the center.

**Tracking detector** Outside the vertex detector is the silicon tracker, which can be seen in Figure 4.26. For its five barrel layers and four endcap layers,  $0.05 \times 100 \text{ mm}^2$  sized silicon strip sensors are planned that will use KPiX ASIC readout chips [46, p. 74ff].

As indicated in Figure 4.24, the detector requirements for the tracker foresee a strict limit on the material budget of about  $0.1 - 0.15 X_0$  in the central region and about  $0.2 - 0.25 X_0$  in the endcap region.

**Calorimeters** The electromagnetic calorimeter (ECAL) will be using KPiX chips as well, as it is also based on silicon sensors. The ECAL with its 30 layers is designed to be a granular imaging calorimeter with a pixel size of  $3.5 \text{ mm} \times 3.5 \text{ mm}$ , meaning that electromagnetic particle showers developing in the tungsten layers between the sensitive silicon layers can not only be measured in width and length, but rather their shower particles can be tracked individually.

The same will be true for the highly segmented hadronic calorimeter (HCAL) with a pixel size of  $1 \text{ cm} \times 1 \text{ cm}$ . With all subdetectors mentioned so far being inside the 5 T solenoid field of the SiD solenoid magnet, particle tracking is therefore possible not only in the tracking subdetectors, but even in the calorimeters. The 40 active layers of the HCAL will contain scintillators and silicon photomultipliers (SiPM) measuring particle showers that are developing in the steel layers in between.

Figure 4.27 shows a simulated event display in the SiD detector, in which the granularity of the calorimeters is apparent.

**Muon system** The muon chamber, which is the only subdetector outside the solenoid magnet, will use  $4 \text{ cm} \times 1.8 \text{ m}$  or  $5.5 \text{ m}$  long scintillator strips with SiPM readout based on the HCAL sensor technology [46, p. 113]. The strips will be arranged such that a layer of vertical strips (with a length of  $1.8 \text{ m}$ ) will be followed by a layer of horizontal strips (with a length of  $5.5 \text{ m}$ ).

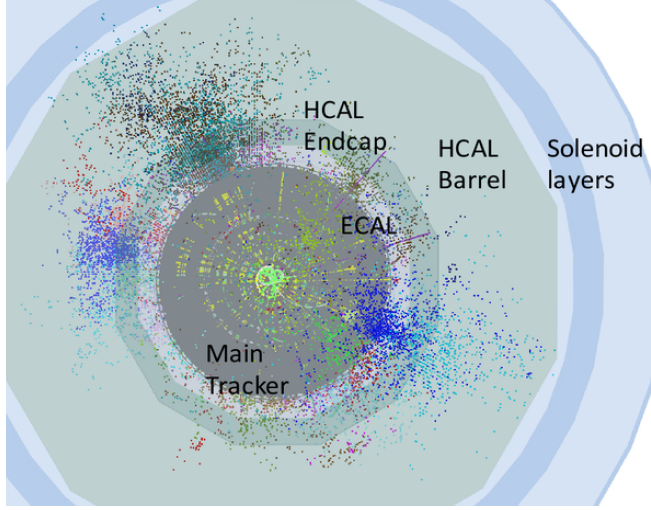


**Figure 4.27.:** *Simulation of a physics event in the SiD detector [74]. The particle showers, which start to develop in the ECAL, are easily distinguishable thanks to the highly granular calorimeters.*

The purpose of the muon system is not only to identify muons being produced in the beam collisions, but also to record the tail of hadronic showers that have started in the HCAL.

Since the muon system is the outermost subdetector, it is exposed to a high background population from the machine background particles that are studied in Chapters 6 and 8. In the simulation, a readout cell size of  $3\text{ cm} \times 3\text{ cm}$  is used.

**Forward system** The forward systems of SiD make the detector hermetic, i.e. the detector is a closed system which can catch particles under almost all solid angles. The forward region covers a polar angle  $\theta > 3\text{ mrad}$ . Boosted particles with high momentum along the beam direction that go under an angle  $\theta < 3\text{ mrad}$  will therefore escape the detector. These losses are unavoidable since detector components cannot be built inside the beam pipe and the detector is not designed for physics that require measurements of these small-angle particles.

The forward system consists of the Luminosity Calorimeter (LumiCal) and the Beam Calorimeter (BeamCal). Apart from making SiD hermetic, the LumiCal will measure the luminosity integrated over time, whilst the BeamCal will give an indication of the instantaneous luminosity by measuring the  $e^+e^-$  pair background from beam-beam interactions, which is explained in Section 2.3.1.1. Since the pair background is directly dependent on the beam qualities (see Chapter 5), the BeamCal measurements will indicate variations in the beam parameters. The LumiCal and the BeamCal are sampling calorimeters using tungsten layers for the particle shower development and semiconductors for the sensitive layers. For simulation studies, the readout cell sizes are set to be  $3.5\text{ mm} \times 3.5\text{ mm}$  for both the LumiCal and the BeamCal.

As the forward region is highly affected by high-energy particles that are typically boosted in the forward direction, the sensors have to be specifically designed to withstand radiation damage. The damage results from large energy depositions from the boosted particles as well as from different

backgrounds, such as the pair background. With this flux of particles hitting the forward system, the BeamCal is expected to have an occupancy of 100 %, i.e. all of the BeamCal pixels are expected to be hit by particles. This large occupancy is accounted for in the readout technology [46, p. 133ff].

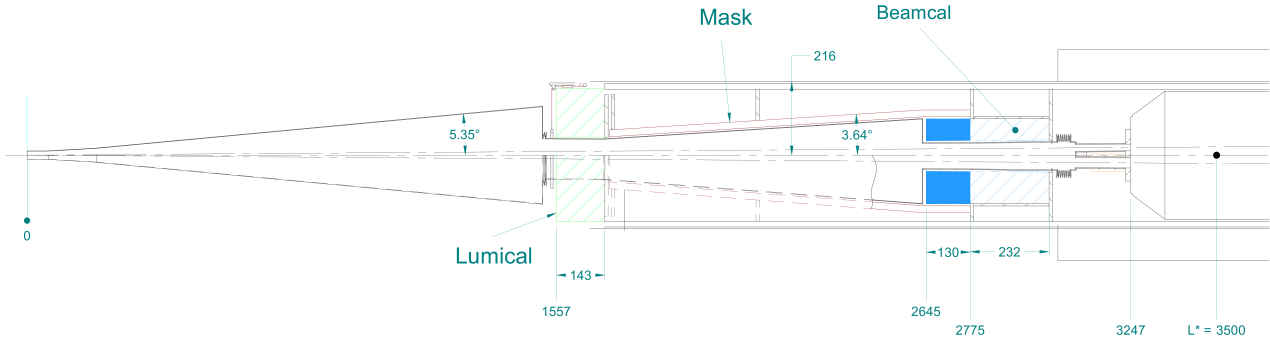


**Figure 4.28.:** Layout drawing of the SiD forward detectors [46, p. 134]. All dimensions are given in mm.

**Pacman** Part of the SiD detector, but not part of the sensitive subdetectors, is “Pacman”. Pacman is a detector specific shielding against machine background that reaches the detector and would increase the detector occupancy. All particles that are produced from the beam interacting with accelerator machine parts, and that reach the detectors, are called machine background. The Pacman shielding is placed on either side of the detector (see Figure 4.20), and has an outer radius of about 2.8 m, hence it covers the full radius of all subdetectors inside the solenoid magnet. The inner layer of Pacman is made of iron, the outer layer of boronated concrete which is specially designed to stop neutrons. The thickness is about 3.4 m [73]. Its use can be seen in the simulation of the machine backgrounds in Chapters 6.2 and 8.5.

#### 4.4.1.2. SiD detector variants

Since the publication of the Technical Design Report about the design details of the ILC accelerator, the detectors, and the facilities, there have been official changes to the design. The changes regarding the overall accelerator and facility design are suggested as Change Requests (CR), and are reviewed and approved by a Technical Change and Management Board [80]. Some of the Change Requests affect the detector designs directly, such as the change of  $L^*$ , the distance between the interaction point (IP) and the last quadrupole magnet (QD0) of the Final-Focus system. But there are also changes to the detector concepts, which are made internally by the detector groups.

There are three major SiD detector design variants that are the subject of discussions, listed in the following. Of these three variants, the impact of the change of  $L^*$  and the anti-DiD field on the vertex detector occupancy are the focus of Section 5.4.

- Change of  $L^*$

As the focal length of the last quadrupole magnet (QD0) of the Final-Focus system, which focuses the beam onto the IP, is smaller than the detector length, both detector concepts have their own QD0 magnet. These magnets are part of the detectors’ push-pull system. The official Change Request CR-002 [81] decided on a common  $L^*$  for both detector concepts. Before, the distance

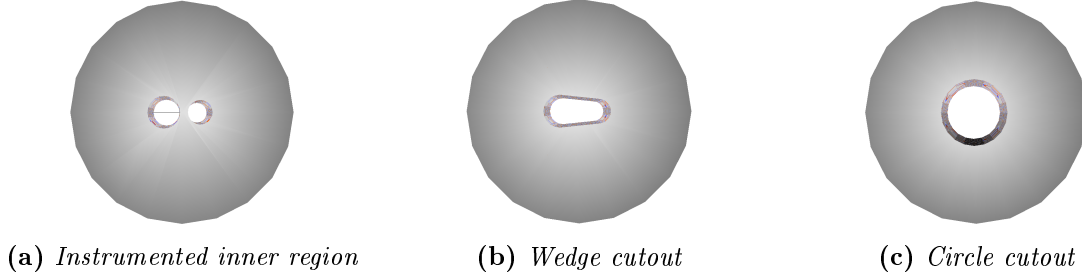


**Figure 4.29.:** Three different design variants of the inner region of the SiD BeamCal. From (a) to (c), the instrumentation of the inner region decreases with an increasing fraction of material cut out.

$(L^*)$  between the IP and QD0 was different for SiD and ILD, as  $L^*$  is dependent on the size of the detector. Since the diverging  $L^*$  values mean different beam operation conditions, CR-002 dictated a change of the detector designs in such a way that  $L^*$  is the same for both detectors, in order to facilitate the beam operation.

For SiD, the dictated change of  $L^*$  from 3.5 to 4.1 m implied in practice that the BeamCal had to be repositioned, since it is attached to the QD0 support structure. The BeamCal moved from a former distance to the IP of 2.95 to 3.265 m [20].

- Design variants of the inner region of the BeamCal

The BeamCal surrounds the ingoing and outgoing beam pipe. For the inner region around the beam pipes, there are three different design variants that include a different amount of instrumentation, as shown in Figure 4.29. By cutting out the area between the beam pipes, the sensitive material is removed from the inner region with the highest density of background flux. Doing so will reduce the overall BeamCal radiation damage, but also lessens the potential for measuring physics events in that region.

The default geometry is Figure 4.29 (a) with the instrumented inner region.

- Anti-DiD Field

The BeamCal is expected to have an occupancy of 100 % due to boosted particles as well as background particles such as the  $e^+e^-$  pairs from beam-beam interactions, as explained before. In order to suppress hits from these  $e^+e^-$  pairs, it was proposed to include an additional magnet in the detector design, the so-called anti-DiD (Detector Integrated Dipole) magnet [82]. The dipole windings of the anti-DiD are directly mounted around the SiD solenoid magnet. Its magnetic field has a value of 60 mT, and causes locally the deflection of the pair background in the region of the BeamCal [46, p. 118]. The pairs are swept into the outgoing beam pipe, which reduces the BeamCal occupancy.

#### 4.4.1.3. Detector readout architecture

The readout architecture for the SiD detector foresees a buffer depth of four in the current design. The number of available buffers is an important issue for the performance of the detector, and is therefore a topic of the SiD simulation studies with respect to the background occupancies. As explained in Section 5.3.2 in more detail, the detector occupancy is the normalized number of cells with a certain amount of hits per detector cell, which is calculated by counting the hits in the individual cells. If the

number of hits per cell exceeds the number of available buffers (the buffer depth), the cell cannot store any further hits, and is then called “dead”.

Since the sensor technology is not yet decided on for the SiD subdetectors, the readout cells in the simulation are determined through the pixelization of the hit positions. The cell sizes are therefore based on realistic sensor pixel sizes, and are defined in the SiD simulation infrastructure.

The buffer depth is in principle a free choice in the detector development phase. The more buffers a sensor has, the more hits can be stored. This does however not come for free, since sensors with a large number of buffers, or with dynamically allocatable buffers, have a higher power consumption. The additional electric circuits that are required to meet the higher demand, and with it the supplementary cooling, lead to a larger material budget, which is not desirable for the vertex detector, for example. A solution for reducing the background occupancy in the SiD vertex detector without increasing the number of sensor buffers is to increase the vertex detector barrel radius. As will be shown in Section 5.2, the pair background has a characteristic density distribution, which extends towards the innermost vertex detector layers. By increasing the vertex detector radius, the pair background occupancy can automatically be reduced. However, as mentioned above, this will affect the vertex reconstruction efficiency negatively, which is critical for a successful ILC program.

A compromise has to be made between necessary buffers and a manageable material budget, and a refined detector optimization is therefore crucial with respect to the occurring background rates.

Table 4.1 lists the ILC beam parameters in the different ILC stages. The ILC will deliver beam trains, which contain 1312 beam bunches in the first stage, at a rate of 5 Hz. Each of the bunches is separated by 554 ns, resulting in a total train duration of 0.72 ms. The time gap of 199 ms between successive trains is used for reading out the analog signals of the detector buffers, and for their digital processing. The motivation of the ILC experiment is to record all measured events without rejecting any of them by the use of triggers, as explained in Section 4.1.

Due to this, the detector background occupancy has to be below a critical acceptance limit. In SiD, a guideline for an acceptable occupancy for background events is that the sum of all dead cells (with a number of hits greater than or equal to the buffer depth) should not exceed 0.01 % ( $10^{-4}$  of all cells):

$$\sum \text{cell}_{\text{dead}} \lesssim 10^{-4} \sum \text{cell} \quad (4.8)$$

For the optimization of the detector readout design and its buffer depth, detailed occupancy studies are therefore needed. In all of the background simulation studies presented in the following chapters, the SiD occupancy has been evaluated with respect to the critical acceptance limit.

#### 4.4.2. The International Large Detector

Like the SiD detector, the International Large Detector (ILD) is a multi-purpose particle detector that is optimized for Particle Flow Algorithms (PFA) (see Section 4.4.1). Its vertex detector is also based on silicon sensors, whereas the tracker is a combination of both, a silicon strip and pixel detector, and a time projection chamber (TPC). Also similar to SiD, the calorimeters are within the solenoid magnet, which is surrounded only by the muon system. The magnetic field of the superconducting solenoid magnet is 3.5 T. Because of having a big gaseous volume, the full detector is bigger than SiD, namely 16 m in height and 14 m in length. Figure 4.30 shows all the subdetectors mentioned above in two schematics of the ILD detector.

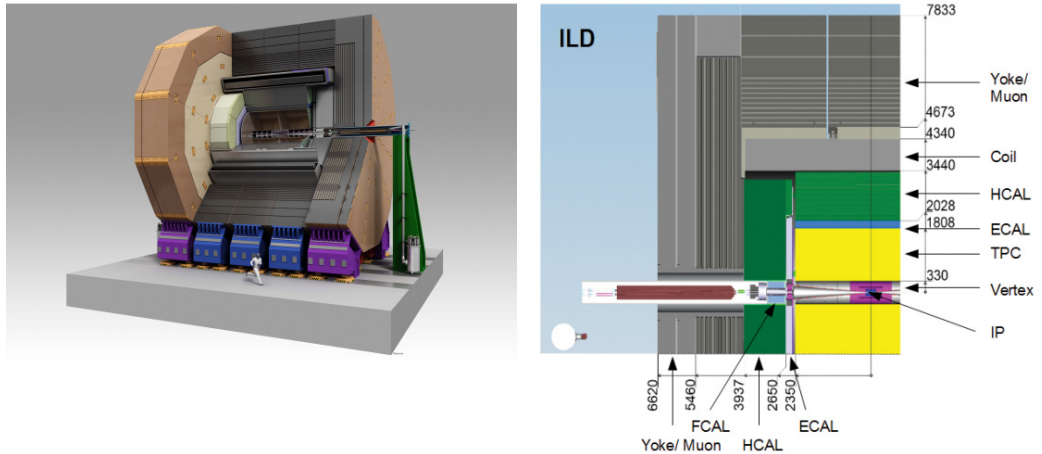


**Figure 4.30.:** The ILD detector consists of the vertex detector (pink), the time projection chamber (TPC) (yellow), the electromagnetic calorimeter (ECAL) (blue), the hadronic calorimeter (HCAL) (green) and the muon system (gray). All subdetectors except the muon system are inside the solenoid magnet [43, p. 34].

# 5 Chapter 5. e<sup>+</sup>e<sup>-</sup> pair background

At the International Linear Collider, the collisions of electron and positron beams are accompanied by the production of background particles. Unlike at hadron colliders, the main background contribution does not arise from QCD processes and underlying events, but rather from the interaction of the colliding beam's electromagnetic fields. The secondary e<sup>+</sup>e<sup>-</sup> pairs form a significant background, the so-called pair background, for the inner detectors, and therefore need to be studied in great detail with respect to the detector arising occupancy.

This chapter discusses first the Monte Carlo event generator in Section 5.1, with which the pair background processes have been generated. Afterwards, the characteristics of these background particles are explained in Section 5.2, followed by several sections on their dependency on ILC running schemes and SiD detector variants. Thus, Section 5.3 presents the dependency on the ILC beam parameters, and Section 5.6 the dependency on the ILC collision energy and the luminosity.

In all sections, the pair background dependencies are analyzed with respect to their impact on the SiD detector performance. Even the detector design itself and its readout architecture have an effect on the pair background occupancy, as shown in Sections 5.4 and 5.5.

The pair background is produced by high cross section processes that are caused by beam-beam interactions. The production processes are described in Section 2.3.1. The secondary electrons and positrons show a characteristic energy and density distribution, which extends to the inner barrel layers and the forward detectors of SiD. Studies of the time distribution and of direct and indirect hits from these particles are presented, with a conclusion on the impact on the detector design. The arising detector occupancy is, however, dependent on the ILC accelerator configurations and the detector geometry. The results of the presented studies are essential for the design choices of the accelerator and the SiD detector.

## 5.1. The Monte Carlo event generator GuineaPig

For studying the effects of the pair background, e<sup>+</sup>e<sup>-</sup> pairs from beam-beam interactions were generated with the Monte Carlo (MC) event generator GuineaPig [83] version 1.4.4. When providing the accelerator beam parameters, the pair background events of one bunch crossing are simulated and the four-vectors of the generated particles are stored in an ASCII output file. The parameters used for generating the pair background for this thesis are given in Appendix A.1.

Since the ASCII files cannot directly serve as input to a full GEANT4 [84, 85] detector simulation, a

conversion tool was developed for the analysis studies presented in this thesis, and instructions on its usage are available in [86]. The tool converts the ASCII output to one of the following file formats, common for ILC detector simulations: stdhep [87] or slcio [88]. These file formats are directly applicable with the GEANT4 based simulation tool SLIC [89], which simulates interactions of the input particles with matter. The simulated geometry model is described in a human-readable format. The flexible geometry description allows the simulation of particle interactions with individual detector geometries. To this end, the geometry description file “sidlo13” of the SiD detector, which was used for the simulation studies in this and in the following chapters, was developed for the SiD Detailed Baseline Design [46, p. 51 ff] and is based on the detector design described in Section 4.4.1 and in [46, p. 69 ff]. The SiD geometry is visualized in an event display of the pair background for a center-of-mass energy of 500 GeV in Figure 5.1. As will be discussed in the following sections, the simulation of the pair background reveals that the pairs populate mainly the inner and the forward SiD subdetectors, but also the calorimeter endcap layers around the beam pipe.

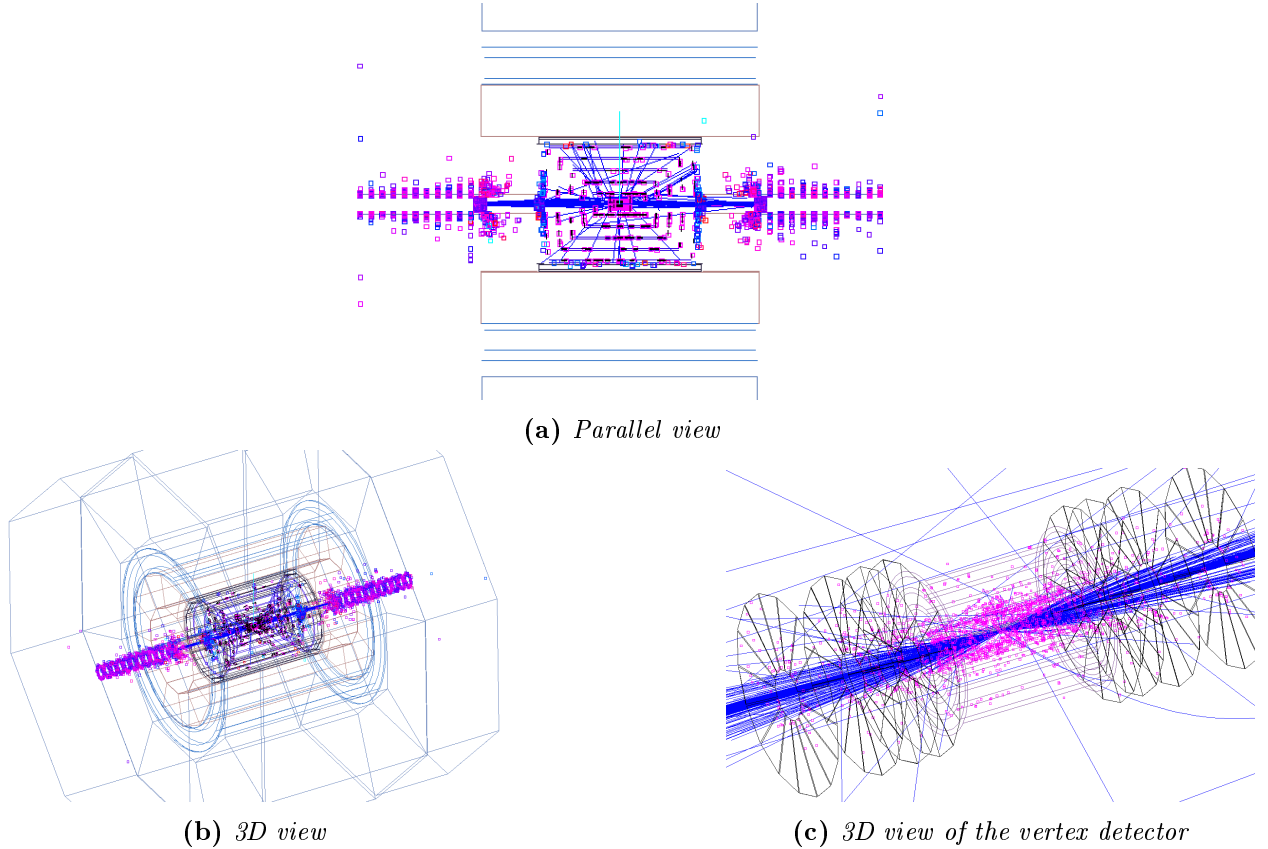


**Figure 5.1.:** Event displays of the pair background in the SiD detector for the ILC stage at a center-of-mass energy of 500 GeV. The event displays were made with WIRED4 [90].

Figure (a) shows the whole SiD detector in a parallel view. Figures (b) and (c) show a three-dimensional visualization.

Hits from the pair background particles can mainly be found in the inner and the forward detectors, but also around the beam pipe in all layers of the calorimeter endcaps.

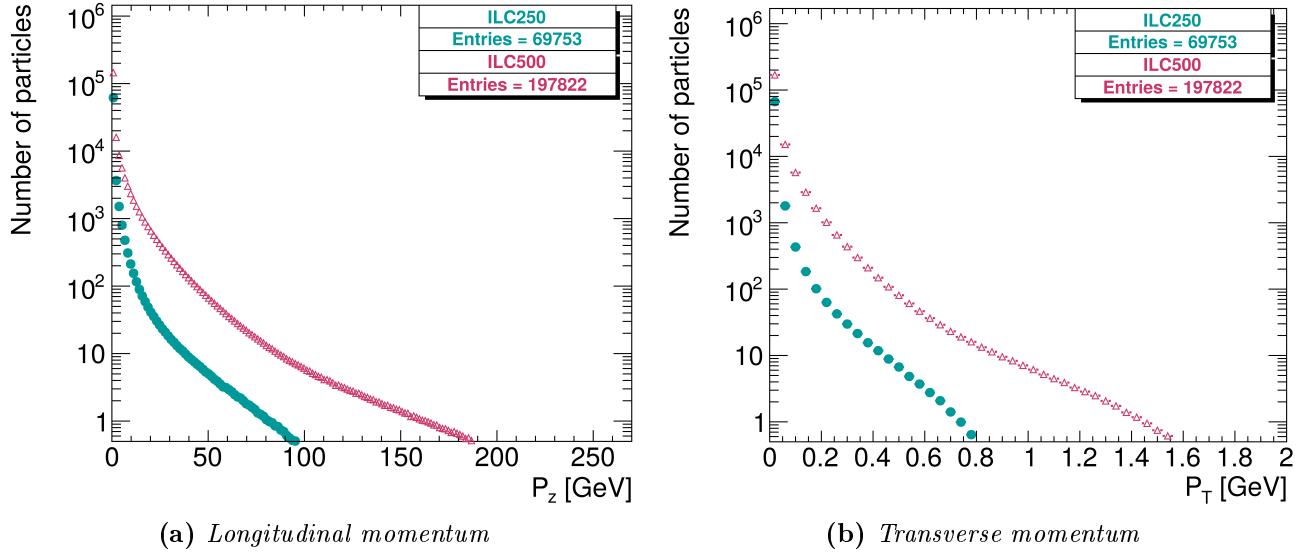


**Figure 5.2.:** Comparison of the simulated pair background momentum distributions for the ILC at 250 GeV and 500 GeV center-of-mass energy, with the longitudinal momentum shown in Figure (a) and the transverse momentum in Figure (b).

## 5.2. Characteristics of the fermion pair processes

By analyzing the generated pair background events, it becomes apparent that the  $e^+e^-$  pairs have a low transverse momentum. Figure 5.2 shows the distribution of their longitudinal and transverse momentum for the two ILC stages at 250 GeV and 500 GeV center-of-mass energy. The longitudinal momentum of the  $e^+e^-$  pairs reaches roughly 80 % of the beam energy, whilst the transverse momentum extends to only 0.8 GeV for the ILC250, and 1.6 GeV for the ILC500.

Due to their low transverse momentum, the pairs are deflected on narrow helical tracks in the magnetic field of the detector solenoid magnet. For the tracking of the helices, it was decided not to use a GEANT4 simulation, since it would deliver only the vertices and the endpoints of the particle tracks. Additional points along the tracks can only be stored when adding active layers in the simulation model. Instead, an algorithm was written that calculates the helix tracks of the pair particles using their four-vectors, in order to get arbitrarily many points on their helix tracks. The track positions are computed from the radius of the helix, its center position and its pitch. Figure 5.3 shows a schematic of the projection of a helix onto the xy-plane. The orientation of the helix is determined by the particle's charge. The following assumptions were made for the algorithm: The magnetic field in the proximity of the IP is homogeneous, with a field strength of 5 T for the SiD solenoid. The particle momenta do not change in the region of interest for this analysis, because of which the helix radius is constant. Any particle interaction with other particles or with matter is not taken into account.

The pair tracks are then plotted using the helix track algorithm to calculate the position in x and y for a given position in z. For the ILC stage at 500 GeV, the pair background track density is shown in Figure 5.4. The density distribution of all the tracks shows a characteristic bell shape, with the highest density along the z-axis. This is true, since the helix tracks originate at the IP, and their radii are small in comparison to their pitches due to the particles' momentum distribution. The red solid lines represent the outline of the beam pipe inside the SiD detector. Up to 6.2 cm from the IP in the

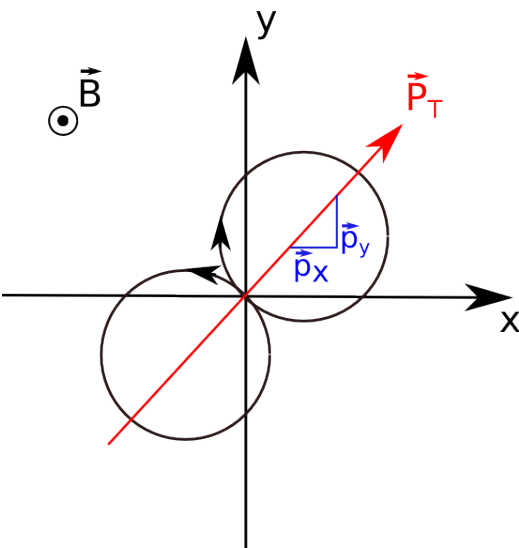


**Figure 5.3.:** This schematic shows the projection of a helix track onto the  $xy$ -plane, with the vector of the transverse momentum ( $P_T$ ) and the  $x$ - and  $y$ -momenta ( $P_x$  and  $P_y$ ). Depending on the particle's charge, the direction of the rotation is either clockwise or anticlockwise. The center, the radius, and the orientation of the projected circle is dependent on the transverse momentum of the particle.

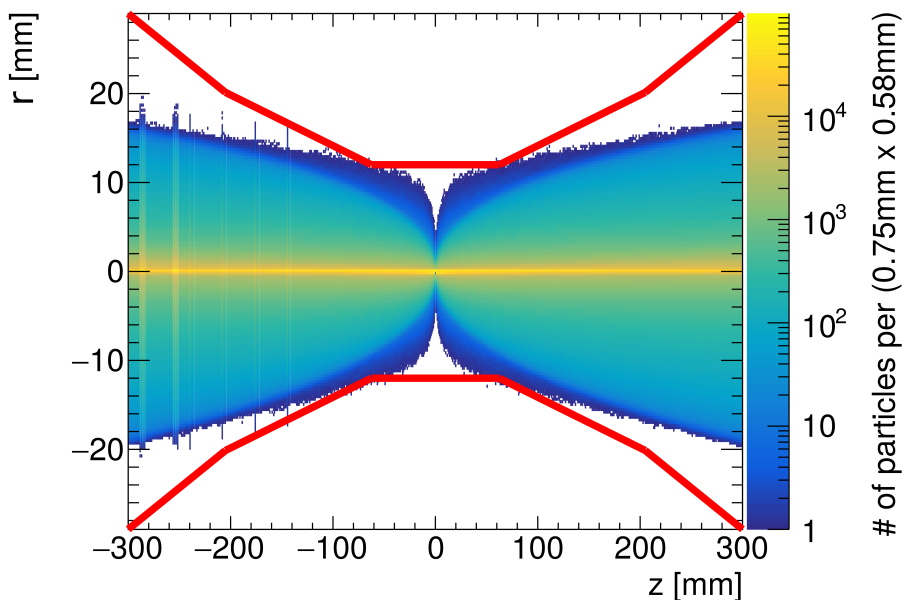


**Figure 5.4.:** Pair background density for one ILC bunch crossing of the ILC500. The figure shows the complete track density distribution of the pairs at a center-of-mass energy of 500 GeV. The color scale shows the number of tracks per unit area. The red solid lines represent the outline of the beam pipe.

z-direction, where the beam pipe increases in width, the beam pipe radius is 12 mm. This is the point of closest approach to the pair background envelope.

As the bell-shaped envelope is symmetric in the positive and negative z-directions, the view of the pair background envelopes in the following figures is chosen to be in the positive z-direction. In reality, the density distributions are not fully symmetric with respect to the z-axis due to the crossing angle of 14 mrad of the ILC beams. This, however, cannot be implemented in GuineaPig. For the purpose of visualizing the density distribution, the approximation without the crossing angle is sufficient. In the following GEANT4 simulation, however, the crossing angle is applied, so that the detector population with the pair background particles is described correctly.

In order to compare the envelope shapes for different ILC center-of-mass energies, Figures 5.5 (a) - (c) show the density distributions at 250 GeV, 350 GeV, and 500 GeV respectively. For the generation of the pair background, the beam parameters of the three different baseline ILC stages were used, which are given in [43, p. 11].

Figure 5.5 (d) shows the individual envelopes containing a certain fraction of all tracks. In this way, it becomes apparent that for higher center-of-mass energies the width of the envelope increases due to the higher transverse momenta of the pairs. For lower center-of-mass energies, the envelopes stay well within the beam pipe radius. At 500 GeV, however, the envelope containing 99.99% of all pair helix tracks crosses the beam pipe, extending towards the innermost layer of the SiD vertex detector barrel, which has a radius of 14 mm. The minimum transverse momentum for reaching the vertex detector barrel is approximately 0.02 GeV. This value can be theoretically calculated by considering the Lorentz force in homogeneous magnetic fields. Charged particles are deflected on circular paths, when the Lorentz force and the centripetal force are in equilibrium:

$$\begin{aligned} q\vec{v} \times \vec{B} &= \frac{m\vec{v}^2}{\vec{r}} \\ qvB \cdot \vec{e}_r &= \frac{mv^2}{r} \cdot \vec{e}_r \\ r &= \frac{p}{q \cdot B} \end{aligned}$$

This can be expressed in terms of  $p$  [GeV],  $B$  [T], and  $r$  [m] by:

$$r[\text{m}] = \frac{p[\text{GeV}]}{0.3 \cdot B[\text{T}]}$$

In order to verify the minimum transverse momentum, which is necessary for the pair particles to reach the innermost vertex detector barrel layer (with a radius of 14 mm), the equation can be converted to:

$$\begin{aligned} \Rightarrow p &= 0.3 \cdot B \cdot r \\ &= 0.3 \cdot 5 \text{ T} \cdot 0.014 \text{ m} \\ &= 0.021 \text{ GeV} \end{aligned}$$

In the subsequent GEANT4 simulation of the pairs hitting the SiD vertex detector this value was confirmed.

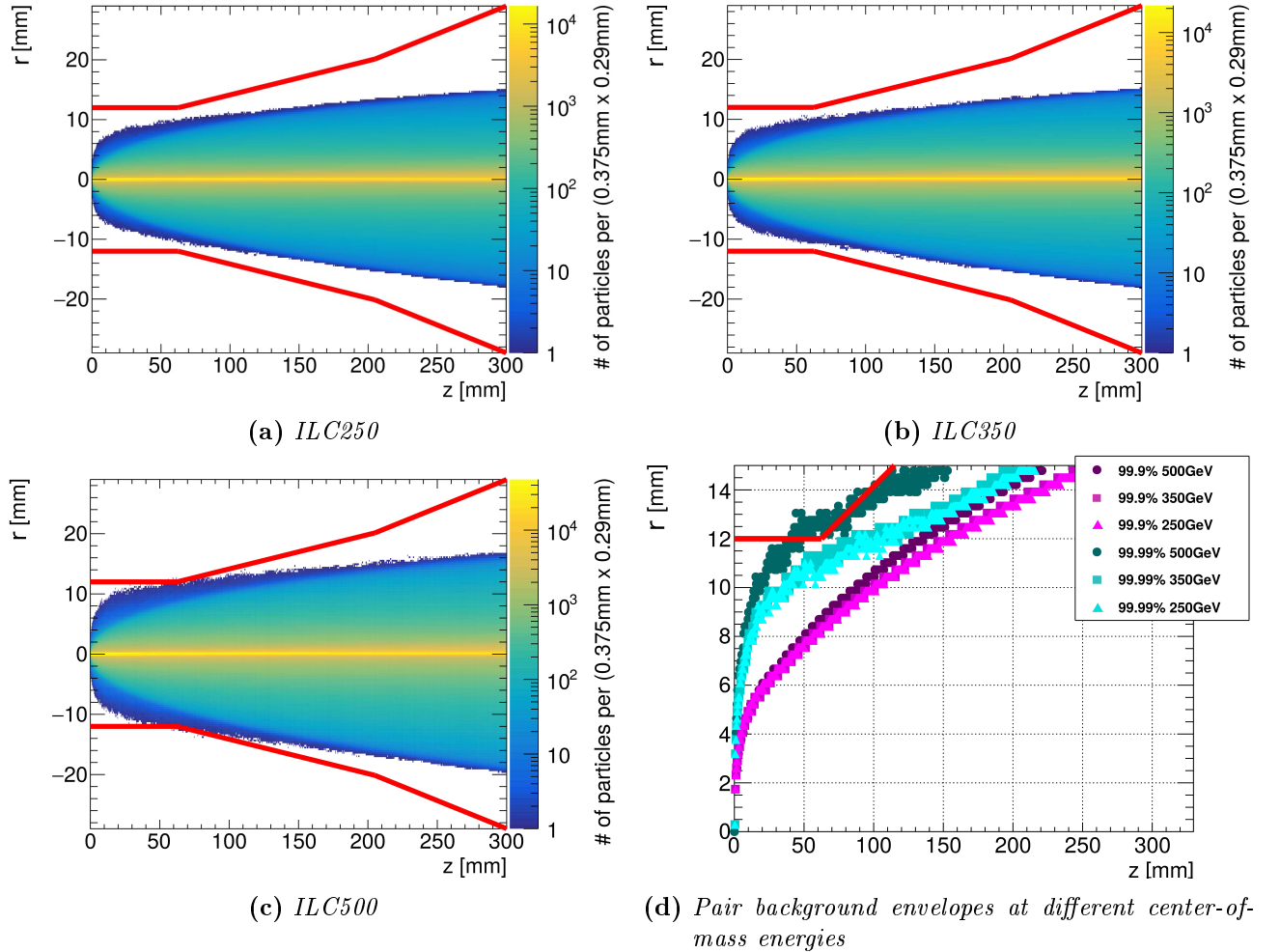


**Figure 5.5.:** Comparison of the pair background density for one ILC bunch crossing at different center-of-mass energies. Figures (a), (b), and (c) show the complete track density distribution of the pairs at a center-of-mass energy of 250 GeV, 350 GeV, and 500 GeV respectively. The color scales show the number of tracks per unit area. The red solid lines represent the outline of the beam pipe.

In Figure (d), the density envelopes of the three ILC stages are compared: at 250, 350, and 500 GeV. For that purpose, not the complete density distribution is plotted, but rather the envelopes containing either 99.9% or 99.99% of all tracks.

**Table 5.1.:** Changes between the baseline and alternative beam parameter sets for the ILC stage at 250 GeV [91]. The highlighted parameter set (A) was chosen to be the new official scheme for the ILC250. A full set of the baseline beam parameters can be found in [43, p. 11].

ILC250 sets	$\epsilon_x$ (μm)	$\beta_x^*$ (mm)	$\beta_y^*$ (mm)
Baseline	10.0	13.0	0.41
(A)	5.0	13.0	0.41
(B)	5.0	9.19	0.41
(C)	5.0	9.19	0.58

## 5.3. Pair background dependency on ILC beam parameters

After having introduced the pair background characteristics, this section will analyze its dependency on the choice of the ILC beam parameters. To this end, Section 5.3.1 presents the new proposed beam parameter schemes for the ILC250 stage. The resulting occupancy in the SiD vertex detector and further subdetectors is then discussed in Sections 5.3.2 and 5.3.3 respectively.

### 5.3.1. Pair background envelopes

As explained in Section 4.2.2, the first ILC stage will be at 250 GeV. Due to this decision in 2017, efforts have been made to study a possible change in the baseline beam parameters for this stage in order to increase the luminosity to  $1.62 \times 10^{34} \text{ cm}^{-2} \text{ s}^{-1}$  [91]. To this end, three alternative beam parameter sets have been suggested, which vary from the original baseline parameters in the emittance and the beta function values. The values which differ are listed in Table 5.1. For all alternative sets, the horizontal emittance  $\epsilon_x$  is reduced. Additionally, the horizontal and vertical beta functions at the IP,  $\beta_x^*$  and  $\beta_y^*$ , are changed for sets (B) and (C). Since both the emittance and the beta function are dependencies of the beam size, they enter indirectly the Equation 3.15 for the beam luminosity.

However, a reduced horizontal emittance implies also an increase in the beam-beam interactions and in the pair background level. For the process of deciding the new official beam parameter set, a study of the impact of this increased pair background on the SiD vertex detector performance was therefore a crucial step. In the following, the simulation studies of the pair background for the four parameter schemes listed in Table 5.1 are presented.

The pair background density plots for the four schemes are shown in Figure 5.6. The width of the envelopes for the new proposed parameter sets (A), (B), and (C) is significantly increased compared to the baseline set (TDR). For the direct comparison of the pair background density from different ILC running scenarios, Figure 5.7 shows a projection of the number of pair particles along the x-axis at the z-position of the first beam pipe kink, where the beam pipe radius increases. It therefore holds more information than the previous plots: the envelope width in x at the specified z-position, and the number of particles at any given x-value, for all beam parameter sets.

First of all, it becomes clear that the number of pair particles does indeed increase for the new beam parameter sets due to the enhanced beam-beam interactions. Compared to the baseline set (the TDR set), the number of particles in set (A) is increased by a factor of 2-3, and by a factor of 6-7 in sets (B) and (C). Furthermore, the so-called pair edge is clearly visible as the rapid decrease in density at around 9 mm from the center. Since the vertical solid lines in the Figure 5.7 represent the beam pipe,

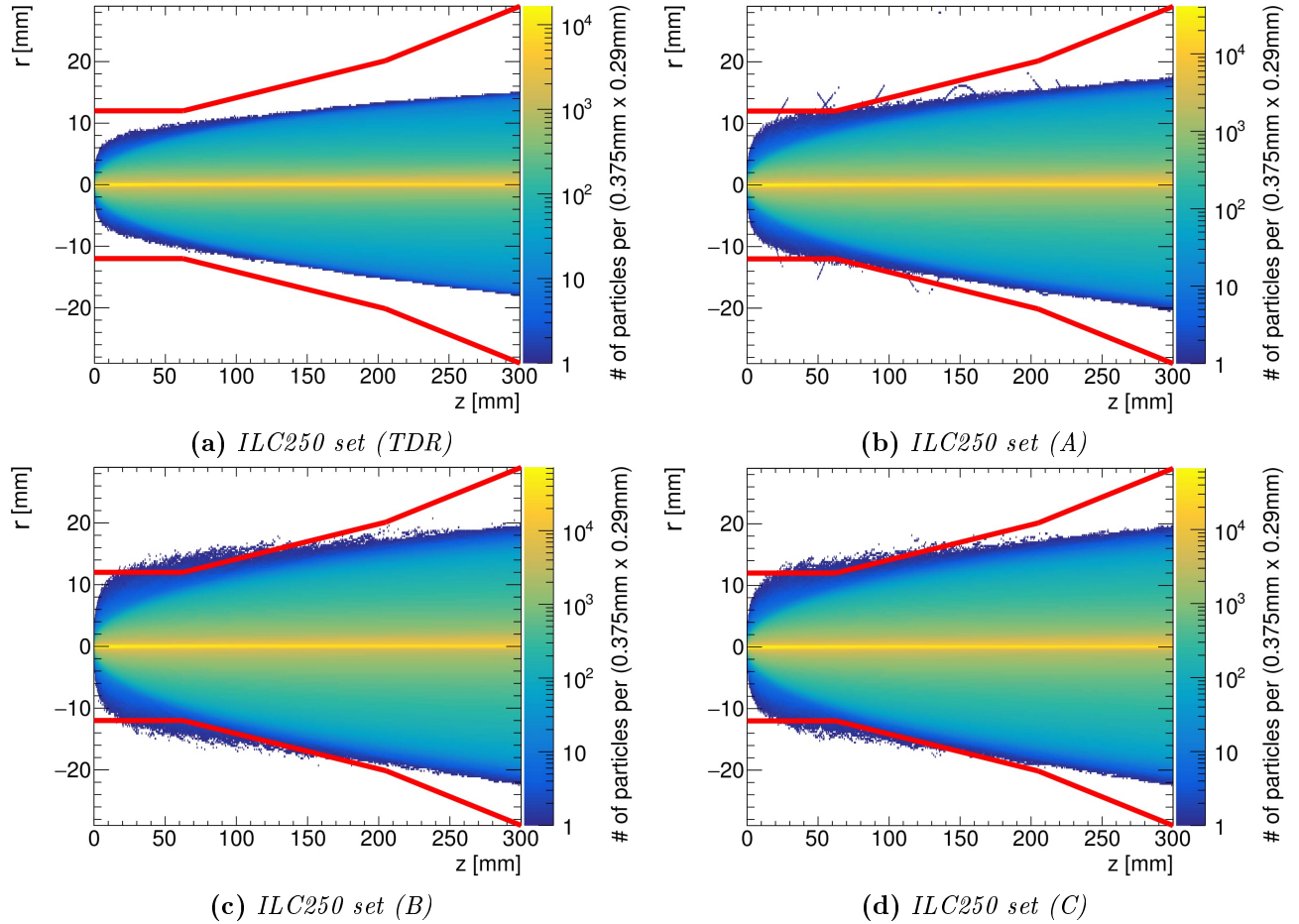


**Figure 5.6.:** Pair background density for the four ILC250 beam parameter sets listed in Table 5.1 per bunch crossing. The color scale shows the number of tracks per unit area. The beam pipe is represented by the red solid lines.

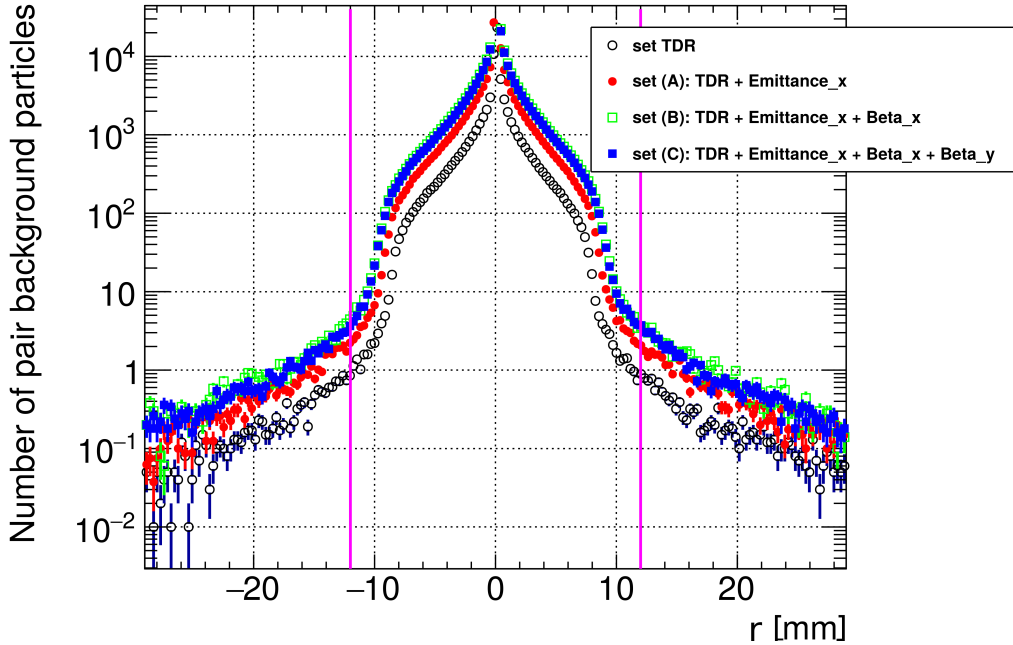


**Figure 5.7.:** Comparison of the pair background density projection for the four different ILC250 beam parameter sets. The plot shows the projected number of pairs along the  $x$ -axis for  $z = 62\text{ mm}$ , which is the  $z$ -position of the first beam pipe kink. The vertical solid lines represent the beam pipe radius at this  $z$ -position.

the pair edge is well contained within the beam pipe. Nevertheless, there are non-zero particle densities observed outside the beam pipe, extending beyond the vertex detector layers. These densities, however, are below 5 particles per  $r$ -bin (0.29 mm). With the track information across the five layers of the vertex detector, the vertices of particles created in the bunch collision can be reconstructed. By populating the innermost layers with background particles, the reconstruction efficiency inevitably declines. The occupancy from the pair background therefore has to be studied with respect to its impact on the detector performance.

### 5.3.2. SiD vertex detector occupancy studies and buffer depth

For the occupancy studies, the GuineaPig four-vectors of the pair particles are input to a full SiD simulation using SLIC, as explained in Section 5.1. The hits in the SiD subdetectors are stored through active readout layers in the simulation model, which represent the detector sensor layers. The detector sensor layers are segmented according to the readout cell sizes of the SiD subdetectors. For the occupancy studies, the number of hits of every detector cell were counted and translated into an occupancy. In the following occupancy plots, the number of cells receiving a certain number of hits can be determined. Taking into account that a detector sensor can only store up to a specific number of hits (the buffer depth), the number of “dead” cells can then be calculated. A cell is defined to be dead when the buffer of its sensor is already completely filled, and no further hits can be stored. This is especially important as the detectors for the ILC will read out their buffers only after every bunch train (1312 bunch crossings). In order to guarantee that cell buffers are not filled only by background hits, a balance has to be found between a sufficient buffer depth and low background levels, depending

on the design of the accelerator and the detectors. As explained in Section 4.4.1.3, the SiD guideline for an acceptable occupancy for background events is that the sum of all cells with a number of hits greater than or equal to the buffer depth should not exceed  $10^{-4}$  of all cells.

The occupancy for all vertex detector layers combined after a full bunch train is shown for the barrel in Figure 5.8 (a) and for the endcaps in Figure 5.8 (b). For producing these plots, the number of hits were counted for each cell, summed up over the full bunch train. A cell size of  $20\text{ }\mu\text{m} \times 20\text{ }\mu\text{m}$  has been assumed for these calculations. Plotting the number of cells with a certain amount of hits, and normalizing these numbers by the total number of cells in all vertex detector layers, results in Figure 5.8 (a) and (b). It can be directly seen which percentage of all cells get hit a certain number of times. Comparing the results from the four different ILC250 beam parameter sets for the vertex detector barrel and endcaps, the occupancy of set (A) is raised by a factor of three with respect to the baseline set (TDR). For set (B) and (C), the occupancy is increased by a factor of about six. In the vertex detector endcaps, the occupancy is in general higher than in the barrel, leading to the fact that cells are hit up to 50 times compared to 40 times for the barrel. The reason for this is that the pair background envelopes widen towards the endcaps, as can be seen from the density plots in Figure 5.6. As the readout design for the vertex detector is not yet decided, optimizations based on simulation recommendations can still be made. In Figure 5.8 (c) and (d), the fraction of dead cells is therefore plotted as a function of the assumed buffer depth of the sensors. The buffer depth states how many hits a sensor can store, before the corresponding cell is blind to any further hits. As explained in Section 4.4.1.3, a compromise has to be found between the number of necessary sensor buffers due to background occupancies and meeting the SiD requirement regarding the material budget of the vertex detector.

In the current detector design, the sensors have a buffer depth of four. The fraction of the dead cells is calculated from the occupancy plots in Figure 5.8 (a) and (b), and depends on the buffer depth. For a buffer depth of four, Figure 5.8 (c) shows that for set (A) approximately  $1.8 \times 10^{-5}$  of all cells in all vertex detector barrel layers are dead, which is an increase with respect to the baseline set of a factor of three. Nevertheless,  $1.8 \times 10^{-5}$  is only about 18% of the critical limit.

As mentioned above, the occupancy in the endcaps is higher, leading to a larger fraction of dead cells. For the vertex detector endcaps, the fraction of dead cells for a buffer depth of four exceed the critical limit for sets (B) and (C) by a few percent (see Figure 5.8 (d)). The fraction for set (A) is still below the critical limit with about  $5 \times 10^{-5}$ .

However, combining the hits of all five vertex detector layers does not provide a meaningful picture of the occupancy in the individual layers. Figure 5.9 shows a comparison of the different vertex detector barrel layers for the ILC250 parameter set (A). The innermost layer (layer 0) is expected to suffer from a larger pair background occupancy than the other layers. This expectation is confirmed, since the fraction of dead cells in layer 0 is  $1.1 \times 10^{-4}$  and just about exceeds the critical acceptance limit. The occupancy in layer 0 is therefore larger by a factor of about four compared to layer 1 for a buffer depth of four. For the same buffer depth value, the fraction in the outer layers gradually drops to about  $4.7 \times 10^{-6}$ .

Comparing exclusively the innermost layer in the different ILC250 sets, Figure 5.10 shows the normalized occupancy and the fraction of dead cells, for the vertex detector barrel and the endcaps separately. In Figure 5.10 (a), the normalized occupancy in all sets is indeed larger by almost one order of magnitude compared to the occupancy for all layers combined, shown in Figure 5.8 (a). The fraction of dead cells for a buffer depth of four in Figure 5.10 (c) is exceeding the critical limit of  $10^{-4}$  of all cells in all new parameter schemes. For set (A), the fraction of dead cells for this buffer depth is about  $1.1 \times 10^{-4}$ .

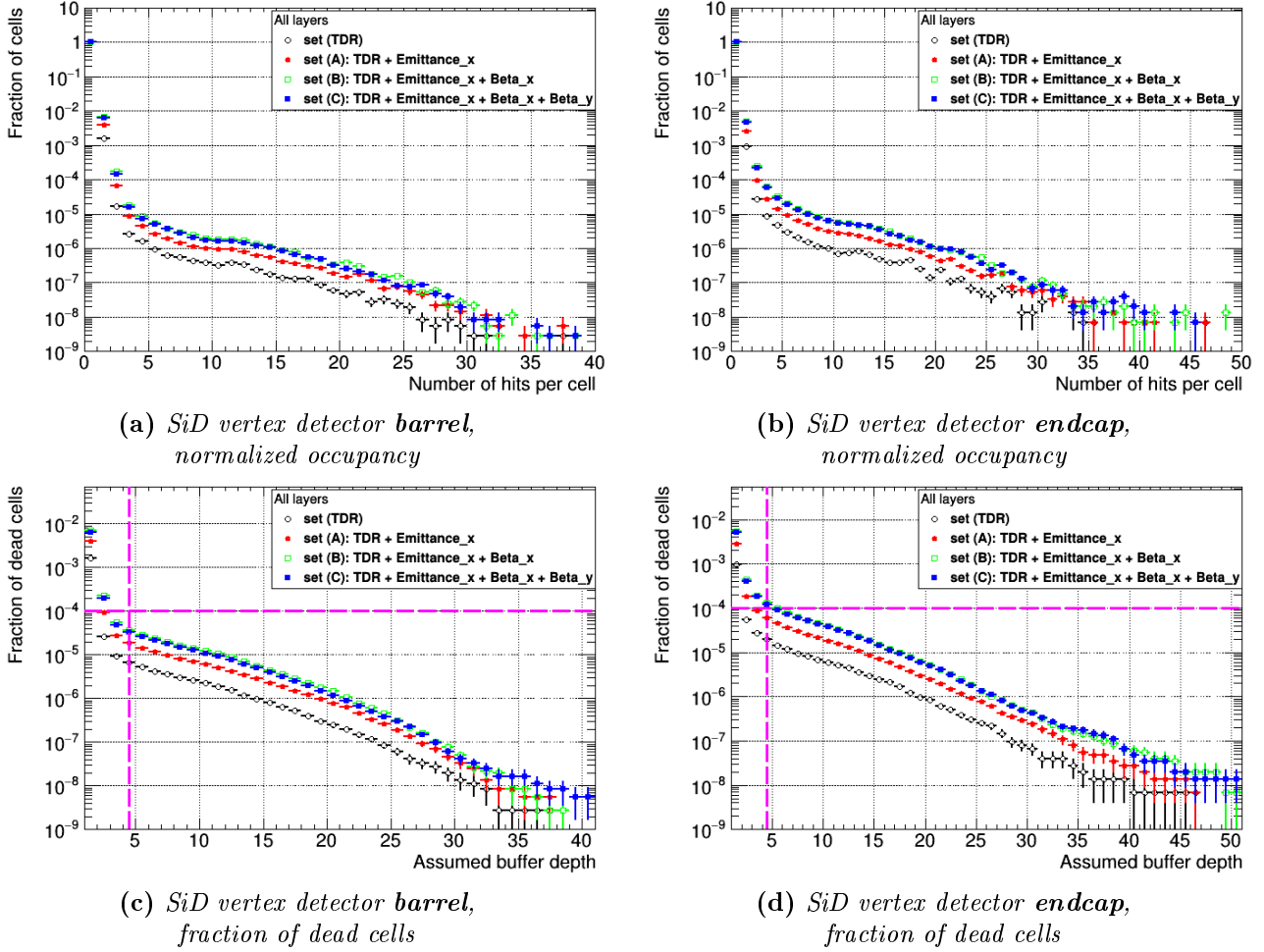


**Figure 5.8.:** ILC250 pair background occupancy in the **SiD vertex detector for all layers combined**, after a full bunch train (1312 bunch crossings). Figure (a) shows the occupancy in the vertex detector barrel, normalized by the total number of cells of all vertex detector barrel layers. Figure (c) shows the fraction of the dead cells in the vertex detector barrel with respect to the total number of cells. Figures (b) and (d) show the equivalent plots for the vertex detector endcaps. In all figures, the four different beam parameter sets for the ILC250 are compared. The dashed lines in (c) and (d) indicate the the buffer depth of four for the current sensor design, and the guideline of  $10^{-4}$  for a critical acceptance limit.

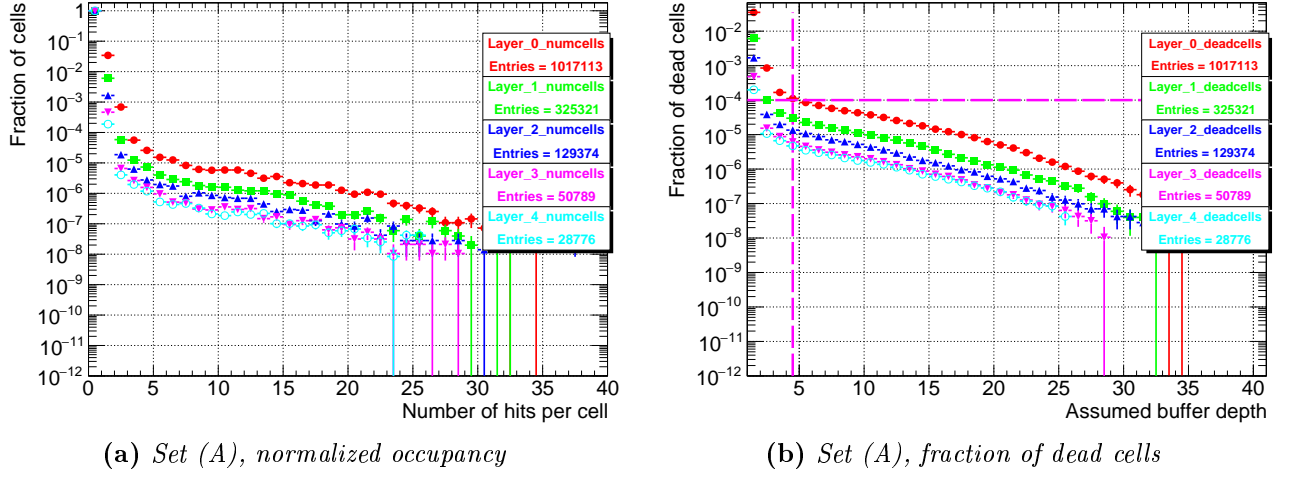


**Figure 5.9.:** ILC250 pair background occupancy in the **individual SiD vertex detector barrel layers**, after a full bunch train (1312 bunch crossings). Figure (a) shows the occupancy in the individual vertex detector barrel layers, normalized by the total number of cells of the layers. Figure (b) shows the fraction of the dead cells in the vertex detector barrel layers with respect to the total number of cells of the layers. In all figures, the four different beam parameter sets for the ILC250 are compared. The dashed lines in (b) indicate the the buffer depth of four for the current sensor design, and the guideline of  $10^{-4}$  for a critical acceptance limit.

**Table 5.2.:** Results of the pair background occupancy study for the different beam parameter sets of the ILC stage at 250 GeV center-of-mass energy. For a buffer depth of four, the fractions of dead cells caused by the pair background occupancy are listed for the individual layers of the vertex detector barrel and endcaps.

	Layer	Baseline set (TDR)	Set (A)	Set (B)	Set (C)
SiD vertex barrel	0	$4.659 \times 10^{-5}$	$1.110 \times 10^{-4}$	$2.110 \times 10^{-4}$	$1.875 \times 10^{-4}$
	1	$9.847 \times 10^{-6}$	$2.980 \times 10^{-5}$	$5.732 \times 10^{-5}$	$5.213 \times 10^{-5}$
	2	$3.902 \times 10^{-6}$	$1.347 \times 10^{-5}$	$2.988 \times 10^{-5}$	$2.707 \times 10^{-5}$
	3	$2.410 \times 10^{-6}$	$6.116 \times 10^{-6}$	$1.299 \times 10^{-5}$	$1.271 \times 10^{-5}$
	4	$1.482 \times 10^{-6}$	$4.690 \times 10^{-6}$	$1.116 \times 10^{-5}$	$9.423 \times 10^{-6}$
SiD vertex endcap	0	$1.807 \times 10^{-5}$	$5.652 \times 10^{-5}$	$1.200 \times 10^{-4}$	$1.123 \times 10^{-4}$
	1	$1.895 \times 10^{-5}$	$6.133 \times 10^{-5}$	$1.269 \times 10^{-4}$	$1.194 \times 10^{-4}$
	2	$1.906 \times 10^{-5}$	$5.882 \times 10^{-5}$	$1.414 \times 10^{-4}$	$1.219 \times 10^{-4}$
	3	$2.126 \times 10^{-5}$	$6.239 \times 10^{-5}$	$1.348 \times 10^{-4}$	$1.321 \times 10^{-4}$

For sets (B) and (C), the fraction reaches about  $2.1 \times 10^{-4}$  and  $1.9 \times 10^{-4}$  of all cells respectively in this innermost layer.

For the endcaps, the plots for the innermost layer only do not show a significant difference to the plots for all layers combined. In contrast to the vertex barrel layers, the endcap layers are perpendicular to the incoming pair background particles, and are hit in approximately equal amounts. Plotting the combined occupancy for all endcap layers is in this case therefore a realistic representation of the individual layers. For a buffer depth of four, only sets (B) and (C) exceed the critical limit.

In addition to the presented results in this section, the results for the individual layers of all ILC250 sets are presented in Figures A.1 (for the vertex detector barrel) and A.2 (for the vertex detector endcaps) in the Appendix, as well as in Table 5.2.

### 5.3.3. Pair background occupancy in further SiD subdetectors

With its five layers, it is crucial for the vertex detector that the pair background does not populate any of its layers in such a way that its performance regarding the vertex reconstruction is compromised. But also in the other SiD subdetectors that are hit by the  $e^+e^-$  pairs, the occupancy should not exceed the critical acceptance limit of  $10^{-4}$  for a given buffer depth.

The fraction of dead cells as a function of the assumed buffer depth is plotted for the SiD tracker as well as the ECAL and HCAL endcaps in Figure 5.11. For both the tracker barrel and endcaps (Figure 5.11 (a) and (b)), the fraction of dead cells stays for all ILC250 parameter sets well below  $10^{-4}$  of all cells for a buffer depth of four.

In the ECAL endcaps, the overall occupancy is so low that only up to four hits per cell are observed. The analysis code therefore calculates the fraction of dead cells only up to a buffer depth of four, as can be seen in Figure 5.11 (c). Nevertheless, for the current buffer depth of four, sets (B) and (C) reach beyond the critical limit. In set (A), however, the fraction of dead cell reaches  $5 \times 10^{-6}$  only.

Similarly in the HCAL endcaps (Figure 5.11 (d)), the fraction of dead cells is calculated for an assumed buffer depth of up to three only. Since there will be at least four buffers for the subdetector sensors, the pair background particles do not affect the calorimeter endcap performance.

The results for further subdetectors can be found in Figure A.3 in the Appendix.

### 5.3.4. Impact of the pair background studies on ILC design choices

As shown in Sections 5.3.1 and 5.3.2, the increase in the beam-beam interaction due to the reduction of the beam emittance for the newly proposed ILC250 beam parameter schemes does lead to a rise in the SiD vertex detector occupancy. This includes that the proposed beam parameter sets (B) and (C) for the ILC250 stage exceed the critical acceptance limit of  $10^{-4}$  in the inner subdetectors for buffer depth of four. In the innermost layer of the vertex detector barrel specifically, these sets exceed the limit for all assumed buffer depths up to eight.

However, except for the innermost vertex detector barrel layer, the occupancy for parameter set (A) is below the limit of  $10^{-4}$  in all other layers of the vertex detector barrel and endcaps for every feasible buffer depth of the detector sensor design. In further SiD subdetectors that are populated by the pair background, the fraction of dead cells for a buffer depth of four does not reach the acceptance limit, which was shown in Section 5.3.3.

The presented results of the SiD occupancy studies for the different beam parameter sets of the ILC250 stage were factored into the ILC Change Request (CR) process for CR-0016 [65]. The Technical Change and Management Board in the end decided on set (A) for the new official ILC beam parameter

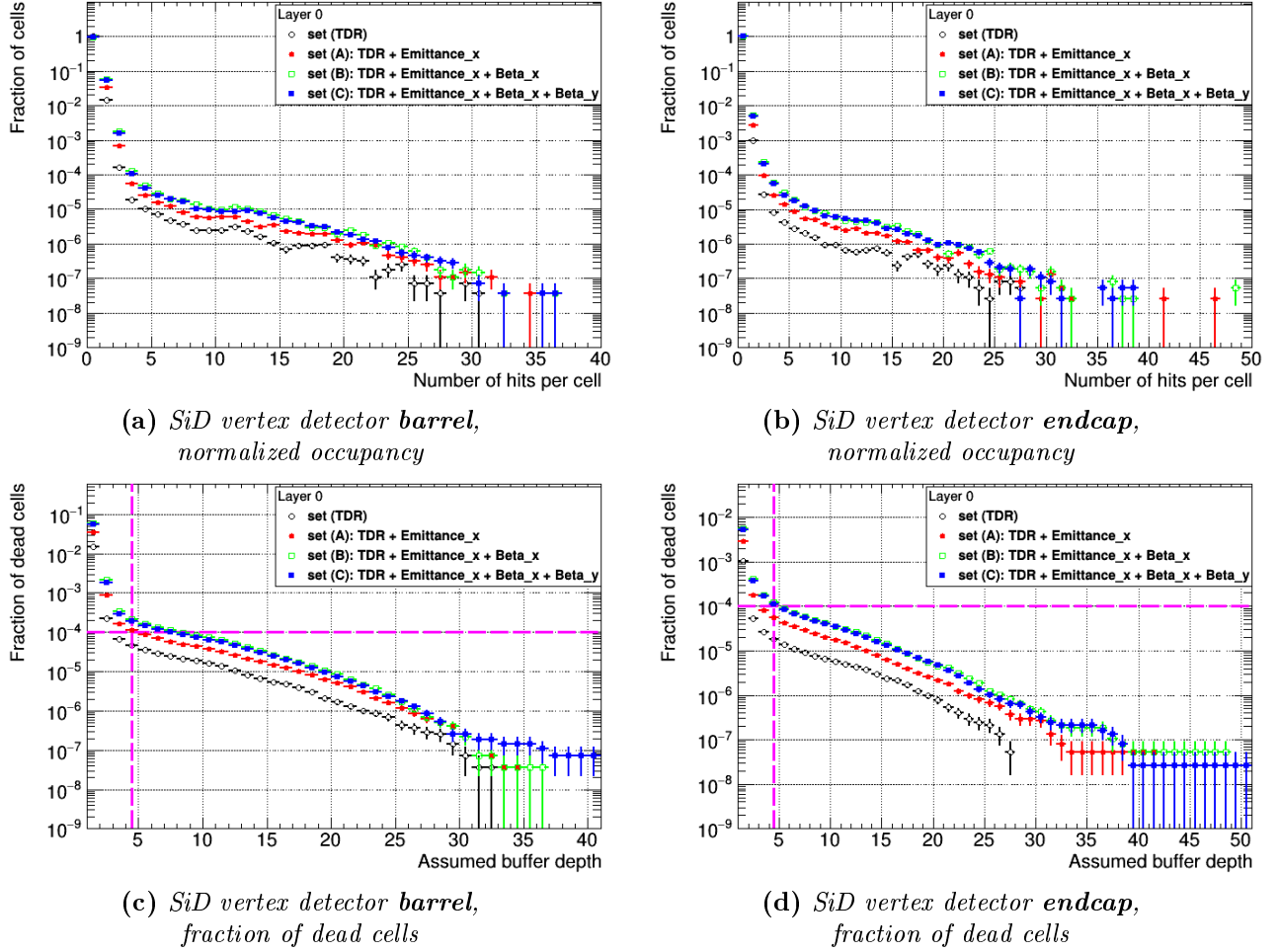


**Figure 5.10.:** *ILC250 pair background occupancy in the innermost SiD vertex detector layer, after a full bunch train (1312 bunch crossings). Figure (a) shows the occupancy in the innermost vertex detector barrel layer, normalized by the total number of cells of this layer. Figure (c) shows the fraction of the dead cells in the innermost vertex detector barrel layer with respect to the total number of cells of this layer. Figures (b) and (d) show the equivalent plots for the vertex detector endcaps. In all figures, the four different beam parameter sets for the ILC250 are compared. The dashed lines in (c) and (d) indicate the the buffer depth of four for the current sensor design, and the guideline of  $10^{-4}$  for a critical acceptance limit.*

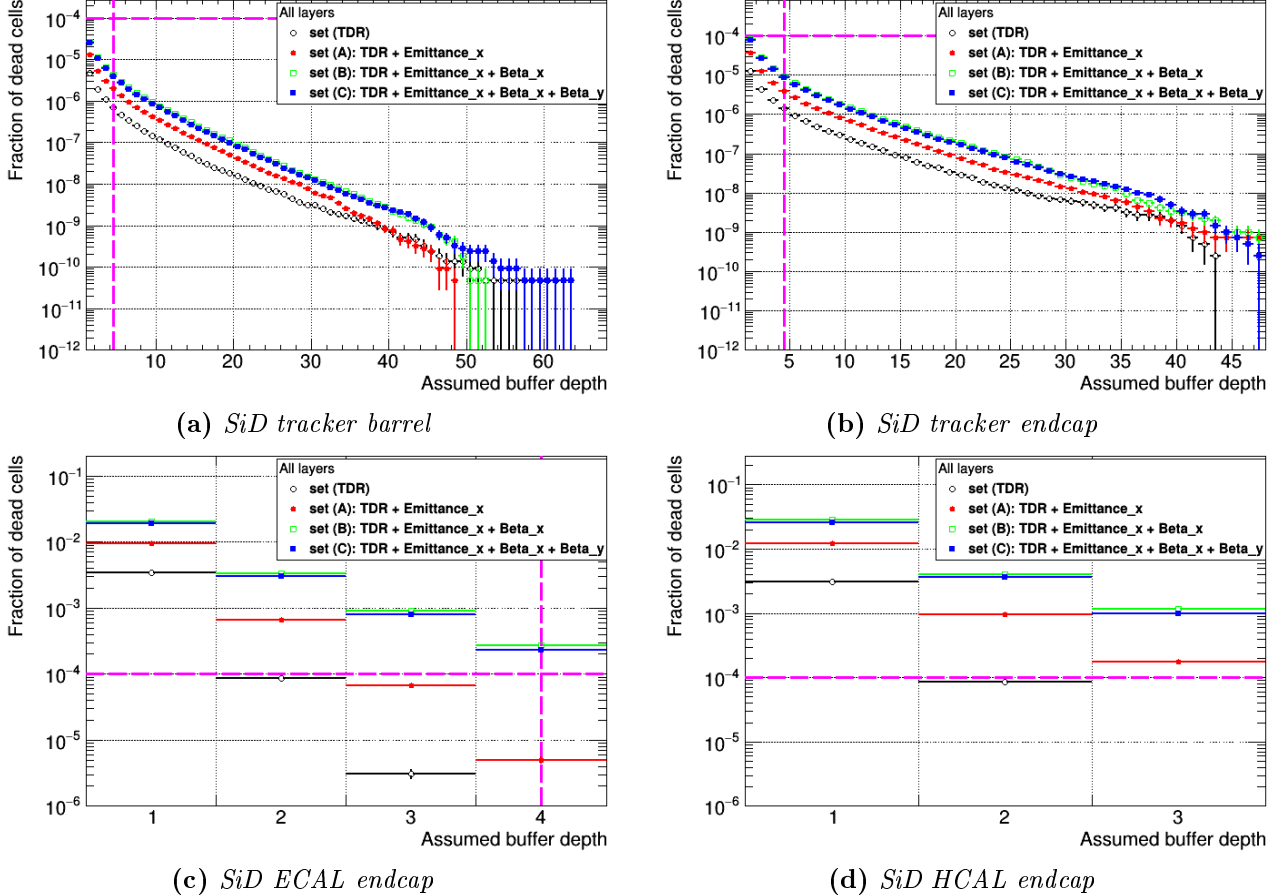


**Figure 5.11.:** ILC250 pair background occupancy in various inner SiD subdetectors after a full bunch train (1312 bunch crossings). The figures show the fraction of the dead cells in the individual subdetectors for all layers combined, with respect to the total number of cells in this subdetector.

The dashed lines indicate the the buffer depth of four for the current sensor design, and the guideline of  $10^{-4}$  for a critical acceptance limit.

set for a center-of-mass energy of 250 GeV, and hence approved the CR-0016 [92]. The results of further studies regarding the ILC250 stage are henceforth produced with this new official beam parameter set (A).

## 5.4. Dependency of the pair background occupancy on detector design choices

Figure 5.12 shows the result from another ILC250 occupancy study, using the ILC250 parameter scheme (A). After having studied the impact of the beam parameters, the effect of different SiD variants on the vertex detector occupancy was also examined. The four geometry variants, which are compared in this plot, are combinations of the old or new  $L^*$  value, with and without the SiD anti-DiD field. The  $L^*$  value describes the distance between the IP and QD0 (the last magnet of the Final-Focus beam line), which is integrated in the detector and connected to the BeamCal. The anti-DiD, which is an additional detector-specific magnet, is designed to deflect pair background particles in the forward regions such that they are swept into the outgoing beam pipe. More information about these detector variants is given in Section 4.4.1.2.

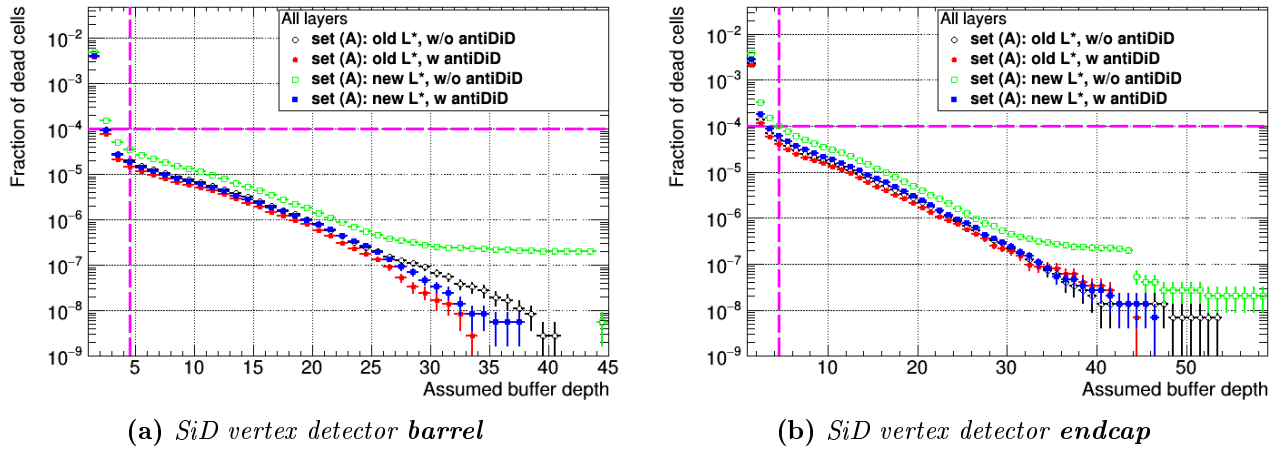


**Figure 5.12.:** *Pair background occupancy for the ILC250 parameter set (A) in all SiD vertex detector layers combined after a full bunch train (1312 bunch crossings). Figures (a) and (b) show the fraction of dead cells with respect to the total number of cells of all vertex detector layers combined, for the barrel and the endcap respectively. Different SiD geometry variants are compared regarding their effect on the pair background occupancy.*  
*The dashed lines indicate the the buffer depth of four for the current sensor design, and the guideline of  $10^{-4}$  for a critical acceptance limit.*

In Figure 5.12 it is shown that the variations on the SiD geometry do not have a significant impact on the vertex barrel and endcap occupancy. Nevertheless, the SiD design including the old  $L^*$  value and the anti-DiD field leads to the lowest occupancy. The occupancy of the current design (with the new  $L^*$  value and the anti-DiD field) is only marginally higher. Since the geometry of the vertex detector and all other subdetectors is unaltered in the studied SiD variants, the difference in the pair background occupancy must be caused by the impact of the  $L^*$  and the anti-DiD field themselves. The change

in the  $L^*$  value implies a change in the position of the BeamCal subdetector. The anti-DiD field is designed to guide the pair background particles through the outgoing beam pipe, so that the number of pair background hits in the BeamCal is reduced. The differences in Figure 5.12 are an indication that the SiD BeamCal affects the vertex detector occupancy from pair background particles. For the clarification of the impact on the pair background occupancy, the following section looks at the hit distribution in the SiD detector.

## 5.5. Hit maps of the SiD subdetectors

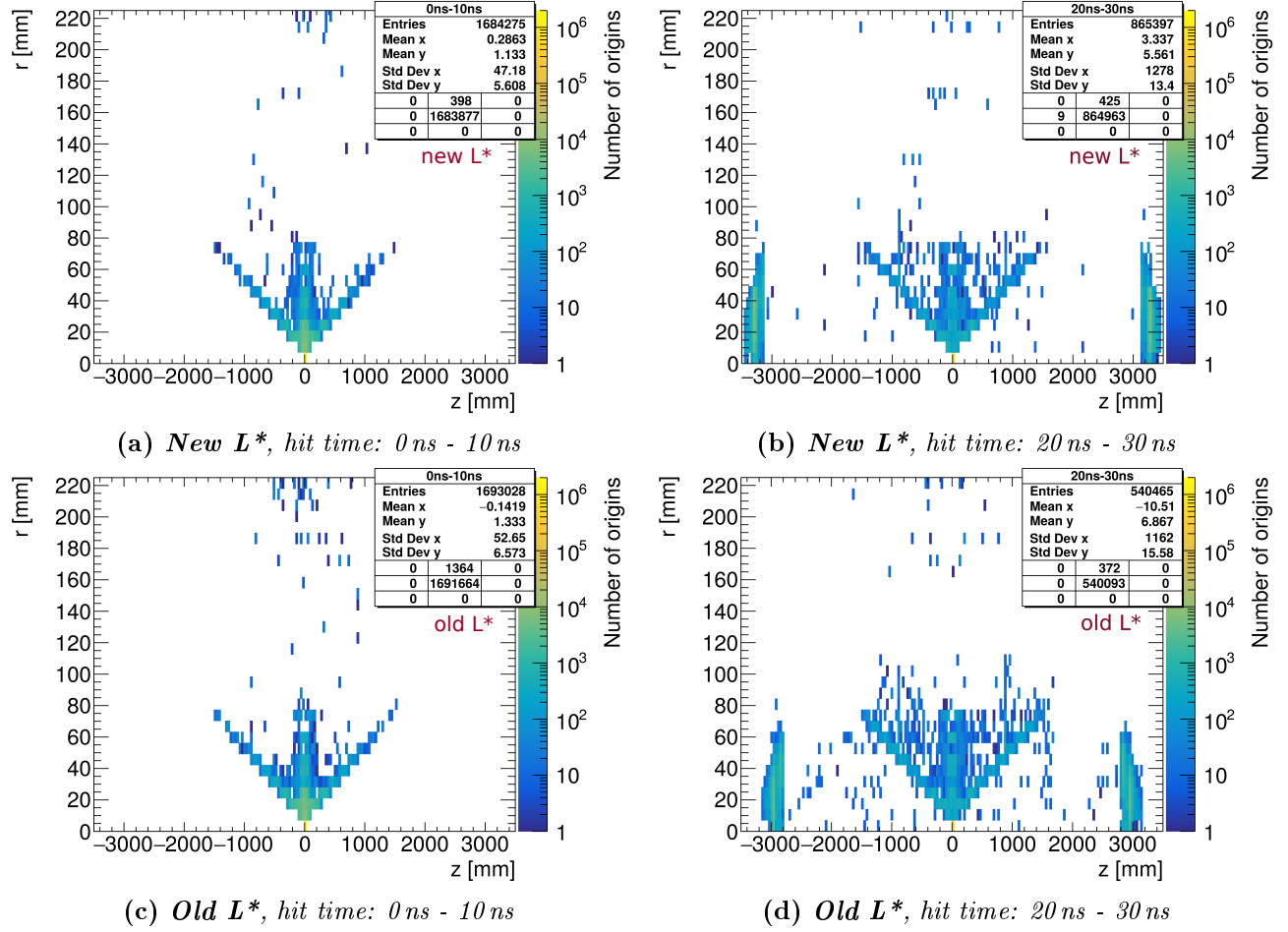
As shown in the sections above, the  $e^+e^-$  pair background arises from beam-beam interactions at the IP. Being boosted in the beam direction, and swept into the outgoing beam pipe by the anti-DiD, the hits in the SiD detector are mainly restricted to the inner subdetectors. However, as indicated by Figure 5.12, the SiD geometry variants have an impact on the vertex detector occupancy from the  $e^+e^-$  pairs.

Figure 5.13 shows maps of the pair background vertices in the SiD detector. A cut was applied to only show the vertices of the pairs that will hit the vertex detector in the given time intervals: up to 10 ns (Figure 5.13 (a)), and between 20 ns and 30 ns after the bunch crossing (Figure 5.13 (b)). In this way, it becomes clear whether the background particles originate at the IP only, or whether they also backscatter from other subdetectors. In the first 10 ns, the majority of particles that hit the vertex detector comes from the IP. Also a few backscatter particles are visible, originating from the innermost detector layers and the central subdetectors. A few nanoseconds later, however, between 20 ns and 30 ns, particles, which were backscattered from the BeamCal positioned about 3.2 m from the IP, hit the vertex detector. These pair background particles travel from the IP towards the BeamCal, where they hit the material and backscattered back towards the vertex detector.

Figures 5.13 (c) and (d) show the equivalent maps but for the SiD geometry variant with the old  $L^*$  value. In the first time interval up to 10 ns, the difference between Figures 5.13 (a) and (c) is negligible. The effect of the  $L^*$  values, however, becomes apparent in Figure (d), since the position of the BeamCal is directly dependent on  $L^*$ . The vertex positions in the BeamCal are now at around 2.8 m from the IP. The number of particles hitting the vertex detector (shown as the entries of the plots) is reduced by about 40 %. This difference in the vertex detector occupancy between the old and new  $L^*$  (both including the anti-DiD field) is also evident in Figure 5.12.

The distance from the IP to the BeamCal and back, which the particles have traveled, takes of the order of several tens of nanoseconds. This time gap is visible in Figure 5.14, which shows the radial position of the hits in the vertex detector barrel and endcaps as a function of the hit time. First, the vertex detector is hit by  $e^+e^-$  pairs arriving directly from the IP. Before pairs have traveled towards the BeamCal and have backscattered, the vertex detector does not accumulate any further hits. From around 20 ns on, particles arrive again at the vertex detector.

This hit time distribution offers the possibility of reducing the background occupancy through time gates. By applying a trigger such that those particles are dismissed, which are hitting the vertex detector between 10 ns and 50 ns after the bunch crossing for example, the number of pair background hits can be reduced by about 12 % [20, p. 27].



**Figure 5.13.:** Maps of the pair background particle vertices in the SiD detector after one bunch crossings. Only those vertices are shown, which originate from pair background particles hitting the SiD vertex detector in the given time intervals. In order to increase the statistics, the results are accumulated for 1312 bunch crossings.

Figure (a) shows the vertices of those pairs, which hit the vertex detector up to 10 ns after the bunch crossing. Similarly, Figure (b) shows the vertices of pairs hitting the vertex detector between 20 ns and 30 ns after the bunch crossing.

Figures (c) and (d) show the equivalent plots created for the SiD detector with the old  $L^*$  value.

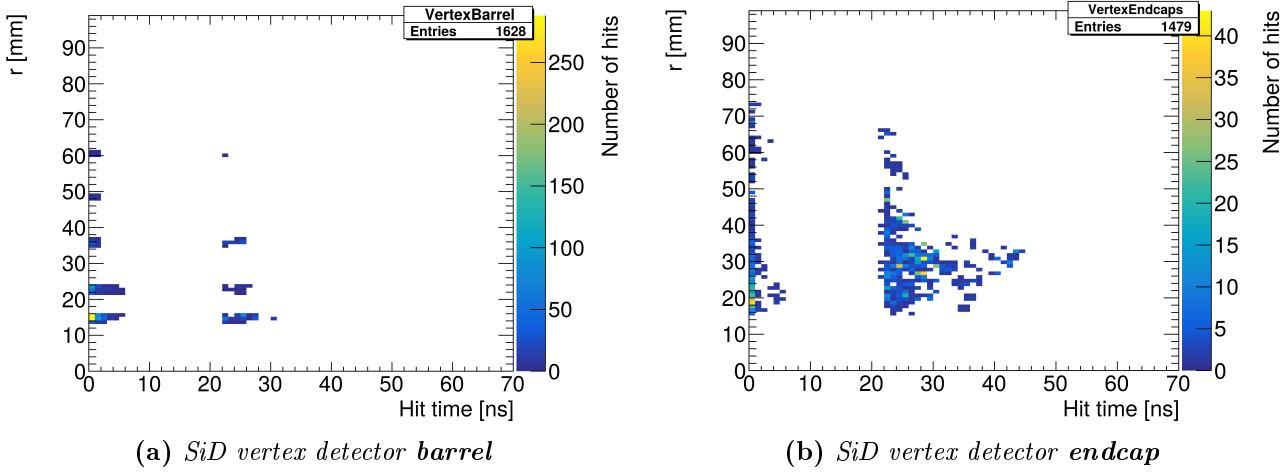


**Figure 5.14.:** Map of the pair background particle hits in the SiD vertex detector as a function of the hit time after one bunch crossings. Figures (a) and (b) show the radial position of hits in the vertex detector barrel and endcaps respectively.

## 5.6. Comparing the pair background occupancy of different ILC stages

As it has been clarified in the previous sections, the pair background envelopes and the arising vertex detector occupancy are dependent on several factors: the ILC beam parameters, the center-of-mass energy, and the SiD geometry regarding the BeamCal and the anti-DiD field.

However, due to the interplay of several of these factors, the dependencies are also not obvious in certain cases, as can be seen in Figure 5.15. The plots compare the SiD vertex detector occupancies from the pair background arising at a center-of-mass energy of 250 GeV and 500 GeV. With the new ILC250 beam parameter set, the resulting occupancies at both center-of-mass energies are very similar, with the occupancy at the ILC500 being higher by a few percent. For a buffer depth of four, the occupancy for both stages exceeds the acceptance limit of  $10^{-4}$ . By increasing the buffer depth by one, both occupancies are already on an acceptable level, below the critical limit.

Overall, the reduction in the beam emittance for the ILC250 stage increases the beam-beam interactions such that the differences between the center-of-mass energies (and therefore the pair background momenta distributions) are nearly compensated. This leads to the positive implication for the SiD detector, that the vertex detector readout architecture can be designed to be suitable for both ILC stages with respect to the pair background.

Finally, another dependency factor has not been discussed yet, namely the dependency on the number of beam bunches per train. The ILC stages in all studies presented so far have 1312 bunches per train. The “Lumi Up” stage, which is listed in Table 4.1, is an ILC stage with a center-of-mass energy of 500 GeV and an upgraded luminosity. The luminosity of this stage is doubled with respect to the ILC500 stage by approximately doubling the number of bunches per train to 2625. Figure 5.16 shows the resulting pair background occupancy in the innermost layer of the vertex detector barrel and endcaps. The fraction of dead cells for a given buffer depth is doubled in both subdetectors for the “Lumi Up” stage, clearly exceeding the critical acceptance limit of  $10^{-4}$  when assuming a buffer depth of four. By increasing the number of buffers to eight, the occupancy for the “LumiUp” stage would fall below this limit.

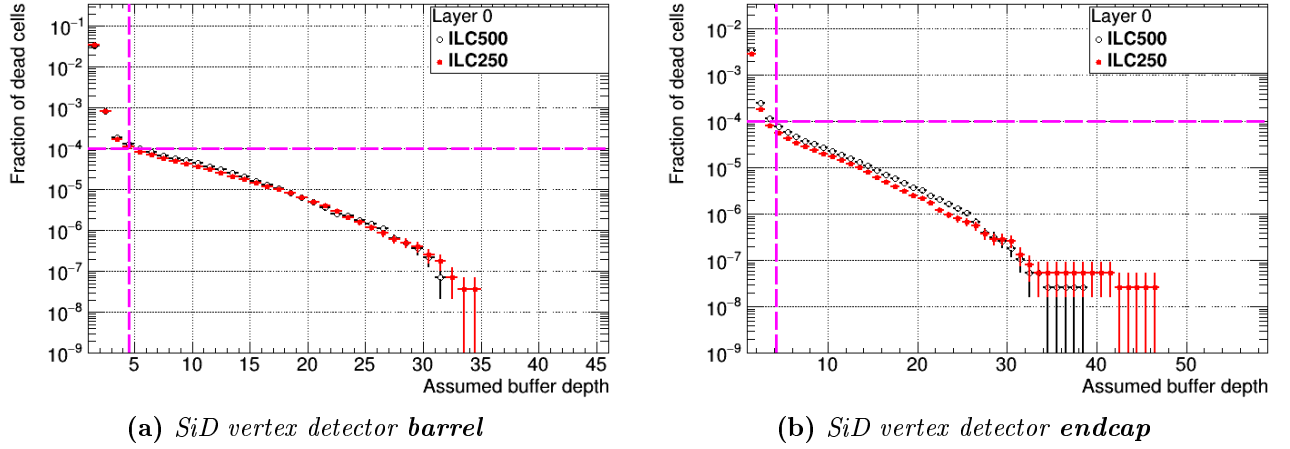


**Figure 5.15.:** Pair background occupancy for the ILC500 in comparison to the ILC250, for the innermost **SiD vertex detector layer**, after a full bunch train (1312 bunch crossings). In both figures, the fraction of dead cells is shown with respect to the total number of cells of the innermost vertex detector layer. Figure (a) shows the results for the vertex detector barrel, Figure (b) shows for the vertex detector endcaps. The dashed lines indicate the the buffer depth of four for the current sensor design, and the guideline of  $10^{-4}$  for a critical acceptance limit.

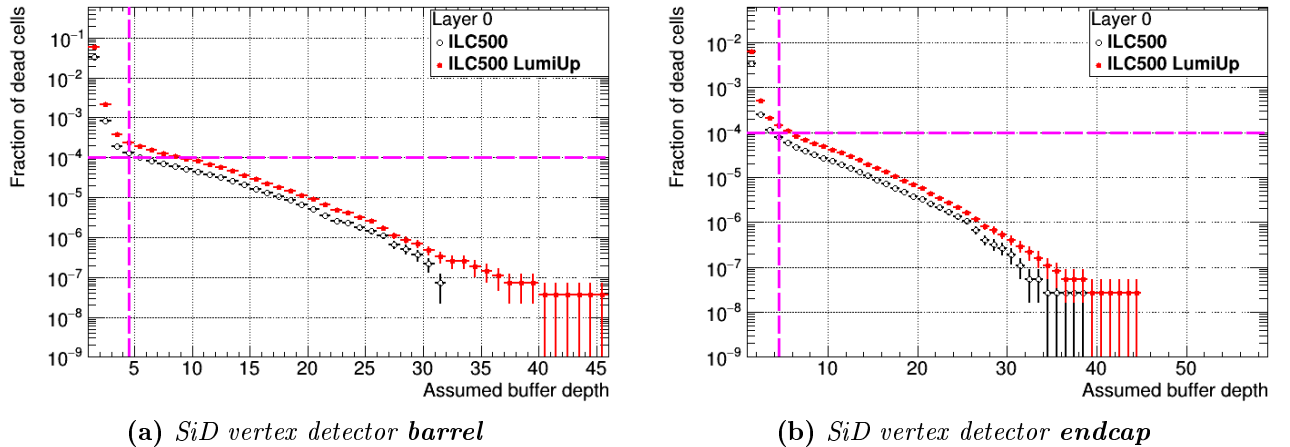


**Figure 5.16.:** Pair background occupancy for the ILC500 in comparison to the ILC500 luminosity upgrade stage, for the innermost **SiD vertex detector layer**, after a full bunch train of 1312/2625 bunch crossings. In both figures, the fraction of dead cells is shown with respect to the total number of cells of the innermost vertex detector layer. Figure (a) shows the results for the vertex detector barrel, Figure (b) for the vertex detector endcaps. The dashed lines indicate the the buffer depth of four for the current sensor design, and the guideline of  $10^{-4}$  for a critical acceptance limit.

**Table 5.3.:** Results of the pair background occupancy study for the different ILC stages: ILC250, ILC500, and ILC500 “LumiUp”. For a buffer depth of four, the fractions of dead cells caused by the pair background occupancy are listed for the innermost layer of the vertex detector barrel.

Time gate	ILC250	ILC500	ILC500 “LumiUp”
without	$1.110 \times 10^{-4}$	$1.290 \times 10^{-4}$	$2.402 \times 10^{-4}$
0 - 10 ns	$8.228 \times 10^{-5}$	$8.167 \times 10^{-5}$	$1.516 \times 10^{-4}$

The number of beam bunches therefore also has a direct impact on the pair background and the SiD occupancy. In order to stay below the critical occupancy limit, the ILC upgrade to the ILC500 “Lumi Up” stage seems to be a suitable time for an upgrade of the SiD vertex detector as well.

**Time gate** After applying a cut on the hit time of the pair background particles in the vertex detector, as suggested by Section 5.5, the occupancy in the different ILC stages was recalculated. The cut was applied such that all hits later than the first 10 ns after the bunch crossing were rejected. The resulting occupancy in the vertex detector barrel and endcaps is shown in Figure 5.17. In the Figures 5.17 (a) - (c), the individual ILC stages are compared with and without the time gate. Figures 5.17 (d) and (e) then show a combined comparison of the three stages, before and after applying the time gate. In all stages, the fraction of dead cells in the most exposed subdetector layer (the innermost vertex detector barrel layer) is reduced by about 25 to 36 % when using the time gate. Table 5.3 lists the fraction of dead cells for a buffer depth of four for the various ILC stages with and without the time gate. For both the ILC250 and ILC500 stage, the occupancy is now below the critical acceptance limit of  $10^{-4}$ . Even for the “LumiUp” stage, the fraction of dead cells is closer to the critical limit.

## 5.7. Conclusion

The pair background arises from the interaction between the electromagnetic fields of the colliding beam bunches. These interactions are dependent on the ILC beam parameters, which therefore affect the pair background characteristics. This chapter has also shown that the pairs, which originate from the IP as well as backscatter from the BeamCal, populate the inner SiD subdetectors. Especially in the vertex detector, it is crucial to investigate the impact of the beam parameters in great detail. As the width of the pair background envelopes varies and the tracks of the pairs reaches towards the innermost vertex detector layers, the occupancy is directly affected by the change in the beam parameters, as explained in Section 5.3.1. The presented studies have shown that the occupancy from the pair background does not only depend on the beam parameters, but also on the center-of-mass energy and the number of beam bunches per train (Section 5.6), as well as on the SiD detector geometry (Section 5.4). These findings are a valuable input to design decisions regarding the ILC accelerator and the SiD detector, and were already consulted for the Change Request decision of the new beam parameters for the ILC stage at a center-of-mass energy of 250 GeV.

In Section 5.6, it was shown that with a buffer depth of four in the current SiD detector readout design, the detector occupancies for the ILC500 and the new parameter set of the ILC250 are comparable. For the ILC500 “LumiUp”, however, the occupancy is increased significantly, because of which the

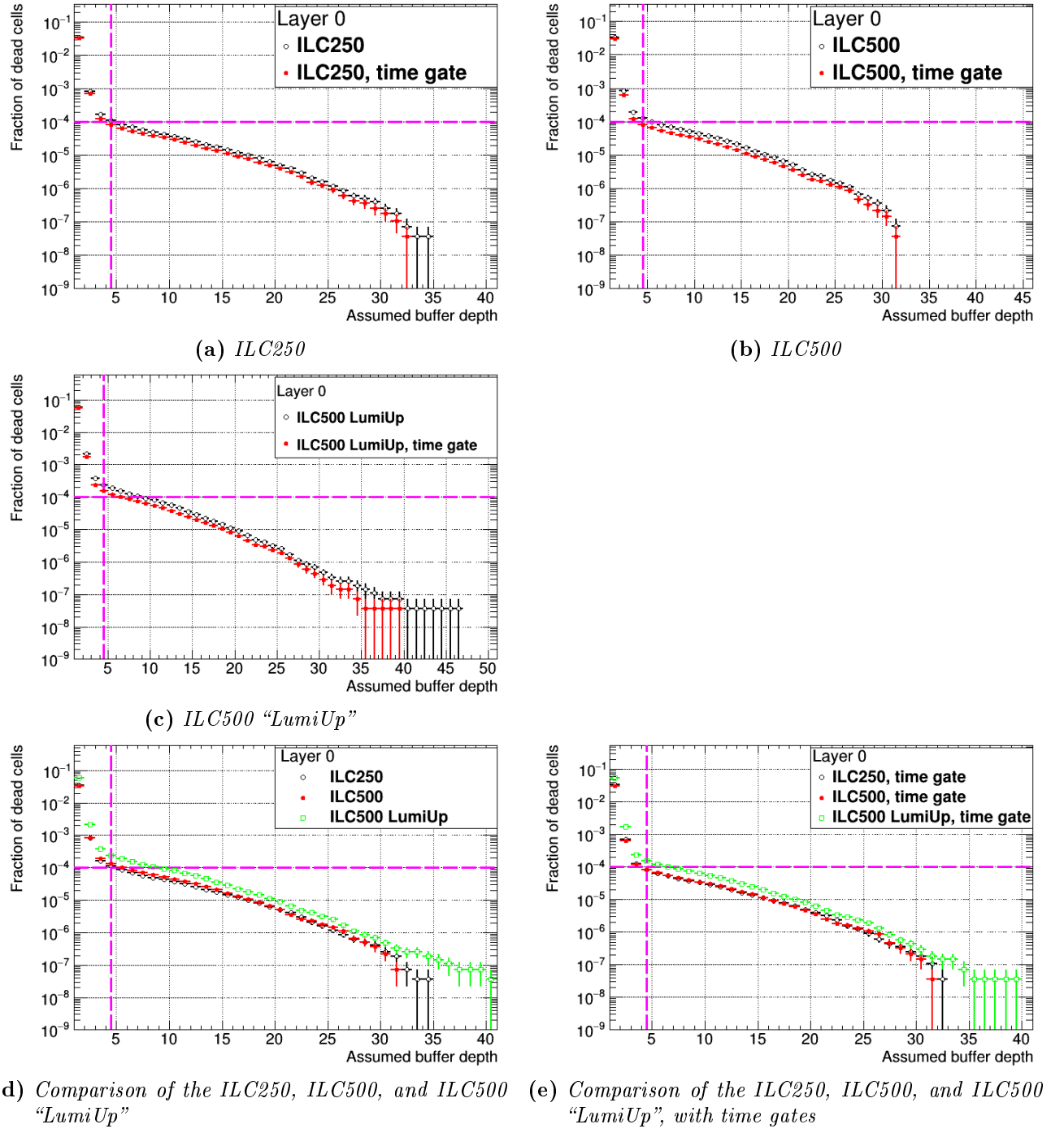


**Figure 5.17.:** Pair background occupancy for the ILC250, ILC500, and the ILC500 "LumiUp" stage, for the **innermost SiD vertex detector barrel layer**, before and after having applied a time gate. In all figures, the fraction of dead cells is shown with respect to the total number of cells of the innermost vertex detector layer. The dashed lines indicate the the buffer depth of four for the current sensor design, and the guideline of  $10^{-4}$  for a critical acceptance limit.

number of buffers has to be raised to eight in order to yield similar detector performances. According to these results, the SiD vertex detector has to be upgraded as well, when the ILC is upgraded to the “LumiUp” stage.

However, the pair background timing study (in Section 5.5) has indicated that time gates can reduce the number of hits in the vertex detector by about 12 %. This has the effect that the pair background occupancy in the vertex detector is reduced by about 25 % to 36 %, as then shown in Section 5.6. For both the ILC250 and the ILC500 stage, that leads to the effect that the occupancy of the SiD vertex detector barrel is reduced to below the critical occupancy limit for a buffer depth of four. Also for the ILC500 “LumiUp” stage, the fraction of dead cells for a buffer depth of four is still above the critical limit, but could be reduced significantly by applying the time gate. Already a buffer depth of six would bring the occupancy below the limit.

Overall, it has been demonstrated that the pair background occupancy in the SiD detector is dependent on the ILC running scheme as well as on the SiD detector geometry. By changing the SiD readout architecture design such that six buffers are used instead of four, and that a time gate is applied that rejects hits after 10 ns, the detector performance in all subdetectors will be comparable throughout all studied ILC stages. An upgrade of the vertex detector for the ILC500 “LumiUp” stage would not be necessary with respect to the pair background occupancy.



# 6 Muon background from the Beam Delivery System

Particles produced in beam interactions with the accelerator components present another source of background for particle detectors. With thorough simulations, the characteristics of the machine background can be understood, and its effect on the detector performances evaluated.

In the first part of this chapter, the arising detector background from muons that are created in the Beam Delivery System of the International Linear Collider is explained. In the second part, different shielding options are discussed with respect to their effectiveness to prevent the muons from reaching the detector experiments. The simulation of the muon production was done with MUCARLO (Section 6.1), before the occupancy in SiD was investigated in a full detector simulation presented in Section 6.2.

After the beam acceleration in the main linacs of the ILC, the Beam Delivery System (BDS) is the part of the accelerator that prepares the beams for collision. As described in Section 4.2.1, it contains numerous subsystems and components for beam collimation and focusing. Depending on the aperture of the collimators, some fraction of the beam halo hits the collimator material, which has the desired effect of collimating the beam, but also the undesired effect of producing background particles.

For defining the beam halo, which surrounds the beam core, the beam core itself has to be defined first in terms of  $\sigma_x$  and  $\sigma_y$ , which are the RMS beam size values at the beginning of the first collimator location in the BDS:  $\sigma_x = 146 \mu\text{m}$  and  $\sigma_y = 9 \mu\text{m}$  [93]. In this study, the core is defined as an ellipse with a horizontal size of  $\pm 5\sigma_x$  and a vertical size of  $\pm 36\sigma_y$  at the beginning of the BDS. The beam halo is the elliptical ring around the beam core, covering  $5\text{--}13\sigma_x$  and  $36\text{--}93\sigma_y$ . The beam particle intensity in the core follows a  $\frac{1}{r}$  distribution, and the beam power of the halo is normalized to 0.1% of the nominal beam power [94].

From interactions between the beam halo and the material of the collimators along the beam line, muons are produced predominantly via the Bethe-Heitler process (see Figure 6.1 (a)). Beamstrahlung photons interact with the nuclei of the machine component material, and pair-produce muons. A production contribution on a few percent level comes additionally from direct annihilation of positrons with atomic electrons [95]. Due to this, there are more muons created in the positron beam line than the electron beam line. The number of created muons is listed in Table 6.1. The Feynman diagram for the annihilation process is shown in Figure 6.1 (b). The muons are boosted in the beam direction, and are traveling towards the interaction region.

To prevent the muons from reaching the detectors, two different shielding systems are studied with respect to their effectiveness and feasibility to be integrated in the BDS. Both systems are based on two ideas: to deflect the muons such that they do not reach the interaction region, and also to stop the muons in the shielding material. The shielding scenarios that are under discussion foresee a combination of the two systems:

- “5 spoilers”:

In the first scenario, five cylindrical spoilers out of magnetized iron are installed at different locations along the BDS: 1358.5 m, 1234.5 m, 1145.5 m, 975.5 m, and 802.5 m from the interaction point (IP), where these locations indicate the midpoint of the spoiler. The spoilers have a radius of 70 cm, and a length of about 5 m. Their magnetic field ranges from about 1.9 T in the center of the spoiler to about 1 T at the outer edge [96, 93]. An illustration of one of these spoilers is given in Figure 6.2 (a). As indicated by the muon tracks through the spoiler, the magnetic field of the cylindrical spoilers is such that either positively or negatively charged muons are deflected away from the beam path into the tunnel walls.

- “5 spoiler + wall”:

In the second scenario, the same five spoilers are located at the same positions as before. But an additional magnetized shielding wall is placed about 400 m from the interaction point.

The wall is about 5 m wide and long, and fills out the complete tunnel height. Its magnetic field strength is about 1.6 T [96, 93]. Figure 6.2 (b) shows an illustration of the wall inside the BDS tunnel.

The motivation for the study presented in this section is to investigate the effect of the muons on the SiD detector. The overall goal is to give a recommendation, based on the study of the detector performance, on the necessity of the magnetized wall in order to keep the detector occupancy below the critical limit of  $10^{-4}$  (as discussed in previous chapters). Arguments against the wall were brought forward regarding costs and safety issues due to its size in the BDS tunnel.

## 6.1. MUCARLO

The interactions between the ILC beam and the machine components in the BDS were simulated with a Monte Carlo tool called MUCARLO [95, 97, 98]. Since the presented study is done for two different ILC stages, at 250 GeV and at 500 GeV, the beam parameters of the respective stage were used accordingly. The geometry lattice of the ILC Beam Delivery System serves as the input geometry to the MUCARLO code, through which the muons are tracked. Figure 6.3 shows the muon tracks

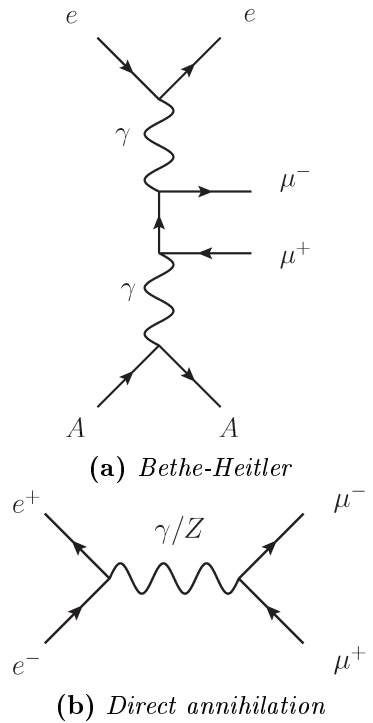


**Figure 6.1.:** Feynman diagrams of the muon pair production via the Bethe-Heitler process and the direct annihilation with atomic electrons.

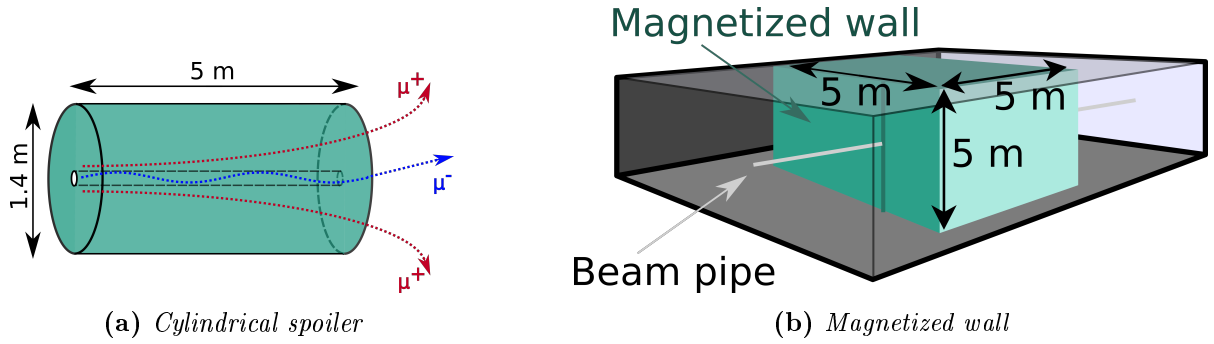


**Figure 6.2.:** Schematic drawings of the magnetized spoiler (a) and the magnetized shielding wall (b) [96, cf. p. 2]. The magnetized wall is illustrated inside the accelerator tunnel.

in the electron-line of the BDS. The muons are created at certain locations along the beam line, are deflected by the magnetic field of beam line components, and lose kinetic energy through scattering in the material of the components the muons hit. In the end, only those muons that reach the IP (at  $z = 0$  m) are stored. Accordingly, Figure 6.3 only shows those muons. In this plot, there is only one red muon track line, which belongs to a negatively charged muon. The spoiler polarities are set to defocus muons with the same charge as the beam charge. Therefore, mainly positively charged muons from the electron beam line will reach the IP. For the positron beam line, the muons reaching the IP are mainly negatively charged.

The main sources of muons were identified in the BDS to be 11 distinct collimators. The following list names these collimators and their position from the IP [93]:

- Primary collimator spoilers (radiation length:  $0.6 X_0$ , half-gap<sup>1</sup>: 930  $\mu\text{m}$  in x, 400  $\mu\text{m}$  in y): SP2 (1508 m), SP4 (1332 m)
- Protection collimators (radiation length:  $30 X_0$ , inner radius: 0.7 cm): PC1 (1452 m), PC2 (1387 m), PC5 (1276 m), PC5A (1242 m), PC6 (1208 m), PC7 (1047 m)
- Absorbers (radiation length:  $30 X_0$ , half-gap: 0.7 cm): AB3 (1420 m), AB5 (1237 m), ABE (852 m)

The protection collimators and absorbers serve the purpose of protecting the magnets of the BDS from particle showers (arising from the beam halo collimation) and from mis-steered primary beams. The number of muons created is proportional to the fraction of the collimator surface that is hit with respect to the beam size, which was determined with the help of the Monte Carlo ray-tracing computer program TURTLE [99]. The general design of these collimators can be found in [100].

Adding up all muons from the different sources on the electron and the positron beam line side, the total number of muons can be calculated that would reach a detector with a radius of 6.5 m at the interaction region. Table 6.1 lists the muon rates per bunch crossing for a center-of-mass energy of 250 and 500 GeV, and for the two different shielding scenarios. At 500 GeV, about 130 muons per bunch crossing would reach the detector in the case that no shielding was installed. This number is reduced to about 4 muons with the five cylindrical spoilers, and to below 1 muon per bunch crossing with an

<sup>1</sup>The term “half-gap” is commonly used for collimator systems. It describes the gap between one of the collimator jaws and an arbitrarily chosen plane (usually the beam center plane). Both of the jaws have the same distance from this plane.

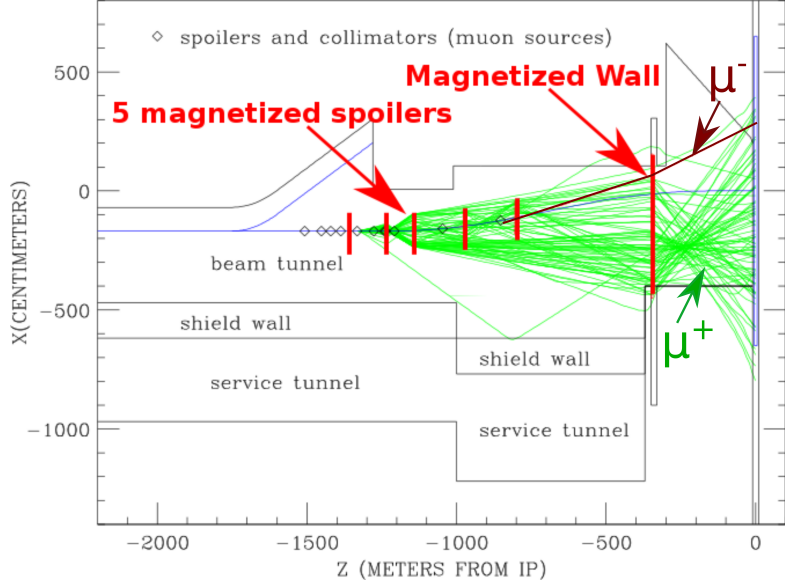


**Figure 6.3.:** Visualization of the muon tracks in the ILC Beam Delivery System (BDS) in the electron beam line [93]. The picture shows the  $xz$ -plane of the BDS tunnel with the beam line components (spoilers and collimators), which serve as muon sources. In this particular example, the muons origin from the electron beam hitting the primary collimator spoiler SP4. The locations of the muon shielding components (the magnetized spoilers and wall) are also indicated. The green/red thin lines represent the tracks of the muons. The general layout of the tunnel model is the same for the electron and the positron beam line, but mirrored at the  $z = 0$  plane.

**Table 6.1.:** Muon rates per bunch crossing for the two shielding scenarios, gained from MUCARLO simulations [93].

Scenario	Muons per bunch crossing in a detector with 6.5 m radius					
	ILC500			ILC250		
	positron line	electron line	total	positron line	electron line	total
No Spoilers	71.6	58.5	130.1	21.1	17.2	38.3
5 spoilers	2.3	2	4.3	0.73	0.57	1.3
5 spoilers + wall	0.34	0.26	0.6	0.016	0.014	0.03

additional magnetized wall. For a lower beam energy of 125 GeV (250 GeV center-of-mass energy), the number of muons that are produced is lower, because of which only around 38 muons reach the detector without shielding. With the two different shielding scenarios, the muon rate is again reduced significantly to a minimum of about 0.03 per bunch crossing.

The output of MUCARLO is a text file containing the four-vectors of the muons 10 m from the IP. These four-vectors can therefore be used as input to a full detector simulation.

An additional study was done using a GEANT4 simulation of the BDS tunnel in order to cross check the MUCARLO results and to thereby verify the MUCARLO simulation. The outcome of that study was that both simulations are in good agreement [94].

## 6.2. Effect of muons on the SiD performance

Since the SiD detector only reads out the hits after every bunch train (1312 bunch crossings), the detector occupancy for the muons has to be studied for a muon rate per train. As in the previous chapter, the full detector simulation was done using SLIC. The geometry input file that was used contained the most recent “sidlo3” geometry of the SiD detector, including the new L\* position, the anti-DiD field, and the Pacman geometry. For details on these detector characteristics, please refer to Section 4.4.1. After a file-format conversion, the MUCARLO output files containing the four-vectors of the muons for the different shielding scenarios and center-of-mass energies served as the particle source input to SLIC.

### 6.2.1. Muon hit distribution

For visualizing the hit distribution in the SiD detector, event displays (see Figure 6.4) were made using WIRED4 [90]. Apart from the overall number of hits in the different event displays, the spatial distribution of the hits is striking. Concentrating on Figure 6.4 (a) first, the muons leave clear horizontal tracks throughout the whole detector. After leaving the BDS tunnel, the muons (which are boosted in the forward direction) enter SiD through the outermost subdetector, and penetrate the full detector. Since the muons are coming from both the electron and the positron beam line, this happens simultaneously from both sides.

The difference in the spatial distribution in the xy-plane between Figure 6.4 (b) and (c) is explained by the geometry of the tunnel, and position of the detector with respect to the tunnel exit. In Figure (a), the rectangular shape in the hit distribution is the imprint of the tunnel. The boosted muons exit the tunnel and directly hit the detector. The asymmetry of the imprint results from the position of the detector. The beam pipe and therefore the central axis through the detectors are not in the center of the BDS tunnel. As can be seen in Figure 6.3, the beam line curves such that it is closer to one of the tunnel side walls than to the other. The top-bottom asymmetry is due to the fact that the detector cavern is below the ground level of the tunnel.

Adding the magnetized wall as an additional muon shielding causes the muons to scatter. The clear tunnel imprint is no longer visible in Figure 6.4 (b). Scattering the muons is not the only effect of the magnetized wall. As can be seen in Figure 6.5, the wall shifts the muon energy to lower values for a respective center-of-mass energy. The muons are deflected away from the forward directions due to the magnetization of the wall, but also lose their energy in the material of the wall. Low energy muons are either stopped completely, or deflected such that they cannot reach the detector. The peak in the energy distributions at lower energies is therefore reduced for the “5 spoilers + wall” scenarios. Additionally, the number of muons per bunch train can directly be compared for the two ILC stages and the different shielding options.

These muons then leave a particular number of hits in the SiD subdetectors by penetrating the full detector. For the comparison between the total number of hits in the four different cases, Figure 6.6 shows a bar chart of the hits collected in each subdetector. The largest number of hits is counted for the endcaps of the muon detector system, which is the subdetector with the largest effective detector area under normal incident of the muons. Also, it is the outermost subdetector, likely to be hit by

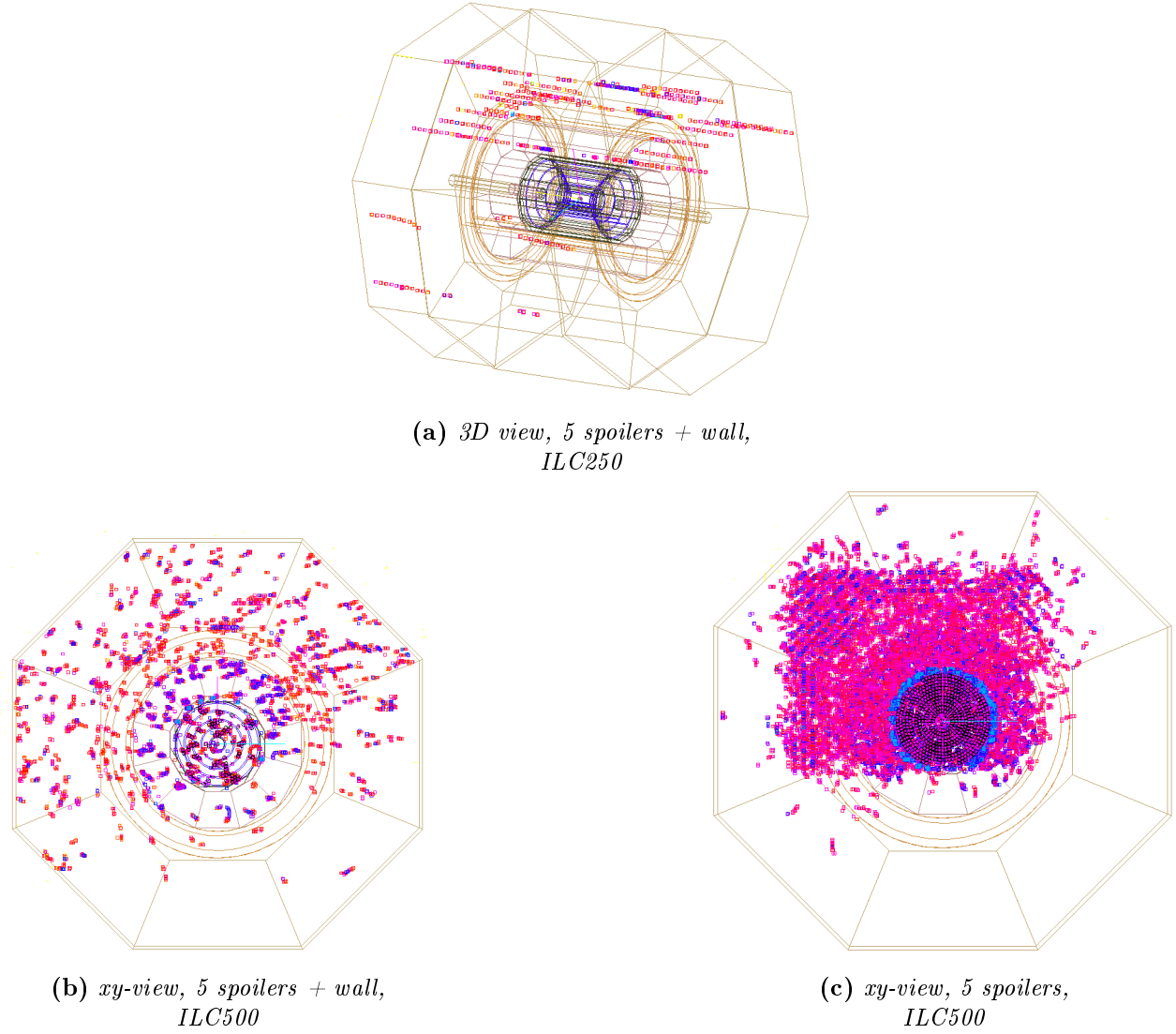


**Figure 6.4.:** Event displays of the muon hits in SiD for different center-of-mass energies and different shielding scenarios.

all of the primary muons. Accordingly, the vertex detector (as the smallest and innermost detector) is hit the least number of times, and in the same manner also the other subdetectors gain representative numbers of hits. Deducing from the hit distributions, the SiD detector will overall suffer from less hits in the ILC250 stage with respect to the ILC500, but adding the magnetized wall to the shielding will yield even smaller hit counts for both center-of-mass energies.

After looking at the total number of hits, which reflects the size and position of the subdetectors in SiD, this fact can be even better derived from the hit time distributions shown in Figure 6.7. The muons emitted from the BDS tunnel arrive first at the endcaps of the muon system, as mentioned above. After penetrating all muon endcap layers, the next outermost subdetector is hit and so on, until

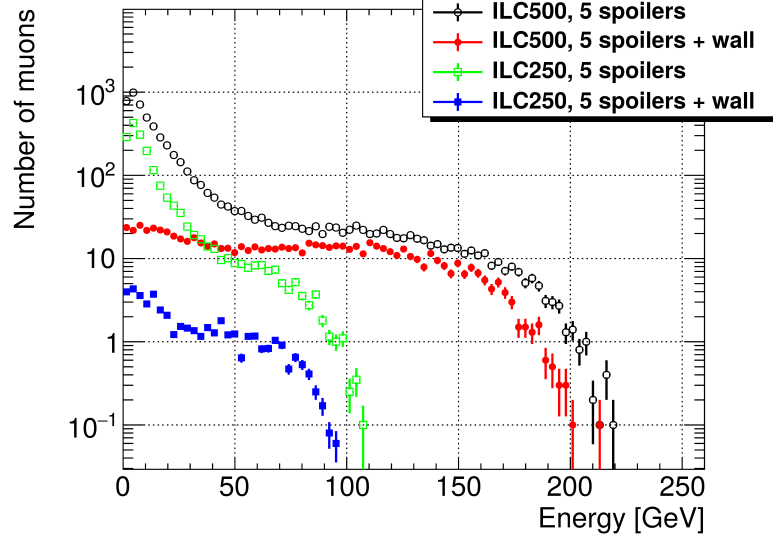


**Figure 6.5.:** Energy distribution of the muons for the different shielding scenarios, and for a center-of-mass energy of 250 and 500 GeV. The number of muons are normalized to a full bunch train for all cases.

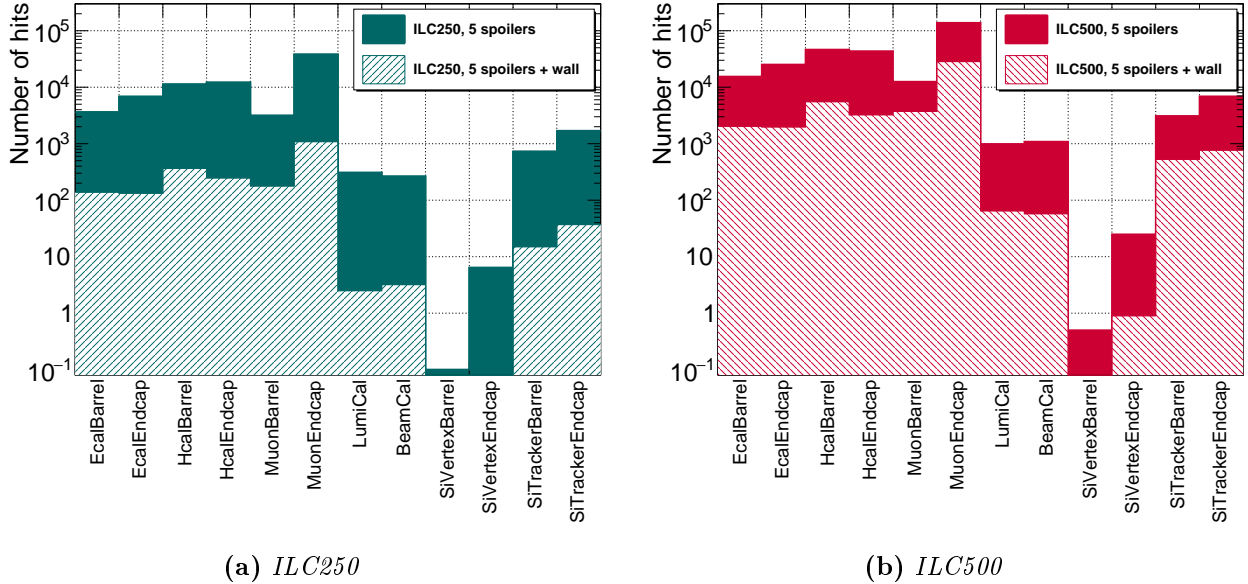


**Figure 6.6.:** Total number of hits in the various SiD subdetectors for both shielding scenarios in the ILC250 stage (a) and ILC500 stage (b). The number of hits come from muons from a full bunch train.

the muons make their way to the opposite muon endcap. The time needed for the muons to penetrate the full detector is hence about 40 ns, independent of the muon shielding and the center-of-mass energy.

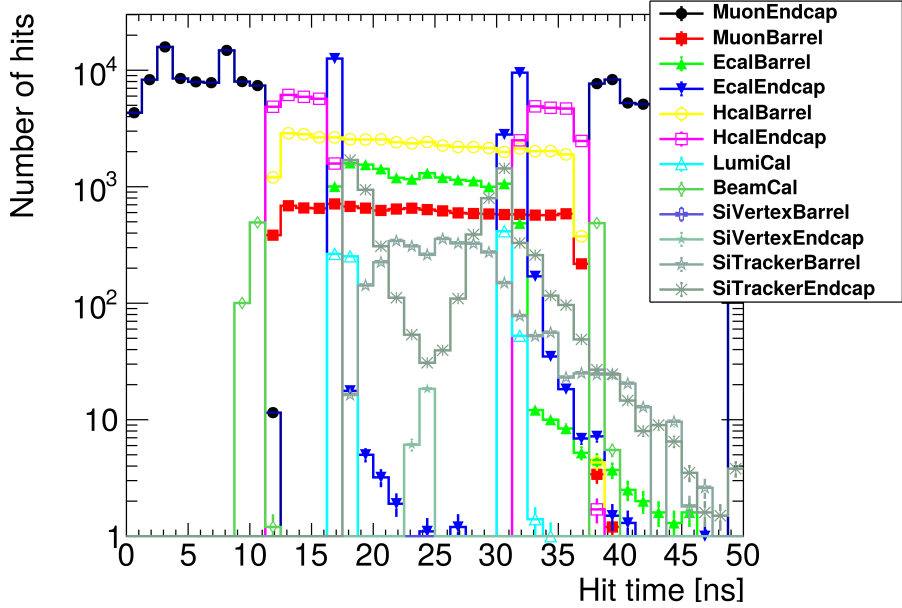


**Figure 6.7.:** Hit time distribution of the BDS muons in the various SiD subdetectors for ILC500 stage and for the “5 spoilers” scenario only. The number of hits are normalized to hits from a full bunch train for all cases.

### 6.2.2. SiD occupancy

The next step is to look at the occupancy of the detector arising from these muon hits. As in Chapter 5.3.2, the number of hits are counted for every cell in the subdetectors, which can be directly translated into a detector occupancy. In the following, the muon occupancy in the SiD HCAL barrel and the tracker endcaps is discussed. As explained in the previous chapter, occupancy plots show how many detector cells are hit a certain number of times. By respecting the rule that the sum of all cells with a number of hits greater than or equal to the buffer depth should not exceed 0.01 % ( $10^{-4}$  of all cells), a statement can be made as to whether given occupancy levels are acceptable. By optimizing the design of the detectors and the accelerator, a balance can be found between a sufficient buffer depth of the detector sensors and low background levels arising from the accelerator.

Figure 6.8 shows the occupancy and the number of dead cells <sup>2</sup> in the HCAL barrel, normalized to its total number of cells. In the current detector design, the HCAL cells have a size of  $1\text{ cm} \times 1\text{ cm}$ . As a result, a maximum of three hits per cell is observed, because of which the x-axis range in Figure 6.8 (b) also reaches to three only. Here, the number of dead cells is shown as a function of the assumed buffer depth. In the theoretical case of a buffer depth of one, about  $10^{-4}$  of all cells would have a full buffer (with one hit) for the “5 spoilers” case in the ILC500. Here, the critical limit for acceptable occupancies of  $10^{-4}$  would just about be reached, all other cases would have acceptable values. Realistically, the HCAL sensor will have a higher buffer depth, namely a buffer depth of four (in the current design) or higher. Since none of the cells are hit by more than three muons, the occupancy in the HCAL barrel is very low and far from the critical limit.

For the SiD tracker endcaps, however, the number of hits per cell reaches a maximum of 30 (see Fig-

<sup>2</sup>A cell is defined to be dead when the buffer of its sensor is already completely filled, and no further hits can be stored. Further details can be found in Chapter 5.3.2.

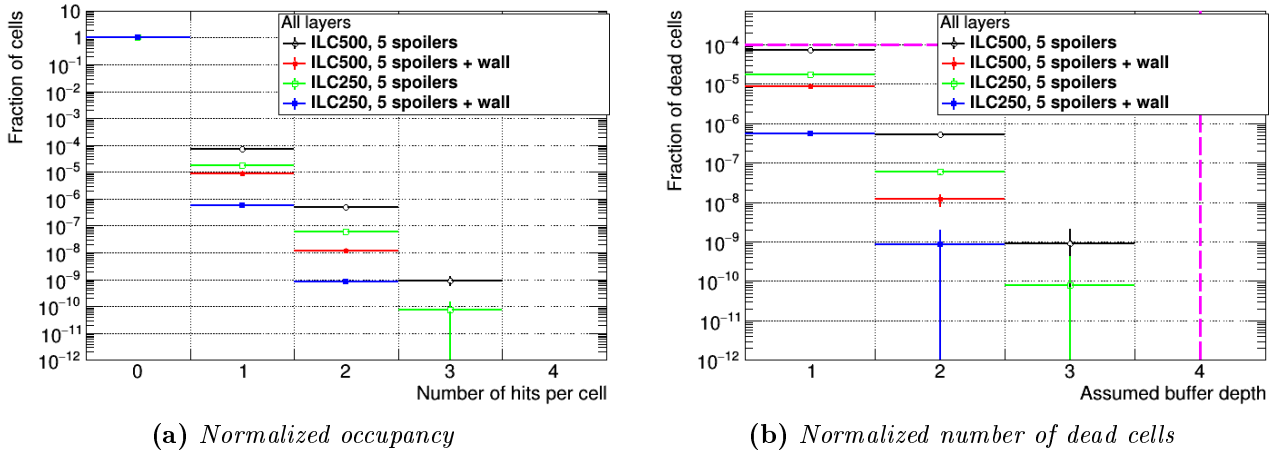


**Figure 6.8.:** Figure (a) shows the muon occupancy in the SiD HCAL barrel after a full bunch train, whilst Figure (b) shows the fraction of dead cells resulting from this occupancy. Both histograms are normalized by the total number of cells in the HCAL barrel. The first bin of Figure (a) contains the total number of cells, because of which the value of this bin is 1 for all cases. The dashed lines in Figure (b) indicate the buffer depth of four for the current sensor design, and the guideline of  $10^{-4}$  for a critical acceptance limit.

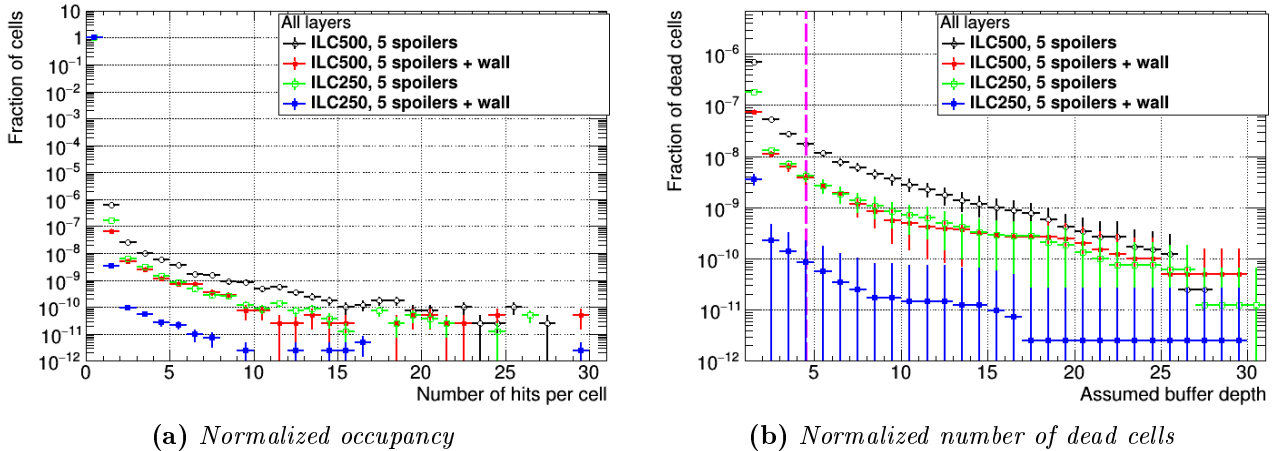


**Figure 6.9.:** Figure (a) shows the muon occupancy in one of the SiD tracker endcaps after a full bunch train, whilst Figure (b) shows the fraction of dead cells resulting from this occupancy. Both histograms are normalized by the total number of cells in the tracker endcap. The first bin of Figure (a) contains the total number of cells, because of which the value of this bin is 1 for all cases. The dashed line in Figure (b) indicate the buffer depth of four for the current sensor design, and the guideline of  $10^{-4}$  for a critical acceptance limit.

ure 6.9). As for the SiD tracker, a readout cell size of  $50\text{ }\mu\text{m} \times 50\text{ }\mu\text{m}$  was assumed, this is at first not to be expected. The total number of hits in the tracker is smaller than in the HCAL, and yet the number of hits per cell reaches a much larger value. The reason for this is that low energy (of the order of several hundred MeV) muons spiral in the magnetic field of the detector solenoid magnet, and by doing so hit the active layer of the tracker endcap several times. An example of a loop performed by such a muon is depicted in Figure 6.10. Although the number of hits per cell ranges up to 30, the occupancy is consistently below  $10^{-6}$  for all cases. The number of dead cells, shown in Figure 6.9 (b), is plotted as a function of an assumed buffer depth of up to 30 accordingly. Assuming the sensors in the SiD tracker will have a buffer depth of four, about  $2 \times 10^{-8}$  of all cells would be dead for the ILC500 with the “5 spoilers” shielding only. Also in this subdetector, the muon occupancy is below the critical limit for SiD for any buffer depth that might be chosen as the sensor design.

In the ILC500 stage, the occupancy for all subdetectors is reduced by at least a factor of five when adding a magnetized wall to the muon shielding. This factor is even higher in the ILC250 stage. Plots of the occupancy for the remaining SiD subdetectors can be found in Appendix B.

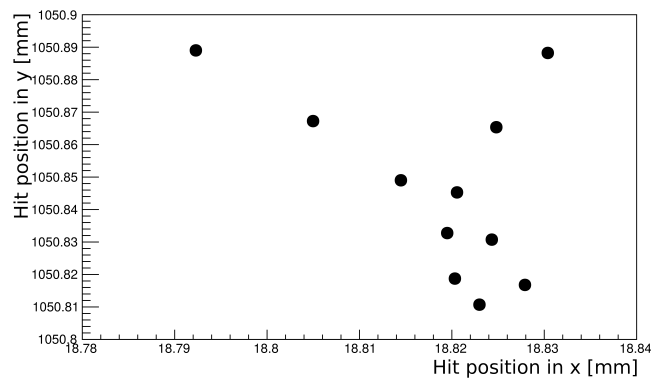


**Figure 6.10.:** Hit position of muon hits in the SiD tracker endcap, in layer number four. The muon spirals whilst penetrating the active layer, and thereby increases the number of cell hits.

### 6.3. Conclusion

This section presented a study of the effect of the muons from the BDS on the SiD occupancy for two different shielding options. For the first option, five magnetized spoilers would be installed at different locations along the beam line. For the second option, a magnetized wall would be placed between these spoiler locations and the interaction region, as an additional shielding device.

In Section 6.2.2, the comparison of the occupancy in these two cases revealed that the magnetized wall reduces the occupancy by a significant amount. Nevertheless, the occupancy level is in both cases far from the critical limit of  $10^{-4}$ , which is especially important in the tracking systems of the SiD detector. For these subdetectors, a minimal background occupancy is crucial to guarantee a high performance in the track reconstruction of physics events. For the first ILC stage, the SiD tracker endcap occupancy for an assumed buffer depth of four is about  $4 \times 10^{-9}$  for the minimal shielding option without the wall. Since in the next ILC stage at a center-of-mass energy of 500 GeV, the number of muons reaching the detector is larger by a factor of three, also the occupancy for the same

buffer depth is increased by about a factor of three for the “5 spoilers” case. However, it still does not exceed  $10^{-7}$ . The total number of muons produced in the BDS in both of the studied ILC stages is listed in Table 6.1.

Overall, the magnetized wall does not seem to be necessary in order to limit the muon occupancy in SiD, for both studied center-of-mass energies. However, the wall serves as a tertiary containment device against muons and other machine background particles. The decision might be to keep the wall anyway for the protection of personnel and maintenance staff, depending on the restrictions imposed by radiation safety regulations. A solution to lessen the price for the wall would be to change its design such that its thickness is reduced and it is not magnetized. The wall would then still serve as additional shielding but does not deflect charged particles. The next step for the studies of the muon shielding would be to also adjust the detector specific Pacman design with respect to different materials and the possibility of magnetizing the Pacman volume.

Additionally, the timing of the muons (discussed in Section 6.2.1) gives reason to study possible time gates in the individual subdetectors. Since the muons hit the muon system first and then penetrate the inner subdetectors, there are distinct hit times. Specific time gates for each subdetector could be decided on, in order to reduce the background occupancy.



# 7

## Chapter 7.

# Beam halo collimators for machine background reduction

After having studied different options for shielding the muon machine background in the ILC Beam Delivery System in Monte Carlo simulations (see Chapter 6), this chapter describes a different approach for reducing the machine background at the IP.

The functionality of a vertical beam halo collimator, which was proposed for the ILC Final-Focus system, was tested by taking measurements of the machine background at the Accelerator Test Facility 2 (ATF2). Sections 7.1 and 7.2 give a brief description of ATF2 and the vertical beam halo collimator. Afterwards, the background measurements are presented in Section 7.3. Additionally, Section 7.4 describes the Monte Carlo simulation of the accelerator and the collimator system, which was done using the accelerator simulation framework BDSIM.

The ILC Final-Focus (FF) system is responsible for focusing and preparing beams for the collision, as explained in Section 4.2. Focusing the beam bunches to nanometer-size is challenging, and requires a multitude of magnets, and diagnostic devices. With such small beam sizes, also the beam pipe radius and the apertures of all beam pipe components are of the order of centimeters. Beam orbit fluctuations can therefore lead easily to interactions between the beam and the beam line components, and hence to the production of machine background particles. In order to reduce the production of machine background, one approach is to install beam halo collimators that cut off the halo around the beam core.

For testing the feasibility of such collimators for future linear colliders such as the ILC, a vertical beam halo collimator [101] has been installed at the Accelerator Test Facility 2 (ATF2). In March 2016, data of the background in the proximity of the collimator were taken in dependency of the aperture of this collimator. This chapter covers the analysis of the data as well as simulation studies done with BDSIM.

## 7.1. The Accelerator Test Facility 2

The Accelerator Test Facility 2 (ATF2) is an extension to the accelerator facility ATF at the High Energy Accelerator Research Center Organization (KEK) in Japan [102]. As can be seen in Figure 7.1, ATF consists of a linear accelerator, which pre-accelerates electrons to 1.3 GeV before they enter the

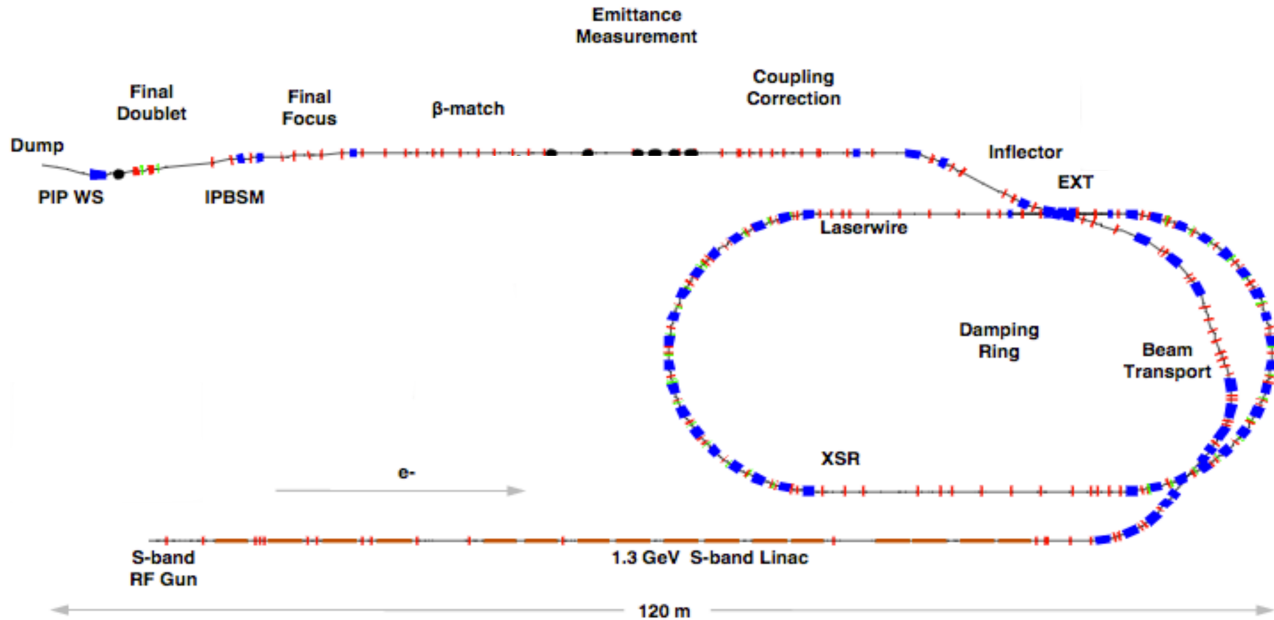


**Figure 7.1.:** A schematic of the ATF accelerator with the ATF2 extension [101, cf. p. 65]. ATF consists of a linear accelerator, a damping ring, the new ATF2 extension with the Final-Focus system, and a beam dump.

damping ring. Afterwards, the beam continues on the ATF2 beam line, which serves as a test bench for the FF system of the ILC.

ATF2 has two main goals:

1. Focusing the low-emittance beam to 37 nm in the vertical plane, which corresponds to the ILC goal of 5.9 nm
2. Demonstrating the stability of the nanometer sized beam at the interaction point

So far, focusing the beam to a size of 40 nm has been shown to be repeatable. Although the beam size goal of ATF2 seems to be large compared to the ILC goal of 5.9 nm, the ATF2 system is directly comparable to the ILC Final-Focus system. The beam size goal has to be scaled up for different lattice and beam conditions.

Additionally, as the ATF serves as a research accelerator, the ATF collaboration allows research groups to test new accelerator and diagnostic components, to operate the accelerator themselves, and to take measurements for their research. ATF therefore offers a unique opportunity for young researchers to conduct their experiments and to gain experience in operating a particle accelerator.

To this end, the vertical beam halo collimator, which was proposed and designed for reducing the machine background at linear colliders, was installed in ATF2 in the beginning of March 2016 by Nuria Fuster-Martinez [101]. In a collaboration with Nuria Fuster-Martinez, valuable experience was gained working together in the installation and operation of diagnostic hardware for particle detection, and in the operation of the ATF beam. Whilst the focus of her research was the construction and installation of the collimator, as well as the measurements of its general functionality, the focus for this part of

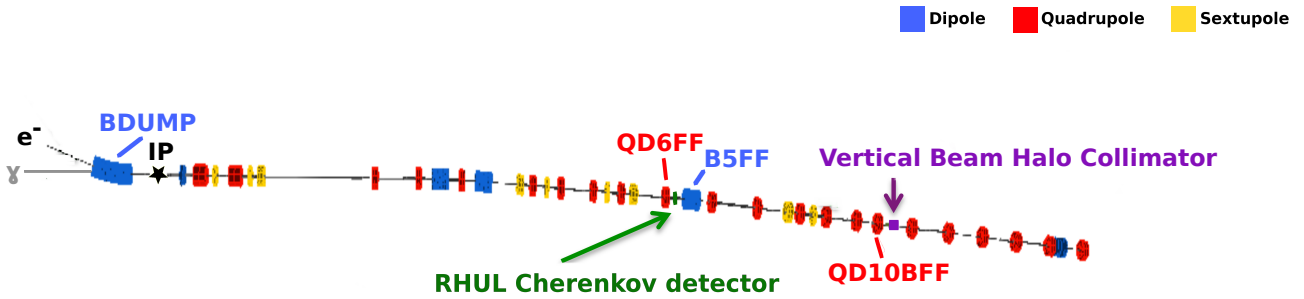


**Figure 7.2.:** A schematic of the ATF2 lattice [104]. The beam direction is from right to left. The beam halo collimator is located before the quadrupole magnet ‘QD10BFF’, the Cherenkov detector is installed downstream between the dipole magnet ‘B5FF’ and the quadrupole magnet ‘QD6FF’. After the interaction point (IP), the electron beam is bent in the last dipole magnet ‘BDUMP’ towards the beam dump.

the thesis at hand was independent measurements of background particles in the proximity of the collimator.

The vertical beam halo collimator and the Cherenkov detector, with which the background level was measured in dependency of the collimator aperture, are both located in the FF section of ATF2. A schematic of the ATF2 lattice with the collimator and the Cherenkov detector is shown in Figure 7.2. The Cherenkov detector was built and setup by a group from the Royal Holloway University of London (RHUL) [103], because of which the detector is in the following sections referred to as the “RHUL Cherenkov detector”. A more detailed description of this detector is given in Section 7.3.1.

## 7.2. Vertical beam halo collimator

The purpose of the vertical beam halo collimator is to cut off the beam halo in the vertical direction, in order to reduce the machine background at the IP. The design drawings of the collimator structure are shown in Figure 7.3. The collimating jaws are inside a structure that is evacuated and connected to the beam pipe of the ATF2 beam line. A picture of the installed collimator is given in Figure 7.4. The actual jaws are made of copper, the other components of stainless steel. The jaws have an overall length of 238 mm, and a cross-sectional area of 24 mm × 24 mm. They can be moved individually to an arbitrary position inside the possible range, so that the inner edge of the jaws can have a distance of between 2.6 and 12 mm to the center. The full aperture of the collimator structure can therefore be between 5.2 and 24 mm. The error on the position of the jaws is about 10 µm.

As every component in a beam line, especially for such small beam sizes, is affecting the electromagnetic field of the passing beam, the collimator is designed to minimize the effect of inducing wakefields [105, 101]. This thesis, however, focuses exclusively on the effect on the background level, as mentioned above.

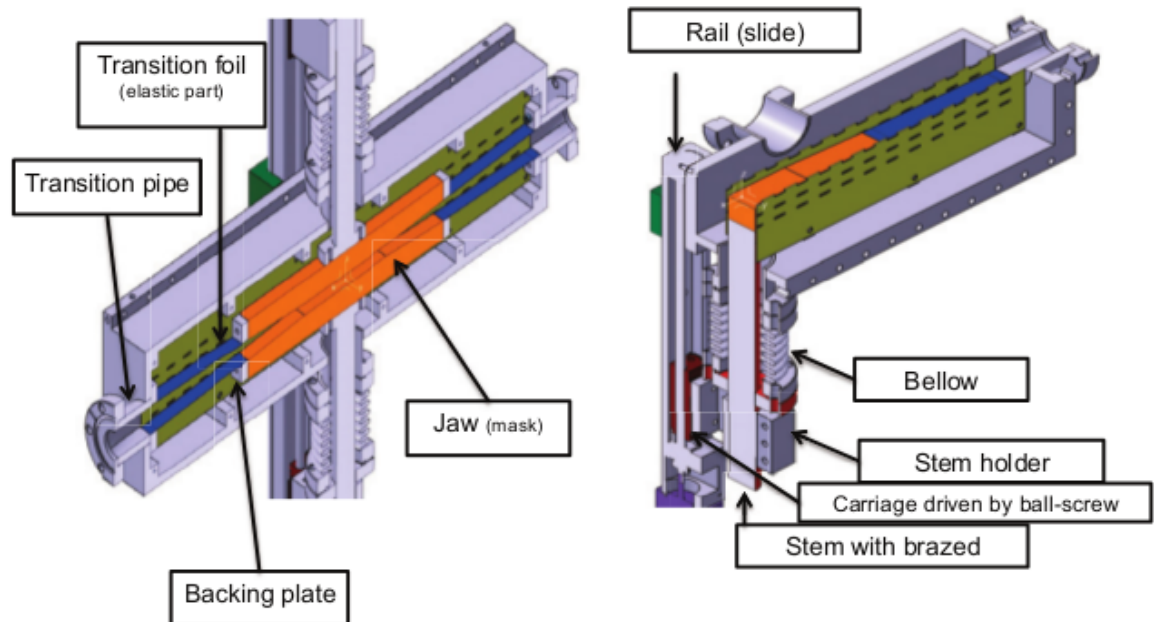


Figure 7.3.: A drawing of the vertical beam halo collimator installed at ATF2 [105].

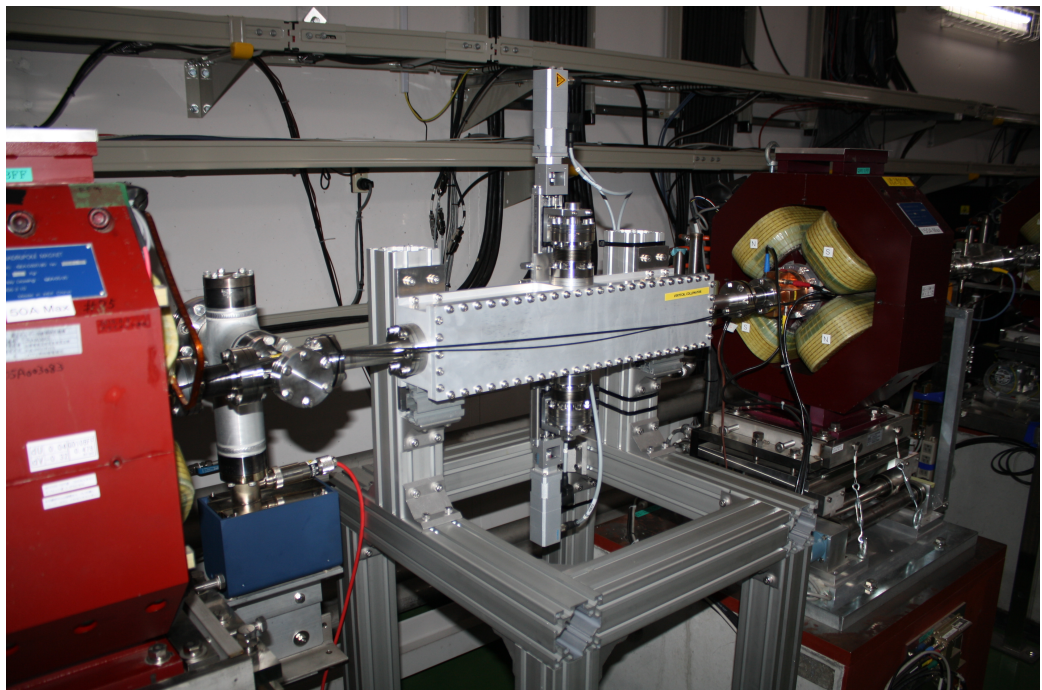
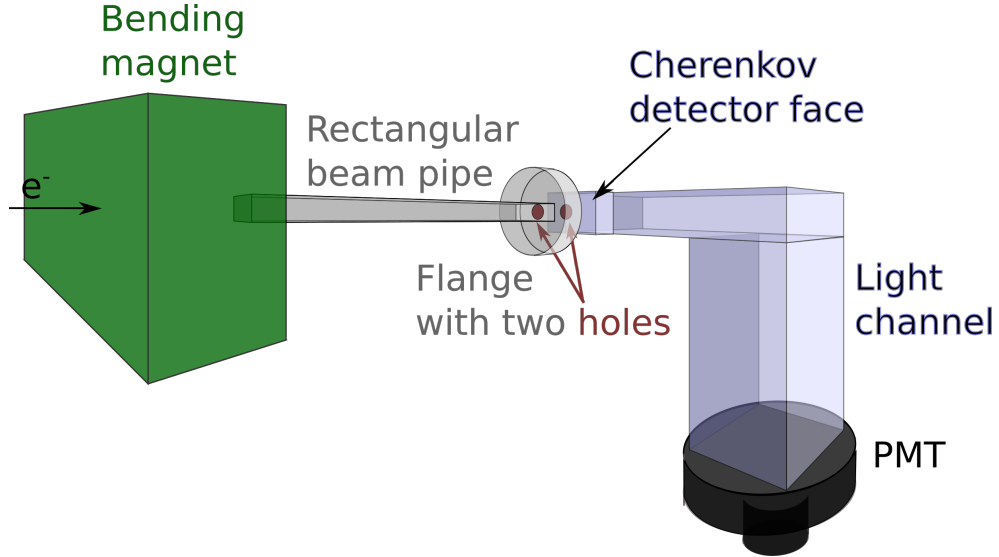


Figure 7.4.: A picture of the vertical beam halo collimator built into ATF2. The collimator jaws are within the evacuated structure. At the top and bottom of the structure, the mover system for the two jaws can be seen.



**Figure 7.5.:** A perspective schematic of the RHUL Cherenkov detector setup in ATF2. The beam electrons are bent in the dipole magnet, and continue through the rectangular beam pipe along the ATF2 beam line, and past the RHUL Cherenkov detector face. Secondary particles from particle showers on the other hand continue through the rectangular beam pipe, and enter the RHUL Cherenkov detector through the second window in the flange. The light signals are collected by the PMT.

## 7.3. Background studies

### 7.3.1. RHUL Cherenkov detector

The RHUL Cherenkov detector [103] uses the Hamamatsu photomultiplier tube (PMT), which was previously installed in a laserwire sensor that was located at the same position in the ATF2 beam line. The Cherenkov detector itself uses aerogel<sup>1</sup> as its radiator medium. A light-guiding pipe, with a profile area of  $10\text{ cm}^2$  and a total length of 35 cm, directs the light from the aerogel to the PMT. Figure 7.5 shows a schematic drawing of the detector setup. Pictures taken of the detector at the ATF2 beam line are shown in Figure 7.6.

It is installed downstream of a dipole magnet, which deflects the beam electrons along the beam line. The entrance of the Cherenkov detector is positioned such that the secondary particles from particle showers can be detected. The beam electrons are deflected past the detector. The detected secondary particles are an indication of the particle showers produced by interactions between the beam and the beam line components.

**PMT noise measurements** Before measurements of the shower particles could be taken, the PMT noise had to be measured. The noise is the signal that is measurable by the PMT, when the beam is turned off. Figure 7.7 (a) shows the mean values of the noise measurements for different PMT voltages. For every point either 500 or 1000 ADC pulses were recorded and averaged. The error bars represent the standard deviation on the mean value calculated with  $SD = \frac{\sigma}{\sqrt{N}}$ , where  $\sigma$  is the RMS of the noise

<sup>1</sup>SP15, index 1.015, 4 slices,  $4\text{ cm}^2$ , 5 cm deep

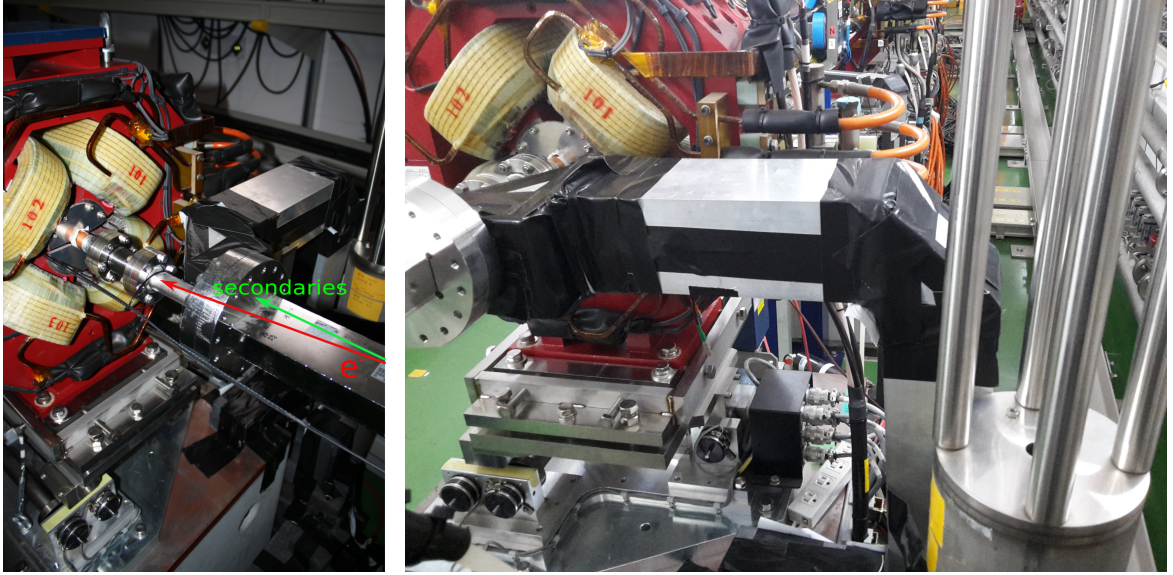


**Figure 7.6.:** Pictures of the RHUL Cherenkov detector in ATF2. The aerogel detector and the light channel are positioned behind a flange that connects the rectangular beam pipe with a circular one. The flange has two openings, one for the circular beam pipe, another one covered by a plastic window through which the secondary particles leave the rectangular beam pipe and enter the RHUL Cherenkov detector.

distribution at each point and  $N$  the number of pulses.

At around 800 V, the effect of dark current in the PMT becomes prominent, because of which the noise rises exponentially. Dark current is the electric current that can arise without a signal input. Some of the possible causes are: the thermionic emission of electrons from the photocathode and the dynodes, leakage current between the anodes and cathodes, and ionization current from residual gases inside the PMT [106, p. 67].

As the data was taken only for the voltages for which noise measurements were done, the mean value of noise is subtracted from every signal pulse appropriately. Therefore, the rise in noise is automatically taken into account for higher voltages.

**PMT voltage calibration measurements** In order to compare data sets that are taken at different PMT voltages, the signals have to be scaled. The rule of scaling the data is derived from the fit to the calibration measurements in Figure 7.7 (b). The data for this calibration is taken for stable beam conditions at a beam intensity of  $0.15 \pm 0.02 \times 10^{10}$ , and then plotted in a double logarithmic plot. The linearity of the data points shows the behavior of the PMT for different voltages according to Equation 7.1 [106]:

$$\mu = A \cdot V^{kn} \quad (7.1)$$

where  $\mu$  is the PMT gain,  $V$  the applied voltage, and  $n$  the number of anodes in the PMT.  $A$  and  $k$  are free parameters. This equation can be rewritten as:

$$\text{signal} = \text{par}_1 \cdot V^{\text{par}_2} \quad (7.2)$$

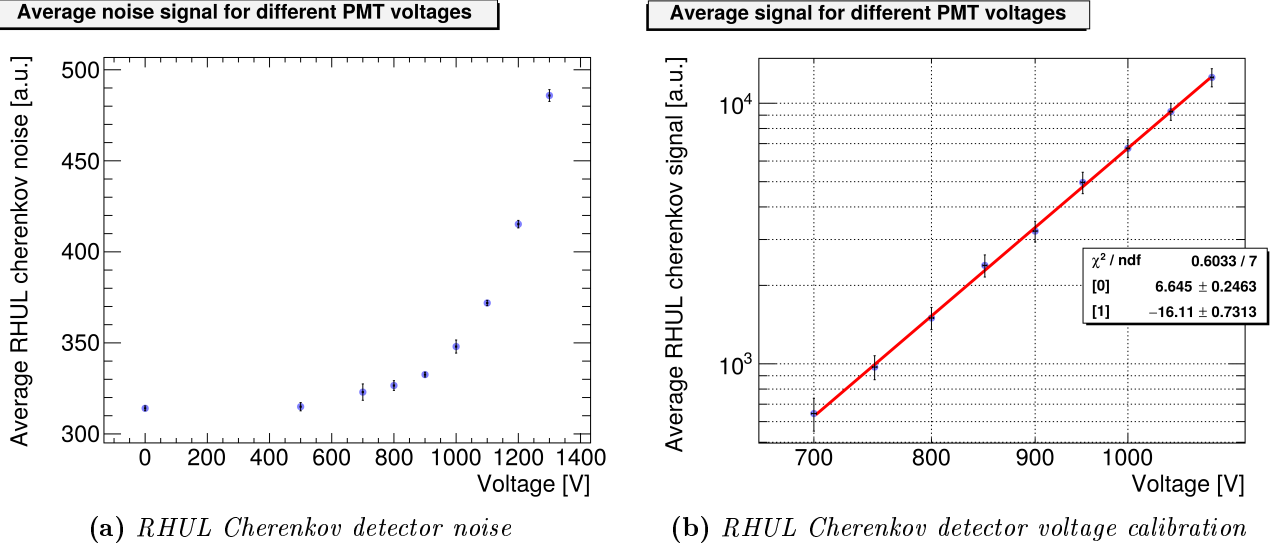


**Figure 7.7.:** Calibration measurements with the RHUL Cherenkov detector.

Figure (a) shows the average PMT noise signal as a function of the voltage applied to the detector PMT. The noise was measured when the ATF beam was turned off. For each voltage, 500 or 1000 ADC pulses of noise were recorded, and the noise was averaged over the number of pulses.

Figure (b) shows the average PMT signal as a function of the voltage applied to the detector PMT. The signal was measured when the ATF beam was stable at a beam intensity of  $0.15 \pm 0.02 \times 10^{10}$ . For each voltage, 500 ADC pulses were recorded, and the signal was averaged over the number of pulses.

After taking the logarithmic of both sides, the equation can be written as:

$$\log(\text{signal}) = \log(\text{par}_1) + \text{par}_2 \cdot \log(V) \quad (7.3)$$

$$y = \{1\} + \{0\} \cdot x \quad (7.4)$$

Equation 7.3 proves the linearity of the graph in the double logarithmic plot and verifies Equation 7.1 from the literature. For the log-log plot, Equation 7.4 is the derived fit function with the fit parameters that are obtained by applying the fit to the data in Figure 7.7 (b). The original signal function is therefore:

$$\text{signal} = 10^{\{1\}} \cdot V^{\{0\}} \quad (7.5)$$

with  $\log(\text{par}_1)$  being the fit parameter  $\{1\}$ , and  $\text{par}_2$  being the fit parameter  $\{0\}$ .

A signal ( $\text{signal}_1$ ) can then be scaled into a new signal ( $\text{signal}_2$ ) according to the voltages by doing:

$$\frac{\text{signal}_1}{\text{signal}_2} = \frac{10^{\{1\}} \cdot V_1^{\{0\}}}{10^{\{1\}} \cdot V_2^{\{0\}}} \quad (7.6)$$

$$\text{signal}_2 = \text{signal}_1 \cdot \left( \frac{V_2}{V_1} \right)^{\{0\}} \quad (7.7)$$

### 7.3.2. Collimator apertures scan at different intensities and vacuum pressures

For the measurements of the background signal in dependency of the collimator aperture, scans of the collimator apertures were done, whilst closing the collimator jaws simultaneously. Figure 7.8 (a) shows the plot of the average detector signals at five different beam intensities. It is clear that the background level rises approximately linearly with increasing intensity. The characteristic shape of the scan is however conserved: the background level is constant when closing the collimator from a full aperture of 24 mm to about 15 mm. When closing to 10 mm the background level drops, and rises again when closing the collimator completely, i.e. to 6 mm full aperture.

The measurements shown in Figure 7.8 (b) were done in a similar way, but for two different vacuum pressures:  $4.9 \times 10^{-7}$  Pa and  $1.06 \times 10^{-6}$  Pa. The data were taken for a beam intensity of  $0.5 \pm 0.03 \times 10^{10}$ . The background level is higher by about a factor of two for the higher vacuum pressure, as expected. Nevertheless, the background level is not simply shifted as expected from the two different pressure values. At the plateau (between 12 and 24 mm), the background level for the higher pressure is larger by almost a factor of two. At an aperture of 10 mm, however, the background is reduced to almost the same level at both pressures.

Independent of the beam intensity or the beam pipe vacuum pressure, the vertical beam halo collimator reduces the background measured with the RHUL Cherenkov detector by up to about 50 %, when closing the collimator to a full aperture of 10 mm. The collimator therefore reduces the background dramatically, especially at high background rates.

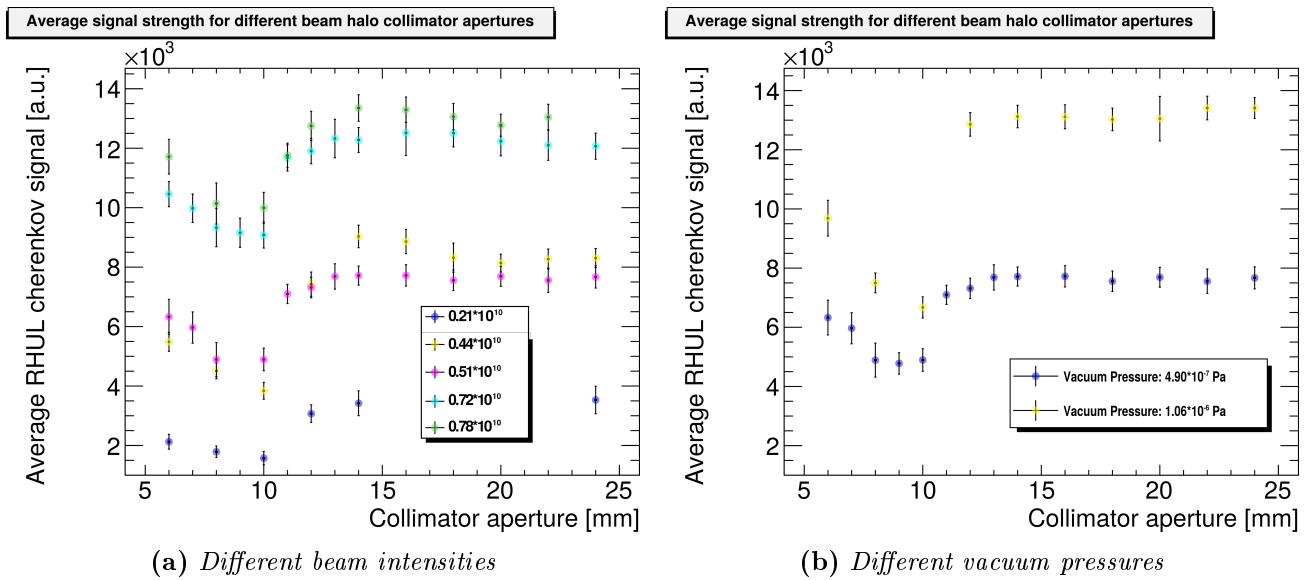


**Figure 7.8.:** Average signal as a function of the full aperture of the vertical beam halo collimator. For Figure (a), the signal was measured for different beam intensities:  $0.21 \times 10^{10}$ ,  $0.44 \times 10^{10}$ ,  $0.51 \times 10^{10}$ ,  $0.72 \times 10^{10}$ , and  $0.78 \times 10^{10}$ . The error on the beam intensity is  $0.02 \times 10^{10}$ . For Figure (b), the signal was measured for a beam intensity of  $0.5 \pm 0.03 \times 10^{10}$ . The vacuum pressure was lowered from  $4.9 \times 10^{-7}$  Pa to  $1.06 \times 10^{-6}$  Pa. For each aperture, 500 ADC pulses were recorded, and the signal was averaged over the number of pulses.

The drop in the measurable background level for a collimator aperture between 15 and 10 mm is on the one hand proof of principle for the collimator. On the other hand, the measured rise in the background level leaves some questions open about the origin of the background particles and the effect of the collimator aperture on particle showers. These questions are addressed in Section 7.4, in which the effect of the collimator is simulated with BDSIM.

## 7.4. Simulation study of the vertical beam halo collimator

As the data in Figure 7.8 in the previous section have shown, the collimator reduces the existing background level if closed to a full aperture of 10 mm. By closing the jaws further, the background level increases again. To address open questions, simulations of the ATF2 lattice including the beam halo collimator were done using BDSIM. The geometry model of the ATF2 accelerator lattice (in its state in the year 2015) already exists as a feature of BDSIM. However, a realistic model of the vertical beam halo collimator had to be added.

### 7.4.1. BDSIM

BDSIM [107] is a GEANT4 extension toolkit for the simulation of particle transport in accelerator beam lines, but also for the simulation of the interaction between the beam particles and the accelerator material. It is developed and supported by RHUL. The geometry of lattice parts are described in classes within the BDSIM framework. Particle accelerator lattices, such as the ATF2 lattice, can easily be built up with the pre-defined components. The magnets and other beam line components available within BDSIM are simplified versions of common components used in particle accelerators. The ATF2 lattice is visualized with the BDSIM software in Figure 7.9.

The simulation studies of ATF2, which are presented in this section were done with BDSIM version 0.95.

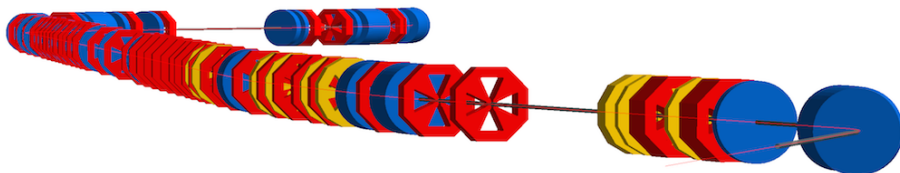


**Figure 7.9.:** A part of the ATF2 lattice visualized with the GEANT4 toolkit BDSIM.

### 7.4.2. Modeling the vertical beam halo collimator

The vertical beam halo collimator was modeled in GDML [108, 109] format according to its technical design drawings. Figure 7.10 shows a visualization of this model, as well as a view of the collimator structure inside the ATF2 lattice. In Figure 7.10 (a), the collimator jaws can be seen, which can be set to an arbitrary y-position inside the structure. With this new feature, BDSIM simulations with different collimator settings were done.

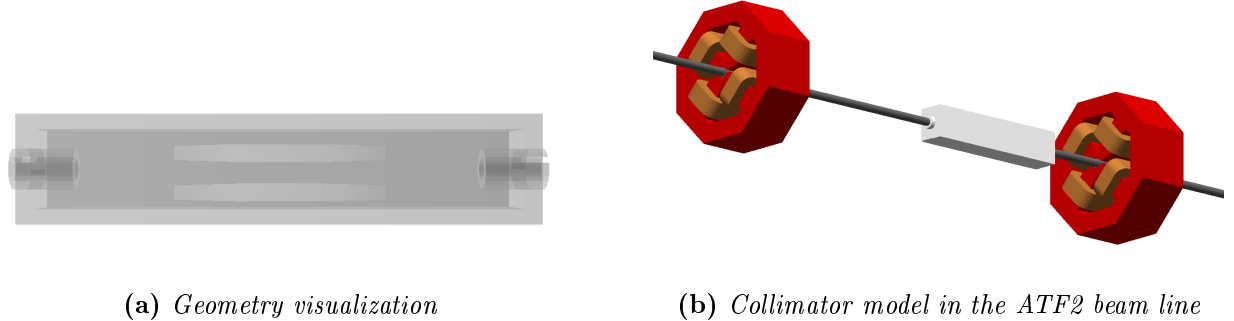


**Figure 7.10.:** Model of the vertical beam halo collimator, used in the BDSIM simulation of the ATF2 beam line lattice.

### 7.4.3. Simulation results

In order to validate the BDSIM simulation, comparisons of the beam parameter development along the beam line have been made for BDSIM and MADX [110]. MADX is a simulation tool for the simulation of beam dynamics at particle accelerators. For this validation, the beam size of the ATF2 beam core was plotted along the beam line for BDSIM and MADX. As shown in Figure 7.11, both simulations of the ATF2 beam dynamics are in good agreement. At the start of the ATF2 beam line, the beam core has a size of  $\sigma_x^{Core} = 51.9 \mu\text{m}$  and  $\sigma_y^{Core} = 15.4 \mu\text{m}$ . At the location of the beam halo collimator ( $S = 9 \text{ m}$ ), the beam core has a size of  $\sigma_x^{Core} = 0.16 \text{ mm}$  and  $\sigma_y^{Core} = 0.28 \text{ mm}$ . For the BDSIM simulation of the background particles, the primary particle beam was then set to be the ATF2 beam halo, excluding the beam core. The beam halo is defined to stretch from  $3\sigma_x^{Core}$  to  $5\sigma_x^{Core}$ , and from  $3\sigma_y^{Core}$  to  $10\sigma_y^{Core}$ . In BDSIM, the beam halo is modeled accordingly, assuming a Gaussian distribution. The beam particles have an energy of 1.3 GeV with an energy spread of 0.08 %.

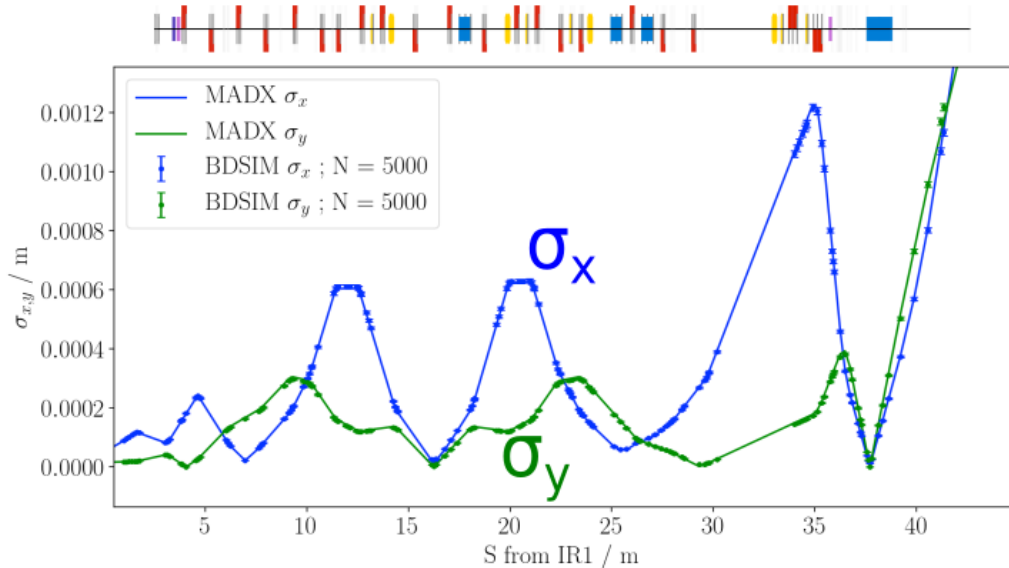


**Figure 7.11.:** Comparison of the ATF2 beam size ( $\sigma_x$  and  $\sigma_y$ ) development along the beam line ( $S [\text{m}]$ ) using BDSIM and MADX.

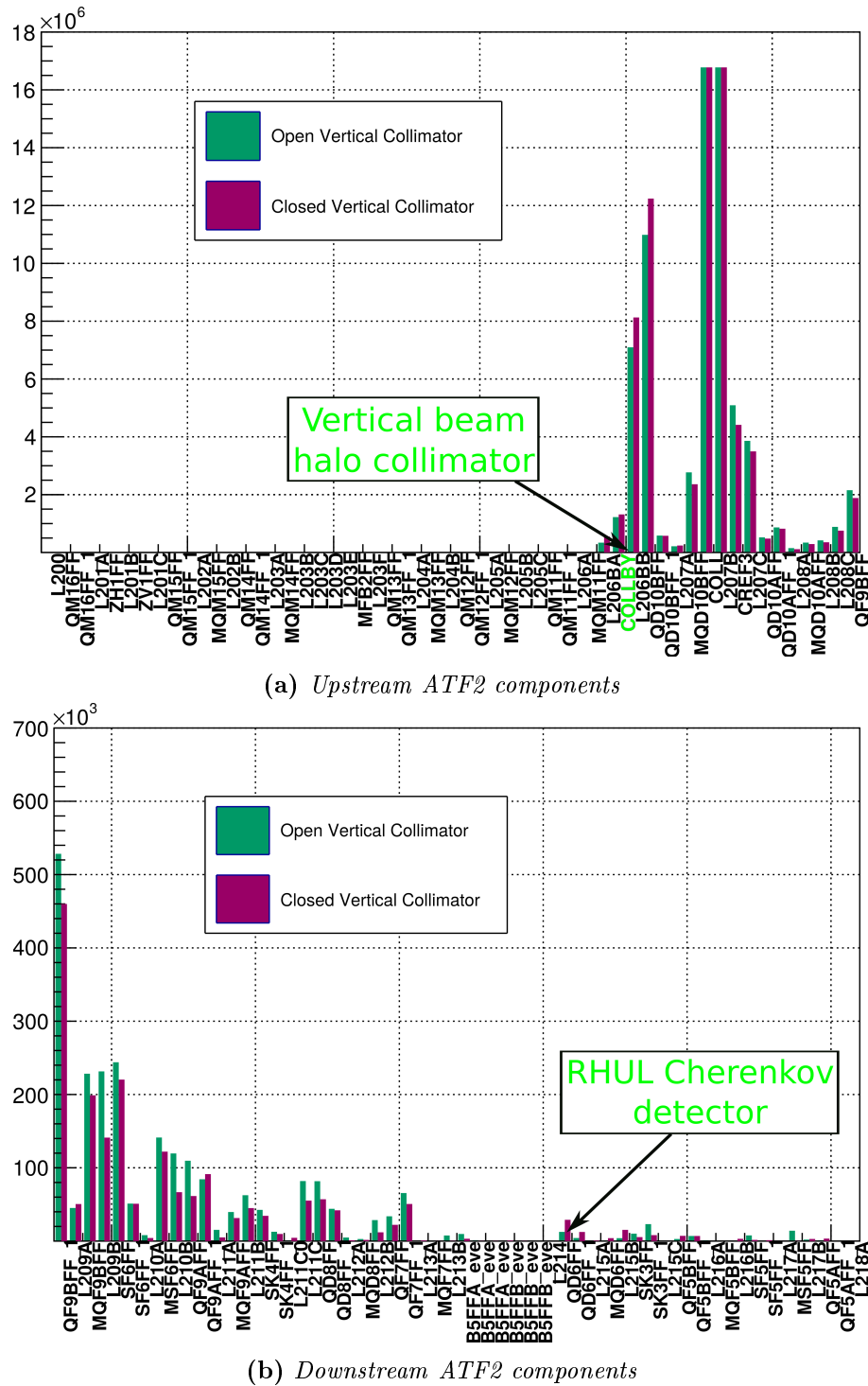


**Figure 7.12.:** Number of secondary particles observed in the ATF2 components directly upstream (a) and downstream (b) of the vertical beam halo collimator (COLLBY). The x-axes show the component names in the ATF2 lattice [111]. Components starting with the letter “L” are drift lengths, components containing the word “COLL” are collimators. All other names belong to magnet components.

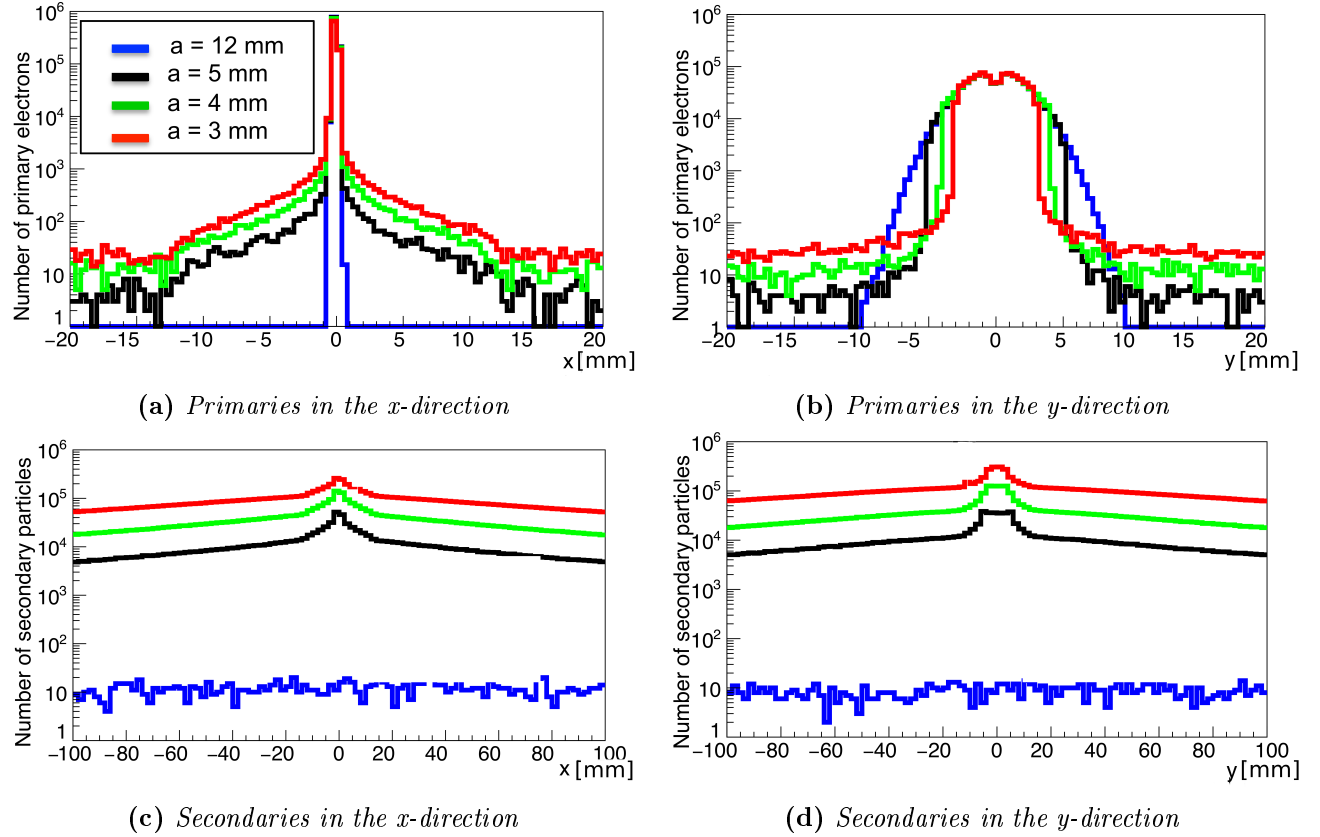


**Figure 7.13.:** Number of primary and secondary particles arriving at the exit of the vertical beam halo collimator [101, cf. p. 152]. Figures (a) and (b) show the number of primary particles in the x- and y-direction for different collimator half apertures. A half aperture of 12 mm corresponds to a completely open collimator (with a full aperture of 24 mm).

Figures (c) and (d) show the number of secondary particles in the x- and y-direction for the same collimator apertures.

Several BDSIM simulation runs were done for different apertures of the vertical beam halo collimator. The results were analyzed regarding the observable number of secondary particles created at the various ATF2 beam line components. A list of the beam line components and descriptions can be found in [111]. For a beam halo population of  $2 \times 10^6$  primary particles, the number of secondary particles in the proximity of the beam halo collimator can be seen in Figure 7.12. The number of particles are given in bar charts for the two collimator apertures: 24 mm (open collimator) and 4 mm (closed collimator). In the direct proximity of the collimator, the number of secondary particles is larger in the case of a closed collimator due to particle showers caused by the intersection of the beam halo with the collimator jaws.

This is shown in Figure 7.13. The number of primary and secondary particles are plotted at the exit of the beam halo collimator for different collimator half apertures. In Figures 7.13 (a) and (b), the x- and y-positions of the primary beam particles are plotted. For an open collimator, the beam is un-disrupted in both planes. When closing the collimator, the cut-off of the beam halo is visible in

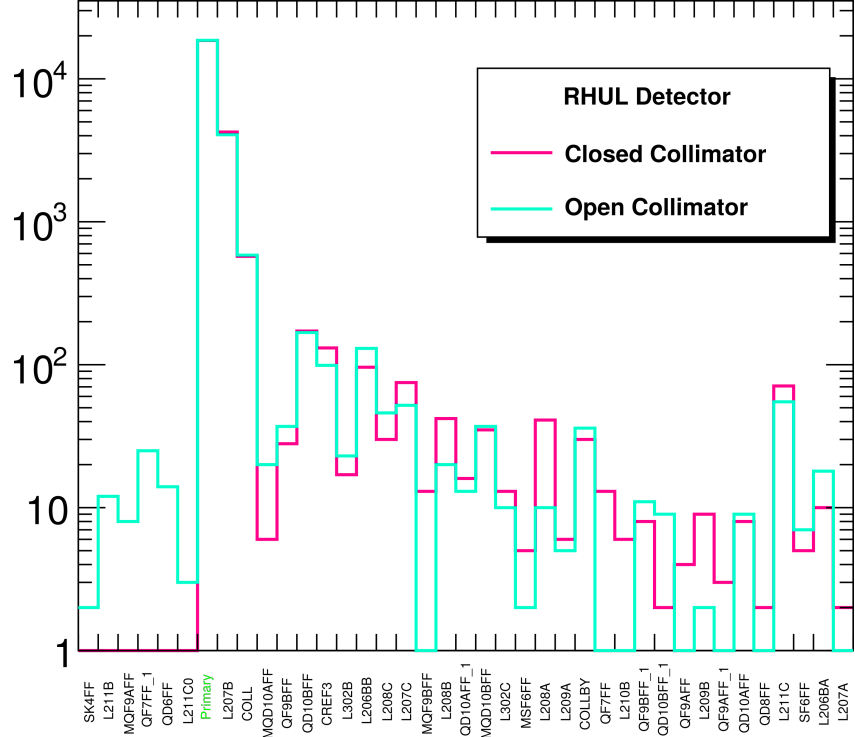


**Figure 7.14.:** Number of secondary particles arriving at the location of the RHUL Cherenkov detector in the case of an open (aperture of 24 mm) and closed (aperture of 4 mm) vertical beam halo collimator (COLLBY). The x-axis shows the component names in the ATF2 lattice [111]. Components starting with the letter “L” are drift lengths, components containing the word “COLL” are collimators. All other names belong to magnet components.

Figure (b). Primary particles are now, however, also spread in both the x- and y-direction. Figures 7.13 (c) and (d) show the positions of the secondary particles. Again for an open collimator, the level of secondary shower particles is low. For smaller collimator apertures, particle showers are created due to the intersection of the beam halo with the collimator jaws. The background level rises by several orders of magnitude.

Figures 7.12 (a) and (b) show furthermore that the number of secondaries further downstream of the collimator is smaller in every beam line component for a closed collimator compared to an open collimator, although more secondaries are produced in the direct proximity of the collimator. The cut off beam halo, therefore, reduces the showers in downstream beam line components.

At the location of the RHUL Cherenkov detector, which is indicated in Figure 7.12 (b), the number of occurring secondary particles is lower by over one order of magnitude in both cases compared to the components close to the collimator. This indicates that the observation of differences in the background suppression by the vertical beam halo collimator is challenging at this location.

Further studies have been conducted to find the origin of the particles that would hit the RHUL Cherenkov detector. To this end, cuts have been applied to the particle positions, such that only particles with x- and y-positions within a window that matches the front face of the RHUL Cherenkov detector are registered. The result is shown in Figure 7.14. The largest contribution are the primary

beam particles. Almost all other contributions are several orders of magnitude smaller. The respective components are all located downstream of the beam halo collimator and upstream of the Cherenkov detector. The number of observed shower particles coming directly from the beam halo collimator (COLLBY) is smaller for the closed collimator than for the open collimator by a few percent. Overall, there is no significant difference in the number of particles between the two studied collimator apertures.

## 7.5. Conclusion

The BDSIM simulation studies of the ATF2 lattice and the effect of the vertical beam halo collimator (Section 7.4) does not yield the desired results comparable to the measured data, which were discussed in Section 7.3.2. Figure 7.12 shows that the level of secondary particles at the location of the RHUL Cherenkov detector is low in comparison to the direct proximity of the vertical beam halo collimator. After discussions with BDSIM developers, it was concluded that the geometry models of the ATF2 beam line and its components are not mature enough for precision studies of the background in dependency of the collimator aperture. In order to improve the model, more accurate measurements of all component apertures along the ATF2 line had to be taken and implemented. The exact apertures are needed for a realistic simulation of the interaction of the beam halo with the beam line material. Additionally, the magnetic fields around the beam line magnets, which also affect the secondary particles, have to be modeled outside the beam line. So far, the implemented field maps only describe the magnetic field around the beam axis.

Overall, the analysis tool, which was written to gain the presented simulation results, is capable of showing the origin of the background particles and the background level at all components along the beam line. The beam halo collimator model, which was created for this simulation study, was provided to the BDSIM developers for its implementation into the ATF2 lattice, which is part of the available examples given in the BDSIM framework.

In Section 7.3.2, it was shown that the background level measured with the RHUL Cherenkov detector is approximately linearly dependent on the beam intensity and the beam pipe vacuum pressure. The measured background rate is also directly affected by the movement of the collimator jaws. Closing the collimator to an overall aperture of 10 mm, the background rate is reduced by about 50 %.

For future studies, the background levels should be measured at locations closer to the beam halo collimator, where higher background levels are expected. The effect of the collimator aperture is therefore easier to observe due to higher statistics and fewer influencing components between the collimator and the background detector. Together with an improved BDSIM model of ATF2, various background studies could be conducted regarding the impact of accelerator components and accelerator running schemes.

**Effect on the background level at IP** The actual aim of the vertical beam halo collimator is to reduce the machine background at the IP. Figure 7.15 shows measurements of background photons at the ATF2 IP in dependency of the vertical beam halo aperture. For all measured beam intensities, the background photon level was reduced by closing the collimator to a half aperture smaller than 6 mm, which corresponds to a full aperture of 12 mm. This and further results concerning studies of the beam halo collimator [101] are a proof of principle for the vertical beam halo collimator.

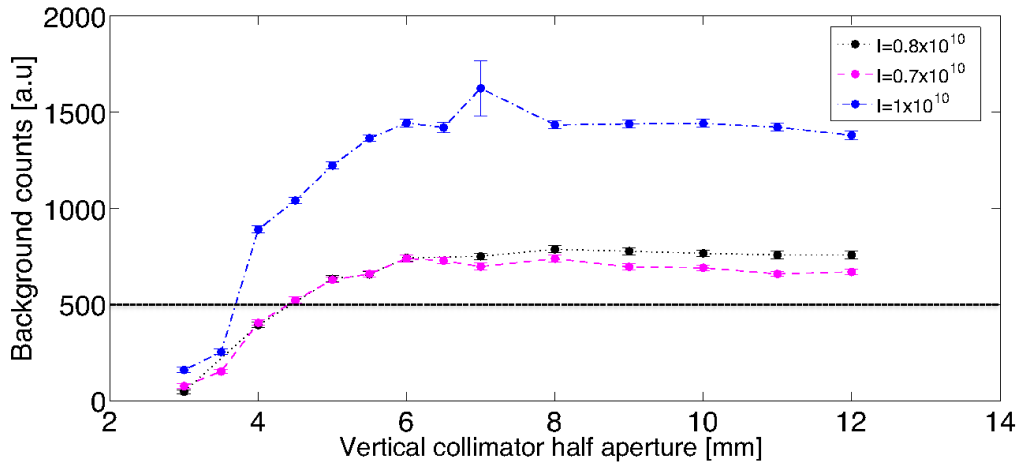


**Figure 7.15.:** Number of photons measured at the ATF2 IP in dependency of the vertical beam halo collimator aperture [101, p. 212]. The collimator aperture is given as the half aperture, which is the distance between the center axis and one collimator jaw. The photons were measured behind the ATF2 IP, where the beam electrons are deflected by the last bending magnet of the beam line lattice. The measurements were done for three beam intensities ( $0.7 \times 10^{10}$ ,  $0.8 \times 10^{10}$ , and  $1.0 \times 10^{10}$ ).



# 8

## Chapter 8.

# Background from the main beam dumps

After every beam collision, the beams of a linear collider are dumped into the main beam dumps. For the International Linear Collider, the main beam dump design is based on a water tank, which is tailored to absorb the beam power over a length of about 12 m.

Section 8.1 describe the simulation tools FLUKA and flair, which were used for the simulation of the main beam dumps. The two studied beam dump designs are presented in Section 8.2. Section 8.3 is focused on the irradiation of the water tank and its surroundings, as well as on the neutrons that are produced due to the interaction of the beam particles with the water molecules.

The second part of this chapter discusses those neutrons which are directed towards the ILC extraction line. The simulation of the neutrons traveling through the extraction line is discussed in Section 8.4. The neutrons reaching the interaction region present an additional background for the experiments. Their effect on the SiD detector is shown in Section 8.5. In the end, a suggestion for an alternative beam dump design is given in Section 8.6.

The spent  $e^+e^-$  beams are directed through the extraction line (EXT) of the ILC towards the main beam dumps. As can be seen in Figure 8.1, the beam dump halls are about 300 m away from the interaction point (IP) in a direct line of sight. The extraction lines have the task of transporting the highly disrupted beams to the dumps, because of which their quadrupole magnets have a large acceptance for offsets in the beam orbit as well as in the beam momentum of up to 60 % [45, p. 139]. The quadrupole magnets are to minimize beam loss so that additional diagnostic devices in the EXT lines can measure the qualities of beam bunches before they are dumped.

The beam dump designs are based on water tanks, which are surrounded by iron and concrete shielding walls. The two different designs that are studied in this chapter are described in detail in

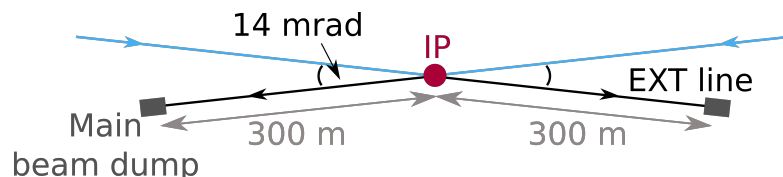


**Figure 8.1.:** Illustration of the interaction region of the ILC with the extraction line (EXT) leading from the IP to the main beam dump halls. The extraction lines are about 300 m long. The illustration is not to scale.

Section 8.2. The choice of a water tank as the beam dump is motivated by the high specific heat capacity of water, which is ideal to dissipate the energy of the beams. The water beam dumps for the ILC have to be able to absorb a beam power of up to about 17 MW<sup>1</sup> for the ILC stage at a center-of-mass energy of 1 TeV [112].

The high energy lepton beam interacts with the water molecules, leading to the emission of neutrons under all solid angles. The central interests of this chapter are the effects of these neutrons reaching back to the interaction region, and the doses that the surrounding area would suffer from. The result is a rise in the occupancy of the detector experiments, and damage to the detector components. The neutron background would firstly contribute to the radiation damage, such as displacement in the silicon sensors, which results in charge traps, reduction of charge transfer, and the overall degrading of the detector performance. Secondly, the immediate irradiation of the beam dump surroundings leads to restricted access for the maintenance staff and personnel. It is therefore crucial to understand the irradiation and the level of neutron background generated by the beam pulses dumped into the ILC main beam dumps.

## 8.1. FLUKA and *flair*

The simulation study of the ILC main beam dumps for this thesis was done using the Monte Carlo simulation tool FLUKA [113, 114]. FLUKA calculates the particle transport and interactions with matter of the user-defined geometry. With the graphical interface *flair* [115], which was specifically developed for FLUKA, complex geometries can be constructed with the help of technical drawings that are imported as templates into the *flair*-geoviewer plug-in (see Figure 8.2). It allows interactive geometry viewing and editing, as well as debugging and three dimensional visualization.

FLUKA's capabilities furthermore cover the calculation of particle densities and energy densities, the activation of material, and the residual dose rates when considering variable cooling times. These functionalities were used for the study of the ILC beam dump designs presented in the following sections.

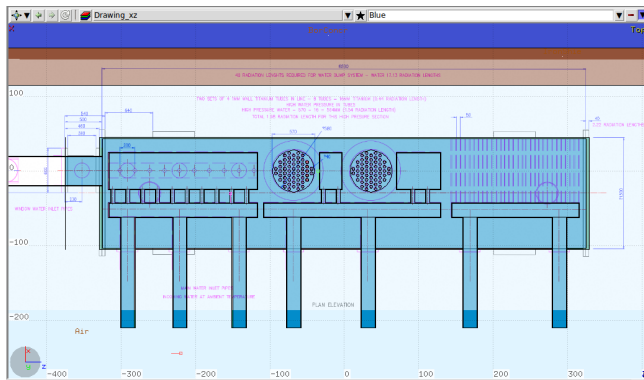


**Figure 8.2.:** Preview of the construction of the ILC beam dump using a technical drawing as a template imported into the *flair*-geoviewer plug-in.

---

<sup>1</sup>This value includes the average beam power of 13.7 MW at a center-of-mass energy of 1 TeV plus safety margins of 20 %.

## 8.2. ILC main beam dump designs

The designs for the main beam dump in this study are based on the technical design drawings that can be found in [116]. The drawings include plans for the surface building, the beam dump hall with the shielding walls around the water tank, and two different designs for the main beam dumps. The design based on the drawing with the identification number 0-TB-0067-210-00-A [116] shall henceforth be called “Design 1”, the second design based on drawing 0-TB-0067-300-00-A [116] shall be called “Design 2”. Figure 8.3 shows a visualization of the beam dump hall modeled within *flair*. The innermost shielding wall around the beam dump vessel is made of iron, and has a thickness of 50 cm. The middle layer of shielding consists of 1.5 m thick boronated concrete, surrounded by a layer of normal concrete, which has a thickness of 2 m. Boronated concrete is enriched with boron for the specific purpose of radiation shielding. The composition of both concrete types, boronated and normal, was adapted from concrete mixtures used in Japanese research centers, as described in [117]. The infrastructure, such as cables and water pipes, is not included in the simulation geometry.

As mentioned in the section above, technical design drawings can be imported into *flair*, and directly used as templates for the construction of the geometry. This was done for the two beam dump designs, which will be explained in detail in the following.

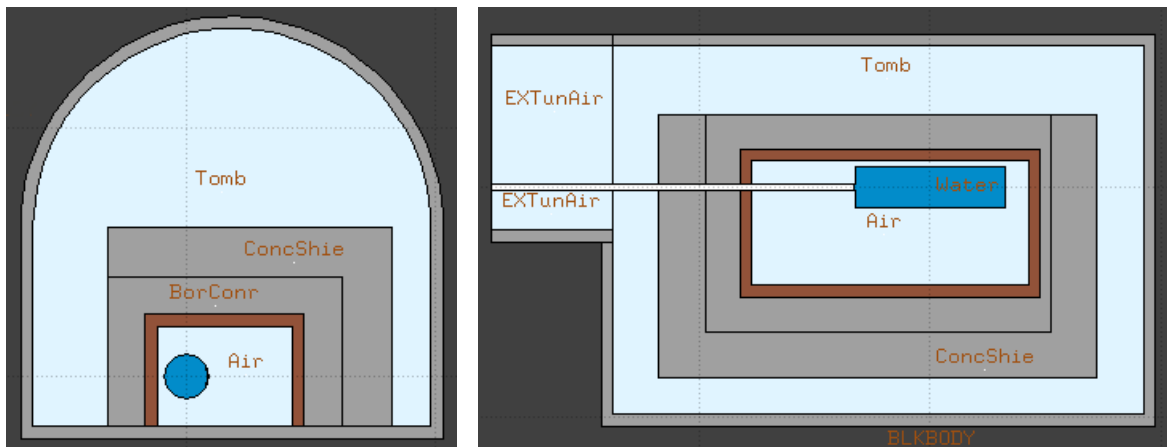


**Figure 8.3.:** Simplified version of the beam dump hall for the purpose of visualization, containing only a simple water tank in the middle of the shielding walls. The geometry was modeled within *flair* according to the technical drawings of the ILC beam dump facility. The left hand picture is the front view, the beam direction is going into the page. The right hand figure shows the top view, in which the water tank is shown in the middle of the different shielding walls. A FLUKA specific feature is the need of having a black body void around the geometry. This void is the border of the tracking region, and stops all particles reaching this edge.

### 8.2.1. Design 1

As both beam dump designs are based on a water tank system, their basic layout is very similar. For both, the water vessel is made out of the stainless steel alloy 316L, and has a diameter of 1.5 m and a length of 6.5 m. The water is pressurized to 10 bar. The window between the vessel and the beam

pipe has a diameter of 30 cm and a thickness of 1 mm. For the window material, the titanium alloy Ti-6Al-4V is foreseen. As can be seen from Figure 8.4, the vessel contains several pipes belonging to an inner vortex system. The turbulence of the water allows the arising heat of up to 150 °C from the beam power to dissipate [118, p. 3].

Overall, the water volume represents a material budget of 18 radiation lengths ( $X_0$ ), which yields an attenuation of about 33 %. An additional  $9X_0$  are placed in the end of the vessel in the form of water cooled copper plates [118, p. 2].

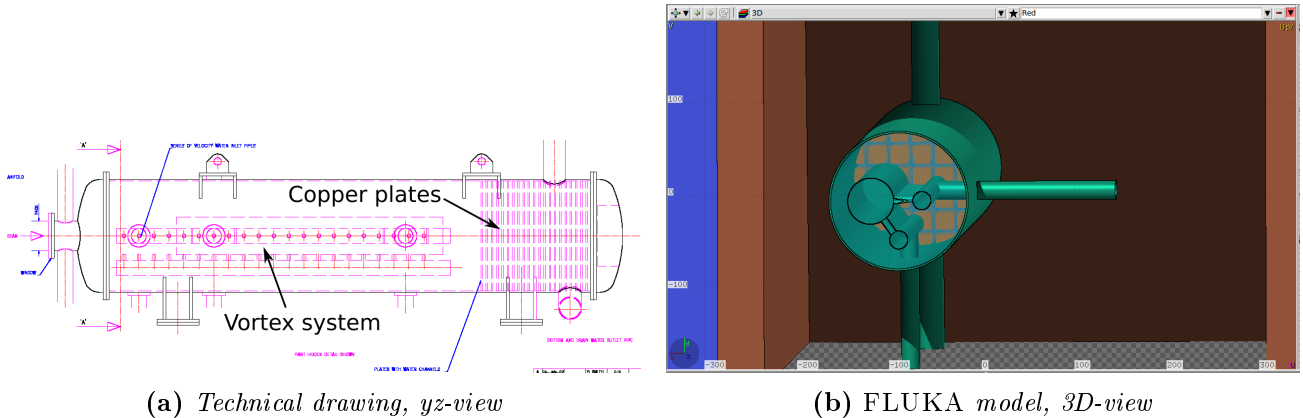


**Figure 8.4.:** Figure (a) shows the yz-view of the beam dump Design 1 from the technical drawing. The FLUKA model constructed within *flair* is shown in Figure (b).

### 8.2.2. Design 2

The basic layout explained above for Design 1 was also adopted for Design 2, so that the measurements of the vessel and the window are the same for both designs. The main difference is the addition of a high pressure water section in the middle of the vessel for Design 2. Figure 8.5 shows the 3D model of Design 2 implemented within *flair*, with the high pressure water section in the middle. The titanium tubes of this system have a diameter of 4 cm, through which high pressure water is pumped.

The vortex system shows also a different design approach. More tubes connect the vortex system with the outside pumps. The copper plates in this design are placed in the end of the vessel as well, for an additional  $9X_0$ .

## 8.3. Simulation studies of the beam dump surrounding

For the FLUKA simulation of the ILC beam being dumped into the water tanks of Design 1 and Design 2 as explained above, the running scheme of the ILC1000B [43, p. 11] stage was chosen. The beam bunches, which are considered un-collided and un-disrupted for this simulation study, have a bunch population of  $1.74 \times 10^{10}$  electrons, and a beam energy of 500 GeV. One beam pulse has 2450 bunches and a duration of 896.7  $\mu$ s. At the location of the main beam dump, the bunches have a size of  $\sigma_x = 2.4$  mm and  $\sigma_y = 0.22$  mm.

In the FLUKA model, the origin of the coordinate system is set to the center axis of the beam pipe in x and y, and to the middle of the water vessel in z. The beam bunches therefore start at a negative

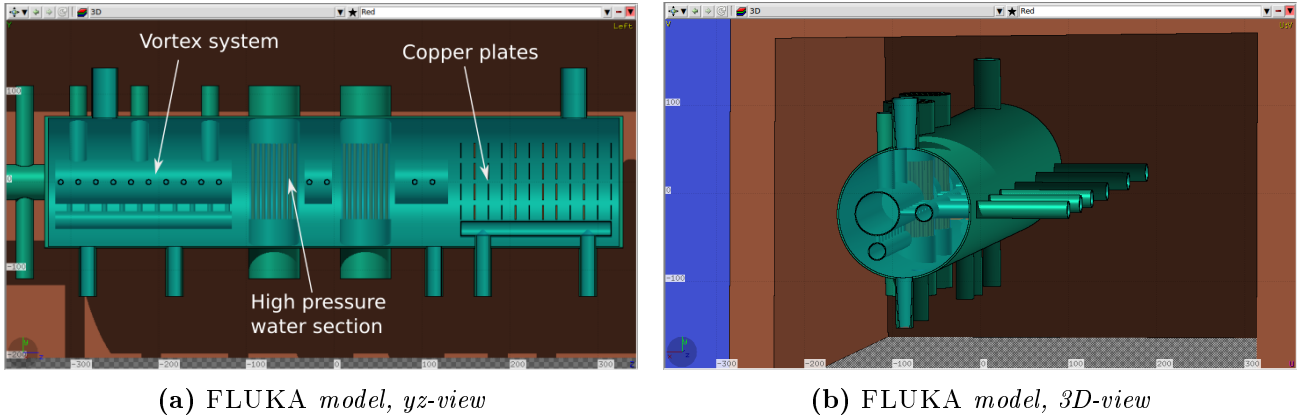


**Figure 8.5.:** Figure (a) shows the yz-view of the FLUKA model of the beam dump Design 2, the 3D-view is shown in Figure (b).

z-position of  $-10\text{ m}$  along the beam pipe center axis. This becomes clear in Figure 8.6, which shows the first FLUKA result, the deposited energy per bunch. The following sections present the expected dose rate and the particle densities.

### 8.3.1. Energy deposition

In FLUKA, various physics quantities can be measured as spatial densities or as double differential distributions in so-called scoring cards. The measured data can then be plotted with *flair*.

In this subsection, the energy deposition per volume is presented in the beam dump surroundings. Figures 8.6 (a) and (b) show the results in the xz-plane of the geometry for  $y = 0 \pm 3\text{ cm}$ . For two dimensional plots, the outlines of the geometry model can be superimposed in the correct plane. In this way, the spatial distribution of the measured physics quantity can directly be associated with the material allocation of the geometry. The comparison between Figure (a) and (b) shows that the energy deposited in Design 1 is well contained within the iron shielding wall. Closest to the vessel, energies of up to about  $10^6 \text{ GeV cm}^{-3}$  are deposited in the iron. For Design 2 however, the spread in the energy deposition reaches beyond the first shielding walls. The reason for this is the larger material density in Design 2 in the form of the high pressure water section in the middle of the vessel, which leads to enhanced particle showering.

Figures 8.6 (c) and (d) show the maximum values of every bin in Figures (a) and (b). The overall distribution of the deposited energy over z is smooth, with a maximum shortly before the vessel center. Nevertheless, the distribution has several sharp peaks which can be identified at locations with large material density. For Design 1, the first sharp peak at  $z \approx -230\text{ cm}$  corresponds to the front side of the vortex tube, the back side of the same tube is also visible through the second peak at  $z \approx 110\text{ cm}$ . The third peak at  $z \approx 220\text{ cm}$  is caused by the beam hitting the first copper plates in the end of the vessel. Accordingly, the sharp peaks in Figure 8.6 (d) for Design 2 also correspond to locations with a higher material density. The first two peaks at  $z \approx -100\text{ cm}$  and  $z \approx 0$  represent the high water pressure sections with their titanium tubes. The last peak at  $z \approx 120\text{ cm}$  originates from the first copper plates, which in this design are located closer to the vessel center. The absolute value for the maximum energy deposited per bunch is between  $\sim 1.4 \times 10^8 \text{ GeV cm}^{-3}$  and  $1.1 \times 10^9 \text{ GeV cm}^{-3}$ , for Design 1 and Design 2 respectively.

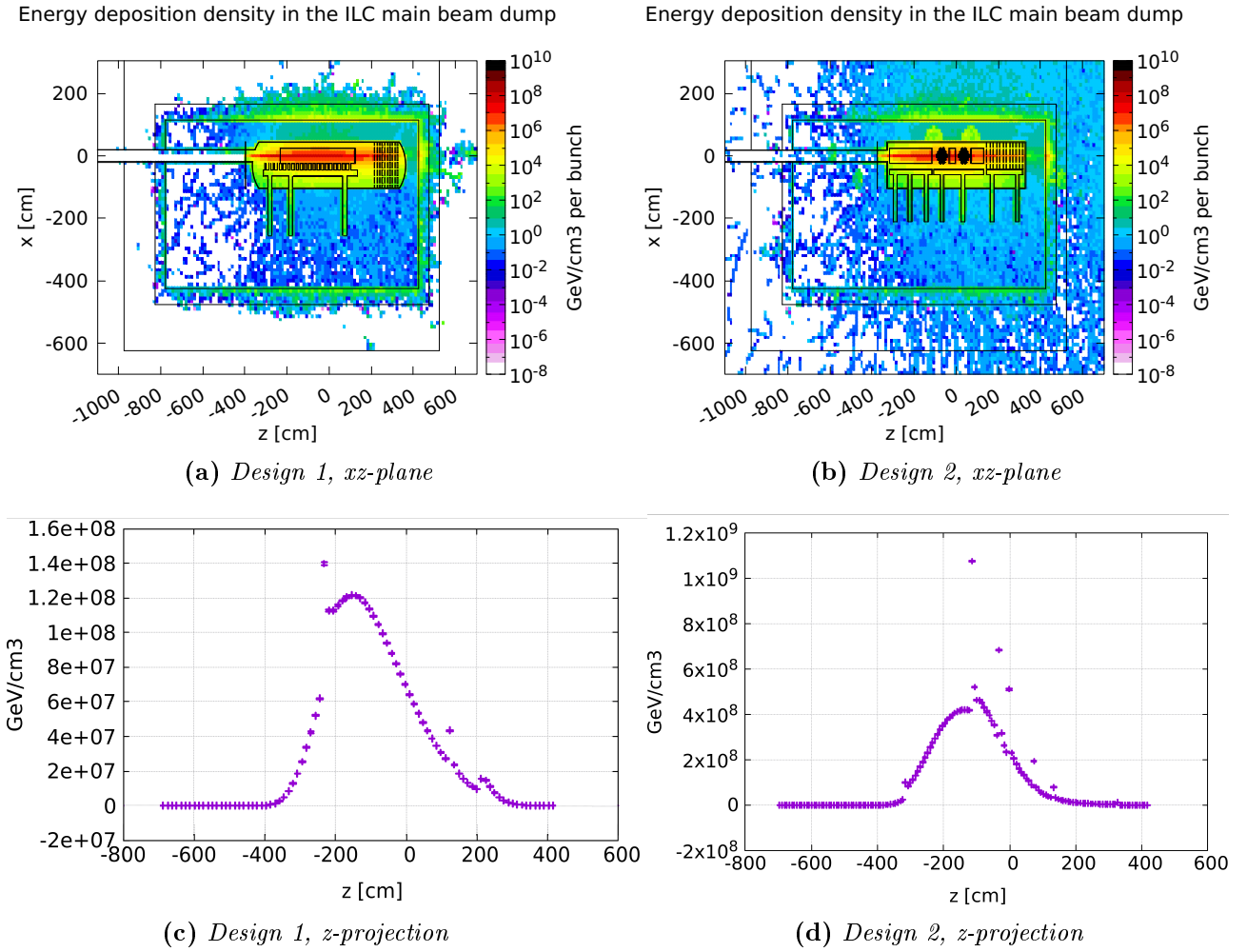


**Figure 8.6.:** FLUKA result of the energy deposition density of one beam bunch in the ILC beam dump Design 1 (a) and Design 2 (b). The view is in the xz-plane of the beam dump surroundings including the shielding walls. The color scale shows the deposited energy in  $\text{GeV}/\text{cm}^3$  per bunch.

Figures (c) and (d) show the maximum values of the energy deposition as a projection on the z axis.

### 8.3.2. Irradiation dose

From the deposited energy, FLUKA can calculate the instantaneous dose equivalent of the beam dumps and their surroundings. Figure 8.7 (a) and (b) show the FLUKA results of the spatial distribution of the dose from one bunch in the xz-plane, (c) and (d) show the projection of the maximum values onto the z axis, equivalent to the energy deposition plots before.

The distributions are comparable for both beam dump designs, the projection plots also again show sharp peaks at the locations of high material density. The maximum dose equivalent from one bunch reaches about 82 Sv in Design 1 and 105 Sv in Design 2.

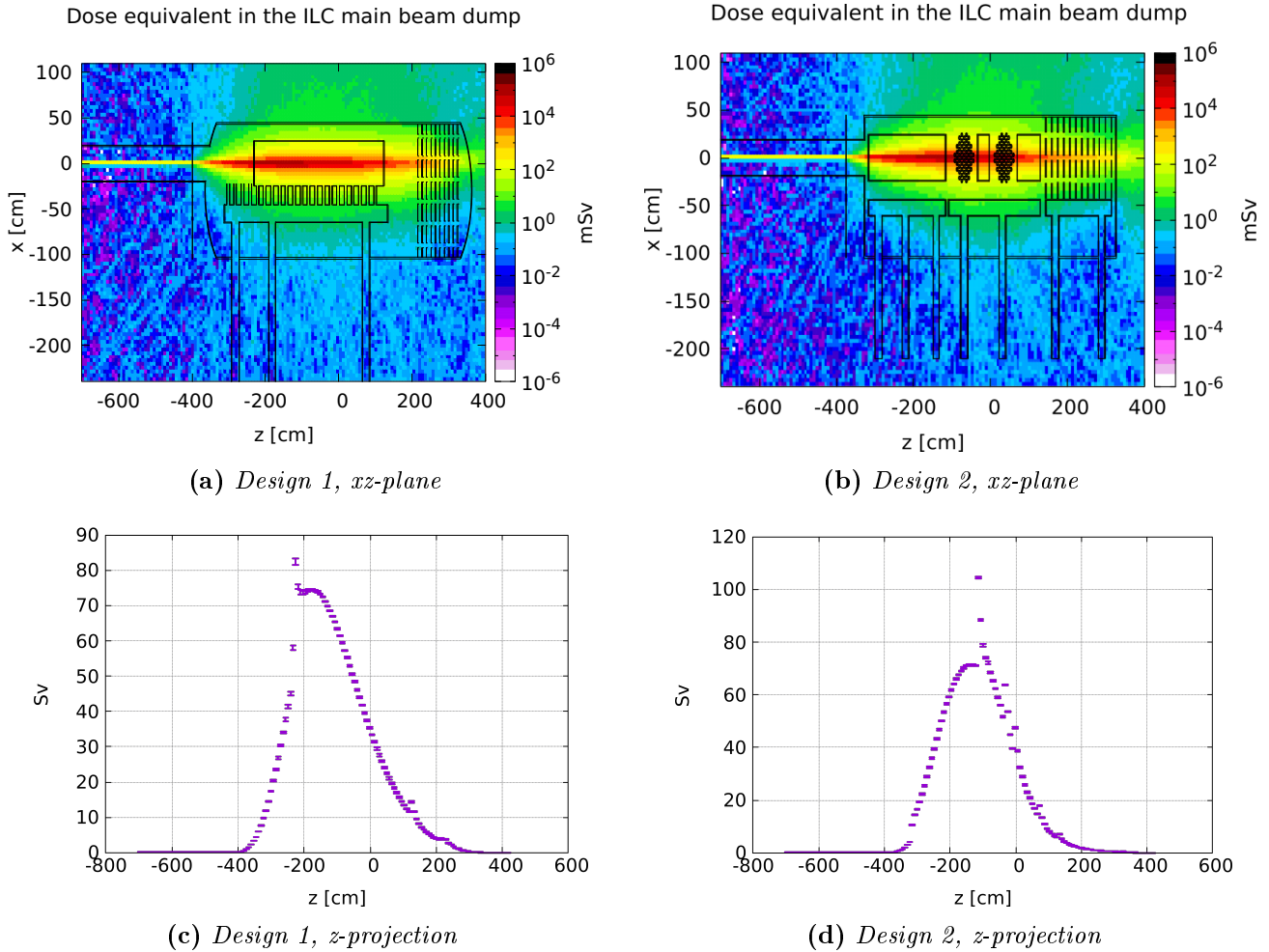


**Figure 8.7.:** FLUKA result of the dose equivalent from one beam bunch in the ILC beam dump Design 1 (a) and Design 2 (b) and their surroundings. The view is in the xz-plane of the beam dump surroundings including the shielding walls. The color scale shows the dose in mSv per bunch. Figures (c) and (d) show the maximum values of the dose as a projection on the z axis. The dose equivalent is here given in Sv.

From this, the remaining dose rate can be calculated after certain cooling times. It was assumed that there has been full beam operation for one month, after which the accelerator is turned off. Considering the cooling times of one minute, one hour, one day, one month, and one year after the moment of the beam operation stop, the remaining dose rate decreases over time. Figures C.1 and C.2 in the Appendix shows the spatial distribution of the dose rate for Design 1 and Design 2 for the cooling times mentioned above. The comparison of the dose rate as a function of the cooling time for the two designs is then given in Figure 8.8.

Already after one minute of cooling time the area in which a dose is measurable is reduced to the beam dump vessel and the direct surroundings. Over the duration of one year the dose is decreasing by at least two orders of magnitude. Nevertheless, the maximum dose rate after one year is about

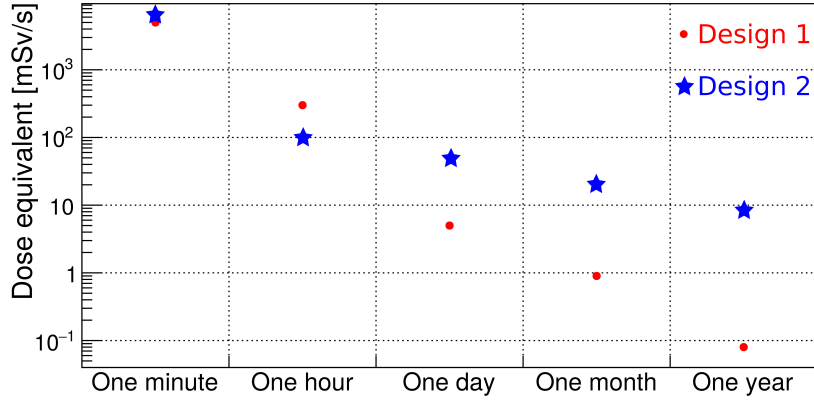


**Figure 8.8.:** Comparison of the maximum dose rate over the cooling time for the two ILC main beam dump designs Design 1 and Design 2.

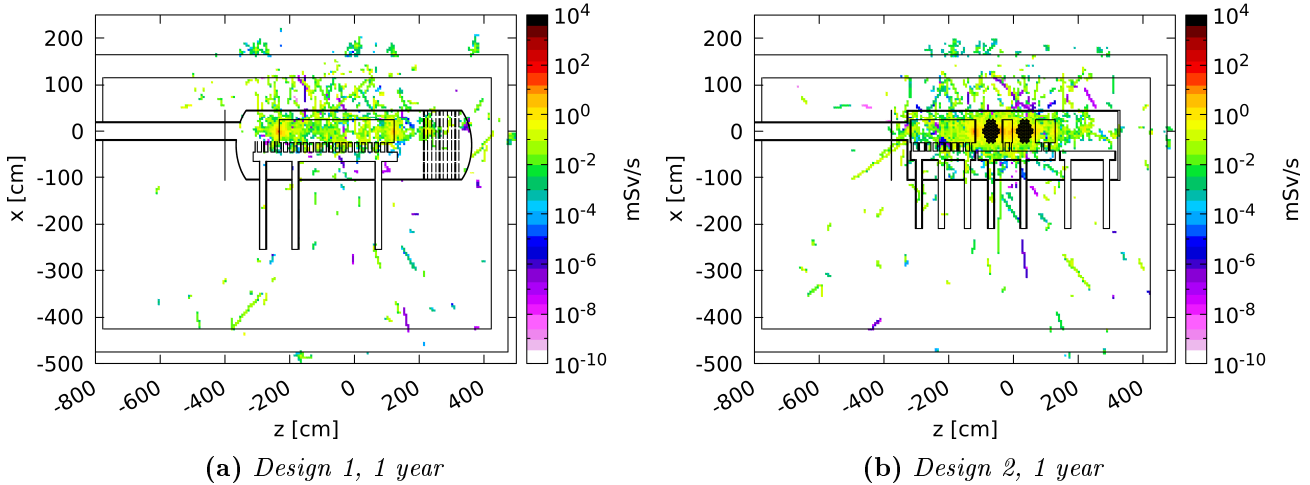


**Figure 8.9.:** FLUKA result of the dose rate in the ILC beam dump Design 1 (a) and Design 2 (b) and their surrounding after one month of beam operation and one year of cooling time. The view is in the  $xz$ -plane of the beam dump surrounding including the shielding walls. The color scale shows the dose rate in  $\text{mSv s}^{-1}$ .

$0.1 \text{ mSv s}^{-1}$  for Design 1, and  $10 \text{ mSv s}^{-1}$  for Design 2 inside the vessel. For a given legal dose limit of  $20 \text{ mSv}$  per year for workers whose work involves radiation activities [119], maintenance personnel would be allowed to work on the beam dump vessel for a very restricted time only. Figure 8.9 shows additionally the spatial distribution of the dose rate after one year for both dump designs. In the direct surroundings, the dose rate ranges around  $0.01 \text{ mSv s}^{-1}$  for both designs. Assuming the maintenance staff do not get in contact with the actual vessel, the allowed duration of stay can be calculated to be about 30 min, before the yearly dose limit is reached. Different considerations have to be made for necessary maintenance on the dump vessel itself. A possible approach is the remote handling of the vessel, including replacements and disposal of its components.

The residual nuclei, which are the cause for the high dose rates, are shown in Figure 8.10. The main contributors are  $^3\text{H}$ ,  $^{49}\text{V}$ ,  $^{54}\text{Mn}$ ,  $^{55}\text{Fe}$ ,  $^{56}\text{Co}$ ,  $^{57}\text{Co}$ ,  $^{58}\text{Co}$ , and  $^{60}\text{Co}$ , with a half-life between  $\sim 1$  and 13 years.

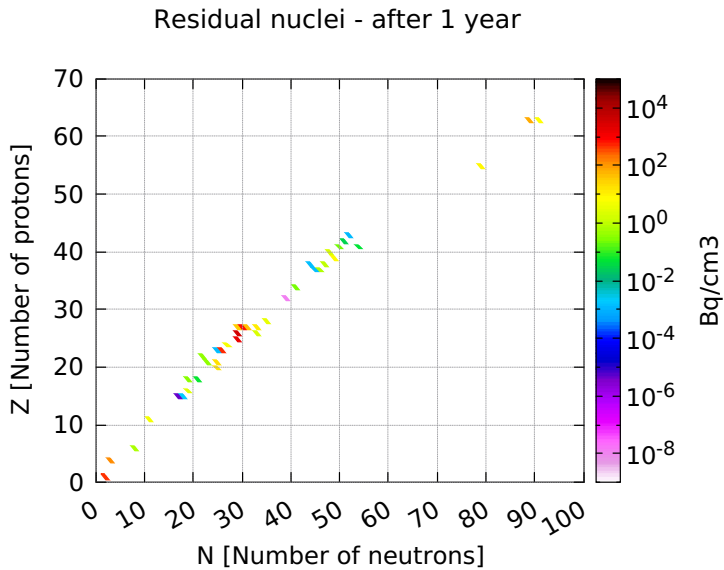


**Figure 8.10.:** Chart of residual nuclei in the beam dump vessel and its surroundings after a cooling time of one year. The axes show the number of protons ( $Z$ ) and the number of neutrons ( $N$ ) of the nuclei, from which the according element can be derived. The color scale indicates the radioactivity in  $\text{Bq}/\text{cm}^3$  of the respective nuclei.

### 8.3.3. Particle fluxes

Particle densities in the geometry can also be evaluated with FLUKA, which is then given as the number of particles per  $\text{cm}^3$ . As an example, Figure 8.11 shows the density distribution of electrons in the  $xz$ -plane for the two ILC beam dump designs. Since the primary beam also consists of electrons, the beam path is also visible coming from negative  $z$  along the beam pipe. Inside the water vessel, the beam is stopped and dissipated, and particle showers start forming. The electrons are boosted in the beam direction, because of which electrons outside the beam dump are mainly observed around and behind the vessel.

This looks quite different for the neutron density distributions (Figure 8.12). The primary electron beam undergoes the electromagnetic particle showers in the beam dump, which is desired in order to absorb the beam power. The produced secondary particles from the particle showers, however, interact with the beam dump material and the water via ionization and photonuclear processes. The products from these processes are neutrons in connection with the radioactive nuclei discussed in Section 8.3.2. Due to the way the neutrons are produced, they can be found under every solid angle, hence also in the backward direction. Since the neutron flux outside the vessel does not show a significant difference between Design 1 and Design 2, the following results are shown for Design 1 only. They are however valid for both designs.

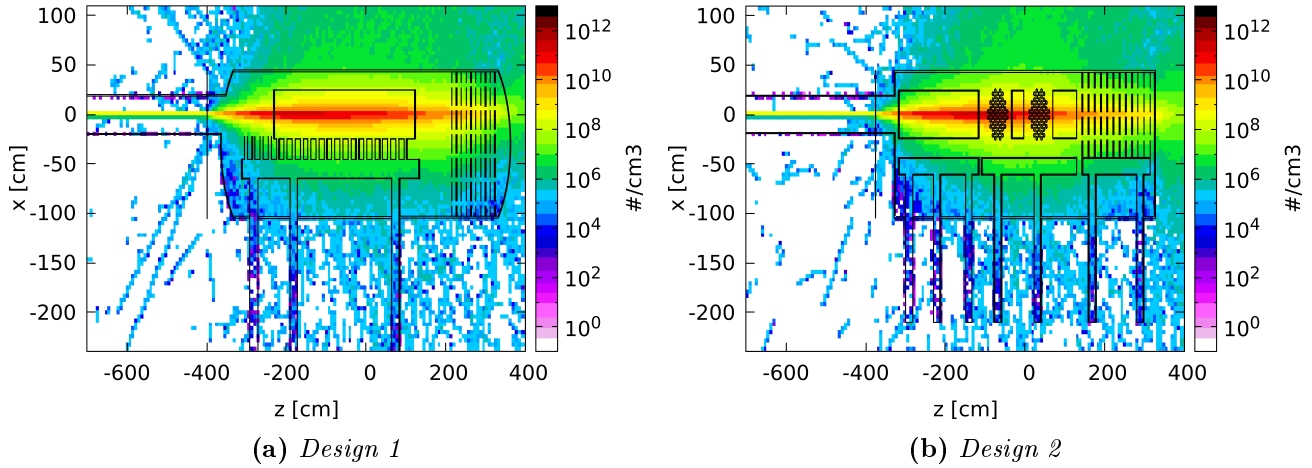


**Figure 8.11.:** FLUKA result of the electron flux from one beam bunch in the ILC beam dump Design 1 (a) and Design 2 (b) and their surroundings. The view is in the xz-plane of the beam dump. The color scale shows the flux in number of particles per  $\text{cm}^3$  per bunch.

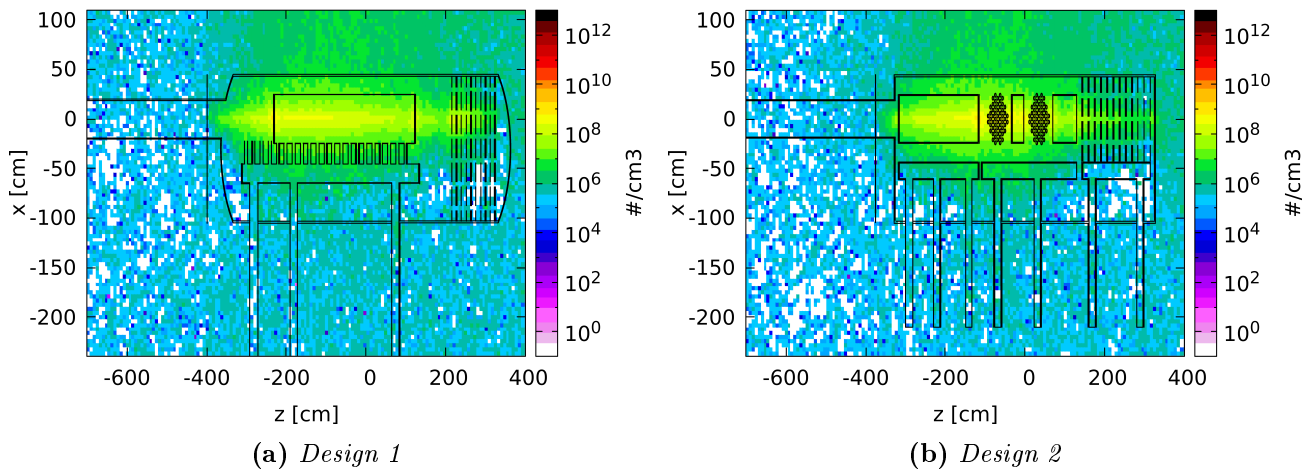


**Figure 8.12.:** FLUKA result of the neutron flux from one beam bunch in the ILC beam dump Design 1 (a) and Design 2 (b) and their surroundings. The view is in the xz-plane of the beam dump. The color scale shows the flux in number of particles per  $\text{cm}^3$  per bunch.

By adding an imaginary scoring plane<sup>2</sup> upstream of the beam dump vessel as indicated in Figure 8.13 (a), the neutrons escaping the beam dump in the direction of the extraction line can be counted. FLUKA then recorded the kinetic energy of the neutrons crossing this scoring plane under various angles to the z-axis. The energy spectra can be seen in Figure 8.13 (b). The spectra range from about 1 meV to 500 MeV, and indicate the number of neutrons under different angles. The graph “0 - 45 degrees” shows the energy spectrum for all neutrons crossing the boundary in the direction of the

<sup>2</sup>Designated plane in the FLUKA geometry model, at which physical quantities can be measured.

extraction line (the negative z-direction) under an angle of up to  $45^\circ$ . The energy spectrum of the neutrons that cross the boundary under an angle between  $45^\circ$  and  $90^\circ$  to the negative z-direction is also displayed in Figure 8.13 (b). The combination of both spectra is shown by the red graph, indicated with “all angles” in the figure legend. The first peak in the meV range represents the thermal neutron energy peak. At the eV range, resonance peaks from resonant elastic scattering of neutrons with a compound nucleus are visible. These resonance peaks are element specific, so that the peaks indicate which materials the neutrons have interacted with. The peaks visible in the plot mainly originate from elastic neutron scattering processes with iron and copper atoms, which leads to resonances in the neutron cross section at around  $10^{-2}$  to  $10^{-1}$  MeV [120, 121]. Finally in the range of  $\sim 100$  MeV, the so-called evaporation or fission peak of fast neutrons is visible.

All the neutrons that pass the scoring plane are oriented in the direction of the extraction line and hence in the direction of the interaction region and the detectors. As can be seen in Section 8.4, the neutrons do not reach the detectors freely. Due to shielding walls and extraction line components, the number of neutrons is reduced.

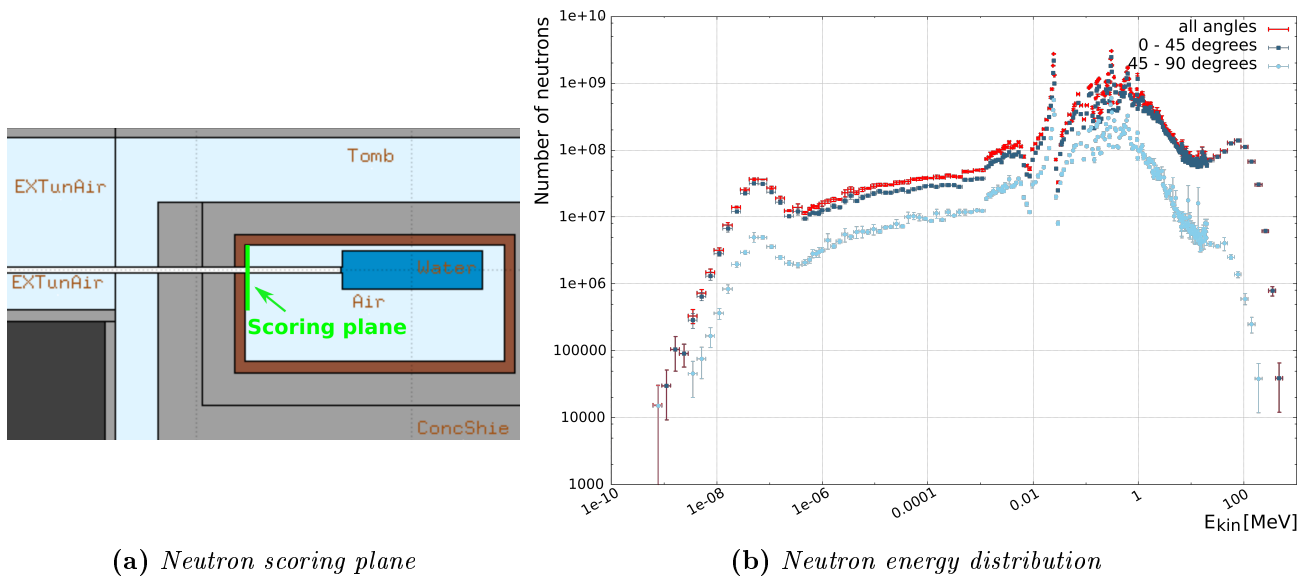


**Figure 8.13.:** Scoring neutrons escaping the beam dump vessel in the direction of the extraction line.

Figure (a) shows the position of the scoring plane in FLUKA in the xz-view of the beam dump hall. At the boundary of the scoring plane, the neutron energy spectrum is recorded.

Figure (b) shows the energy spectra of the neutrons, which are produced in the beam dump Design 1 from one ILC beam bunch, and which cross the scoring plane indicated in Figure (a). The different graphs stand for different crossing angles to the z-axis. The red graph (“all angles”) is the combination of the other two graphs (“0 - 45 degrees” and “45 - 90 degrees”).

## 8.4. Simulation studies of the extraction line

The neutrons, which are created in the ILC beam dumps and directed towards the interaction region, are not freely traveling through the extraction line. As mentioned before, the extraction line lattice consists of magnets and collimators, which for the neutrons represent shielding obstacles. An accelerator lattice is the sequence of all beam line components.

The first device of the extraction line lattice is the focusing quadrupole QDEX1, closest to the IP. Like the last quadrupole QD0 of the final-focus system, QDEX1 is also an integrated part of the two detector experiments. Since the neutrons escaping the extraction line shall be input to a full detector simulation, the FLUKA model of the EXT line therefore does not include QDEX1. The model rather ends at 9.3 m from the IP, which will then be the starting point of the escaping neutrons for the following GEANT4 simulation of the SiD detector. The component of the FLUKA model closest to the IP is the cryostat containing QFEX2A, the only other superconducting magnet of the EXT lattice next to QDEX1. The cryostat is followed by 13 quadrupole models, which prepare the spent beams for diagnostic measurements and which shall prevent any beam loss [45, p. 139 ff, 122, 123]. The following eight dipole magnets are part of the energy diagnostic section. The polarimeter section containing four dipole magnets, measures the polarization level of the beam. Finally, the collimators located at various positions along the EXT line are protection collimators, shielding the beam line devices from irradiation.

The goal of this FLUKA simulation is to obtain the number and the distribution of neutrons reaching the detectors. The models of the EXT line components are therefore simplified models aimed at representing the shielding objects with the correct sizes and positions along the line. The beam line infrastructure, like vacuum pumps and valves are not accounted for in the simulation. Figure 8.14 shows the FLUKA model of the extraction line.

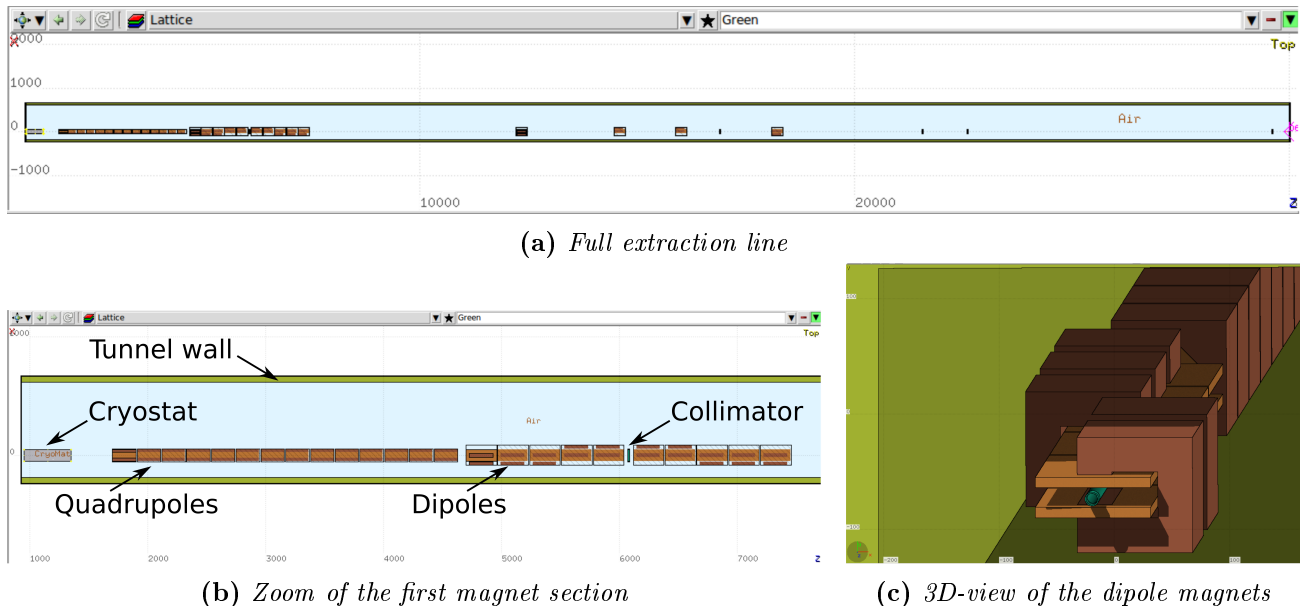


**Figure 8.14.:** Pictures of the ILC extraction line, modeled within FLUKA. The full model is shown in a xz-view in Figure (a). Figures (b) and (c) show closeup views of the magnet section in the beginning of the extraction line.

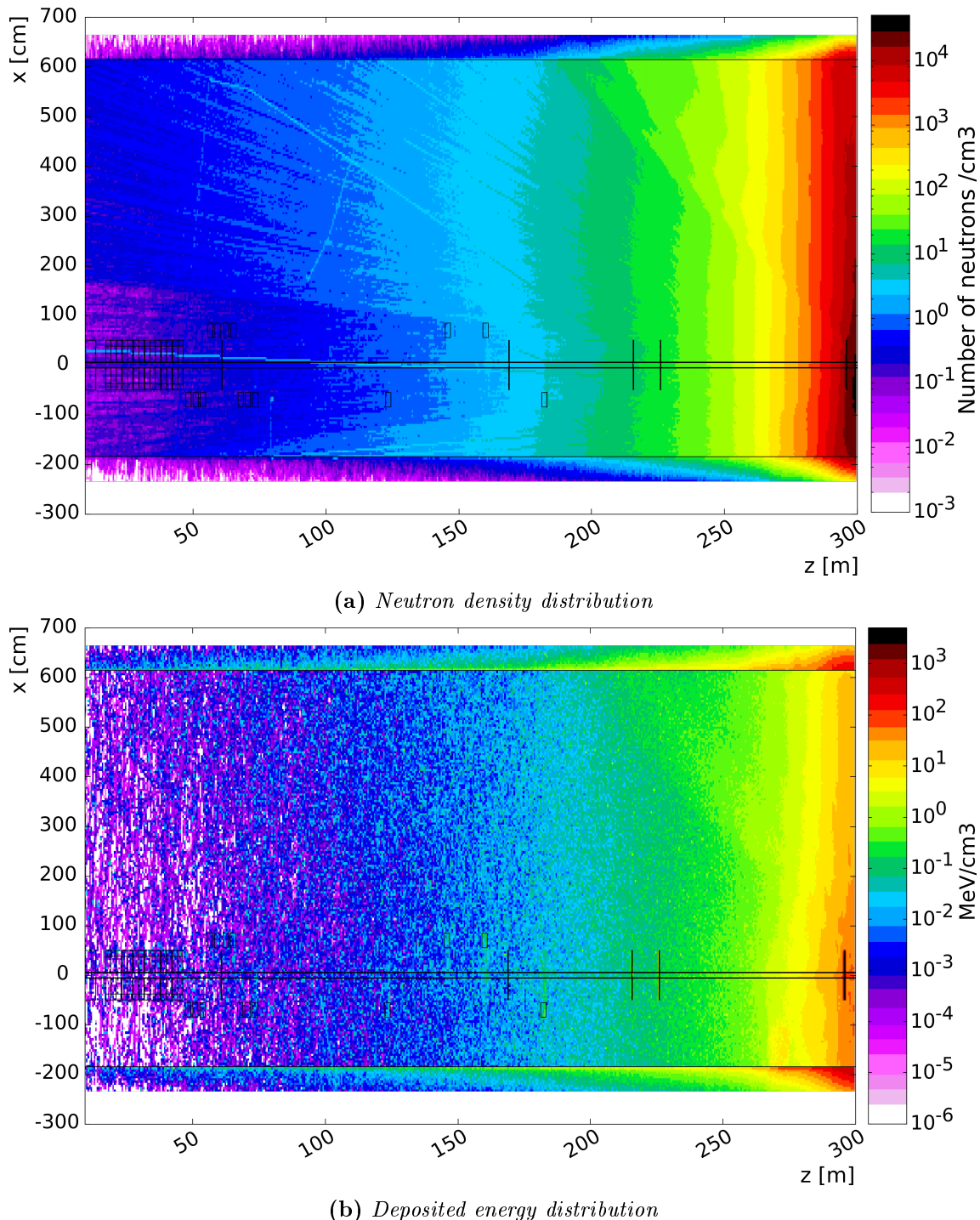


**Figure 8.15.:** Figure (a) shows the spatial distribution of the neutrons in the ILC extraction line tunnel simulated with FLUKA. The color scale shows the number of neutrons per unit area, normalized to the rate resulting from one ILC beam bunch dumped in the water vessel.

Figure (b) shows the spatial distribution of the deposited energy in the ILC extraction line tunnel simulated with FLUKA. The color scale shows the deposited energy in MeV per unit area, normalized to the results from one ILC beam bunch dumped in the water vessel.

The tunnel stretches from 9.3 m from the IP to 300 m, where the entrance to the beam dump hall is located. It has a width of 8 m.

The design and locations of the beam line components are taken from the most recent ILC lattice drafts [124, 125]. The magnets are simulated without their respective magnetic field maps, since the neutron tracks are not affected by magnetic fields. The neutrons, which reach the extraction line past the beam dump shielding walls, are tracked through the extraction line geometry described above. The resulting neutron density in the tunnel is shown in Figure 8.15 (a) in a view of the xz-plane. Close to the beam dump hall, at around  $z = 300$  m, the neutron density reaches over  $10^4 \text{ cm}^{-3}$ . This density sinks to about  $1 \text{ cm}^{-3}$  close to the interaction region at  $z = 9.3$  m. The beam line components shield the neutron flux such that the neutron density between about  $-200$  cm and  $200$  cm in x is reduced to about  $0.1 \text{ cm}^{-3}$ .

The resulting deposited energy is shown in the xz-plane in Figure 8.15 (b). Due to the high density of neutrons close to the beam hall, the energy density here reaches up to  $10^2 - 10^3 \text{ MeV cm}^{-3}$ . Also according to the neutron density distribution, the deposited energy close to the interaction region drops to about  $0.1 - 1 \text{ keV cm}^{-3}$ .

Here, at  $z = 9.3$  m, another imaginary scoring plane is placed in the FLUKA simulation, to score the neutrons crossing the boundary between the extraction line and the interaction region. These neutrons can directly be used in a GEANT4 simulation of the SiD detector. The results are presented in Section 8.5.

## 8.5. SiD occupancy study of the beam dump neutrons

The scored neutron four-vectors at  $z = 9.3$  m of the extraction line tunnel are converted into stdhep format, and used as input to a full detector simulation of SiD. For one original ILC beam bunch, which was dumped in the main beam dump, approximately  $5.9 \times 10^6$  neutrons reach the end of the EXT tunnel. Of these neutrons, about  $1.67 \times 10^6$  enter the SiD detector and leave hits in the outer endcap layers. Their momentum distributions are shown in Figure 8.16. The momenta in x and y ( $P_x$  and  $P_y$ ) reach about 40 - 50 MeV. The distribution for  $P_y$  is symmetric around 0,  $P_x$  is however shifted to positive values. This is due to the geometry of the extraction line tunnel and the neutron spatial

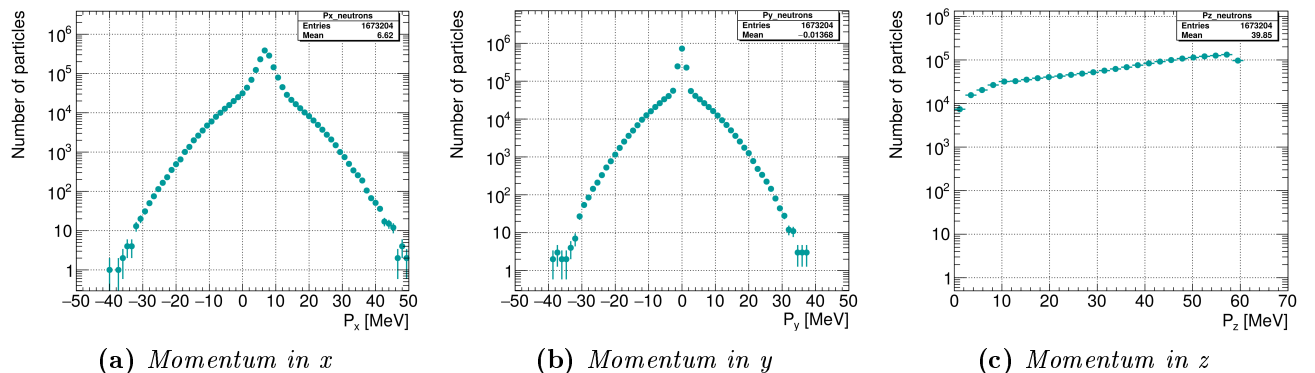


**Figure 8.16.:** Momentum distribution of neutrons in SiD, which originate from one extraction line side. The momentum distributions in x, y, and z are given in Figures (a), (b), and (c) respectively.

distribution at the exit of the tunnel. The neutrons originate in the beam dump hall around the beam pipe axis, i.e. around (0,0) in the xy-plane. Due to the shape of the extraction tunnel, neutrons with momenta directed in the negative x-direction are absorbed by the tunnel wall along the extraction line. Additionally, the extraction line components shield the neutron flux around the beam line axis, cutting away further neutrons that are pointed in the negative x-direction. Since the beam line axis is vertically in the center of the tunnel, which reaches from  $-2\text{ m}$  to  $2\text{ m}$ , the y-distribution of the neutron momenta is symmetrical around 0 MeV.

The  $P_z$  distribution reaches from 0 to 60 MeV, with more particles at higher energies. The low  $P_z$  neutrons have missed the detector or have been absorbed in the non-active calorimeter layers and the Pacman shielding (see Section 4.4.1).

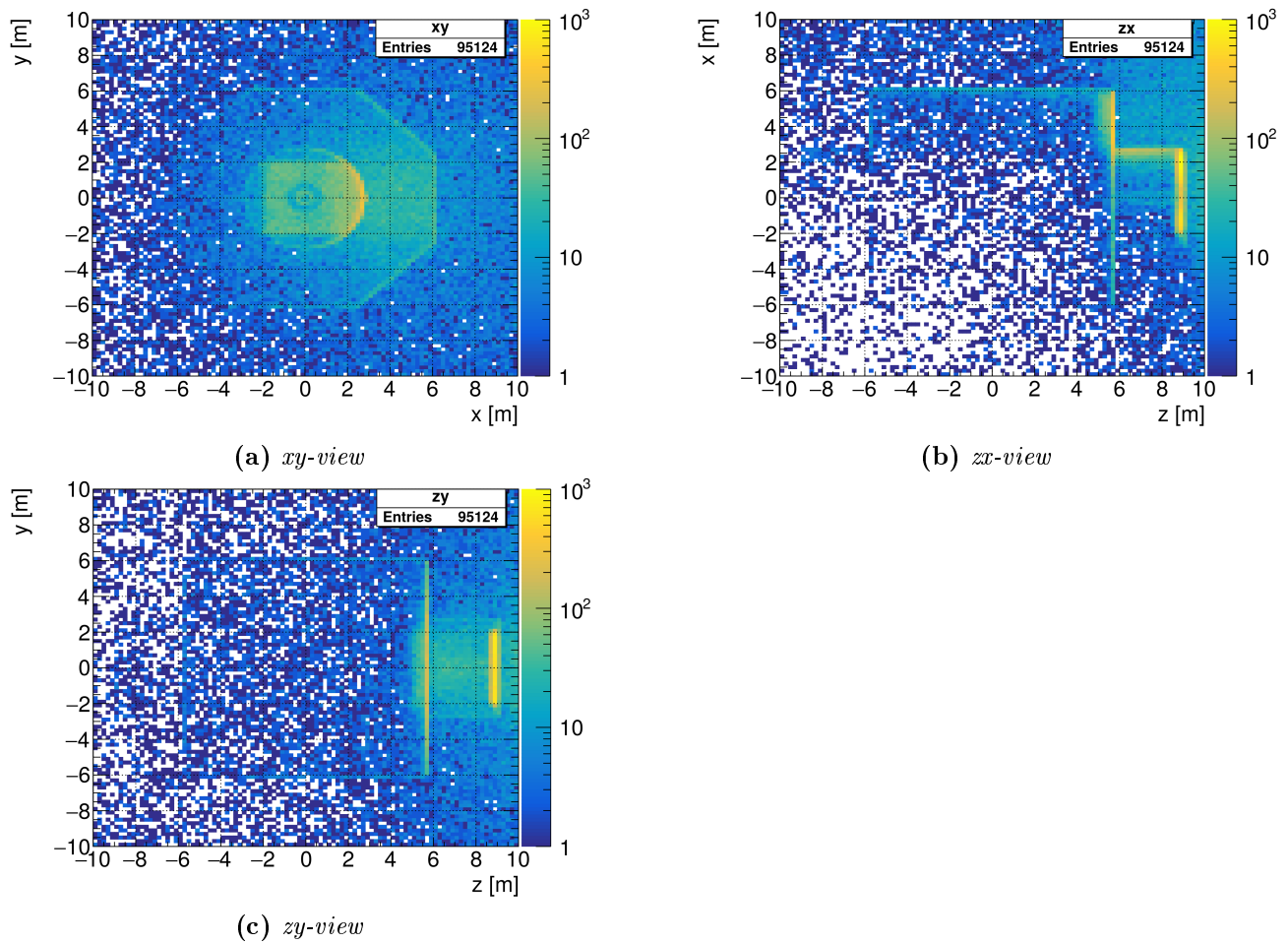


**Figure 8.17.:** Maps of the positions in the simulated geometry model, where the beam dump neutrons that have not left any hits in SiD have been absorbed. The views of the xy-plane, zx-plane, and zy-plane are given in Figures (a), (b), and (c) respectively. The color scale shows the number of neutron endpoint positions per  $20\text{ cm} \times 20\text{ cm}$ .

Figure 8.17 shows the positions in the xy-, zx-, and zy-plane, where neutrons that have not left hits in the SiD detector have been absorbed. The Pacman shielding, which is located behind the endcaps of the SiD muon system (stretching in z from about 5.8 m to 9.2 m from the IP), is clearly visible in all three Figures 8.17 (a), (b), and (c). Here, up to  $10^3$  neutrons per unit area are absorbed in the boronated concrete of the Pacman shielding. But also in the outermost non-active layers of the SiD muon system a significant amount of neutrons are stopped.

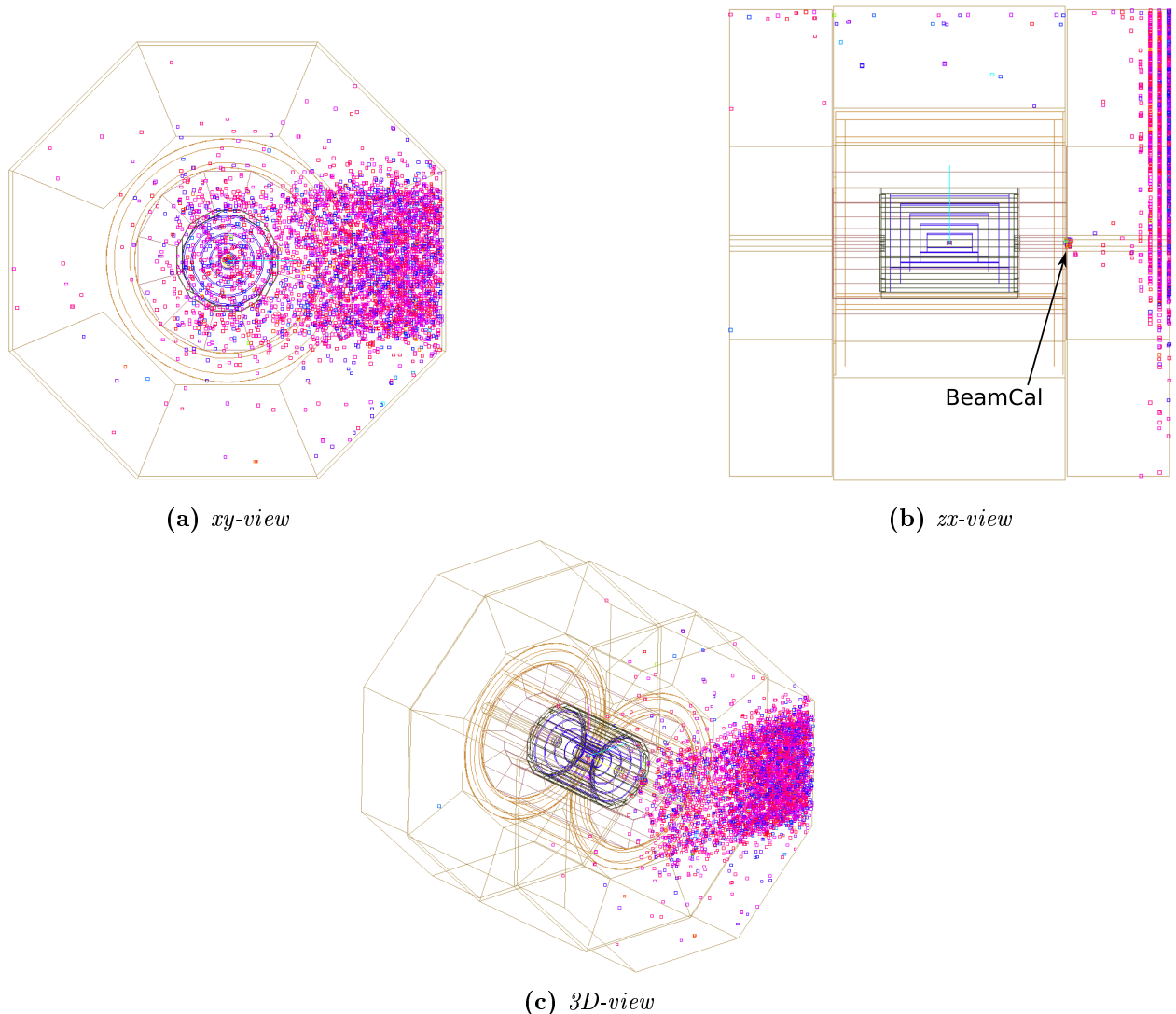


**Figure 8.18.:** Event displays created with WIRED4 of the SiD hits from ILC beam dump neutrons. The views of the xy-plane, zx-plane, and a 3D-view are given in Figures (a), (b), and (c) respectively.

The spatial distributions of the neutrons, which hit the active layers of the SiD detector, are best seen in an event display of the SiD detector. Figure 8.18 shows the WIRED4 event displays in various views. The hits are mainly restricted to the outer layers of the muon system. Their spatial distribution is determined by the shape of the extraction line tunnel. In Figure 8.18 (b), hits in the SiD BeamCal are also visible.

From one ILC bunch dumped in the main beam dump, the number of hits in the SiD subdetectors from the resulting neutrons from one of the extraction line tunnels are given in a bar chart in Figure 8.19. As already expected from the event displays in Figure 8.18, the SiD muon endcaps get the most hits with about  $1.5 \times 10^4$ . About two orders of magnitude fewer hits are counted in the muon barrel and the BeamCal. Also the LumiCal subdetector is hit about 20 times by neutrons from one beam dump. All other inner SiD subdetectors are shielded by the outer subdetectors and the Pacman shielding, and are not hit.

Figure 8.20 shows the time of the hits in the SiD muon system and the BeamCal with respect to the time of their creation, which is the time of the ILC beam being dumped in the main beam dump. Due to its high energy, the time of the beam arriving at the main beam dump can be approximated as the time of the bunch crossing. Using this approximation, the neutrons arrive at the SiD detector up to 100  $\mu$ s after the bunch crossing. Since every bunch is separated by 554 ns (see Section 4.4.1.3), the neutrons coincide with the next 180 ILC bunches.

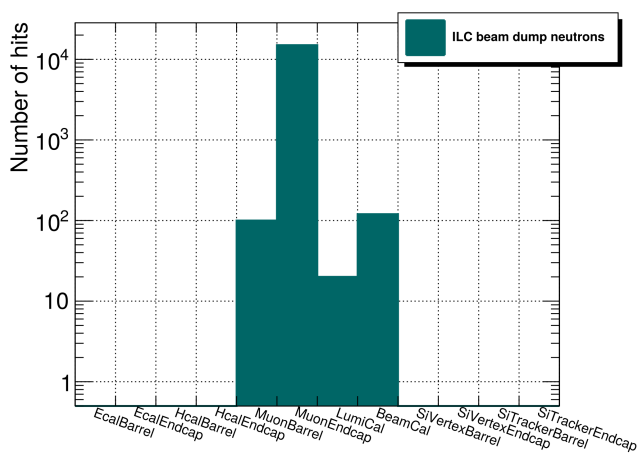


**Figure 8.19.:** Bar chart of the number of hits in the individual SiD subdetectors from neutrons coming from one ILC main beam dump, after a beam bunch has been dumped.

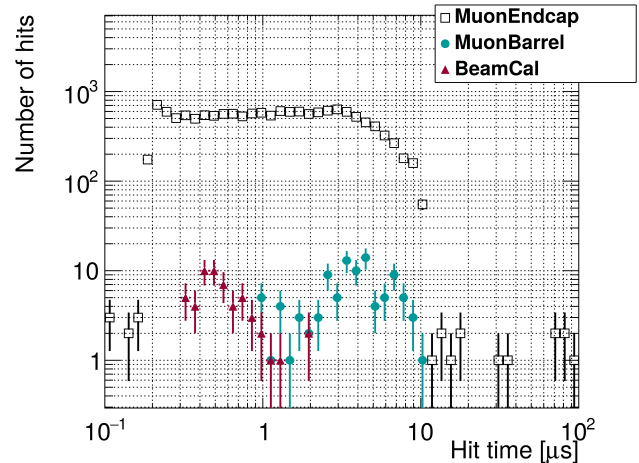


**Figure 8.20.:** Hit time distribution in the SiD subdetectors that are hit by neutrons coming from one ILC main beam dump, after a beam bunch has been dumped.

By counting the number of hits per cell in the BeamCal and the muon barrel and endcaps, the number of dead cells is calculated for the assumed buffer depths in the subdetectors. This was done in the same way as described in Sections 5.3.2 and 6.2.2. A cell is called “dead”, when all its buffers are filled and no further hits can be stored. Figure 8.21 shows the fraction of dead cells as a function of the assumed buffer depth in the SiD muon system and the SiD BeamCal. Since the muon endcaps collect the most neutron hits, the fraction of dead cells were calculated for up to a buffer depth of five. In the muon

barrel, however, all hit cells are hit only one time, because of which only the first bin is filled in this plot (Figure 8.21 (a)). Similarly for the BeamCal, the cells are hit up to two times.

Although these studies are done for neutrons from one ILC bunch only and the occupancy would rise for a bunch-train-worth of neutrons accordingly, the actual number of hits in the scintillating active layers of the muon system would depend on the scintillator material, and the noise threshold of the readout silicon photomultipliers (SiPM).

Rather than increasing the detector occupancy, the neutron background will more importantly affect the subdetectors with respect to the radiation damage it causes. From the presented GEANT4 simulation, it was calculated that the neutron flux for the outermost layer of the muon endcaps is about 530 neutrons  $\text{m}^{-2} \text{s}^{-1}$ . For the BeamCal, the flux is about 4 neutrons  $\text{cm}^{-2} \text{s}^{-1}$ . The expected neutron flux in the BeamCal from secondary photons, which excite giant nuclear dipole resonances [126] and hence cause the emission of neutrons, is considered to be  $5 \times 10^{13}$  neutrons  $\text{cm}^{-2} \text{yr}^{-1}$  [46, p. 134], which is about  $1.6 \times 10^6$  neutrons  $\text{cm}^{-2} \text{s}^{-1}$ . Due to this, the BeamCal will be designed to use radiation hard materials regardless of the additional neutron flux from the main beam dumps.

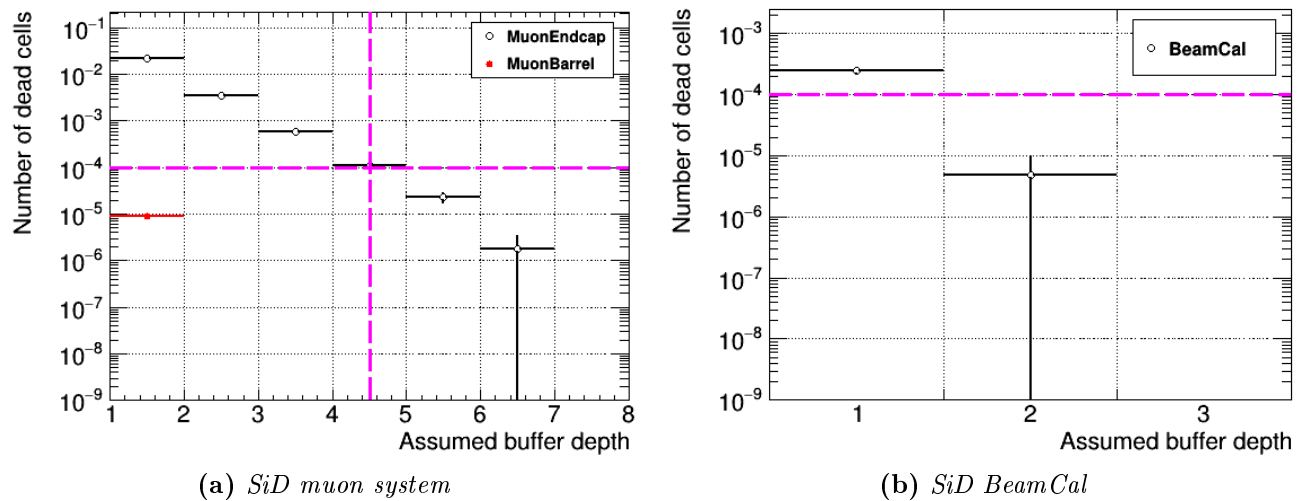


**Figure 8.21.:** Fraction of dead cells in the SiD muon barrel and muon endcap (Figure (a)) and in the SiD BeamCal (Figure (b)) in all layers combined, for neutrons originating from one ILC beam bunch being dumped. The fraction is calculated by computing the number of dead cells for a given buffer depth, and normalizing the numbers by the total number of cells in the respective subdetector.

The dashed lines indicate the buffer depth of four for the current sensor design, and the guideline of  $10^{-4}$  for a critical acceptance limit.

## 8.6. Alternative beam dump design

The current ILC main beam dump designs are based on a water vessel. The previous sections have shown that due to the high material density, the ILC beam bunches are stopped over a distance of about 12 m. This leads to a large energy dissipation in the beam dump and its surroundings. The resulting high dose rates from the irradiation limits the time the maintenance staff will be allowed to be in the proximity of the beam dumps. There are, however, other beam dump designs, which do not

lead to restricting dose rates of the dumps surroundings.

In the following paragraphs, results from a FLUKA study are presented concerning the effect of using a gaseous beam dump for the ILC beam. Such gas dumps have been studied before in the context of the TESLA accelerator [127, 128]. A vessel filled with noble gas requires a dump length of at least 1 km in order to dissipate and absorb the beam energy.

### 8.6.1. Deposited energy and irradiation dose

In the FLUKA model of this simple gaseous beam dump, a copper vessel with a length of 1 km and a diameter of 150 cm has been assumed. The vessel has a wall thickness of 55 cm, in order to act as shielding simultaneously, and is filled with nitrogen gas. Figure 8.22 shows the deposited energy and the resulting instantaneous dose equivalent from one ILC beam bunch, which has the same characteristics as before in Section 8.3. From the plots, it becomes apparent that the maximum deposited energy reaches  $10^8 \text{ GeV cm}^{-3}$  as well as in the water beam dumps before (see Section 8.3.1). This is, however, restricted to the back wall of the vessel. In the surroundings, no observable energy is deposited.

The maximum dose equivalent in the gaseous dump is smaller by over one order of magnitude compared to the results for the water vessels (see Section 8.3.2). Again, the dose is restricted to the gas vessel. In the direct surroundings, a dose equivalent level of about  $10^{-4} \text{ mSv cm}^{-3}$  is reached, which is a difference of two to three orders of magnitude compared to the water beam dump.

### 8.6.2. Neutron flux

In addition, a scoring plane has been added to the FLUKA model of the gaseous beam dump in a similar way and position as in Section 8.3.3. The aim was to score neutrons, which are created in the vessel and are oriented in the direction of the extraction line.

In this gas vessel design, however, there is no observable flux of neutrons that travel back towards the interaction region.

## 8.7. Conclusion and outlook

This chapter has presented several studies concerning the ILC main beam dumps. The two studied designs that were described in Section 8.2 are based on a 12 m long water vessel. Both vessel designs, which had been developed for the currently foreseen ILC main beam dumps, contain sophisticated vortex flow systems for dissipating the deposited energy of the beam bunches. Additional copper plates in the end of the vessels present enough radiation lengths to fully absorb the beam. The high material densities, however, have been identified with the presented FLUKA simulations of the dump designs (Section 8.3) to lead to high levels of deposited energy inside and outside of the beam dump. In the water but also in the vessel and shielding materials, radioactive nuclei are produced, which activate the water and the surroundings. Activation studies in Section 8.3.2 have shown that the resulting dose rates after one year of cooling time still reach up to  $10 \text{ mSv s}^{-1}$ , which represents a large risk for maintenance personnel and demands a restriction of their duration of stay.

Furthermore, particle fluxes have been studied in Section 8.3.3, especially the neutron flux that originates in the water vessel and reaches back towards the extraction line. Section 8.4 presented a second FLUKA simulation of the neutrons traveling through the extraction line towards the interaction region, which yielded the four-vectors of the  $5.9 \times 10^6$  neutrons arriving at the SiD detector.

In a full GEANT4 detector simulation, the hits of the neutrons in the SiD subdetectors have been

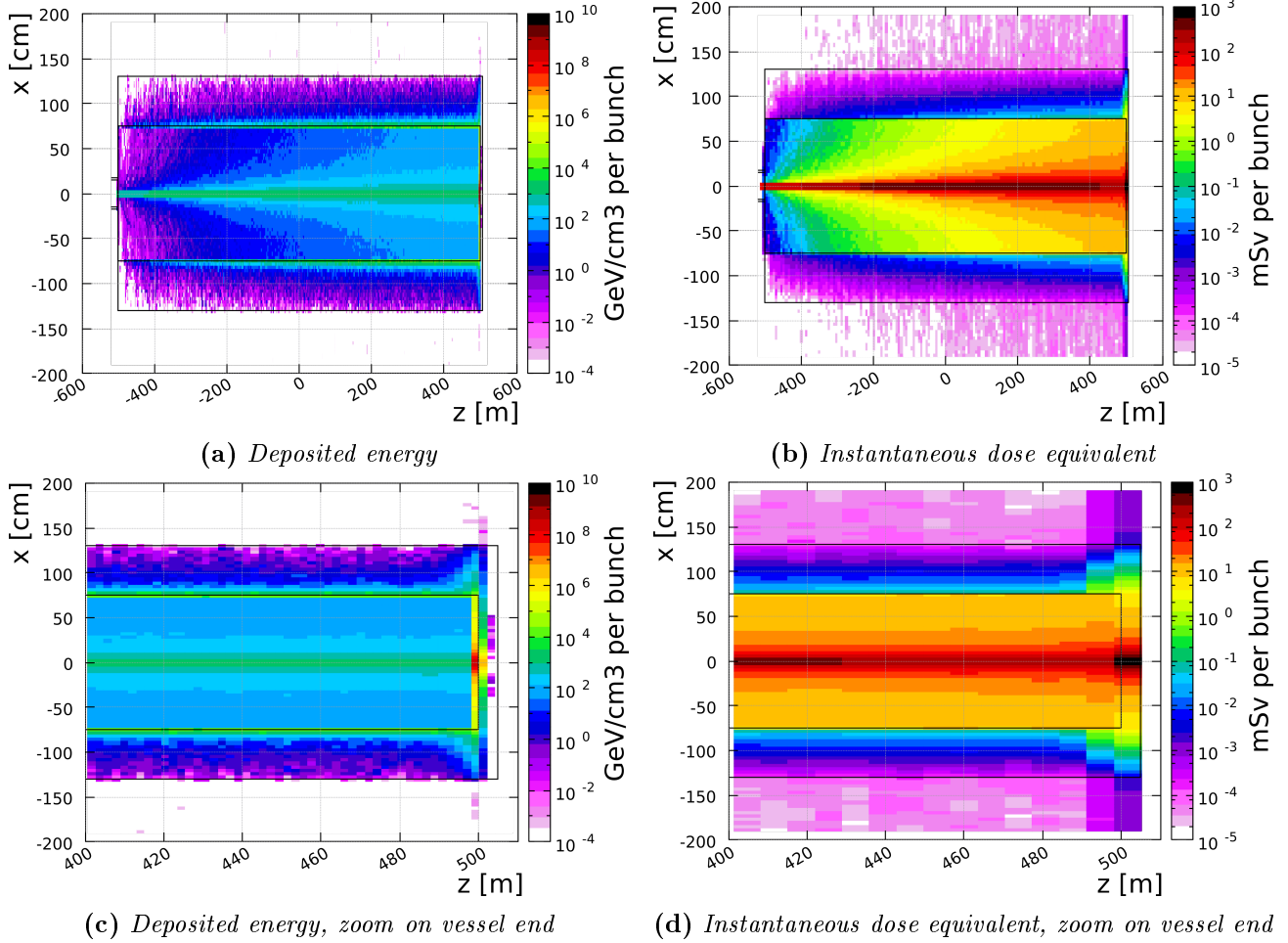


**Figure 8.22.:** FLUKA simulation results of a gaseous beam dump vessel.

Figures (a) and (c) show the deposited energy per ILC bunch in the  $xz$ -plane. The color scale indicates the energy in  $\text{GeV}/\text{cm}^3$ .

Figures (b) and (d) show the resulting dose equivalent in the  $xz$ -plane. The color scale indicates the dose equivalent in  $\text{mSv}/\text{cm}^3$ .

counted, and the arising occupancy has been shown (Section 8.5). Due to the neutron momenta and their spatial distribution, the hits are contained within the outermost layers of the SiD muon system and the BeamCal.

The results of the activation study but also of the neutron background study suggest to consider a different approach for the ILC main beam dumps. In an additional FLUKA simulation explained in Section 8.6, a model of a gaseous beam dump has been studied with respect to the deposited energy, the dose equivalent, and the arising neutron flux. In all three matters, the gaseous beam dump design yields results that are several orders of magnitude better than the water dump designs. The beam energy is dissipated throughout the length of the gas dump, and is then fully absorbed at the end of the 1 km long vessel. This leads to a spatial restriction of the irradiation to the gas volume and the vessel back wall. In addition, no measurable neutron flux at the entrance to the beam dump hall was observed in the FLUKA simulation.

Overall, a gaseous dump seems to be more suitable with respect to the irradiation and the radiation safety. Due to the required length of the vessel, in order to fully dissipate and absorb the beam power, the cost for the necessary tunnel is a clear disadvantage of this approach. For calculating the construction cost of the ILC main linac tunnel, an estimation of 22 000€ per one meter of tunnel length has been used [129]. Using this estimation, the cost for the two required gaseous beam dump tunnels (each is 1 km long) would be in total 44 million€. Due to the ILC cost constraints, a gaseous beam dump has not been considered as an option for the ILC. The clear advantages, however, are not to be neglected. Even if the gaseous beam dumps are a large cost addition, they would save the expenses of costly radiation safety measures for the water dump surroundings, such as the remote handling systems which have been mentioned above.



# 9

## Chapter 9.

# Results: prospects, requirements, and limits for the International Linear Collider

Detailed studies of different background sources for the International Linear Collider have been presented in Chapters 5 - 8. They cover the  $e^+e^-$  pair background from beam-beam interactions, the machine background from the interaction of the beam with the beam line components, and the neutron background from the ILC main beam dumps.

All of these background sources have been examined in extensive simulation studies using various physics event generators and Monte Carlo simulation tools, such as GuineaPig (for Chapter 5), MCARLO (for Chapter 6), BDSIM (for Chapter 7), and FLUKA (for Chapter 8). The impact on the SiD detector from the background particles was then simulated in the GEANT4 based simulation tool SLIC, using the SiD simulation infrastructure. Additionally, the functionality of a vertical beam halo collimator has been tested through measurements of the machine backgrounds at the Accelerator Test Facility 2.

Overall, a broad range of background sources has been studied, which has brought insights of the impact of the accelerator design on the background. The full detector simulations have then shown the effect of the background particles on the SiD detector performance. The following sections will briefly recap and contextualize the results of the previous chapters.

## 9.1. Keeping the detector background below the critical acceptance limit

Achieving the ILC goal of measuring particle properties and their interactions with unprecedented precision relies on the detectors being able to exploit their state-of-the-art technologies. This in turn depends on clean environments for the detectors. A balance has to be found between accelerator design and detector design optimizations, in order to minimize the detector background. The SiD guideline for an acceptable background limit is that no more than  $10^{-4}$  of all cells in the individual subdetectors shall be filled up with background hits above the buffer depth of the sensors. Any cell that reaches its buffer depth is declared a “dead” cell, as it can no longer record new hits until the buffers are read out. This guideline was used throughout the chapters in order to make recommendations on acceptable background levels from the respective background sources, based on the detailed simulation studies that have been done for this thesis.

## 9.2. Impact of the ILC running scheme on the background level

As Chapter 5 has shown, the pair background is dependent on certain factors, such as the ILC center-of-mass energy, the number of bunches per train, and the beam parameters themselves. These dependencies result in requirements and limits that can be formulated for the International Linear Collider. The pair background studies done for the newly proposed beam parameters for the ILC250 stage showed the effect of changes in the parameter sets on the pair background envelopes and the arising occupancy in SiD. Three new sets ((A), (B), and (C)) had been suggested, for which the horizontal beam emittance is reduced by a factor of two in comparison to the original baseline parameter set. For sets (B) and (C), the beta function values had additionally been changed (as shown in Table 5.1). In the SiD vertex detector, for which a minimal background level is crucial, the pair background occupancy for sets (B) and (C) exceeded the critical acceptance limit in the various vertex detector layers by up to a factor of two. In the innermost vertex detector barrel layer, set (A) exceeds this limit as well, but only by approximately 10 %. In all other layers and SiD subdetectors, the occupancy for set (A) stays below the critical limit. The full set of occupancy results can be found in Table 5.2. The results of this study have already been input to the ILC design decision made for the Change Request CR-0016. Set (A) has been chosen for the new official parameter set of the ILC250 stage.

When upgrading the ILC to later stages, such as the ILC500 and the ILC500 “LumiUp”, the pair background occupancy rises, pushing the fraction of dead cells in the SiD vertex detector above the critical limit by up to 240 %, as shown in Table 5.3.

Regarding the machine background, the ILC center-of-mass energy, as well as the beam intensity and the beam pipe vacuum pressure have been found to affect the machine background level directly. The specific effects are described below, together with suggestions on accelerator design optimizations.

**Possible accelerator design optimizations to constrain the background levels** As mentioned above, design choices regarding the beam parameters affect the beam induced backgrounds. Studying the effects on the pair background occupancies in SiD allowed to make recommendations on the design decision, such as selecting the ILC250 beam parameter set (A) as the new official parameter scheme for the first ILC stage.

The machine background is dependent on the ILC accelerator conditions as well, as has been shown in Chapters 6 and 7. The number of muons from the Beam Delivery System rises by a factor of three when upgrading the ILC from a center-of-mass energy of 250 GeV to 500 GeV, as has been shown in Chapter 6. For both shielding options under discussion, the fraction of dead cells for a buffer depth of four is reduced to below  $2 \times 10^{-8}$  of all cells in the SiD tracker. In all other subdetectors, the occupancies are negligible. Although the minimal shielding option for the muons was found to be sufficient for limiting the SiD detector occupancy, the additional shielding wall serves as a tertiary containment device, which is required due to radiation safety regulations.

The measurements of the machine background at the Accelerator Test Facility 2 (ATF2), presented in Chapter 7, have shown that the machine background is linearly dependent on the beam intensity and the beam pipe vacuum pressure. The vertical beam halo collimator, which has been tested at ATF2 regarding its functionality, has proven itself to reduce the background level at the interaction point regardless of the beam intensity or vacuum pressure conditions. The measurements taken in the proximity of the collimator showed a background reduction of up to about 50 %, when closing the collimator.

Chapter 8 discussed the current ILC main beam dump designs. Since they are based on a water vessel, the beam power can be sufficiently absorbed over a short length. This, however, implies that

the beam energy has to be dissipated effectively with the help of high-pressure water flow vortices. Locations of high material densities lead to a high concentration of deposited energy, and to high dose rates due to the irradiation of the water and the surrounding materials. Even after one month of beam time and then a cooling period of one year, the dose rate in the proximity of the beam dump reaches about  $10 \text{ mSv s}^{-1}$  for one of the two proposed dump designs, which tightly restricts the duration of stay for the maintenance personnel. The maintenance personnel would only be allowed to work in the proximity of the beam dump vessel for up to about 30 minutes before the yearly legal dose limit is reached. Additionally, the beam dumps represent another source of background for the detectors at the interaction region. Neutrons from photonuclear interactions between the secondary particles of the developing particle showers and the water molecules can be found at every solid angle, and hence also in the backward direction towards the IP. A simulation of the neutrons traveling back through the extraction line tunnel revealed that about  $5.9 \times 10^6$  neutrons arrive at the interaction region. The hits of the neutrons that reach to the SiD detector are restricted to the outermost layers of the muon system and the BeamCal.

A proposed solution to both of these issues is to use a gaseous beam dump instead of a water beam dump, which would decrease the expected dose by 2-3 orders of magnitude. The gaseous dumps do not create a neutron background for the detectors. The clear disadvantage of these dumps is, however, their sheer length required for fully dissipating the ILC beam power. For two 1 km long dump vessels, the construction cost for the dump tunnels was roughly estimated to be about 44 million €. The ILC cost constraint needs to be weighed up against the expenses that would be saved for the high radiation safety measures needed for the water dump designs.

## **9.3. Impact of the SiD design on the background level**

When all possible optimizations of the accelerator design have been made, the detectors have to consider the background levels in their geometric design as well as in their readout architecture. Chapter 5 compared different SiD geometry variants with respect to their impact on the detector occupancy from the pair background, and discusses the effect of applying time gates. The detectors can therefore influence the background levels themselves through various means.

**Possible SiD design optimizations to constrain the background levels** The detector specific anti-DiD field, for example, sweeps the pair background particles through the outgoing beam pipe, and therefore reduces the number of pairs hitting the SiD BeamCal. This in turn also reduces the overall pair background occupancy in the inner subdetectors by up to 30 %, as described in Figure 5.12.

In addition, the detectors have their own shielding device, Pacman, which is installed on the outside of the muon system. The detector simulation of the beam dump neutrons arriving at the SiD detector, which has been discussed in Chapter 8, has proven that Pacman shields the incoming neutrons from hitting the inner subdetectors effectively. A proposal made in Chapter 6 suggests to magnetize Pacman in order to effectively shield also the muons coming from the Beam Delivery System.

Studies of the timing of the individual background sources have shown that time gates can reduce the detector occupancy significantly. In Chapter 5, the direct effect of applying a time gate to the SiD vertex detector has been discussed. The number of hits from the pair background can be reduced by 12 %, when rejecting all hits later than 10 ns after the bunch crossing. This leads to a decrease in the vertex barrel occupancy such that the occupancy for a buffer depth of four is below the critical acceptance limit for the ILC stages at 250 GeV and 500 GeV. Even when upgrading the ILC to the

ILC500 “LumiUp” stage, the occupancy is only 150 % of the critical occupancy (compared to 240 % without time gates). Already increasing the buffer depth by two would bring the occupancy below the critical limit in this ILC stage as well. This would have the effect that the detector performance in all SiD subdetectors will be comparable throughout all studied ILC stages.

Apart from that, also the hit time distribution of the muons from the Beam Delivery System show distinct ranges for the individual SiD subdetectors, as shown in Chapter 6.

With a complete study encompassing all background sources, individual time gates could be applied to the different SiD subdetectors in order to effectively attenuate the background occupancy. All in all, the detectors have the potential to optimize their designs with respect to reducing the background levels further.

# 10

---

## Chapter 10. Conclusion

The International Linear Collider will be a linear  $e^+e^-$  collider at the precision frontier, and therefore complementary to the LHC. The physics goals of the different ILC stages include measurements of the properties and the interactions of the Higgs boson and the top quark, as well as dark matter and BSM searches. The aim for these measurements is to have unprecedented precisions. Examples have been given in Section 4.1, showing order of magnitude increases in precision at the ILC in comparison to the LHC. In order to achieve such levels of precision, a balance has to be found between accelerator design and detector design optimizations with respect to minimizing the detector background.

This thesis has motivated the need for detailed background studies for the ILC. To this end, Chapter 5 describes the beam induced  $e^+e^-$  pair background and its dependencies on ILC running schemes. Looking at different beam parameter sets and ILC stages, the pair background was found to be a significant background source, which needs to be confined by both ILC and detector optimizations. Failing to do so would mean that the pair background occupancy would negatively affect the performance of the vertex detector and the aimed-for precision measurements.

In extensive simulations, further background sources have been studied as well. Proposed shielding options to prevent the muon machine background from the Beam Delivery System from reaching the detectors are discussed in Chapter 6. Although even the minimal shielding option shields the muons successfully from the detectors, the additional shielding wall serves as a tertiary containment device, which is required due to radiation safety regulations.

Direct measurements of machine background levels at the Accelerator Test Facility 2 have been taken for different machine conditions, in order to validate the functionality of a beam halo collimator for the ILC. This has been done successfully, and all details on the measurements and according Monte Carlo simulation studies are presented in Chapter 7.

Finally, Chapter 8 analyzes the ILC main beam dumps, which are based on water vessels. Dumping the ILC beam causes a high radiation dose of the surroundings, restricting the duration of stay severely for the maintenance personnel. Additionally, it creates neutrons traveling back to the interaction region, affecting the outer subdetectors of the detector experiments with respect to the detector occupancy and causing radiation damage. As an alternative approach, gaseous beam dumps have been suggested, which show results that are orders of magnitude better.

In the process of these analyses, the impact on the SiD detector has been investigated. By applying the SiD guideline for an acceptable background limit, the occupancies in the detector have been studied, and recommendations have been made accordingly with respect to limiting the background levels below the critical acceptance limit. These recommendations have also been tested and have been found to

be successful. The results of the presented studies and the given recommendations are summarized in Chapter 9. They are a valuable input to design decisions, and design changes based on the given recommendations to both the ILC and SiD have already been made or are currently under consideration.

Although all of the presented studies are done for the SiD detector only, the generated simulation data have been made available to the ILC community. With a detailed understanding of the various background sources, the detector background levels can be reduced even further due to refined optimizations of the accelerator and the detectors. This will enable the ILC and its experiments to achieve their goals of unprecedented precision measurements.

# A Appendix A.

## Pair background

This appendix gives additional details on the simulation study of the pair background induced by beam-beam interactions, described in Chapter 5.

### A.1. GuineaPig event generation

The parameters used as input for GuineaPig are given in this section. For detailed explanations of the GuineaPig parameters, refer to the GuineaPig manual [130].

The parameters are provided in a file called “acc.dat”. Its content must have a certain format, for which an example showing the nominal parameters used for the ILC500 stage is following:

```
$ACCELERATOR:: ILC-500GeV
{energy=250.0; particles=2.0; beta_x=11.0; beta_y=0.48;
emitt_x=10.0; emitt_y=0.035; sigma_z=300.0; f_rep=5.0; n_b=1312;
charge_sign=-1; scale_step=1.0; waist_y=250;
espread.1=0.00124; espread.2=0.0007; which_espread=3;}
$PARAMETERS:: par_pairs
{n_z=12; n_t=6; n_m=80000; cut_z=3.5*sigma_z.1; n_x=256; n_y=256;
cut_x=4*sigma_x.1; cut_y=4*sigma_y.1; pair_ecut=1e-3; pair_q2=2;
beam_size=1; grids=7; store_beam=1; do_pairs=1; track_pairs=1;
store_pairs=1; do_photons=1; store_photons=1; do_hadrons=1;
do_jets=1; do_coherent=1; electron_ratio=1; photon_ratio=1;
do_eloss=1; do_espread=1; rndm_seed=1; rndm_load=0; rndm_save=0;}
```

For the ILC250 stage, the parameters are exchanged with according the beam parameter values taken from Table 4.1.

## A.2. SiD occupancy for the ILC250 parameter sets

### A.2.1. Pair background occupancy in the SiD vertex detector

Figures A.1 and A.2 show the pair background occupancy in the individual layers of the SiD vertex detector barrel and endcaps respectively. The full study is explained in Section 5.3.

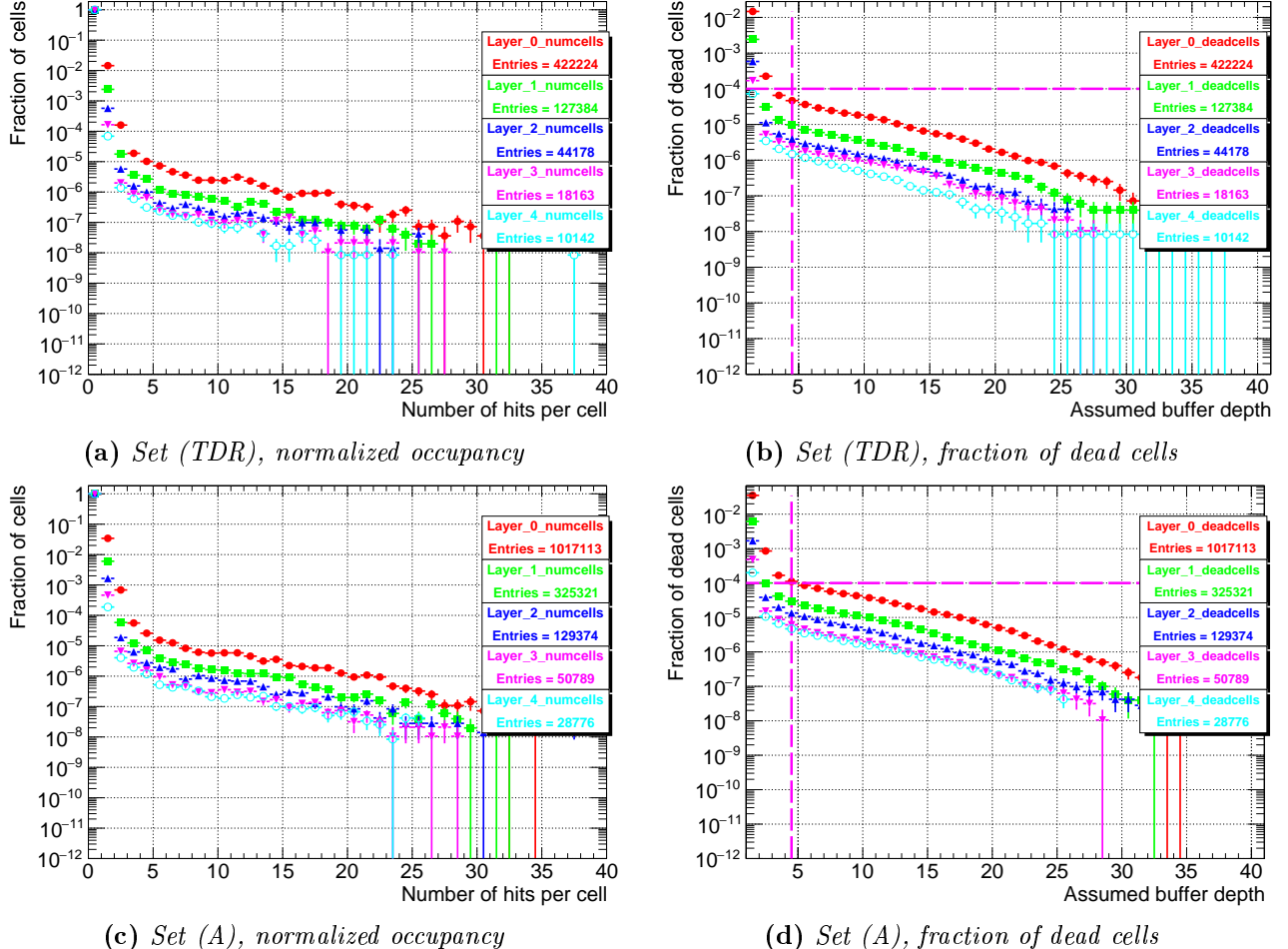


**Figure A.1.:** *ILC250 pair background occupancy in all SiD vertex detector barrel layers, after a full bunch train (1312 bunch crossings). The left hand figures show the occupancy in the individual vertex detector layer, normalized by the total number of cells of the corresponding layer. The right hand figures show the fraction of the dead cells in the individual vertex detector layer, with respect to the total number of cells. The dashed lines indicate the the buffer depth of four for the current sensor design, and the guideline of  $10^{-4}$  for a critical acceptance limit.*

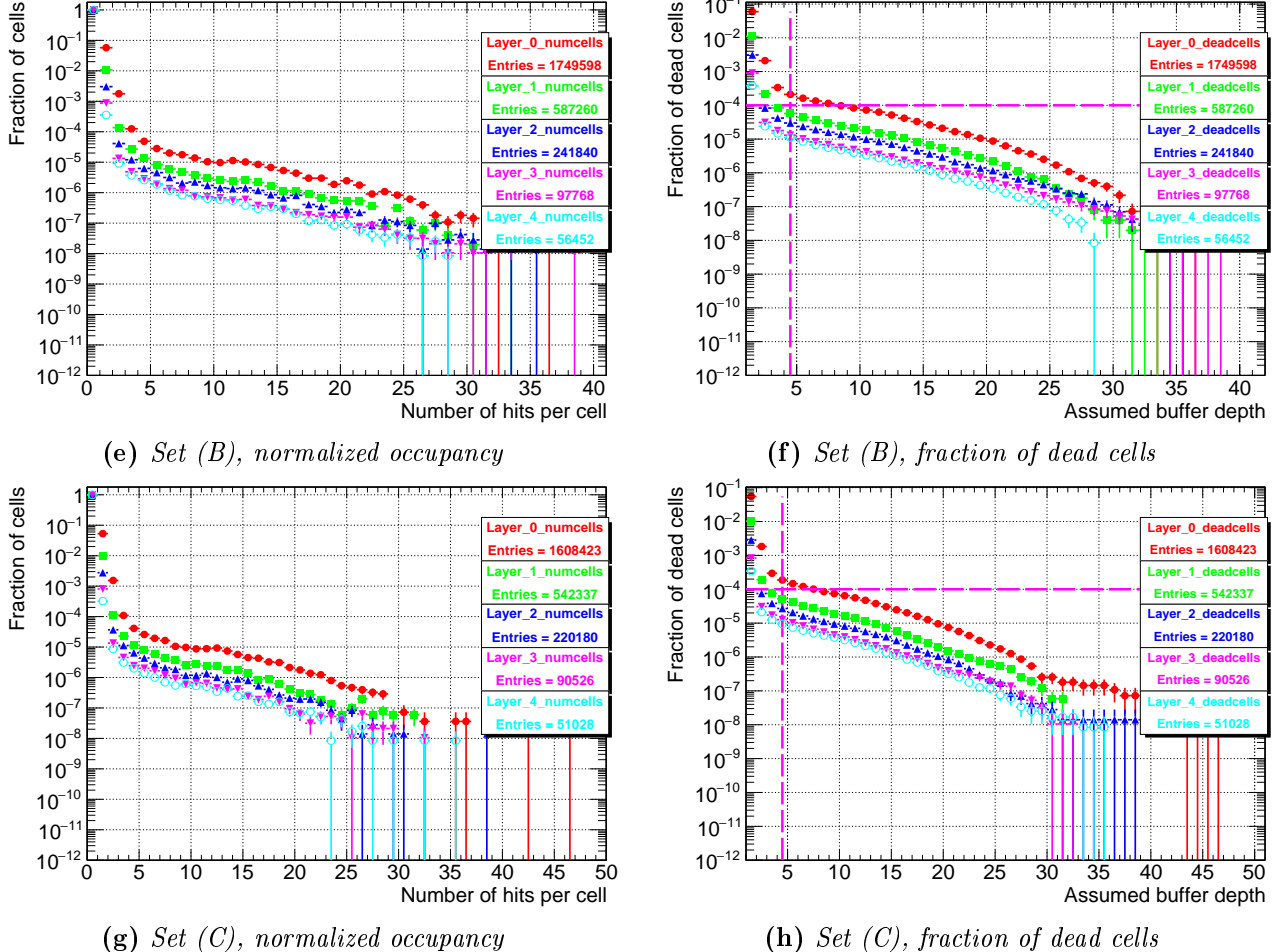


**Figure A.1.:** ILC250 pair background occupancy in all SiD vertex detector barrel layers, after a full bunch train (1312 bunch crossings). The left hand figures show the occupancy in the individual vertex detector layer, normalized by the total number of cells of the corresponding layer. The right hand figures show the fraction of the dead cells in the individual vertex detector layer, with respect to the total number of cells. The dashed lines indicate the the buffer depth of four for the current sensor design, and the guideline of  $10^{-4}$  for a critical acceptance limit.

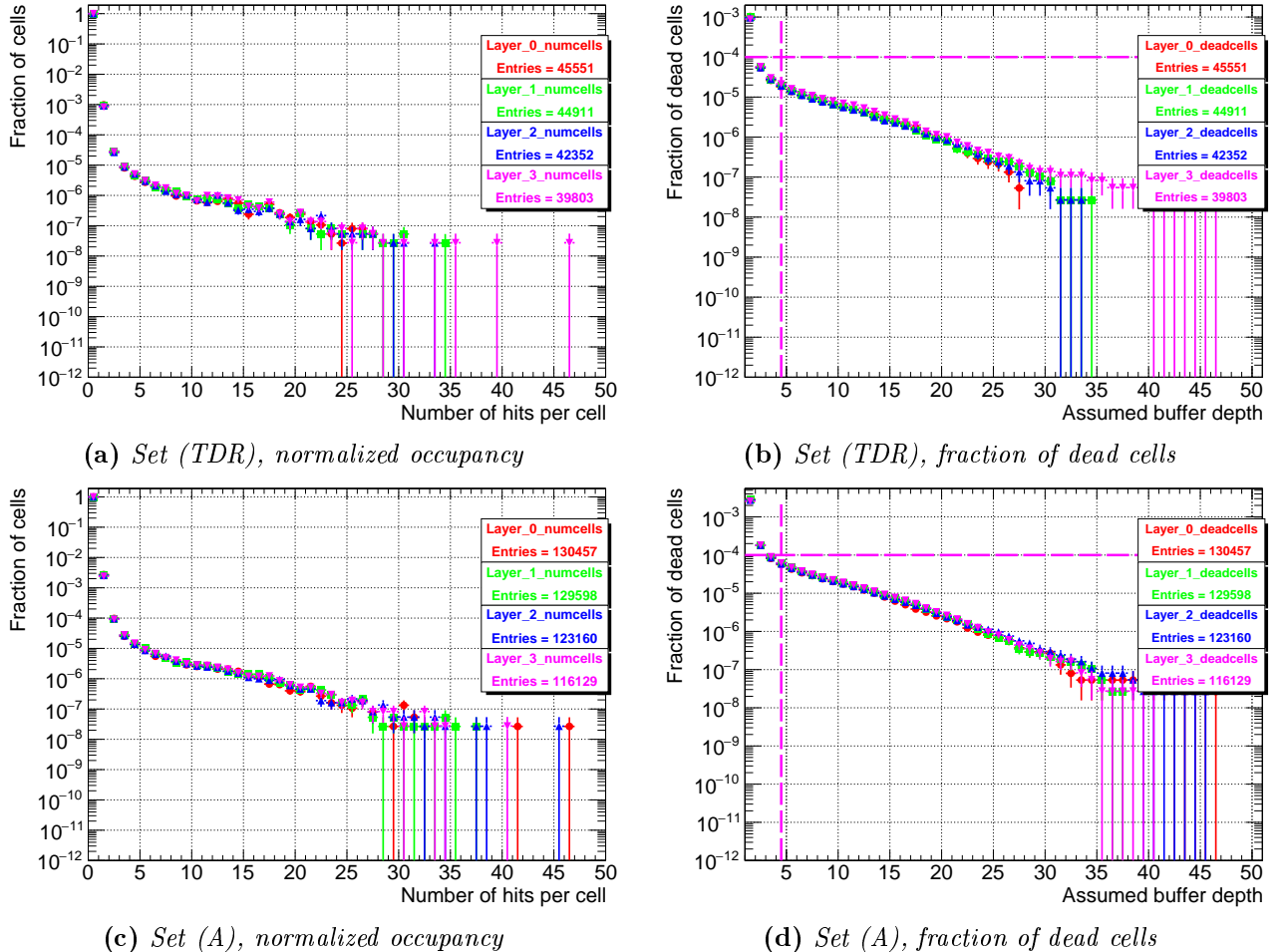


**Figure A.2.:** ILC250 pair background occupancy in all SiD vertex detector endcap layers, after a full bunch train (1312 bunch crossings). The left hand figures show the occupancy in the individual vertex detector layer, normalized by the total number of cells of the corresponding layer. The right hand figures show the fraction of the dead cells in the individual vertex detector layer, with respect to the total number of cells. The dashed lines indicate the the buffer depth of four for the current sensor design, and the guideline of  $10^{-4}$  for a critical acceptance limit.

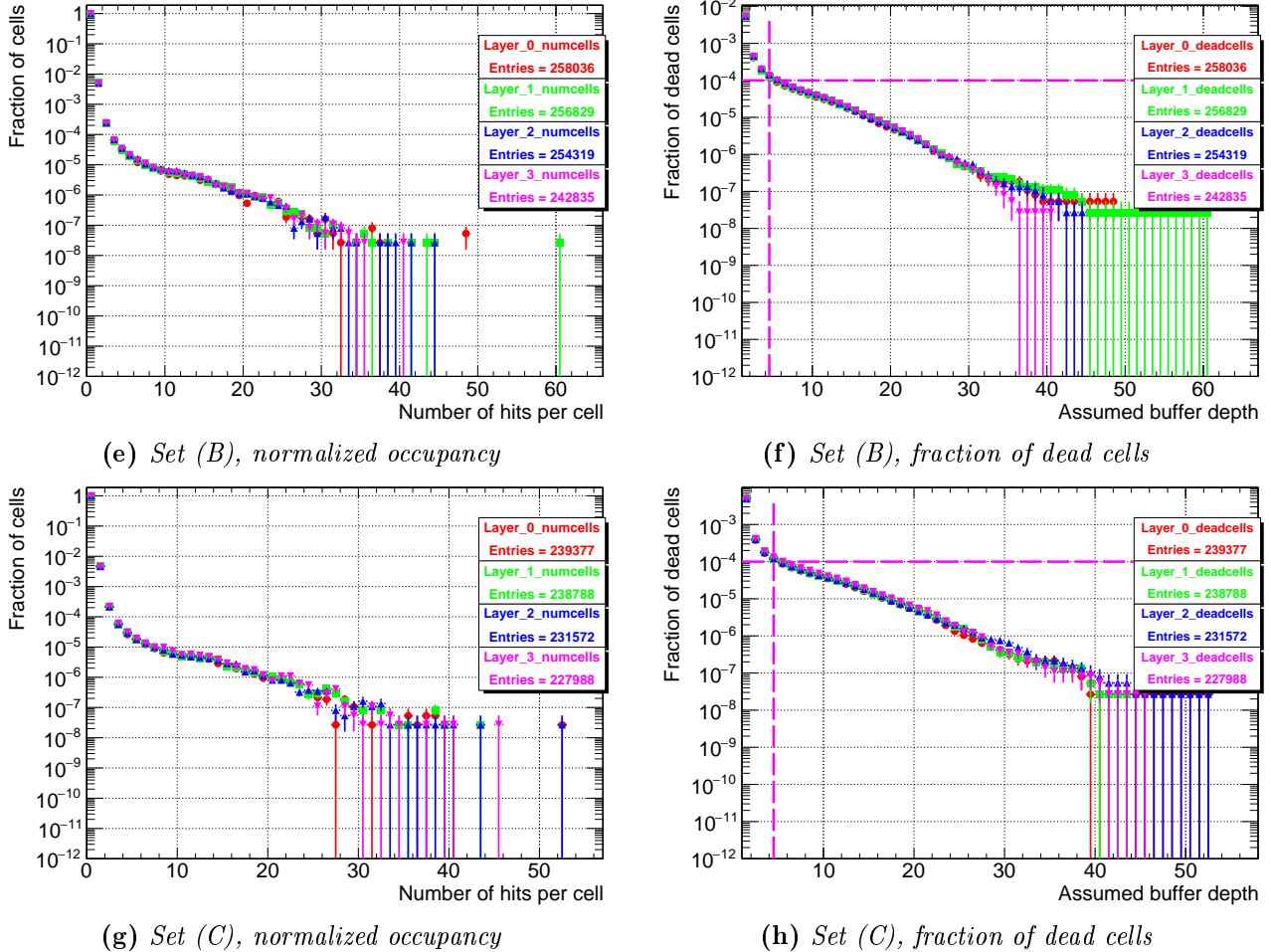


**Figure A.2.:** ILC250 pair background occupancy in all SiD vertex detector endcap layers, after a full bunch train (1312 bunch crossings). The left hand figures show the occupancy in the individual vertex detector layer, normalized by the total number of cells of the corresponding layer. The right hand figures show the fraction of the dead cells in the individual vertex detector layer, with respect to the total number of cells. The dashed lines indicate the the buffer depth of four for the current sensor design, and the guideline of  $10^{-4}$  for a critical acceptance limit.

### A.2.2. Pair background occupancy in further SiD subdetectors

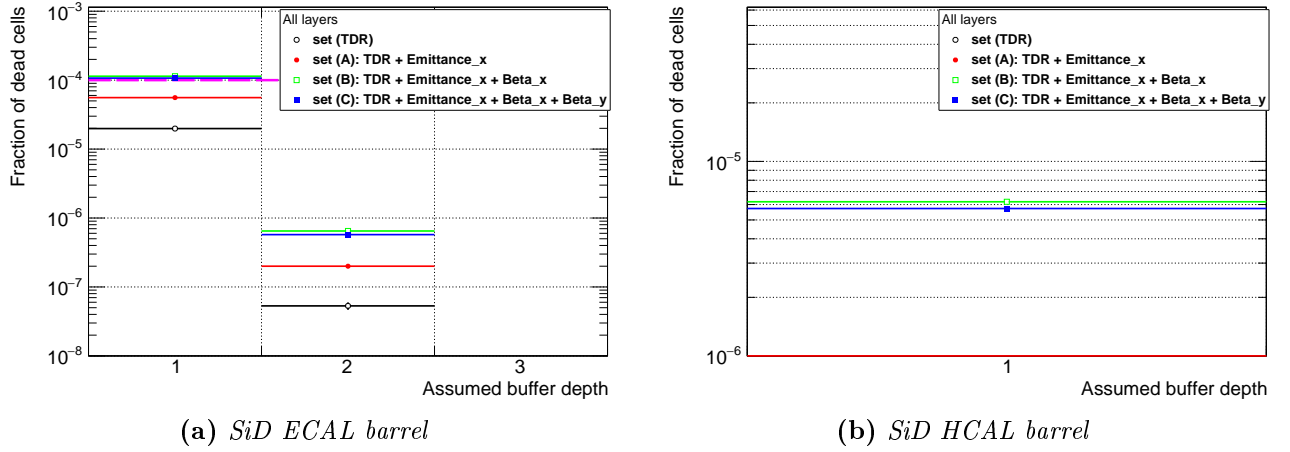


**Figure A.3.:** *ILC250 pair background occupancy in the SiD calorimeter barrels after a full bunch train (1312 bunch crossings). The figures show the fraction of the dead cells in the individual subdetectors for all layers combined, with respect to the total number of cells in this subdetector.*

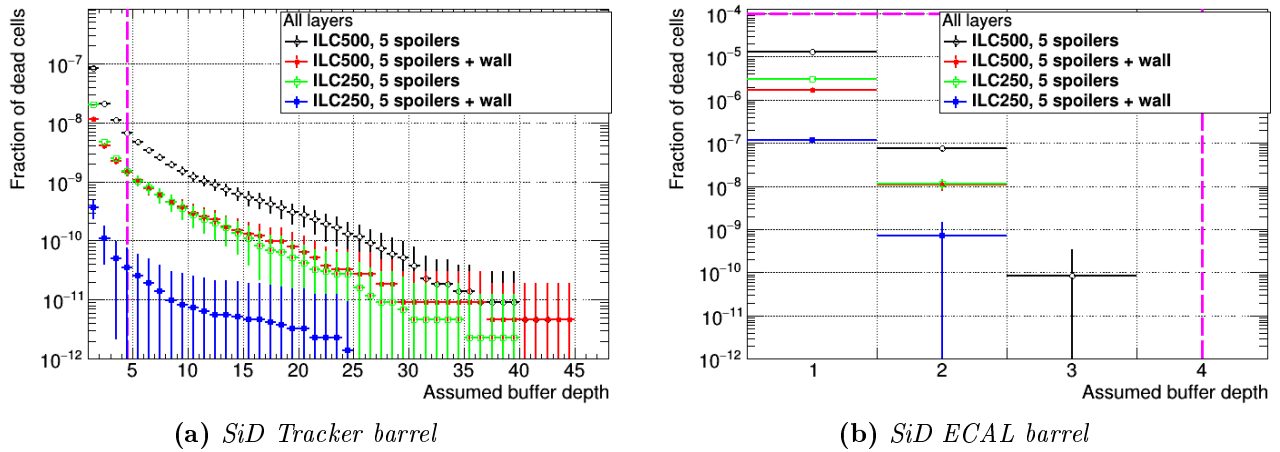
*The dashed lines indicate the the buffer depth of four for the current sensor design, and the guideline of  $10^{-4}$  for a critical acceptance limit.*

# B

## Appendix B.

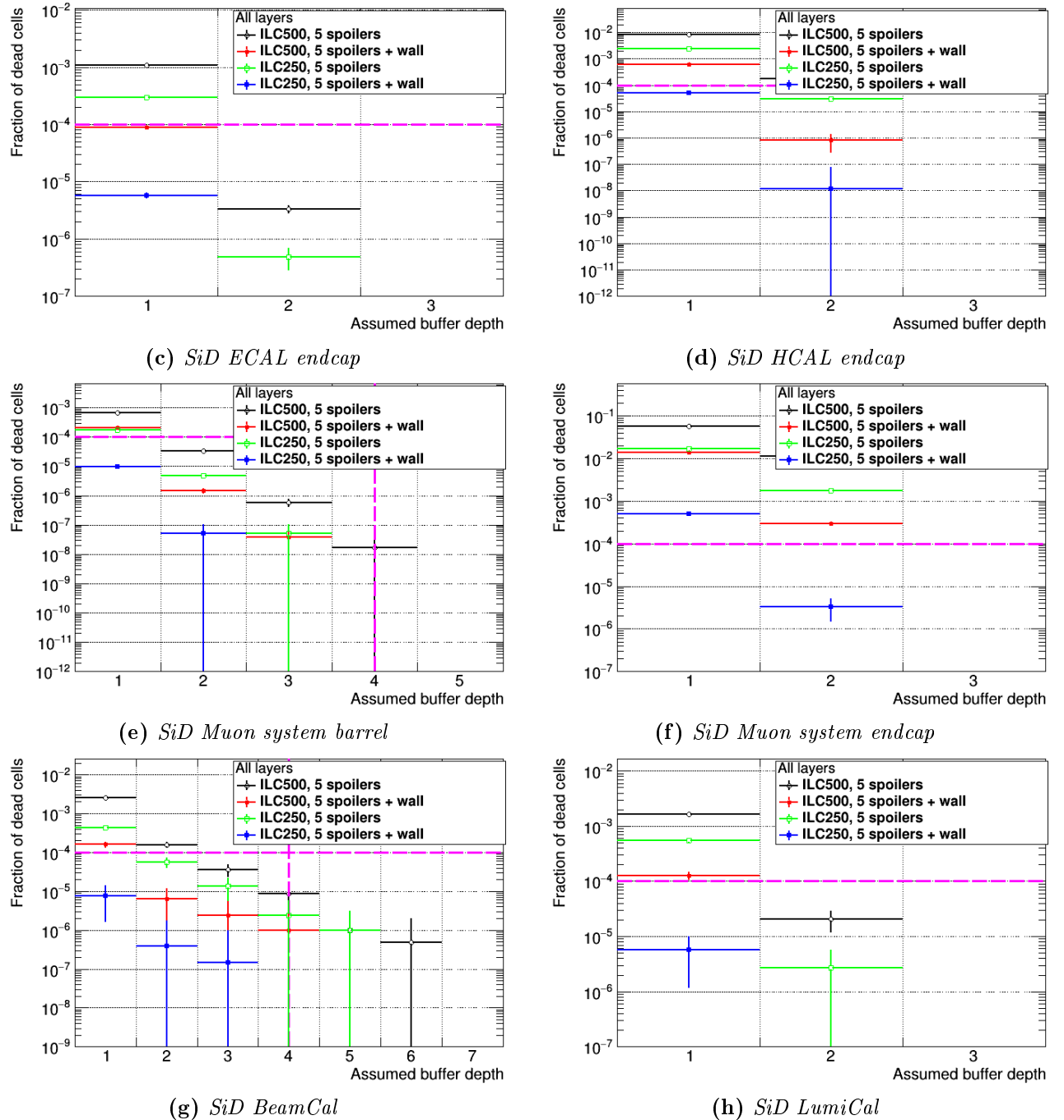
# Muon background from the Beam Delivery System

Figure B.1 shows occupancy plots belonging to the study of the muons from the Beam Delivery System (BDS) presented in Chapter 6.



**Figure B.1.:** *BDS muon background occupancy in the SiD subdetectors after a full bunch train (1312 bunch crossings). The plots show the fraction of dead cells with respect to the total number of cells in the respective SiD subdetector.*

*The dashed lines indicate the the buffer depth of four for the current sensor design, and the guideline of  $10^{-4}$  for a critical acceptance limit.*



**Figure B.1.:** BDS muon background occupancy in the SiD subdetectors after a full bunch train (1312 bunch crossings). The plots show the fraction of dead cells with respect to the total number of cells in the respective SiD subdetector. The dashed lines indicate the the buffer depth of four for the current sensor design, and the guideline of  $10^{-4}$  for a critical acceptance limit.

# C

## Appendix C.

# Background from the main beam dumps

Figures C.1 and C.2 show the dose rate for the ILC main beam dump designs after certain cooling times. The full study is explained in Chapter 8.

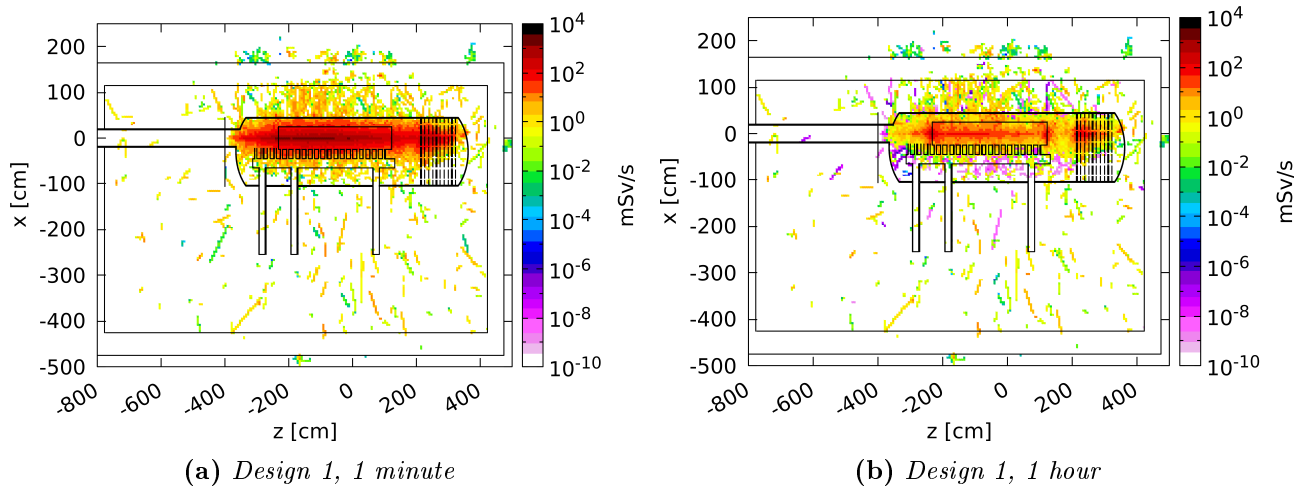


**Figure C.1.:** FLUKA result of the dose rate in the ILC beam dump Design 1 and their surrounding after one month of beam operation and certain cooling times. The cooling times are given in the captions of the individual subfigures. The view is in the  $xz$ -plane of the beam dump surrounding including the shielding walls. The color scale shows the dose rate in  $\text{mSv s}^{-1}$ .

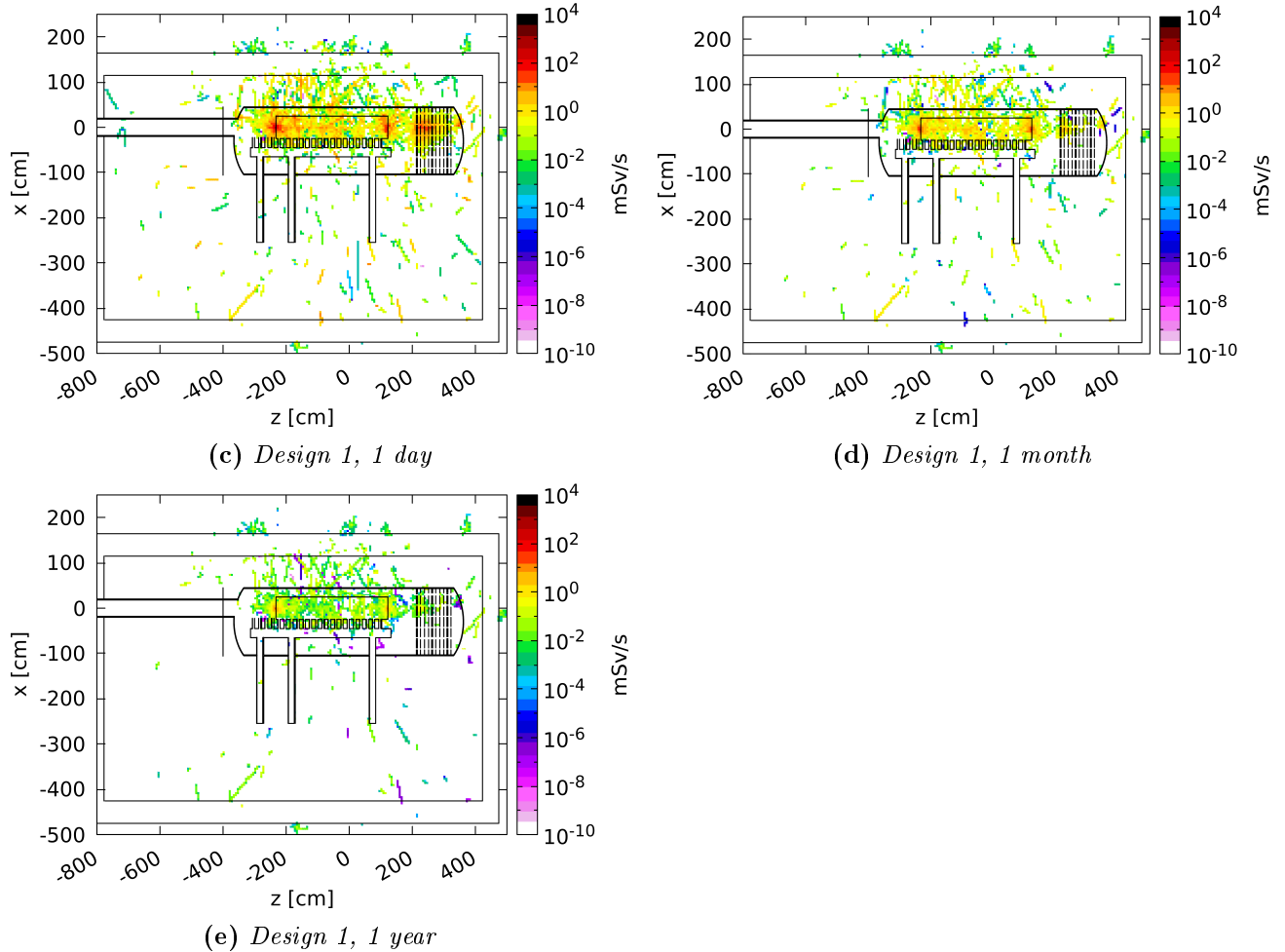


**Figure C.1.:** FLUKA result of the dose rate in the ILC beam dump Design 1 and their surrounding after one month of beam operation and certain cooling times. The cooling times are given in the captions of the individual subfigures. The view is in the  $xz$ -plane of the beam dump surrounding including the shielding walls. The color scale shows the dose rate in  $\text{mSv s}^{-1}$ .

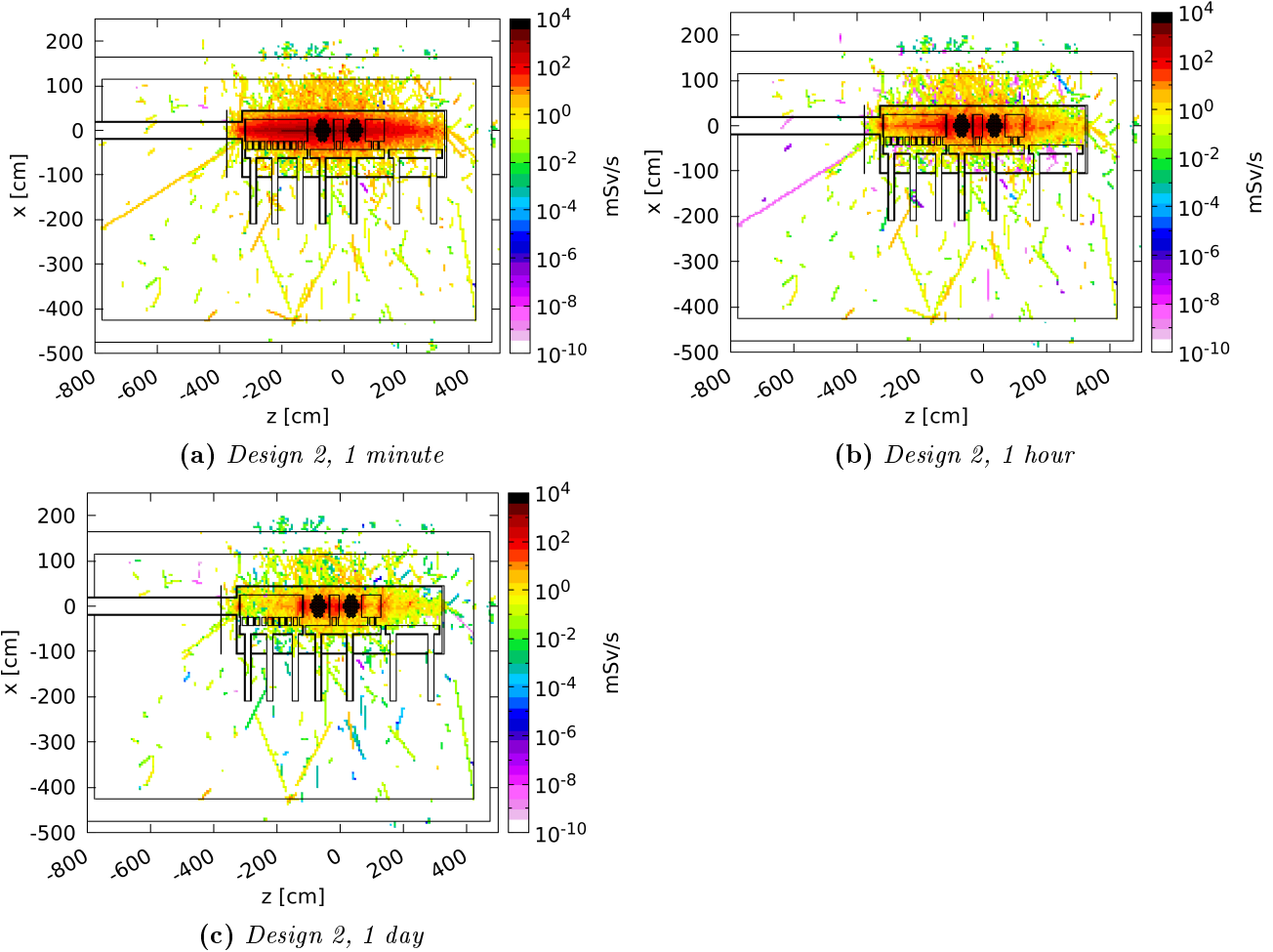


**Figure C.2.:** FLUKA result of the dose rate in the ILC beam dump Design 2 and their surrounding after one month of beam operation and certain cooling times. The cooling times are given in the captions of the individual subfigures. The view is in the xz-plane of the beam dump surrounding including the shielding walls. The color scale shows the dose rate in  $\text{mSv s}^{-1}$ .

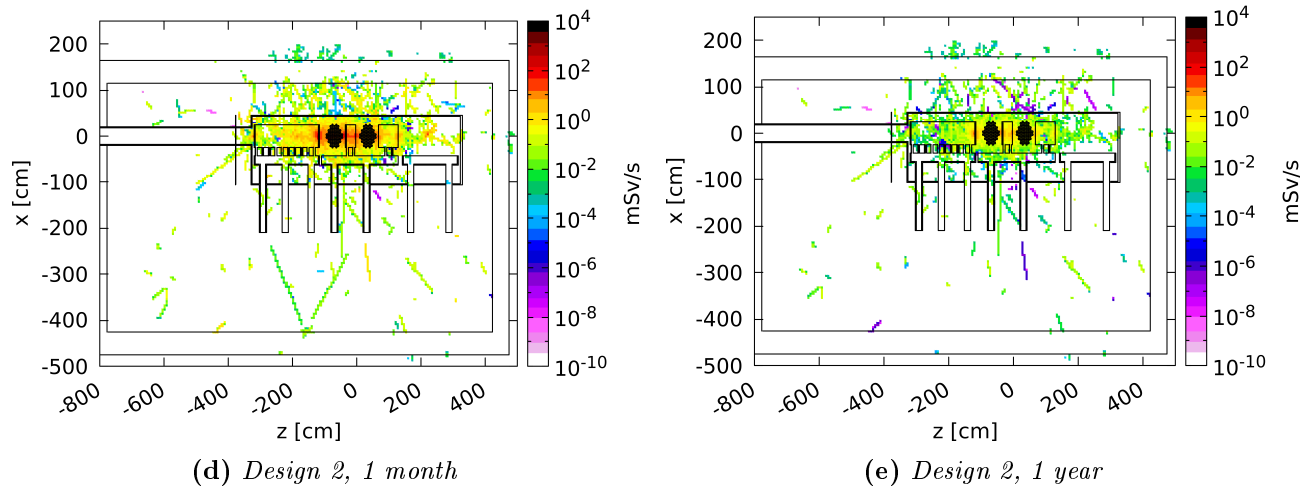


**Figure C.2.:** FLUKA result of the dose rate in the ILC beam dump Design 2 and their surrounding after one month of beam operation and certain cooling times. The cooling times are given in the captions of the individual subfigures. The view is in the xz-plane of the beam dump surrounding including the shielding walls. The color scale shows the dose rate in  $\text{mSv s}^{-1}$ .

# Bibliography

- [1] G. Aad et al. [ATLAS Collaboration]. “Observation of a new particle in the search for the Standard Model Higgs boson with the ATLAS detector at the LHC”. In: *Physics Letters B* 716.1 (2012), pages 1 –29. ISSN: 0370-2693. DOI: <https://doi.org/10.1016/j.physletb.2012.08.020>. URL: <http://www.sciencedirect.com/science/article/pii/S037026931200857X> (cited on pages 1, 8, 24).
- [2] S. Chatrchyan et al. [CMS Collaboration]. “Observation of a new boson at a mass of 125 GeV with the CMS experiment at the LHC”. In: *Physics Letters B* 716.1 (2012), pages 30 –61. ISSN: 0370-2693. DOI: <https://doi.org/10.1016/j.physletb.2012.08.021>. URL: <http://www.sciencedirect.com/science/article/pii/S0370269312008581> (cited on pages 1, 8, 24).
- [3] CERN. *The Large Hadron Collider*. <https://home.cern/topics/large-hadron-collider>. 2018 (cited on page 1).
- [4] D. Griffiths. *Introduction to Elementary Particles*. Second Edition. WILEY-VCH Verlag GmbH & Co. KGaA, Weinheim, 2010. ISBN: 978-3-527-40601-2 (cited on pages 3, 4, 5, 6).
- [5] E. Rutherford. “The scattering of alpha and beta particles by matter and the structure of the atom”. In: *Phil. Mag. Ser. 6* 21 (1911), pages 669–688. DOI: [10.1080/14786440508637080](https://doi.org/10.1080/14786440508637080) (cited on page 3).
- [6] A. Salam, J. C. Ward. “Electromagnetic and weak interactions”. In: *Physics Letters* 13.2 (1964), pages 168–171. ISSN: 0031-9163. DOI: [https://doi.org/10.1016/0031-9163\(64\)90711-5](https://doi.org/10.1016/0031-9163(64)90711-5). URL: <http://www.sciencedirect.com/science/article/pii/0031916364907115> (cited on page 4).
- [7] S. Weinberg. “A Model of Leptons”. In: *Phys. Rev. Lett.* 19 (21 Nov. 1967), pages 1264–1266. DOI: [10.1103/PhysRevLett.19.1264](https://doi.org/10.1103/PhysRevLett.19.1264). URL: <https://link.aps.org/doi/10.1103/PhysRevLett.19.1264> (cited on page 4).
- [8] S. Glashow. “Partial-symmetries of weak interactions”. In: *Nuclear Physics* 22.4 (1961), pages 579–588. ISSN: 0029-5582. DOI: [https://doi.org/10.1016/0029-5582\(61\)90469-2](https://doi.org/10.1016/0029-5582(61)90469-2). URL: <http://www.sciencedirect.com/science/article/pii/0029558261904692> (cited on page 4).
- [9] A. Salam, J. C. Ward. “On a Gauge Theory of Elementary Interactions”. In: *Physical Review* 19 (Nov. 1964), pages 165–170 (cited on page 4).
- [10] M. Gell-Mann. “The Eightfold Way: A Theory of strong interaction symmetry”. In: *CTSL-20, TID-12608* (1961) (cited on page 4).
- [11] C. Patrignani et al. (Particle Data Group). “Review of Particle Physics”. In: *Chin. Phys. C*40.10 (2016), page 100001. DOI: [10.1088/1674-1137/40/10/100001](https://doi.org/10.1088/1674-1137/40/10/100001) (cited on pages 4, 7, 29, 35).
- [12] MissMJ. *Standard Model of Elementary Particles*. [https://commons.wikimedia.org/wiki/File:Standard\\_Model\\_of\\_Elementary\\_Particles.svg](https://commons.wikimedia.org/wiki/File:Standard_Model_of_Elementary_Particles.svg). Licensed under the Creative Commons Attribution 3.0 Unported license (cited on page 4).

- [13] J.-C. Brient. *Improving the Jet Reconstruction with the Particle Flow Method; an Introduction*. CALOR04 conference proceedings, Perugia April 2004, <https://arxiv.org/abs/physics/0412149>. 2004 (cited on pages 7, 48).
- [14] X. Mo et al. “Physics cross sections and event generation of e+ e- annihilations at the CEPC”. In: *Chinese Physics C* 40.3 (2016), page 033001. URL: <http://stacks.iop.org/1674-1137/40/i=3/a=033001> (cited on page 9).
- [15] J. Stirling (Imperial College London). *Parton Luminosity and Cross Section Plots*. [http://www.hep.ph.ic.ac.uk/~wstirlin/plots/crosssections2012\\_v5.pdf](http://www.hep.ph.ic.ac.uk/~wstirlin/plots/crosssections2012_v5.pdf) (cited on page 9).
- [16] K. Yokoya et al. “Beam-beam phenomena in linear colliders”. In: *Frontiers of Particle Beams, Lecture Notes in Physics* 400 (1992). Edited by M. Dienes et al. (cited on pages 10, 11).
- [17] A. Sailer. “Radiation and Background Levels in a CLIC Detector due to Beam-Beam Effects, Optimisation of Detector Geometries and Technologies”. PhD thesis. 2012. URL: <https://edoc.hu-berlin.de/bitstream/handle/18452/17305/sailer.pdf?sequence=1> (cited on page 10).
- [18] F. Andrianala et al. “Beam parameter optimization at CLIC using the process e+ e- → HZ → Hqq at 380GeV”. In: *Nuclear Instruments and Methods in Physics Research Section A: Accelerators, Spectrometers, Detectors and Associated Equipment* 842 (2017), pages 76–85. ISSN: 0168-9002. DOI: <https://doi.org/10.1016/j.nima.2016.10.046>. URL: <http://www.sciencedirect.com/science/article/pii/S0168900216310919> (cited on page 10).
- [19] A. Vogel. “Beam-Induced Backgrounds in Detectors at the ILC”. Universität Hamburg, Diss., 2008. PhD thesis. 2008. DOI: 10.3204/DESY-THESIS-2008-036. URL: <https://bib-pubdb1.desy.de/record/84444> (cited on page 10).
- [20] T. Barklow et al. *A Study of the Impact of High Cross Section ILC Processes on the SiD Detector Design*. <https://arxiv.org/abs/1609.07816v1>. Sept. 2016 (cited on pages 12, 54, 73).
- [21] E. Rutherford. “Collision of alpha particles with light atoms. IV. An anomalous effect in nitrogen”. In: *The London, Edinburgh, and Dublin Philosophical Magazine and Journal of Science* 37.222 (1919), pages 581–587. DOI: 10.1080/14786440608635919 (cited on page 15).
- [22] M. Livingston, J. Blewett. *An Introduction to Particle Accelerators*. McGraw-Hill Bool Company, Inc., 1962 (cited on page 15).
- [23] E. Wilson. *An Introduction to Particle Accelerators*. First Edition. Oxford University Press, 2001. ISBN: 0-19-850829-8 (cited on pages 16, 17).
- [24] F. Hinterberger. *Physik der Teilchenbeschleuniger und Ionenoptik*. Second Edition. Springer-Verlag Berlin Heidelberg, 2008. ISBN: 978-3-540-75281-3. DOI: 10.1007/978-3-540-75282-0 (cited on pages 16, 19).
- [25] C. Adolphi et al. [ILC Collaboration]. *The International Linear Collider Technical Design Report - Volume 3.I: Accelerator R&D in the Technical Design Phase*. arXiv:1306.6353 [physics.acc-ph]. 2013 (cited on pages 16, 28).
- [26] P. Castro (Accelerator Physics Group (MPY), DESY). *Introduction to Accelerator Physics*. DESY Summer Student Programme 2013 - Common Lectures and HEP Lectures, <https://indico.desy.de/getFile.py/access?contribId=4&resId=0&materialId=slides&confId=7744>. July 2013 (cited on page 16).
- [27] J. Eichmeier, M. Thumm. *Vacuum Electronics: Components and Devices*. Springer-Verlag Berlin Heidelberg, 2008. ISBN: 978-3-540-71928-1 (cited on page 18).

[28] Andre.holzner. *Magnetic field of an idealized quadrupole with forces*. [https://en.wikipedia.org/wiki/File:Magnetic\\_field\\_of\\_an\\_idealized\\_quadrupole\\_with\\_forces.svg](https://en.wikipedia.org/wiki/File:Magnetic_field_of_an_idealized_quadrupole_with_forces.svg). Licensed under the Creative Commons Attribution 3.0 Unported license. 2012 (cited on page 19).

[29] H. Wiedemann. *Particle Accelerator Physics*. Third Edition. Springer-Verlag Berlin Heidelberg, 2007. ISBN: 978-3-540-49043-2 (cited on pages 20, 21, 23).

[30] T. Wangler. *RF Linear Accelerators*. Second Edition. WILEY-VCH Verlag GmbH & Co. KGaA, Weinheim, 2008. ISBN: 978-3-527-40680-7 (cited on page 20).

[31] M. Conte, W. MacKay. *An Introduction to the Physics of Particle Accelerators*. Second Edition. World Scientific Publishing Co. Pte. Ltd., Singapore, 2008. ISBN: 981-27-7960-4 (cited on page 20).

[32] A.-S. Müller. *Phase focusing*. Illustrations in lecture about Accelerator Physics held at Karlsruhe Institute of Technology (KIT), Karlsruhe. 2012 (cited on page 22).

[33] M. Kuriki. *Electron source for Linear Colliders*. 10th International Accelerator School for Linear Colliders. Dec. 2016. URL: <https://agenda.linearcollider.org/event/7333/contributions/38081/attachments/31043/46497/MKA2-1.pdf> (cited on page 23).

[34] J. Wenninger (CERN). “Approaching Nominal Performance at LHC”. In: ISBN: 978-3-95450-182-3. Proceedings of IPAC2017, Copenhagen, Denmark. 2017. URL: <http://accelconf.web.cern.ch/AccelConf/ipac2017/papers/moyaa1.pdf> (cited on page 23).

[35] M. Aaboud et al. [ATLAS Collaboration]. “Measurement of the Inelastic Proton-Proton Cross Section at  $\sqrt{s} = 13$  TeV with the ATLAS Detector at the LHC”. In: *Phys. Rev. Lett.* 117 (18 Oct. 2016), page 182002. DOI: 10.1103/PhysRevLett.117.182002. URL: <https://link.aps.org/doi/10.1103/PhysRevLett.117.182002> (cited on page 24).

[36] J.-E. Augustin et al. “Discovery of a Narrow Resonance in e+ e- Annihilation”. In: *Phys. Rev. Lett.* 33 (23 1974), pages 1406–1408. DOI: 10.1103/PhysRevLett.33.1406. URL: <https://link.aps.org/doi/10.1103/PhysRevLett.33.1406> (cited on page 24).

[37] M. Perl et al. “Evidence for Anomalous Lepton Production in e+ e- Annihilation”. In: *Phys. Rev. Lett.* 35 (22 Dec. 1975), pages 1489–1492. DOI: 10.1103/PhysRevLett.35.1489. URL: <https://link.aps.org/doi/10.1103/PhysRevLett.35.1489> (cited on page 24).

[38] SLAC National Accelerator Laboratory, Menlo Park, CA. *SPEAR History*. URL: <https://www-ssrl.slac.stanford.edu/content/spear3/spear-history> (cited on page 24).

[39] K. Wille. *The Physics of Particle Accelerators: An Introduction*. Oxford University Press, 2000. ISBN: 0-19-8505550-7 (cited on pages 25, 38).

[40] *The Large Electron-Positron Collider*. Archived on the CERN Document Server: <http://cds.cern.ch/record/1997351>. July 2012. URL: <https://home.cern/about/accelerators/large-electron-positron-collider> (cited on pages 26, 27).

[41] *Limitations on performance of e+e- storage rings and linear collider beam systems at high energy*. Proceedings of the workshop on possibilities and limitations of accelerators and detectors, held at Fermi National Accelerator Laboratory, October 15-21, 1978. Fermi National Accelerator Laboratory. Batavia, IL: Fermi National Accelerator Laboratory, 1979. URL: <http://www.slac.stanford.edu/spires/find/books/www?cl=QCD183:I22:1978> (cited on page 26).

- [42] H. Schopper. *LEP - The Lord of the Collider Rings at CERN 1980-2000: The Making, Operation and Legacy of the World's Largest Scientific Instrument*. Springer Science & Business Media, 2009. ISBN: 978-3-540-89300-4 (cited on page 26).
- [43] T. Behnke et al. [ILC Collaboration]. *The International Linear Collider Technical Design Report - Volume 1: Executive Summary*. arXiv:1306.6327 [physics.acc-ph]. 2013 (cited on pages 28, 36, 37, 41, 42, 43, 44, 47, 56, 61, 63, 112).
- [44] H. Baer et al. [ILC Collaboration]. *The International Linear Collider Technical Design Report - Volume 2: Physics*. arXiv:1306.6352 [physics.acc-ph]. 2013 (cited on pages 28, 32, 49).
- [45] C. Adolphsen et al. [ILC Collaboration]. *The International Linear Collider Technical Design Report - Volume 3.II: Accelerator Baseline Design*. arXiv:1306.6328 [physics.acc-ph]. 2013 (cited on pages 28, 37, 38, 39, 41, 42, 43, 109, 120).
- [46] T. Behnke et al. [ILC Collaboration]. *The International Linear Collider Technical Design Report - Volume 4: Detectors*. arXiv:1306.6329 [physics.acc-ph]. 2013 (cited on pages 28, 47, 48, 49, 50, 51, 53, 54, 58, 126).
- [47] ATLAS Collaboration. “Event display of a H->4e candidate event”. General Photo. July 2012. URL: <https://cds.cern.ch/record/1459495> (cited on page 28).
- [48] A. Miyamoto. “ILC event examples with ILD simulation”. Aug. 2016. URL: <http://www-jlc.kek.jp/~miyamoto/evdisp/html/250-zh-e1e1h/frontview.png> (cited on page 28).
- [49] K. Fujii et al. *Physics Case for the 250 GeV Stage of the International Linear Collider*. arXiv:1710.07621v2, <https://arxiv.org/pdf/1710.07621.pdf>. Nov. 2017 (cited on pages 30, 31, 32, 36, 45, 46).
- [50] K. Fuji et al. *Physics Case for the International Linear Collider*. <https://arxiv.org/abs/1506.05992v2>. June 2015 (cited on pages 31, 34, 36).
- [51] J. Tian, K. Fujii. *Measurement of Higgs couplings and self-coupling at the ILC*. arXiv:1311.6528, <https://arxiv.org/pdf/1311.6528.pdf>. Nov. 2013 (cited on page 32).
- [52] J. Tian. *ILC 250 (focusing on Higgs physics)*. Annual ILC detector meeting, KEK, [https://agenda.linearcollider.org/event/7489/contributions/38316/attachments/31416/47307/ILC250\\_20170331\\_AnnualDetectorMeeting.pdf](https://agenda.linearcollider.org/event/7489/contributions/38316/attachments/31416/47307/ILC250_20170331_AnnualDetectorMeeting.pdf). Mar. 2017 (cited on page 33).
- [53] K. Fuji et al. *The Potential of the ILC for Discovering New Particles*. <https://arxiv.org/abs/1702.05333>. Feb. 2017 (cited on pages 34, 35, 36).
- [54] C. Patrignani et al. (Particle Data Group). “Review of Particle Physics”. In: *Chin. Phys.* C40.10 (2016). 2017 update, page 100001 (cited on page 34).
- [55] J. Strube. “Measurement of the Higgs Boson Coupling to the Top Quark and the Higgs Boson Self-coupling at the ILC”. In: *Nuclear and Particle Physics Proceedings* 273 (2016). 37th International Conference on High Energy Physics (ICHEP), pages 2463–2465. ISSN: 2405-6014. DOI: <https://doi.org/10.1016/j.nuclphysbps.2015.09.426>. URL: <http://www.sciencedirect.com/science/article/pii/S2405601415009153> (cited on page 35).
- [56] H. Haber. “Introductory low-energy supersymmetry”. In: *Proceedings, Theoretical Advanced Study Institute (TASI 92): From Black Holes and Strings to Particles: Boulder, USA, June 1-26, 1992*. 1993, pages 589–686 (cited on page 35).

[57] Y. Chae, M. Perelstein. “Dark Matter Search at a Linear Collider: Effective Operator Approach”. In: *JHEP* 05 (2013), page 138. DOI: 10.1007/JHEP05(2013)138. arXiv: 1211.4008 [hep-ph] (cited on page 36).

[58] ILC GDE. *ILC Technical Design Report*. 2013. URL: <https://www.linearcollider.org/ILC/Publications/Technical-Design-Report> (cited on page 37).

[59] H. Olsen, L. Maximon. “Photon and Electron Polarization in High-Energy Bremsstrahlung and Pair Production with Screening”. In: *Phys. Rev.* 114 (3 May 1959), pages 887–904. DOI: 10.1103/PhysRev.114.887. URL: <https://link.aps.org/doi/10.1103/PhysRev.114.887> (cited on page 38).

[60] A. Ushakov. *Yield Estimation of Undulator Positron Source*. Talk at LCWS17 in Strasbourg, <https://agenda.linearcollider.org/event/7645/contributions/40012/attachments/32382/49171/Ushakov-LCWS17.pdf>. Oct. 2017 (cited on page 38).

[61] D. Reschke et al. “Performance in the vertical test of the 832 nine-cell 1.3 GHz cavities for the European X-ray Free Electron Laser”. In: *Phys. Rev. Accel. Beams* 20 (4 Apr. 2017), page 042004. DOI: 10.1103/PhysRevAccelBeams.20.042004. URL: <https://link.aps.org/doi/10.1103/PhysRevAccelBeams.20.042004> (cited on page 40).

[62] N. Walker. *The European XFEL - Experience and Lessons Learned*. Talk at LCWS17 in Strasbourg, <https://agenda.linearcollider.org/event/7645/contributions/39682/attachments/32185/48802/LCWS17-NJW.pdf>. Oct. 2017 (cited on page 40).

[63] European X-Ray Free-Electron Laser Facility GmbH. *The European XFEL*. URL: [https://www.xfel.eu/index\\_eng.html](https://www.xfel.eu/index_eng.html) (cited on page 40).

[64] G. Burt et al. *Crab cavities for linear colliders*. arXiv:0810.2880 [physics.acc-ph]. 2008 (cited on page 42).

[65] ILC Technical and Change Management Board. *Change Request No. ILC-CR-0016, Luminosity Improvement at 250GeV CM*. EDMS No: D\*1159725. Sept. 2017 (cited on pages 42, 43, 69).

[66] O. Brüning, et al. *LHC Design Report, Volume I*. CERN-2004-003-V-1, <https://cds.cern.ch/record/782076/files/CERN-2004-003-V1-ft.pdf>. 2004 (cited on page 43).

[67] ATLAS collaboration. *Characterization of Interaction-Point Beam Parameters Using the pp Event-Vertex Distribution Reconstructed in the ATLAS Detector at the LHC*. ATLAS-CONF-2010-027, <http://cds.cern.ch/record/1277659/files/ATLAS-CONF-2010-027.pdf>. May 2010 (cited on page 43).

[68] ICFA panel. *ICFA Statement on the ILC Operating at 250 GeV as a Higgs Boson Factory*. LCB Conclusion Report, <http://icfa.fnal.gov/wp-content/uploads/ICFA-Statement-Nov2017.pdf>. Nov. 2017 (cited on page 44).

[69] S. Michizono. *ILC accelerator status and optimization*. Talk at LCWS17 in Strasbourg, <https://agenda.linearcollider.org/event/7645/contributions/39680/attachments/32180/48800/LCWS2017v3.pdf>. Oct. 2017 (cited on pages 44, 45).

[70] M. Stanitzki, N. Walker (DESY). *Cost reduction of the ILC 250GeV stage*. Private communication. Dec. 2017 (cited on page 44).

[71] ILC Strategy Council. *Announcement of the results of the ILC candidate site evaluation in Japan*. <http://ilc-str.jp/topics/2013/08281826/>. Aug. 2014 (cited on page 46).

[72] B. Warmbein. “The road to Kitakami”. In: *LC Newsline - The Newsletter of the Linear Collider Community* (Feb. 2014). <http://newsline.linearcollider.org/2014/02/20/the-road-to-kitakami/> (cited on page 46).

[73] M. Oriunno. *SiD detector visualization, New Magnet Design pic1*. SID Engineering Website, <https://confluence.slac.stanford.edu/display/SiD/SID+Engineering>. 2016 (cited on pages 47, 48, 53).

[74] M. Stanitzki. *The SiD Detector at the ILC - Precision physics at the energy frontier*. Talk at High Energy Physics Conference at HKUST Jockey Club Institute for Advanced Study, [http://ias.ust.hk/program/shared\\_doc/2017/201701hep/HEP\\_20170125\\_Marcel\\_Stanitzki.pdf](http://ias.ust.hk/program/shared_doc/2017/201701hep/HEP_20170125_Marcel_Stanitzki.pdf). Jan. 2017 (cited on pages 49, 51, 52).

[75] H. Aihara et al. “SiD Letter of Intent”. In: (2009). arXiv: 0911.0006 [physics.ins-det] (cited on page 49).

[76] A. White. *The SiD Detector - Status and Plans*. Talk at LCWS17 in Strasbourg, [https://agenda.linearcollider.org/event/7645/contributions/39686/attachments/32174/48776/SiD\\_Plenary\\_LCWS2017\\_Oct23.pdf](https://agenda.linearcollider.org/event/7645/contributions/39686/attachments/32174/48776/SiD_Plenary_LCWS2017_Oct23.pdf). Oct. 2017 (cited on page 50).

[77] M. Stanitzki. *The International Linear Collider, Precision physics at the energy frontier*. <http://agenda.linearcollider.org/event/7389/attachments/30605/45783/pnnl.pdf>. Sept. 2016 (cited on page 50).

[78] R. Lu [CMS Collaboration]. “Status and Plan for The Upgrade of The CMS Pixel Detector”. In: *Nuclear and Particle Physics Proceedings* 273 (2016). 37th International Conference on High Energy Physics (ICHEP), pages 1029–1033. DOI: <https://doi.org/10.1016/j.nuclphysbps.2015.09.161>. URL: <http://www.sciencedirect.com/science/article/pii/S2405601415006501> (cited on page 50).

[79] H. Spieler. *Semiconductor Detector Systems*. Series on Semiconductor Science and Technology. OUP Oxford, 2005. ISBN: 9780198527848. URL: <https://books.google.de/books?id=MUMb3y37yqYC> (cited on page 50).

[80] Deutsches Elektronen-Synchrotron. *Official Website for the TCMB: "Change Management. Maintaining the ILC Technical Design"*. <http://ilc.desy.de/cm/>. 2017 (cited on page 53).

[81] ILC Technical and Change Management Board. *Change Request No. ILC-CR-002, Baseline optics to provide for a single L\**. EDMS No: D\*1082495. 2014 (cited on page 53).

[82] B. Parker, A. Seryi. “Compensation of the effects of a detector solenoid on the vertical beam orbit in a linear collider”. In: *Physical Review Special Topics - Accelerators and Beams* 8.4 (2005), page 041001 (cited on page 54).

[83] D. Schulte. “Study of Electromagnetic and Hadronic Background in the Interaction Region of the TESLA Collider”. DESY-TESLA-97-08, TESLA-97-08. PhD thesis. 1997. URL: <http://inspirehep.net/record/888433/files/shulte.pdf> (cited on page 57).

[84] S. Agostinelli et al. “GEANT4: A Simulation toolkit”. In: *Nucl. Instrum. Meth. A* 506 (2003), pages 250–303. DOI: [10.1016/S0168-9002\(03\)01368-8](https://doi.org/10.1016/S0168-9002(03)01368-8) (cited on page 57).

[85] J. Allison et al. “Geant4 developments and applications”. In: *IEEE Transactions on Nuclear Science* 53.1 (Feb. 2006), pages 270–278. ISSN: 0018-9499. DOI: [10.1109/TNS.2006.869826](https://doi.org/10.1109/TNS.2006.869826) (cited on page 57).

[86] A. Schütz, J. Strube. *Confluence page Simulation of the background events for the SiD detector*. <https://wikis.bris.ac.uk/display/sid/Simulation+of+the+background+events+for+the+SiD+detector> (cited on page 58).

[87] L. Garren. *StdHep 5.06.01*. [http://cd-docdb.fnal.gov/cgi-bin/RetrieveFile?docid=903&filename=stdhep\\_50601\\_manual.pdf&version=15](http://cd-docdb.fnal.gov/cgi-bin/RetrieveFile?docid=903&filename=stdhep_50601_manual.pdf&version=15). Nov. 2006 (cited on page 58).

[88] F. Gaede. *LCIO*. <http://lcio.desy.de/>. Apr. 2016 (cited on page 58).

[89] N. Graf, J. McCormick. “Simulator for the linear collider (SLIC): A tool for ILC detector simulations”. In: *AIP Conf. Proc.* 867 (2006). [,503(2006)], pages 503–512. DOI: 10.1063/1.2396991 (cited on page 58).

[90] FreeHep. *WIRED4 - World-Wide Web Interactive Remote Event Display*. <http://wired4.freehep.org/> (cited on pages 58, 85).

[91] A. Schütz. “Impact of the new ILC250 beam parameter set on the SiD vertex detector occupancy arising from  $e^+e^-$  pair background”. In: *International Workshop on Future Linear Collider (LCWS2017) Strasbourg, France, October 23-27, 2017*. 2018. arXiv: 1801.04156. URL: <https://inspirehep.net/record/1647951/files/arXiv:1801.04156.pdf> (cited on page 63).

[92] ILC Technical and Change Management Board, B. List. *ILC Technical and Change Management Board meeting at LCWS17*. <https://agenda.linearcollider.org/event/7645/sessions/4531/#20171026>. Sept. 2017 (cited on page 72).

[93] L. Keller (SLAC). *Results from MUCARLO simulations*. Private email conversation (cited on pages 81, 82, 83, 84).

[94] G. White. *BDS Muon Backgrounds and Shielding*. Talk at LCWS16 in Morioka, Japan, [https://agenda.linearcollider.org/event/7371/contributions/38120/attachments/30983/46387/ILC\\_muons.pptx](https://agenda.linearcollider.org/event/7371/contributions/38120/attachments/30983/46387/ILC_muons.pptx). Dec. 2016 (cited on pages 81, 85).

[95] L. Keller. *Muon Background in a 1.0 TeV Linear Collider*. <http://www.slac.stanford.edu/pubs/slacpubs/6250/slac-pub-6385.pdf>. 1993 (cited on pages 81, 82).

[96] A. Drozdin et al. “Suppression of muon backgrounds generated in the ILC beam delivery system”. In: *Conf. Proc. C070625* (2007). PAC07-THPMN100, SLAC-PUB-12741, FERMILAB-CONF-07-276-AD, page 2945. DOI: 10.2172/922037, 10.1109/PAC.2007.4440629 (cited on pages 82, 83).

[97] S. Rokni, L. Keller, W. Nelson. *Calculation of Muon Background in Electron Accelerators using the Monte Carlo Computer Program MUCARLO*. <http://www.slac.stanford.edu/cgi-wrap/getdoc/slac-pub-7054.pdf>. 1995 (cited on page 82).

[98] L. Keller. *Muon Background in a 0.5 TeV Linear Collider*. <http://www.slac.stanford.edu/pubs/slacpubs/5500/slac-pub-5533.pdf>. 1991 (cited on page 82).

[99] U. Rohrer. *Graphic Turtle Framework*. [http://aea.web.psi.ch/Urs\\_Rohrer/MyWeb/turtle.htm](http://aea.web.psi.ch/Urs_Rohrer/MyWeb/turtle.htm) (cited on page 83).

[100] B. Fell et al. “Mechanical Design of Collimators for the ILC”. In: (Mar. 2018). EUROTeV-Report-2008-044. URL: [https://www.researchgate.net/publication/30419377\\_Mechanical\\_Design\\_of\\_Collimators\\_for\\_the\\_ILC](https://www.researchgate.net/publication/30419377_Mechanical_Design_of_Collimators_for_the_ILC) (cited on page 83).

- [101] N. Fuster-Martinez. “Beam Halo Collimation and Induced Wakefield Studies for Future Linear Colliders: the ATF2 Case”. Universidad de Valencia, Instituto de Fisica Corpuscular (IFIC). PhD thesis. 2017. URL: <http://roderic.uv.es/handle/10550/59295> (cited on pages 93, 94, 95, 104, 106, 107).
- [102] KEK-ATF. *Accelerator Test Facility (ATF)*. <http://atf.kek.jp/twiki/bin/view/Public/TopPageE?redirectedfrom=Public.WebHome>. 2015 (cited on page 93).
- [103] L. Nevay (RHUL). *2015 06 Visit to ATF2*. <https://twiki.ph.rhul.ac.uk/twiki/bin/view/PP/JAI/ATF2201506visit>. Feb. 2016 (cited on pages 95, 97).
- [104] N. Fuster-Martinez (IFIC, CERN). *ATF2 collaboration, measurements using the vertical beam halo collimator*. Private communication. 2016-2017 (cited on page 95).
- [105] N. Fuster-Martinez et al. “Design Study and Construction of a Transverse Beam Halo Collimation System for ATF2”. In: ISBN: 978-3-95450-168-7. Proc. 6th International Particle Accelerator Conference, Richmond, VA, USA, paper WEPMN059. 2015. URL: <http://jacow.org/IPAC2015/papers/wepmn059.pdf> (cited on pages 95, 96).
- [106] Hamamatsu Photonics K.K. Editorial Committee. *PHOTOMULTIPLIER TUBES - Basics and Applications*. Third Edition (Edition 3a with minor revisions). Hamamatsu Photonics K.K. Electron Tube Division, Aug. 2007 (cited on page 98).
- [107] Beam Delivery Simulation (BDSIM), Royal Holloway, University of London. *BDSIM*. <http://www.pp.rhul.ac.uk/bdsim/manual/>. Dec. 2017 (cited on page 101).
- [108] R. Chytracek et al. “Geometry Description Markup Language for Physics Simulation and Analysis Applications”. In: *IEEE Transactions on Nuclear Science* 53.5 (Oct. 2006), pages 2892–2896. ISSN: 0018-9499. DOI: [10.1109/TNS.2006.881062](https://doi.org/10.1109/TNS.2006.881062) (cited on page 101).
- [109] W. Pokorski. *Geometry Description Markup Language (GDML)*. <http://gdml.web.cern.ch/GDML/>. Apr. 2017 (cited on page 101).
- [110] CERN - BE/ABP Accelerator Beam Physics Group. *MAD - Methodical Accelerator Design*. <http://madx.web.cern.ch/madx/>. Mar. 2018 (cited on page 102).
- [111] L. Nevay (RHUL). *Elements in the ATF2 beamline*. <https://twiki.ph.rhul.ac.uk/twiki/bin/view/PP/JAI/ATF2201609visit>. July 2017 (cited on pages 103, 104, 105).
- [112] B. List. *ILC Beam Dump Specifications*. EDMS No: D\*1145045. Sept. 2016 (cited on page 110).
- [113] T. Böhlen et al. “The FLUKA Code: Developments and Challenges for High Energy and Medical Applications”. In: *Nuclear Data Sheets* 120 (2014), pages 211–214. ISSN: 0090-3752. DOI: <https://doi.org/10.1016/j.nds.2014.07.049>. URL: <http://www.sciencedirect.com/science/article/pii/S0090375214005018> (cited on page 110).
- [114] A. Ferrari et al. “FLUKA: a multi-particle transport code”. In: *CERN-2005-010, SLAC-R-773, INFN-TC-05-11* (2015) (cited on page 110).
- [115] V. Vlachoudis. “FLAIR: A Powerful But User Friendly Graphical Interface For FLUKA”. In: *Proc. Int. Conf. on Mathematics, Computational Methods & Reactor Physics (M&C 2009), Saratoga Springs, New York* (Apr. 2009) (cited on page 110).
- [116] B. Smith. *0-TB-0067-300-00-A, 0-TB-0067-210-00-A, 0-TB-0067-404-00-A, 0-TB-0067-410-00-A*. Technical report. Rutherford Appleton Laboratory, 2006 - 2007 (cited on page 111).

[117] K. Okuno et al. “Application of neutron shield concrete to neutron scattering instrument TAIKAN in J-PARC”. In: *Progress in Nuclear Science and Technology* 4 (Jan. 2014), pages 619–622 (cited on page 111).

[118] B. Smith. *18MW Water Beam Dump Concept*. Technical report. Report no. 088-D-006-01. CCLRC Technology Department - Project Engineering Division - Mechanical Design Group, Jan. 2007 (cited on page 112).

[119] Bundesamt für Strahlenschutz. *Ionisierende Strahlung, Grenzwerte im Strahlenschutz*. <https://www.bfs.de/DE/themen/ion/strahlenschutz/grenzwerte/grenzwerte.html>. Nov. 2017 (cited on page 116).

[120] Los Alamos National Security, LLC for the U.S. Department of Energy’s NNSA. *US standard ENDF/B data*. <https://t2.lanl.gov/nis/data/endf/>. 2011 (cited on page 119).

[121] S. Mughabghab. *Atlas of neutron resonances; 6th ed.* Amsterdam: Elsevier, 2018. URL: <https://cds.cern.ch/record/2291455> (cited on page 119).

[122] K. Moffeit et al. “Proposal to modify the polarimeter chicane in the ILC 14 mrad extraction line”. In: *SLAC-PUB-12425* (Mar. 2007). URL: <http://slac.stanford.edu/pubs/slacpubs/12250/slac-pub-12425.pdf> (cited on page 120).

[123] E. Marin et al. “ILC Extraction Line Simulations with TDR Parameters”. In: *SLAC-PUB-15938* (Apr. 2014). URL: <http://www.slac.stanford.edu/cgi-wrap/getdoc/slac-pub-15938.pdf> (cited on page 120).

[124] John Adams Institute for Accelerator Science at the Royal Holloway University of London. *BDSIM ILC model*. [https://bitbucket.org/jairhul/bdsim-ilc-model/src/3175c75648e8/bdsimTwiss-model/20160713/0\\_linearOptics/?at=master](https://bitbucket.org/jairhul/bdsim-ilc-model/src/3175c75648e8/bdsimTwiss-model/20160713/0_linearOptics/?at=master). 2016 (cited on page 122).

[125] G. White. *ILC lattice, Beam Delivery*. <https://bitbucket.org/whitegr/ilc-lattices/src/2d4fbf42e87638cca85f0a7fedd946b92bada923/deckfiles/BeamDelivery/ilc621.edl1.xsif?at=master&fileviewer=file-view-default>. 2016 (cited on page 122).

[126] B. Berman, S. Fultz. “Measurements of the giant dipole resonance with monoenergetic photons”. In: *Rev. Mod. Phys.* 47 (3 July 1975), pages 713–761. DOI: [10.1103/RevModPhys.47.713](https://doi.org/10.1103/RevModPhys.47.713). URL: <http://link.aps.org/doi/10.1103/RevModPhys.47.713> (cited on page 126).

[127] F. Richard et al., editor. *TESLA: The superconducting electron-positron linear collider with an integrated X-ray laser laboratory. Technical design report. Pt. 1: Executive summary*. Hamburg: DESY, 2001. ISBN: 3935702019. URL: <https://bib-pubdb1.desy.de/record/352463> (cited on page 127).

[128] N. Tesch. *ILC at DESY, Radiation Protection and Beam Dumps*. <http://www.desy.de/d3/html/ilc.html>. 2006 (cited on page 127).

[129] B. List, N. Walker (DESY). *Cost estimation for tunnel construction*. Private communication. Apr. 2018 (cited on page 129).

[130] *GuineaPig Manual (SLAC NLC webpage version)*. <http://www-sldnt.slac.stanford.edu/snowmass/Software/GuineaPig/gpman.pdf> (cited on page 137).



# Acknowledgements

First of all, I would like to express my gratitude to my supervisors Günter Quast, Eckhard Elsen, and Marcel Stanitzki for giving me the opportunity to develop my scientific skills, my knowledge, and my own personality. Thanks to the E-JADE funding, I traveled to conferences and workshops all over the world, and spent several months in Japan. The experiences I gained will be beneficial for my whole life.

My mentor Thomas Schörner-Sadenius was a great help during the whole time, both work-related and personally.

I enjoyed the enthusiastic collaboration with the SiD Optimization group. During the meetings, the knowledge transfer and guidance of the students was extremely fruitful and exemplary. At this point, I would like to thank especially Jan Strube for his continuous support.

For their help with proof reading and giving advice on various topics, I am very grateful to Nicholas Walker, Paul Schütze, and Jan Dreyling-Eschweiler.

For giving me advice and support for my research projects, I would like to thank several people who assisted me on different steps along the way. First, many thanks to Lewis Keller and Glen White, with whom I collaborated on the muon background study. Lewis provided me with the generated MUCARLO events, and answered every question I had. Thank you very much for that!

From Alfredo Ferrari, Francesco Cerutti, and Vasilis Vlachoudis I got expert advice on FLUKA, and how to get the results I needed for my ILC beam dump study. Thank you for your help and your patience.

Thanks also to Benno List, who gave me valuable input on the different aspects of the beam dump issues.

I will never forget the time in Japan, at ATF2 and the University of Tokyo. Not only the work experience I gained, but also the friends I met are a great gift. I am very grateful to the ATF collaboration for giving me the chance to work at this accelerator facility, and to learn a great many things about the operation of particle accelerators. I thank Nuria Fuster-Martinez for our fruitful and harmonic collaboration during and after the data-taking shifts at ATF2.

My deepest gratitude also goes to Sachio Komamiya who welcomed me into his working group at the University of Tokyo, and invited me to the beautiful Hanami party.

I would like to show my appreciation to Stewart Boogert and Laurie Nevay for their support and collaboration on my BDSIM simulation of ATF2.

But this is not all I took with me from Japan: Thanks to all the Terunuma's Turtles!

I will cherish the memories of our adventures in and outside of Japan. I hope the friends we gained will stick together even beyond the world of research.

At this point, I would like to thank again Glen White not only for his support during my time as a Ph.D student but also for being a true friend.

---

*Acknowledgements*

---

Finally, my biggest thanks goes to Phillip Hamnett. I am sure the last years would not have been the same without him. Thank you deeply for all the support and motivation you gave me every day.

Meinen herzlichsten Dank geht an meine Eltern und meine Familie, die mich immer unterstützen, bei allen Taten und Entscheidungen. Am Ende dieses Lebensabschnittes möchte ich ihnen danken für alles, was sie mir ermöglicht haben. Ohne sie würde ich nun sicherlich nicht diese Doktorarbeit in den Händen halten können. Danke euch!